Structure, Metamorphism, and Tectonics of the Northern Oman-UAE Ophiolite and Underlying Metamorphic Sole

Tyler Ambrose

Thesis submitted to the University of Oxford
for the degree of Doctor of Philosophy
in
Geology and Mineralogy



Department of Earth Sciences
and Linacre College,
University of Oxford

Michaelmas, 2017

Supervised by Prof. Mike Searle and Prof. Dave Waters

Declaration

The contents of this thesis are all my own work, except where otherwise stated. The views and opinions expressed herein are mine and not necessarily those of any other person or body unless so attributed.

Copyright ©, by Tyler Ambrose, 2017.
All rights reserved.

No part of the material protected by this copyright notice may be reproduced or utilised in any form or by any means, electronic or mechanical, including photocopying, recording or by any information storage and retrieval system, without written permission from the copyright owner.

Printed in the United Kingdom.

For Matt and Pauline Ambrose

Abstract

Structure, Metamorphism, and Tectonics of the Northern Oman-UAE Ophiolite and Underlying Metamorphic Sole

Tyler Ambrose
Linacre College, Oxford

Michaelmas, 2017

Ophiolites—thrust sheets of oceanic lithosphere that have been emplaced onto the continental margin—provide the opportunity to explore the structure and genesis of oceanic crust. As many ophiolites formed above subduction zones, they also allow for the investigation of mantle wedge and subduction interface processes. This thesis examines the Oman-United Arab Emirates (UAE) ophiolite, which is the largest and most intensely studied ophiolite on Earth. Three distinct problems are addressed. (1) Recent research has proposed that the architecture and tectonic evolution of the ophiolite in the UAE differs from in Oman. In Chapter 2, I test this hypothesis by integrating new geological mapping and field observations with previously published maps of the ophiolite in the UAE. My results indicate that the ophiolite is gently folded, but otherwise largely intact. I demonstrate that the architecture of the ophiolite in the UAE is not significantly different from in Oman. Thus, there is no basis for a different tectonic evolution as recently proposed. (2) Observations from experiments and small-scale natural shear zones indicate that volumetrically-minor phases can control strain localization. In Chapter 3, I test the hypothesis that minor phases control strain-localisation at plate boundaries. To do so, I analyzed peridotites from the base of the ophiolite, a palaeosubduction interface. My results demonstrate that minor phases limited olivine grain growth, which led to rheological weakening. (3) The mechanisms by which metamorphic soles detached from the downgoing slab and accreted to the hanging-wall mantle is unclear. In Chapter 4, I examine a transect across the metamorphic sole in the UAE. My results reveal that granulite formation was more extensive than is typically considered. I propose that granulite formation resulted in rheological strengthening, which caused the subduction interface to migrate into the downgoing slab and accrete the metamorphic sole.

Extended Abstract

Structure, Metamorphism, and Tectonics of the Northern Oman-UAE Ophiolite and Underlying Metamorphic Sole

Tyler Ambrose

Linacre College, Oxford

Michaelmas, 2017

Ophiolites are thrust-sheets of oceanic crust and upper mantle that have been emplaced onto continental margins. Ophiolites present the opportunity to directly examine the structure of oceanic lithosphere and investigate processes such as mantle melting, sea-floor spreading, and crustal genesis. Moreover, as many ophiolites formed above subduction zones, they also provide the opportunity to investigate mantle wedge and slab-interface processes. The Late-Cretaceous Oman-United Arab Emierates (UAE) ophiolite is the largest and most intensely studied ophiolite on Earth. The Oman-UAE ophiolite comprises Tethyan oceanic crust and upper mantle formed between ∼96.5–95.5 Ma at a spreading center above a newly-initiated intraoceanic subduction zone. The ophiolite was subsequently emplaced onto the previously passive continental margin of Arabia when the leading edge of the Arabian plate reached the subduction zone at ∼79 Ma. Immediately beneath ophiolite is the metamorphic sole, which comprises metavolcanic and metasedimentary rock that detached from the downgoing slab and accreted to the base of the hanging-wall mantle. Thus, the Oman-UAE

ophiolite provides the opportunity to study both sea-floor spreading and subduction-zone processes.

Despite the considerable insight provided by ophiolites and metamorphic soles, many questions regarding their tectonic evolution remain unresolved. This thesis presents three independent chapters that investigate different aspects of the ophiolite and metamorphic sole. Although this thesis focusses on the Oman-UAE ophiolite, each chapter has implications for other ophiolites, sea-floor spreading, and subduction-zone processes in general.

In chapter 2, I explore the structure and internal architecture (i.e., pseudostratigraphy) of the ophiolite in the UAE. Several recent studies, including the largest ever focused on the UAE, have suggested that the pseudostratigraphy of the ophiolite in the UAE is considerably different from Oman. This has led some researchers to propose that the UAE portion of the ophiolite underwent a separate magmatic and tectonic evolution. I present a profile along a new road-section in the UAE that reveals continuous exposure of the entire ophiolite section and places key constraints on the internal architecture. I infer the geometry of the ophiolite thrust sheet and propose a model for the structure, pseudostratigraphy, and evolution of the ophiolite in the UAE that is simplified, yet more consistent with geochemical and geochronological data. My results indicate that (1) the architecture of ophiolite in the UAE is similar to Oman and there is no reason to infer a different tectonic history, (2) the ophiolite sequence is gently folded but largely intact, (3) extension and magmatism during formation of the ophiolite was more broadly distributed than typically thought, and (4) the entire magmatic sequence was generated in a short time ($\sim$1 Myr) and thus the ophiolite cannot be compared to the long-lasting (>100 Myr) fast-spreading East Pacific rise.

In Chapter 3, I investigate the rheological evolution of peridotites from the base of the mantle section. Studies of experimentally deformed rocks and small-scale natural shear zones have demonstrated that volumetrically minor phases can control strain

localisation by limiting grain growth and promoting grain-size sensitive deformation mechanisms. These small-scale studies are often used to infer a critical role for minor phases in the development of plate boundaries. However, the role of minor phases in strain localisation at an actual plate boundary remains to be tested by direct observation. In order to test the hypothesis that minor phases control strain localisation at plate boundaries, I conducted microstructural analyses of peridotite samples collected along a ∼1 km transect across the base of the UAE ophiolite. The base of the ophiolite is marked by the Semail thrust, which represents the now exhumed contact between subducted oceanic crust and the overlying mantle wedge. As such, the base of the ophiolite provides the opportunity to directly examine a former plate boundary.

My results demonstrate that the mean olivine grain size is inversely proportional to the abundance of minor phases (primarily orthopyroxene, as well as clinopyroxene, hornblende, and spinel), consistent with suppression of grain growth by grain-boundary pinning. My results also reveal that mean olivine grain size is proportional to CPO strength (both of which generally decrease towards the metamorphic sole), suggesting that the fraction of strain produced by different deformation mechanisms varied spatially. Experimentally-derived flow laws indicate that under the inferred deformation conditions, the viscosity of olivine was grain-size sensitive. As such, grain size, and thereby the abundance of minor phases, influenced viscosity during subduction-related deformation along the base of the mantle wedge.

I calculate an order of magnitude decrease in the viscosity of olivine towards the base of the ophiolite, which suggests strain was localized near the subduction interface. My data indicate that this rheological weakening was primarily the result of more abundant minor phases near the base of the ophiolite. My interpretations are consistent with those of previous studies on experimentally deformed rocks and smaller-scale natural shear zones that indicate minor phases can exert the primary control on strain localisation. However, I demonstrate for the first time that minor phases can control

strain localisation at the scales relevant to a major plate boundary.

Finally, in Chapter 4, I focus on the geological evolution of the metamorphic sole. Metamorphic soles are common beneath many ophiolites and comprise metamorphosed basalt, gabbro, and sediment that detached from the downgoing slab and accreted to the base to the hanging-wall mantle. Metamorphic soles are characterized by an inverted metamorphic field gradient, from granulite and amphibolite facies rocks at the structurally highest levels, down through greenschist and sub-greenschist facies rocks at structurally lower levels. Remarkably, the highest-grade sections of many metamorphic soles records similar peak pressure-temperature conditions of 10–12 kbar, corresponding to depths of 30–40 km, and 700–900 °C. However, the mechanism by which metamorphic soles detached from the downgoing slab and accreted to the hanging-wall mantle is unclear. The similar metamorphic conditions and ubiquity beneath Tethyan-type ophiolites indicates the development of metamorphic soles is governed by some fundamental process. To unravel burial, accretion, and exhumation of metamorphic soles, I conducted petrological analyses of samples collected across a 250 m thick section of the Masafi (UAE) metamorphic sole.

Thermobarometric analyses of garnet-clinopyroxene amphibolites from the top 85 m of sole indicate peak pressure-temperature conditions of 700–900 °C and 10–12 kbar. Structurally lower (85–250 m below the peridotites) epidote- and bi-mineralic (i.e., amphibole + plagioclase) amphibolites record similar pressures of 10–12 kbar, but temperatures that are ∼100 °C colder. Thus, although pressures are reasonably constant across the entire 250 m section, the temperatures decrease stepwise.

Most of the observed textures and geochemical trends result from incomplete retrogression. Textural evidence indicates that granulite formation of the sole was more pervasive than typically considered. I propose that granulite formation of the downgoing slab resulted in rheological strengthening that caused the subduction interface to migrate downwards into the slab and thereby accrete a slice (i.e., the sole) to the hanging-

wall mantle. The initial slice accreted was the garnet-clinopyroxene amphibolites with minor metasediment. As rocks in the subduction zone cooled and more sediments reached the trench, continued underplating occurred at similar pressures but colder temperatures. The peak granulite facies assemblage is overprinted by amphibolite–greenschist facies retrograde textures. The retrogressive fluids were likely sourced from structurally-lower thrust sheets as deformation migrated deeper into the slab. I suggest that retrogressive hydration of the sole resulted in a viscosity reduction and the development of the gneissic foliation.

Pressures recorded by the Oman-UAE sole indicate burial to depths 2–3 times deeper than can be accounted for by the ∼12 km thickness of the ophiolite. The commonly proposed models for sole exhumation are (1) buoyancy-driven return flow along the subduction interface, and (2) slab flattening. I speculate that retrogression of the granulite assemblage was concomitant with hydration and crystallization of high-temperature amphibole in the hanging-wall peridotites (as presented in Chapter 3). This would imply that the base of the ophiolite and the metamorphic sole were juxtaposed at depths of 30–40 km and later exhumed along a flattening slab.

Acknowledgements

First of all, I thank my supervisors Mike Searle and Dave Waters for envisioning the project and many hours of discussion. I also thank Lars Hansen and Dave Wallis, who became supervisors along the way, and without whom this thesis would have been very different.

My project was part of a larger geophysical program led by Tony Watts at Oxford and Mohammed Ali at the Petroleum Institute. I thank them for including a geological project alongside the geophysics. I also thank Mohammed for making sure I was alive during the several months spent camping alone in wadis. My project would have never been possible if it had not been for the generous support of the Petroleum Institute. I thank Aisha Al Suwaidi, who managed to secure additional funding to cover my international fees. It was very fortuitous that Mike and Aisha happened to sit down at coffee one morning! I thank Brook Keats for countless hours of teaching me basic geophysics and what a string is. I thank Simone Pilia for intense debate.

It has been a pleasure to be a part of the Hard Rock group. My first encounter with someone from the group was in the Annapurna guest house in Kathmandu in 2012. I had just finished two months of field work for my masters. One morning while waiting in the lobby I struck up a conversation with a man sporting a similar moustache. This man turned out to be Owen Weller, who over a year later suggested I apply for a PhD at Oxford. If it hadn't been for this encounter I would never have considered. I thank Brendan Dyck for always being willing to help out, except for when he submitted his

thesis and primarily became a distraction. But at least my tennis skills improved. I thank Tom Lamont for his never-ending entertainment and contagious enthusiasm for Naxos. I do not thank Tom for waking everyone up in the middle of the night on the beach at Dadna with his laptop buried in the sand as he looked at photos of Naxos. I thank Rich Palin for his help with Thermocalc. I thank the 4th years who, by the quality of their projects, scared me into getting a lot of work done early in my first year. I thank Nick Gardiner for introducing me to elevenses. I thank Anna Bidgood for organizing everything. Josh Combs, thanks for the pants. I thank Jacob Forshaw for all the discussions about the sole.

I thank Naomi Saunders, Tin Tin Nainng, Mohammed Al Fahmi, Arola Moreras, Anna Rufas Blanco, and Annie Cheng for the great company in 30.16. It turned out to be a good thing they crammed so many of us in there. I thank Rebecca Morgan, Rob Owen, Brook Keats, Brooke Tozer, Peter Gyring, Luke Jenkins, and Lars Hansen for teaching me to code. I thank Jon Wells for the excellent thin sections, which were often ready quicker than expected. I thank Jon Wade, Phil Gopon, and Emilie Bruand for guidance on the probe and giving me a reasonable discount. I thank Nick Tosca for the keys to his office and use of his microscope. I thank Ahmed for taking me out of the wadi, hydrating me, and hosting me on his goat farm, which happened to be located directly on top of the Semail thrust. I thank Stanley at the Curry House in Fujairah for the excellent thali and allowing me to use the restaurant as an office.

A defining experience of my time in Oxford was playing hockey for the Blues and Canadians. I thank every player that I skated with, from Oxford to Subotica and everywhere in between. I can not imagine how different these past three years would have been without hockey.

I thank Stephen Johnston for lighting the spark of curiosity and first teaching me what it means to be a scientist. I thank Kyle Larson and Carl Guilmette, my MSc supervisors. My PhD would have been a lot more difficult if not for everything they

taught me. I also thank NSERC who have continued to support me from UVic, to UBC, and most recently Oxford.

The biggest thanks goes to my family, whose have always supported me through my different endeavours. I thank my mum and dad for always encouraging me and teaching me how to work hard. Finally, I thank Courtney Dean for convincing me that I was capable of making it to Oxford. Spending the last 11 years together has been greater than I could ever have imagined. And thanks for Logan, the newest member of the family.

Contents

Declaration i

Abstract iv

Extended Abstract v

Acknowledgments x

Contents xvi

List of Figures xviii

List of Tables xix

1 Introduction **1**

1.1 Background 1

1.2 The Oman-UAE ophiolite 2

1.2.1 History of geological research 2

1.2.2 Tectonic framework 3

1.2.3 Ophiolite pseudostratigraphy 6

1.2.4 The Oman-UAE metamorphic sole 6

1.3 Statement of the problems 8

1.4 Structure of the thesis 10

1.5 A note on the use of pronouns 12

2 3D structure of the northern Oman – UAE ophiolite: widespread, short-lived, supra-subduction zone magmatism **13**

2.1 Introduction 13
2.2 Previous Work in the UAE 18
2.3 Geophysical constraints and extent of the ophiolite 19
2.4 Field constraints on the structure and architecture 23
2.4.1 Mantle sequence 23
2.4.2 Moho Transition Zone 26
2.4.3 Crustal Sequence 32
2.4.4 Metamorphic Sole 36
2.5 Discussion 38
2.5.1 Is the ophiolite in the UAE different from Oman? 38
2.5.2 Regional structure of the ophiolite in the UAE 38
2.5.3 Architecture of the ophiolite in the UAE 40
2.5.4 The Oman-UAE ophiolite as an analogue for mid-ocean ridges . 47
2.5.5 How was seafloor spreading accommodated during ophiolite formation? 48
2.6 Conclusion 50

3 Controls on the rheological properties of peridotite at a palaeosubduction interface: a transect across the base of the Oman-UAE ophiolite 52
3.1 Introduction 52
3.2 Geologic Setting 54
3.3 Methods 59
3.3.1 Sample collection and preparation 59
3.3.2 Microstructural analysis 60
3.3.3 Mineral abundances 63
3.4 Results 64
3.4.1 Petrography 64
3.4.2 Grain size and subgrain size 69

3.4.3 Crystallographic preferred orientations 71
3.4.4 Microstructure as a function of position 74
3.4.5 Relationships among grain size, minor-phase abundance, and texture strength 76
3.5 Discussion 77
3.5.1 Controls on strain localisation along the base of the Oman-UAE ophiolite 77
3.5.2 The influence of minor phases on olivine grain size 78
3.5.3 Deformation mechanisms and rheology of the subduction interface 80
3.5.4 Orientation of CPOs and strain geometry at the subduction interface 85
3.5.5 Tectonic Implications 86
3.6 Conclusions 87

4 Burial, accretion, and exhumation of the Oman-UAE metamorphic sole 89

4.1 Introduction 89
4.1.1 Burial of metamorphic soles 90
4.1.2 Accretion of metamorphic soles 90
4.1.3 Exhumation of metamorphic soles 91
4.1.4 Focus of this study 92
4.2 Oman-UAE metamorphic sole 93
4.2.1 Study area 94
4.3 Petrography and mineral chemistry 99
4.3.1 Sampling strategy and analytical methods 99
4.3.2 Garnet 102
4.3.3 Clinopyroxene 108
4.3.4 Amphibole 111

4.3.5 Plagioclase 114
4.3.6 Epidote 117
4.3.7 Other minerals 118
4.4 Thermobarometry 119
4.4.1 Amphibole-plagioclase thermometry 119
4.4.2 Garnet-clinopyroxene thermometry 123
4.4.3 Multi-equilibrium thermobarometry 123
4.5 Phase Equilibria Modelling 127
4.5.1 Model system and bulk rock composition 127
4.5.2 Uncertainty in phase equilibria models 127
4.5.3 Results and discussion 129
4.6 Discussion 133
4.6.1 Metamorphic conditions 133
4.6.2 Thickness of the garnet-clinopyroxene amphibolites 135
4.6.3 Retrogression of the amphibolites 139
4.6.4 Fabric evolution in the amphibolites 142
4.6.5 Tectonic implications 143
4.7 Conclusion 149

5 Conclusion **151**

5.1 Summary of results and conclusions 151
5.2 Further questions and future work 153

References **158**

Appendices **175**

A EBSD maps **176**

B Electron microprobe analyses **185**

List of Figures

1.1 Simplified geological map of the Oman-UAE ophiolite 4

1.2 Simplified ophiolite pseudostratigraphy 7

2.1 Geological map of the United Arab Emirates 15

2.2 Block model of the ophiolite 22

2.3 Field photographs of the mantle section 25

2.4 Field photographs of the Moho transition zone 28

2.5 Panoramic field photographs of the Moho transition zone 31

2.6 Field photographs of the crustal section 34

2.7 Panoramic field photograph of the 'vinaigrette' unit 35

2.8 Field photographs and a photomicrograph of the metamorphic sole . . 37

2.9 Pseudostratigraphy of the ophiolite 41

2.10 Schematic diagrams for the map pattern 43

3.1 Regional geological map and cross-section of the study area 56

3.2 Field photos of the Oman-UAE ophiolite mantle section 57

3.3 Representative peridotite photomicrographs 66

3.4 Electron backscatter diffraction maps 68

3.5 Histograms of olivine grain size and subgrain size 70

3.6 Olivine pole figures 73

3.7 Microstructural relationships 75

3.8 Mean olivine grain size as a function of mean minor-phase grain size and minor-phase volume fraction 79
3.9 Rheological properties 83

4.1 Simplified geological map of the northern UAE 96
4.2 Geological map and cross-section of the study area 97
4.3 Field photographs 98
4.4 Photomicrographs of garnet-clinopyroxene amphibolites 104
4.5 Photomicrographs and backscattered electron images of retrograde textures in garnet-clinopyroxene amphibolites 105
4.6 Garnet compositional profiles and elemental maps. 106
4.7 Mean clinopyroxene compositions against structural distance below the peridotites 110
4.8 Photomicrographs and backscattered electron images of epidote- and bi-mineralic amphibolites 112
4.9 Amphibole classification diagrams 115
4.10 Mean amphibole compositions against distance below the peridotites . 116
4.11 Plagioclase composition against distance below peridotites 118
4.12 Thermometry results plotted against distance from the peridotites . . . 122
4.13 Results of average-P and average-PT 126
4.14 Results from phase equilibria modelling 132
4.15 ACF ternary diagram displaying bulk-rock compositions 138
4.16 Schematic tectonic evolution of the metamorphic sole through time . . 146

List of Tables

3.1 Results from microstructural analysis 62

4.1 Sample descriptions 100
4.2 Mineral chemistry 101
4.3 Amphibole, plagioclase, and clinopyroxene compositions 109
4.4 Geothermometry results 120
4.5 Results from average-P and average-PT 125
4.6 Modal mineral abundances 127
4.7 Bulk-rock compositions 128

Chapter 1

Introduction

1.1 Background

Ophiolites are thrust-bound slices of oceanic crust and upper mantle that have been emplaced onto the continental margin (e.g., Hess, 1962; Dietz, 1963; Gass, 1968; Coleman, 1971; Dewey and Bird, 1971; Moores and Vine, 1971). Ophiolites provide the opportunity to directly study the structure and genesis of oceanic lithosphere. As many ophiolites formed above subduction zones (e.g., Miyashiro, 1973; Dilek and Furnes, 2011), they also provide the opportunity to investigate processes in the mantle wedge, slab-interface, and downgoing slab. Metamorphic soles are thin (10s–1000s of m thick) sub-greenschist to granulite facies, highly-sheared thrust-sheets structurally juxtaposed against the base of some ophiolites (Williams and Smyth, 1973). Whereas ophiolites are the hanging-wall of the subduction zone, metamorphic soles are accreted slices of the downgoing slab (e.g., Searle and Malpas, 1980; Casey and Dewey, 1984). Thus, ophiolites allow for the direct examination of former subduction interfaces. It is not surprising that ophiolites have led to many important discoveries and played a central role in the plate tectonic revolution (Moores, 1982 and references therein).

Despite decades of intense study, fundamental questions remain regarding the structural, metamorphic, and tectonic evolution of ophiolites and metamorphic soles. This thesis consists of three standalone chapters with distinct objectives that aim to an-

swer some of these questions. The focus of each chapter is on the northern section of Oman-United Arab Emirates (UAE) ophiolite and metamorphic sole, but the results are relevant to further south in Oman and ophiolites in general.

From the outset, it is important to note that there are several different types of ophiolites. Moores (1982) divided ophiolites into Tethyan-type and Cordilleran-type. Although this classification does not include all ophiolites (e.g., Wakabayashi and Dilek, 2003), it is a reasonable simplification that includes the majority. Tethyan-type ophiolites, such as the Oman-UAE and Troodos ophiolites, were emplaced onto passive continental-margins when the edge of the continent reached the subduction zone. In contrast, Cordilleran-type ophiolites, such as those along the western margin of North America, were scraped off the downgoing slab and emplaced into accretionary prisms. As this thesis is on the Oman-UAE ophiolite the implications are relevant to other Tethyan-type ophiolites but not necessarily Cordilleran-type.

1.2 The Oman-UAE ophiolite

A more thorough introduction to the structure and tectonic evolution of the Oman-UAE ophiolite is presented in Chapter 2. A detailed introduction to the metamorphic sole is presented in Chapter 4. At the expense of some repetition, some key concepts are discussed here for thoroughness.

1.2.1 History of geological research

Early geological surveys of the Oman-UAE mountains were carried out by Pilgrim (1908) and Lees (1928). The first comprehensive mapping and stratigraphic analysis of the entire Oman-UAE mountains was conducted by Petroleum Development Oman and Shell geologists through the late 1960s and early 1970s (Reinhardt, 1969; Glennie et al., 1973, 1974). This work defined the structural and stratigraphic framework that are still, for the most part, used today. It was Reinhardt (1969) who first interpreted the ophiolite as a thrust sheet of oceanic lithosphere. Two major studies through the

1970s and 1980s built upon this earlier work. A United States Geological Survey team conducted detailed mapping along a 25 km wide strip to the south of Muscat, summarized in a special issue of Journal of Geophysical Research (Coleman and Hopson, 1981). Around the same time, a group from the Open University conducted detailed mapping in northern Oman, the results of which are summarized in a Geological Society of London Memoir (Lippard et al., 1986).

Through the 1980s a collaboration between French universities resulted in the publication of a special volume of Tectonophysics (Boudier and Nicolas, 1988). From 1982–1986, the French Geological Survey (BRGM), under contract to the Omani government, mapped the eastern and southeastern mountains at the 1:100 000 scale (Rabu et al., 1993). Conferences in Edinburgh and Muscat on the Oman-UAE mountains led to the publication of two special volumes by the Geological Society of London (Robertson et al., 1990b; Rollinson et al., 2014). From 2002 to 2013 the British Geological Survey (BGS) mapped the entire UAE at various scales from 1:20k to 1:100k (Styles et al., 2006; Thomas and Ellison, 2014). The BGS maps are the first comprehensive compilation of the geology of the UAE. Two papers on the geology and tectonics of the ophiolite also resulted from the project (Goodenough et al., 2010, 2014).

1.2.2 Tectonic framework

The Oman-UAE mountains (Figure 1.1) record the opening and closure of an ocean basin. Rifting of the Arabian plate in the Late-Permian led to the opening of the Neo-Tethys and passive margin sedimentation through most of the Mesozoic (Lees, 1928; Allemann and Peters, 1972; Glennie et al., 1974). The onset of ocean closure was marked by subduction initiation, though the setting in which subduction initiates is debated. Subduction has been proposed to initiate at transform faults and/or fracture zones (e.g., Stern and Bloomer, 1992; Casey and Dewey, 1984), passive continental margins (Dewey and Bird, 1970), oceanic detachment faults (Maffione et al., 2015), and oceanic spreading centers (Spray and Spray, 1983; Boudier et al., 1988).

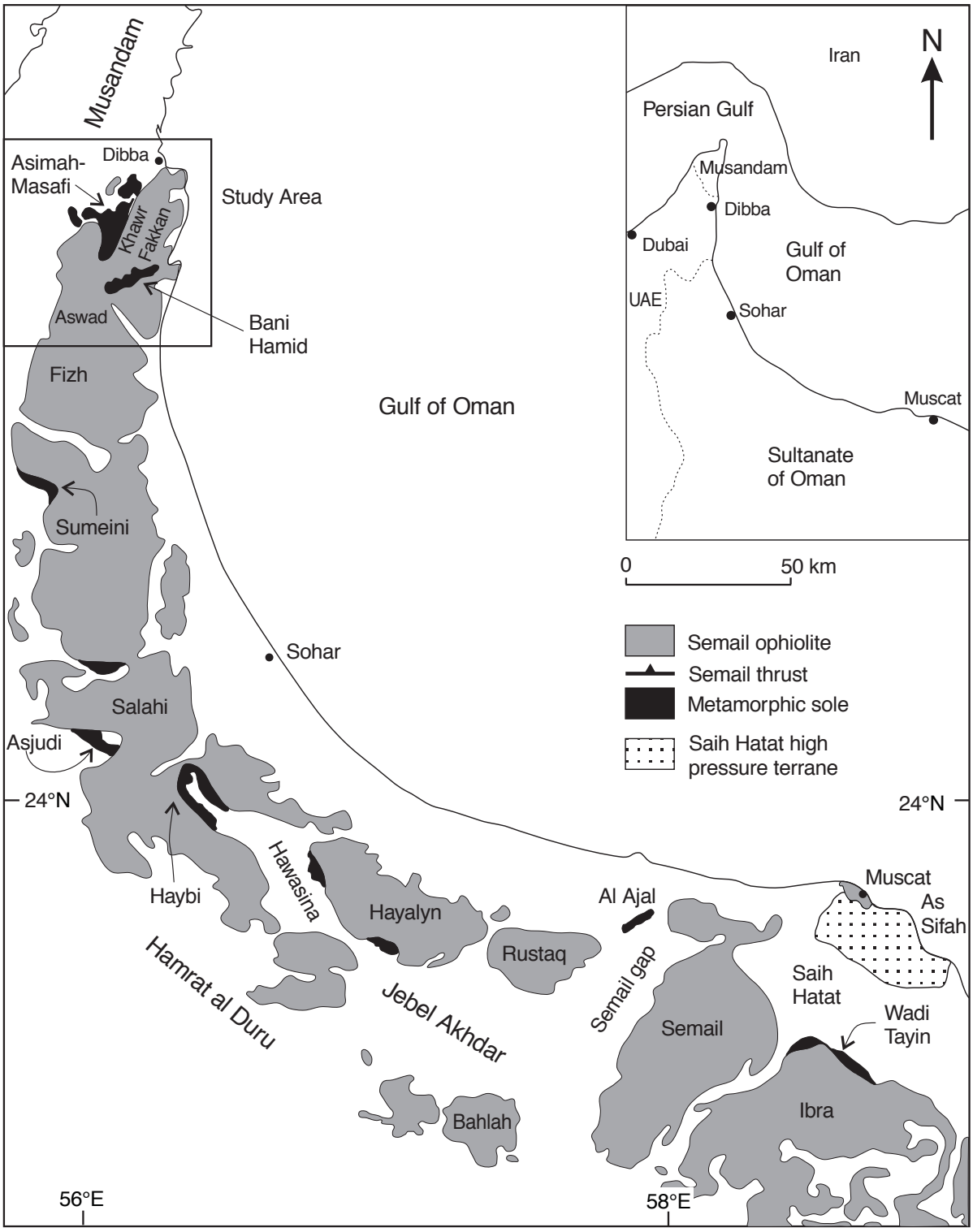


Figure 1.1: Simplified geological map of the Oman-UAE ophiolite and metamorphic sole (modified from Cox et al., 1999)

The ophiolite comprises oceanic lithosphere from the hanging-wall of the newly initiated subduction zone (e.g., Searle and Malpas, 1980; Pearce et al., 1981; Searle and Malpas, 1982). Whether the ophiolite formed at a mid-ocean ridge prior to subduction initiation, or at a spreading centre above the subduction zone, was the subject of intense debate for decades. To some researchers, the data indicated a fast-spreading mid-ocean ridge, analogous to the East Pacific Rise (e.g., Reinhardt, 1969; Coleman, 1981; Boudier et al., 1988, 1997; Nicolas and Boudier, 2015, 2017). Other researchers, however, argued that the structural relationships and geochemical signature could only be explained by formation at a spreading center above a subduction zone (Pearce et al., 1981; Alabaster et al., 1982; Lippard, 1986). Because no distinct topographic island-arc was present, the term supra-subduction zone (SSZ) ophiolite was introduced (Pearce et al., 1981). As discussed in Chapter 2, most researchers now support a model in which at least part of ophiolite formed above a subduction zone.

U-Pb zircon ages from the crustal section of the ophiolite and cross-cutting plagiogranite dykes indicate that the ophiolite crystallized over the surprisingly short time span from 96.5–95.5 Ma (Warren et al., 2005; Rioux et al., 2012, 2013, 2016). Cooling ages from both the ophiolite and metamorphic sole reveal rapid cooling below 550 °C within 1–2 Myr following ophiolite formation (Hacker, 1994; Hacker et al., 1996; Roberts et al., 2016). Following subduction initiation, closure of the Tethys proceeded as the entire ophiolite was thrust over a series of thrust-sheets composed of distal-ocean (Haybi and upper Hawasina complexes) to proximal passive-margin successions (Hamrat Duru and Sumeini thrust sheets) and finally onto the Arabian continental margin (Glennie et al., 1973; Searle, 1988b; Searle and Cox, 1999; Searle, 2007). Subduction ceased at ∼79 Ma when the leading edge of the Arabian continental margin was subducted to eclogite faces (Warren et al., 2003; Searle et al., 2004; Warren et al., 2005). The obduction-emplacement process was complete by ∼70 Ma and is marked by the return of shallow-marine passive-margin sedimentation (Glennie et al. 1973).

There is often confusion surrounding the terms emplacement and obduction and their relationship to subduction. Some authors also use the term ‘intra-oceanic thrust-

ing' as opposed to subduction. In this thesis, obduction refers to the processes of thrusting the ophiolite over the downgoing slab. Emplacement more specifically refers to thrusting of the ophiolite onto the continental margin following closure of an ocean basin. Ultimately, both obduction and emplacement result from subduction.

1.2.3 Ophiolite pseudostratigraphy

The ophiolite is up to ∼100 km wide and spans nearly 500 km, from the Dibba zone in the northern UAE to the Wahiba sands southeast of Muscat (Figure 1.1). The ophiolite consists of upper mantle peridotite and a complete crustal section of layered and massive gabbro at the deepest levels, through sheeted dykes structurally higher, overlain by basaltic flows, and finally pillow basalt that erupted on the ocean floor (Figure 1.2). The entire ophiolite has been cut by felsic, mafic, and ultramafic dykes (Python and Ceuleneer, 2003; Rollinson, 2009; Rollinson and Adetunji, 2013). Unlike other Tethyan-type ophiolites (e.g., Himalayan and Alpine) that have been dismembered during continent-continent collision, the Oman-UAE ophiolite is relatively intact, since in this region, the Arabia plate has not yet collided with the Eurasian plate (Searle et al., 2014). Due to its exceptional preservation, the Oman-UAE ophiolite is commonly used as template for other poorly exposed and structurally complex ophiolites.

1.2.4 The Oman-UAE metamorphic sole

The metamorphic sole (or simply 'sole') is present beneath the entire Oman-UAE ophiolite, but most studies have focussed on three of the best exposed localities: the Masafi (or Asimah) window in the northern UAE, Jebel Sumeini in northern Oman, and Wadi Tayyin to the south of Muscat (Figure 1.1). The metamorphic sole is bound at the top by the Semail thrust, which separates the overlying banded ultramafics along the base of the ophiolite (Reinhardt, 1969; Allemann and Peters, 1972; Glennie et al., 1974). Beneath the metamorphic sole are unmetamorphosed underlying thrust sheets of the Haybi complex (Searle et al., 1980; Searle and Malpas, 1980). The sole

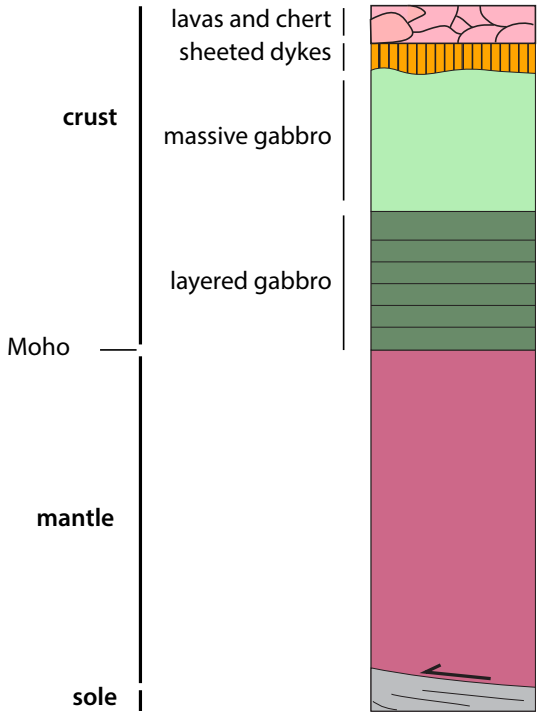


Figure 1.2: Simplified ophiolite pseudostratigraphy decided upon by participants of the 1972 Penrose conference on ophiolites (Anonymous, 1972).

is characterized by a steep inverted metamorphic field gradient that passes downward from garnet-clinopyroxene amphibolites down through epidote-amphibolite, amphibolite, and greenschist facies metabasic and metasedimentary rocks (Searle and Malpas, 1980; Hacker and Mosenfelder, 1996; Gnos, 1998). U-Pb zircon dates demonstrate that metamorphism of the sole was synchronous with crystallization of the crustal sequence of the overlying ophiolite (Rioux et al., 2016). Ar/Ar cooling ages from amphibole indicate rapid exhumation to below ∼550 °C in only 1–2 Myr following crystallization of the crustal section of the ophiolite (Hacker, 1994; Hacker et al., 1996).

The sole comprises metamorphosed basalt, gabbro, and sediment that detached from the downgoing slab and accreted to the base to the hanging-wall mantle (Allemann and Peters, 1972; Searle and Malpas, 1980, 1982). Pressure-temperature estimates of garnet-clinopyroxene amphibolites from the Oman-UAE sole are consistently between 10–12 kbar (30–40 km) and 700–900 °C (Hacker and Gnos, 1997; Gnos, 1998; Cowan et al., 2014; Soret et al., 2017). As discussed in Chapter 2, the original (i.e., pre-erosion) thickness of the ophiolite was likely ∼12 km (e.g. Nicolas et al., 2000), which

implies that the sole formed about three times deeper than can be accounted for by the preserved thickness of the ophiolite. The exact nature of what the sole accreted to, and at what depth is unclear. Thus, I try to avoid genetic terms such as 'future-ophiolite' and 'mantle-wedge' (i.e., viscous flowing mantle) in favour of the term 'hanging-wall mantle'.

As opposed to the 'normal' metamorphic sole, the Bani Hamid sole is a slice of uniformly granulite facies metasediments and minor metabasic rocks that has been exposed by out-of-sequence thrusting (Figure 1.1; Gnos and Kurz, 1994; Gnos and Nicolas, 1996; Searle et al., 2015). Searle et al. (2015) suggested that Bani Hamid is the metamorphosed equivalent of dolomitic cherts, calcareous turbidites, and alkali volcanics of the Haybi complex. Despite similarly high-temperatures of 850 ± 60 °C, thermobarometry estimates from Bani Hamid indicate considerably lower pressures of just 5.6 ± 0.5kbar (Searle et al., 2015). Given that metamorphism post dates that of the normal sole by ∼2–3 million years (Searle et al., 2015), the high-temperatures and low pressures of Bani Hamid are enigmatic. It is expected that following subduction initiation the mantle wedge would have progressively cooled and temperatures at such pressures recorded by Bani Hamid would have been lower.

1.3 Statement of the problems

This thesis sets out to solve several outstanding questions regarding the evolution of the Oman-UAE ophiolite and metamorphic sole. Each chapter focusses on fairly different aspects of the ophiolite and metamorphic sole and contains a more detailed introduction. The motivation behind each chapter can be summarized in a single question:

- **Chapter 2: Is the architecture and tectonic evolution of the ophiolite in the UAE distinct from Oman?** Constraining the present-day structure and architecture (i.e., pseudostratigraphy) of the ophiolite is critical to inferring past processes. As the ophiolite is completely exposed it may seem surprising that

the structure and architecture remain debated. Several recent studies (including the largest ever to focus on the UAE), however, have proposed that the northern segment of the ophiolite is considerably different from further south in Oman (Styles et al., 2006; Goodenough et al., 2010, 2014). These studies have led several groups of researchers to infer a different tectonic and magmatic evolution for the northern segment of the ophiolite (Goodenough et al., 2010, 2014; Nicolas and Boudier, 2017).

- **Chapter 3: What controls strain localization at plate boundaries?** Observations from experiments and small-scale natural shear zones demonstrate that volumetrically-minor phases can control strain localization. These small-scale studies are often used to infer a critical role for minor phases in the development of plate boundaries. However, while observations of the role of minor phases in strain localisation have been made from the thin-section to the outcrop scale, it remains to be tested with direct observation whether this process is applicable to strain localisation at an actual plate boundary. The contact between the ophiolite and metamorphic sole represents a palaeosubduction interface, and thus the unique opportunity to directly investigate a former plate boundary.

- **Chapter 4: What controlled accretion of the metamorphic sole and how was it exhumed?** It is well established that metamorphic soles represent detached slices of the downgoing slab (e.g., Williams and Smyth, 1973; Searle et al., 1980; Searle and Malpas, 1980, 1982; Casey and Dewey, 1984; Hacker, 1990b, 1991; Hacker and Mosenfelder, 1996; Gnos, 1998). However, the mechanism by which metamorphic soles detached from the downgoing slab and accreted to the hanging-wall mantle is unclear. Additionally, an exhumation mechanism is required to explain pressures that are 2–3 times deeper than can be accounted for by the thickness of the ophiolite.

1.4 Structure of the thesis

Chapters 2–4 present three independent studies intended for separate publication. Chapter 2 includes a general introduction to the Oman-UAE ophiolite. The chapters progress in the order that the research was carried out, which also forms a logical progression. The chapters transition in the spatial extent of the study area, from the regional scale presented in Chapter 2, to a ∼1 km long transect of the basal peridotites in Chapter 3, and finally a 250 m transect of the sole in Chapter 4. This, coincidentally, also corresponds to a progression down structural-section, from the crustal and mantle sequences of the ophiolite in Chapter 2, to the base of the mantle section in Chapter 3, and finally the underlying metamorphic sole in Chapter 4.

In chapter 2, I explore the structure and architecture of the ophiolite in the UAE. Specifically, I test the hypothesis that the architecture of the ophiolite in the UAE is distinct from Oman. To test this hypothesis, I conducted approximately 2 months (out of a total of 4) of fieldwork in the UAE. The majority of this time was focussed on a new road through the ophiolite that exposed new 10s–100s of meters tall road cuts. Although the entire ophiolite offers near complete exposure, complex magmatic relationships are easily obscured by ubiquitous desert varnish. These roads-cuts are likely the best exposure of the Moho anywhere on Earth. Based on observations along this road cut and several other transects, I present 3-dimensional geological models for the ophiolite in the UAE. My findings indicate that the UAE portion of the ophiolite is not significantly different from further south in Oman, as previously suggested (Styles et al., 2006; Goodenough et al., 2010, 2014; Nicolas and Boudier, 2017). Thus, I argue that entire ophiolite shares a similar tectonic history.

In chapter 3, I investigate the rheological evolution of peridotites from the base of the ophiolite. Specifically, I test the hypothesis that volumetrically minor phases controlled strain localization during subduction. To test this hypothesis, I collected samples from a kilometer-long transect across the base of the ophiolite adjacent to the Masafi window. Electron backscatter diffraction (EBSD) was used to quantify trends and relationships in grain size, mineral abundance, and crystallographic preferred ori-

entation. My results indicate that minor phases pinned olivine grain boundaries and limited grain growth, which promoted grain size sensitive deformation mechanisms and led to rheological weakening. Similar processes have been observed in experimentally deformed rocks and small-scale natural shear zones (Herwegh et al., 2011 and references therein), and predicted to operate at plate boundaries (e.g., (Bercovici and Ricard, 2012)). But this is the first time minor phases have been demonstrated to exert a control on an actual plate boundary.

In Chapter 4, I investigate the burial, accretion, and exhumation of the metamorphic sole. Specifically, I test the hypothesis that accretion of the sole was controlled by granulite formation in the downgoing slab. Previous models have suggested that the sole accreted when increasing temperatures resulted in weakening of the slab and concomitant downward migration of the subduction interface (Hacker, 1990b, 1991; Agard et al., 2016). These models, however, did not consider metamorphic reactions in the sole. To elucidate the metamorphic history of the sole, I conducted detailed mapping and sample collection near the southern closure of the the Masafi window. Chapter 4 presents detailed petrological analyses, including mineral chemistry, conventional thermobarometry, multi-equilibrium thermobarometry, and phase equilibria modelling, of samples collected across a 250 m thick section of the sole. My results indicate that extensive granulite formation led to rheological strengthening of the subducting slab, downward migration of the subduction interface, and accretion of the metamorphic sole.

Finally, Chapter 5 concludes the thesis and ties the three chapters into a cohesive narrative. Although some questions have been answered, there are many more that have not and new ones that have arisen. I conclude the thesis with recommendations for future research.

1.5 A note on the use of pronouns

Each chapter is intended for publication on its own. At the time of submission, Chapters 2 is in review in Geochemistry, Geophysics, and Geophysics, while Chapter 3 is in review in Earth and Planetary Science Letters. Chapter 4 has not yet been submitted, but it has been written with the intention to do so. As these three papers will have coauthors, they have been written in the first person plural.

Chapter 2

3D structure of the northern Oman – UAE ophiolite: widespread, short-lived, supra-subduction zone magmatism

2.1 Introduction

The Oman-UAE ophiolite (Figure 2.1), a thrust sheet of Tethyan oceanic lithosphere that was emplaced onto the formerly passive continental margin of Arabia, is the largest and most intensely studied ophiolite on Earth (Reinhardt, 1969; Glennie et al., 1973, 1974; Coleman and Bailey, 1974; Pearce et al., 1981; Lippard et al., 1986; Rabu et al., 1993). The ophiolite exposes upper mantle peridotite and a complete crustal section that consists of layered and massive gabbro at the deepest levels, through sheeted dykes structurally higher, overlain by basaltic flows, pillow basalts, and pelagic sediments (Reinhardt, 1969; Glennie et al., 1973, 1974). The entire ophiolite has been thrust over a series of thrust-sheets composed of distal-ocean (Haybi and upper Hawasina complexes) to proximal passive-margin successions (Hamrat Duru and Sumeini thrust sheets) and finally onto the Arabian continental margin (Glennie et al., 1973; Searle

and Cox, 1999; Searle, 2007). The obduction–emplacement process was complete by ∼70 Ma and is marked by the return of shallow-marine passive margin sedimentation (Glennie et al. 1973). Unlike most other ophiolites that have been dismembered during later continent-continent collision, the Oman-UAE ophiolite is relatively intact, since in this region, the Arabian plate has not yet collided with the Eurasian plate (Searle et al., 2014). The Oman-UAE ophiolite has been fundamental to understanding other more structurally complex and poorly exposed ophiolites. The Oman-UAE ophiolite also provides the opportunity to directly investigate the genesis and structure of oceanic-lithosphere (Sinton and Detrick, 1992; Boudier et al., 1996, 1997; Nicolas and Boudier, 2015) and subduction-zone processes (e.g., Chapter 3, Searle and Cox, 1999, 2002; Pearce, 2003; Stern, 2004; Wakabayashi et al., 2010; Rollinson and Adetunji, 2013). Despite the fundamental contributions of the Oman-UAE ophiolite to a wide-range of geological processes, the exact tectonic setting and internal structure of the ophiolite remain unclear.

Some researchers interpret data from the Oman-UAE ophiolite as indicating a fast-spreading mid-ocean ridge, analogous to the East Pacific Rise (e.g., Reinhardt, 1969; Coleman, 1981; Boudier et al., 1988, 1997; Nicolas and Boudier, 2015, 2017. Detailed mapping and geochemical analysis of the volcanic stratigraphy in northern Oman, however, identified considerable geochemical and petrological variability in the volcanic sequence (Pearce et al., 1981; Alabaster et al., 1982; Lippard, 1986). Based on field structural-mapping and immobile trace element geochemistry, Pearce et al. (1981) and Alabaster et al. (1982) proposed a model consisting of an early constructive-margin phase in a marginal basin, producing lavas similar, albeit distinct from mid-ocean-ridge basalt (Geotimes unit), and a later immature island-arc phase forming more boninite-type lavas (Lasail unit). Because no distinct topographic island-arc was present, the Lasail unit was referred to as a supra-subduction zone (SSZ) volcanic sequence. Juteau et al. (1988) and Ernewein et al. (1988) subsequently proposed similar models to Pearce et al. (1981), consisting of an earlier spreading phase, and a later subduction-related phase. However, the models of Juteau et al. (1988) and Ernewein et al. (1988) differed

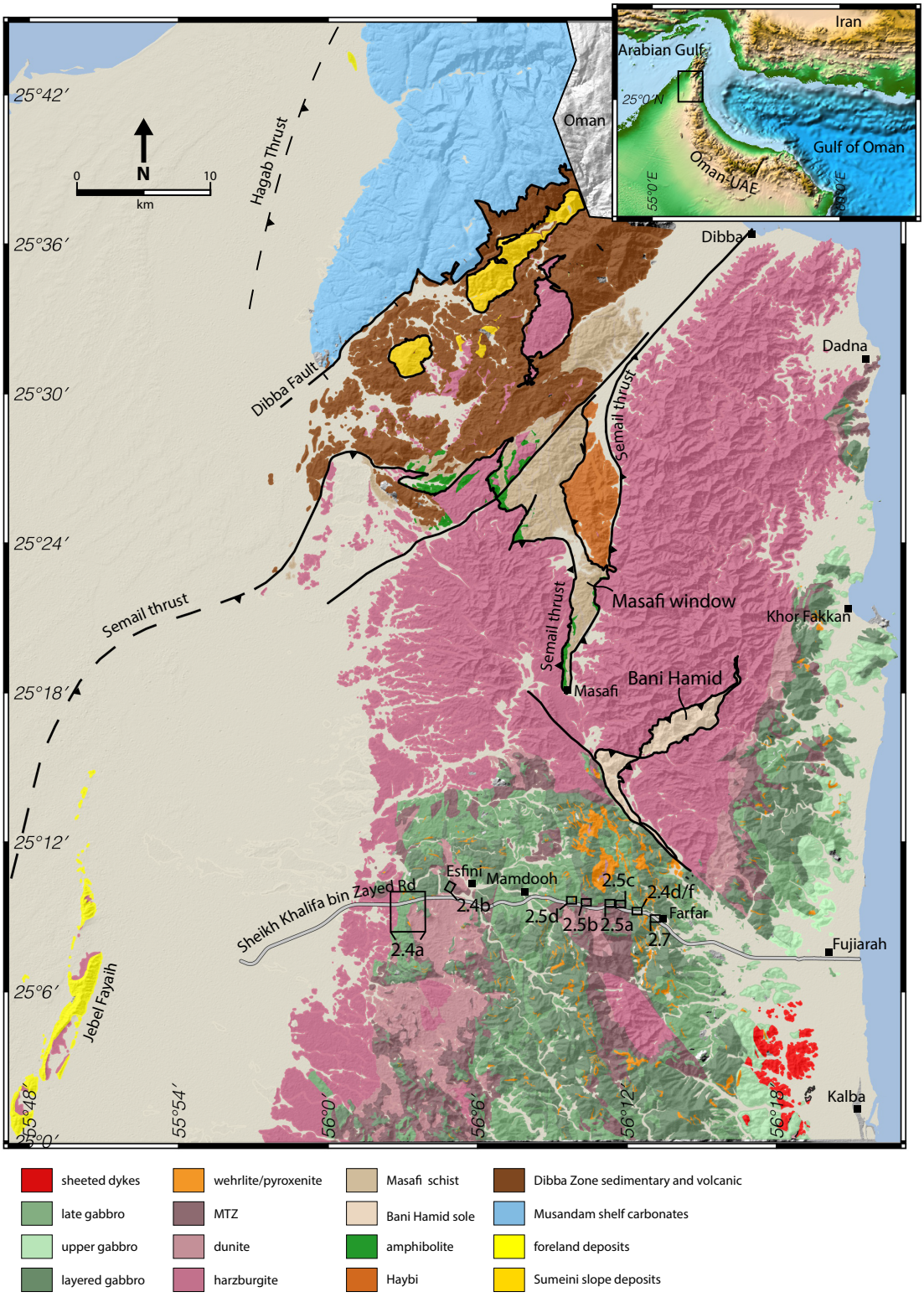


Figure 2.1: Geological Map of the UAE (modified after BGS maps), showing the location of the Sheikh Khalifa Bin Zayed road and reference locations to subsequent figures. For comparison, we have kept the BGS subdivision of the gabbros.

in that the initial phase of magmatism occurred at a mid-ocean ridge distal to any subduction zone. Ernewein et al. (1988) divided the lavas into the V1, V2, and V3 series, which they related to changes in tectonic settings, from mid-ocean ridge (V1), to SSZ (V2), and finally post subduction (V3).

Over the last few decades, most researchers have supported similar, hybrid tectonic models for the Oman-UAE ophiolite, consisting of an early mid-ocean ridge phase, and a later SSZ phase (Umino et al., 1990; Ishikawa et al., 2002; Dilek and Flower, 2003; Godard et al., 2006; Yamasaki et al., 2006; Arai et al., 2006; Python et al., 2008; Rollinson, 2009; Dare et al., 2009; Goodenough et al., 2010, 2014; Tsuchiya et al., 2013; Yoshikawa et al., 2015). Although most researchers have attributed geochemical variation to transitions in tectonic setting, some have continued to support a pure mid-ocean ridge model, arguing that the geochemical variations can be explained by a heterogeneous mantle source (Moores et al., 2000; Takazawa et al., 2003; Godard et al., 2006) or circulation of seawater (Boudier et al., 2000; Abily et al., 2011), without the need to invoke proximal subduction.

More recently, two discoveries have strongly supported a model in which the entire ophiolite formed above a subduction zone. First, MacLeod et al. (2013) demonstrated that major-element fraction trends of V1 (Geotimes) lavas and sheeted dyke samples required water concentrations considerably higher than observed at mid-ocean ridges. Second, Rioux et al. (2016) demonstrated that U-Pb zircon ages of c. 96.17±0.022 and 94.82±0.035 Ma that date peak metamorphism of the metamorphic sole (i.e., the downgoing slab) overlap with U-Pb zircon crystallization ages of c. 96.4–95.5 Ma from plagiogranites and gabbros related to the V1 (Geotimes unit) series of the ophiolite (Warren et al., 2005; Rioux et al., 2012, 2013). Thus, subduction of basalts and sedimentary rock to oceanic-mantle depths of 30–40 km (Cowan et al., 2014) beneath the ophiolite was synchronous with crystallization of the crustal section of the ophiolite. There is considerable structural, geochemical, and geochronological variation amongst ophiolites that indicate their formation in a wide range of tectonic settings (e.g., Dilek and Furnes, 2011). However, in the case of the Oman-UAE ophiolite, the

evidence strongly supports the model of the entire ophiolite forming above a subduction zone.

Most research on the ophiolite has focussed on Oman, with relatively little attention paid to the northern sections in the UAE. Several recent studies have suggested that the magmatic, structural, and tectonic evolution of the ophiolite in the UAE are distinct from the ophiolite in Oman (Goodenough et al., 2010, 2014; Nicolas and Boudier, 2017). Under contract to the Ministry of Energy, the British Geological Survey (BGS) mapped the entire ophiolite in the UAE at the 1:50K scale (Styles et al., 2006). Based on their results, they proposed that the crustal section of the ophiolite in the UAE consists of two distinct phases of magmatism: an early open mid-ocean ridge phase, and later cross-cutting phase related to subduction (Goodenough et al., 2010, 2014). Although similar hybrid-models have been proposed in Oman (e.g. Ernewein et al., 1988; Juteau et al., 1988; Ishikawa et al., 2002), Goodenough et al. (2010, 2014) argued that the volume of the cross-cutting magmatism was considerably larger in the UAE and was related to ductile shear zones that rooted into the mantle. The BGS interpretation was apparently driven by two factors: (1) previously published models for the ophiolite forming during a transition from a mid-ocean ridge setting to a subduction-zone setting, and (2) an anomalously high exposure of gabbro and Moho transition zone (MTZ) lithologies in the southern UAE (See figure 1 in Goodenough et al. 2014).

However, the BGS model is inconsistent with recent evidence that the entire ophiolite formed above a subduction zone ((MacLeod et al., 2013; Rioux et al., 2016)). Several hypotheses can reconcile the data. (1) It is possible that the ophiolite formed during a transition from mid-ocean ridge to SSZ, and that the geochemical and geochronological data has been misinterpreted, thus the BGS model is plausible. (2) It is possible that the part of ophiolite in UAE is a separate body and underwent a distinct tectonic evolution, thus the geochemical and geochronological data from Oman is not directly relevant. (3) Finally, it is possible the entire ophiolite formed above a subduction zone, the geochemical and geochronological data has been accurately interpreted, and

that the seemingly large extent of gabbro and MTZ lithologies can be explained by magmatic and structural relationships.

Here we test the hypothesis that the architecture of the UAE portion of the ophiolite is different from Oman and may thereby reflect a separate evolution. We integrated geological mapping and field observations with previously published 1:50k BGS maps that cover the entire UAE (Styles et al., 2006; Goodenough et al., 2010, 2014). We present a transect to the west of Fujairah that utilizes new road exposures that provide the unique opportunity to investigate a complete and fully exposed section through the ophiolite, from the mantle section up to the sheeted dykes. This cross-section, as well as observations from other locations of the ophiolite, allow us to constrain the 3-dimensional structure and architecture of the ophiolite in greater detail than has previously been possible. Our findings indicate that the internal structure of the ophiolite in the UAE is not significantly different from Oman. Thus, there is no evidence to suggest a separate tectonic history. We present models for the regional structure and architecture of the ophiolite in the UAE that are consistent with observations in Oman as well as geochronological, geochemical, and petrological constraints.

2.2 Previous Work in the UAE

The first field mapping studies in the UAE part of the Oman Mountains was carried out by the Institute of Geological Sciences Greenwood and Loney (1968) and Huntings Geology and Geophysics Ltd. Huntings Geology and Geophysics (1976) who mapped the entire country at the 1:1,000 000 and 1:500 000 scale, predominantly from aerial photographs. The Shell team of Glennie et al. (1973, 1974) mapped the whole UAE and Oman parts of the mountain belt and produced the first comprehensive geological map. Selected areas, mainly the metamorphic rocks along the Dibba zone beneath the ophiolite were studied by Allemann and Peters (1972), Searle and Malpas (1980, 1982) and Searle (1988a,b). Fujairah Emirate was mapped at the 1:50 000 scale by the Council for Geoscience (South Africa) under government contract (Grantham et al.,

2004). More recently, the BGS was commissioned to map the entire country, beginning in 2002 and finishing in 2013, at various scales from 1:20 000 to 1:100 000 (Styles et al., 2006; Thomas and Ellison, 2014). The BGS maps are the first comprehensive compilation of the geology of the UAE. Two papers on the geology and tectonics of the ophiolite also resulted from the project (Goodenough et al., 2010, 2014).

Gnos and Nicolas (1996) and Gnos (1998) mapped and estimated the metamorphic conditions of the sub-ophiolitic sole in the Masafi window and at Bani Hamid. Further work on Bani Hamid by Searle et al. (2015) produced a detailed geologic map, constrained the timing of peak granulite facies metamorphism, and refined the structural and metamorphic history. Cox et al. (1999) studied the geochemistry of peraluminous leucogranite dykes that intrude the mantle section near Dadna. Jacobs et al. (2015) reported cooling ages for samples from the metamorphic sole at Masafi as well as the ophiolite. Roberts et al. (2016) presented zircon and rutile U-Pb dates from the metamorphic soles at Masafi and Bani Hamid. Rioux et al. (2016) provided an exhaustive review of the geochronology of the entire ophiolite and obtained new U-Pb zircon and rutile dates for the ophiolite and metamorphic sole in Oman.

2.3 Geophysical constraints and extent of the ophiolite

The ophiolite forms a nearly 500 km long by up to 100 km wide arc shaped belt from northeast Oman to the Dibba zone, a structurally complex area that exposes the underlying thrust sheets (Figure 2.1; Searle, 1988b; Robertson et al., 1990a). The UAE portion of the ophiolite, ∼70 km of the total length of the belt, consists of two blocks separated by the Wadi Ham Fault: the Khor Fakkan block to the north, and the Aswad block to the south (Gnos and Nicolas, 1996). While inferences can be made from the surface geology, and is the focus of this chapter, geophysics is required to constrain the subsurface. In conjunction with the BGS (Styles et al., 2006) a high-resolution airborne magnetic and gamma-ray spectral survey was flown by Fugro, and

a deep seismic survey along 4 profiles was conducted by WesternGeco. The unpublished aeromagnetic data indicate the ophiolite extends in the subsurface for about 10 km west of the peridotite exposure at Jebel Faiyah (Figures 2.1 and 2.2; Batty et al., 2004). The data also suggest that the ophiolite extends 6–10 km offshore most of the eastern UAE, and up to 40 km offshore of Dibba (Batty et al., 2004). Two of the WesternGeco deep-seismic profiles run east-west across the ophiolite and provide some constraints on its thickness. A northern profile (D4) crossed the mantle sequence west of Dadna and was interpreted as showing a westward tapering wedge that thickens from 0 m at the Masafi metamorphic sole, to ∼5 km near the coast (Tarapoanca et al., 2010). The resolution at the base of the ophiolite, however, was poor, and thus the thickness particularly near the coast is speculative. A southern profile (D1) crossed the mantle sequence south of Masafi, but was only able to resolve the base of the ophiolite west of the Wadi Ham fault. Tarapoanca et al. (2010) interpreted the results to indicate that the ophiolite is wedge shaped and thickens from near zero at the Wadi Ham fault, to ∼2 km to the west where it terminates near the latitude of Jebel Faiyah.

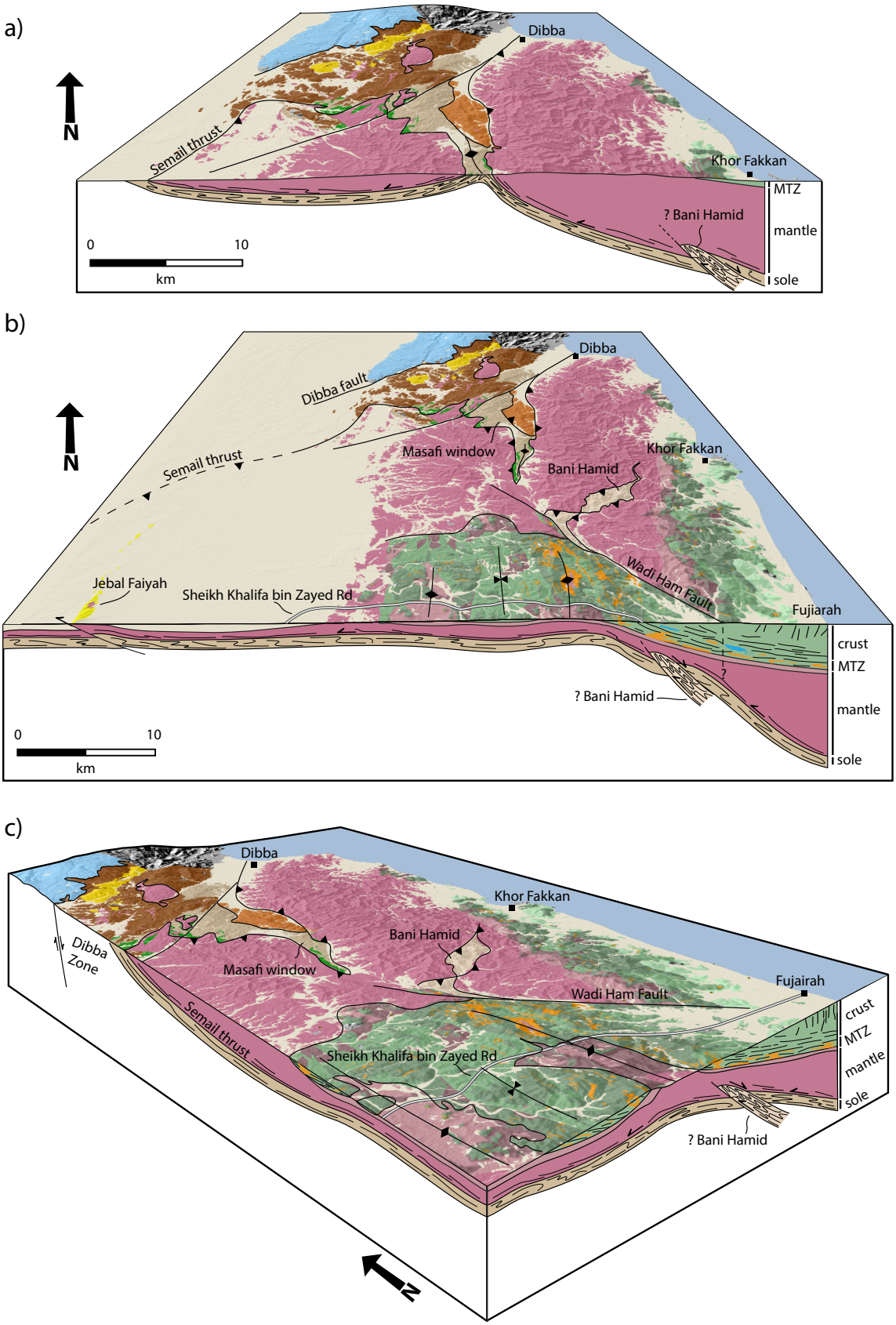

a)
N
Dibba
Semail thrust
Khor Fakkan
MTZ
? Bani Hamid
mantle
0
10
km
sole
b)
N
Dibba
Dibba fault
Semail thrust
Masafi window
Khor Fakkan
Bani Hamid
Wadi Ham Fault
Jebal Faiyah
Sheikh Khalifa bin Zayed Rd
Fujiarah
crust
MTZ
? Bani Hamid
mantle
0
10
km
sole
c)
Dibba
Khor Fakkan
Bani Hamid
Dibba
Zone
Masafi window
Fujairah
Wadi Ham Fault
crust
MTZ
Semail thrust
Sheikh Khalifa bin Zayed Rd
mantle
sole
? Bani Hamid
N

Figure 2.2 ***(preceding page)*****:** Simplified 3-dimensional block models presenting the large-scale structure of the ophiolite. (a) East-west section across the Masafi Window. (b) East-west section near the Sheikh Khalifa Bin Zayed road as discussed in the text. See Figure 2.1 for the locations of figures that constrain the structures (c) East-west and north-south section through the UAE ophiolite. The north-south section shows how the map pattern can be explained by a gently southward dipping ophiolite. In all three panels a speculative location of the Bani Hamid thrust slice is shown. See Figure 2.1 for key.

2.4 Field constraints on the structure and architecture of the ophiolite in the UAE

New road cuts along the Sheik Khalifa Bin Zayed motorway to the west of Fujairah in the southern UAE provide continuous exposure across the ophiolite from the mantle section through to the sheeted dykes (Figures 2.1 and 2.2). This section documents these new exposures as well as key field observations from elsewhere in the UAE that are used to constrain the structure and architecture.

2.4.1 Mantle sequence

Along the Sheikh Khalifa Bin Zayed motorway, the mantle sequence outcrops from where the mountains begin to rise out of the desert gravels through to the high mountains (Figure 2.1). The mantle sequence consists of serpentinized harzburgite and subordinate dunite (Figure 2.3A). Mantle peridotites are cut by orthopyroxenite veins, gabbro sweats, and gabbroic–doleritic dykes (Python and Ceuleneer, 2003). The geochemical signature of plagiogranite dykes that intrude the upper part of the mantle sequence indicate mixing between crustal, mafic, and mantle sources (Rollinson, 2009, 2014). A range of biotite leucogranites and peraluminous andalusite + garnet + biotite cordierite leucogranite dykes indicate melting of a sedimentary protolith beneath the obducted ophiolite (Cox et al., 1999). Lineations and foliations are typically absent or poorly developed. However, the base of the ophiolite, exposed around the Masafi window and at Bani Hamid (Figure 2.1), consists of mylonitized harzburgite and dunite with a well-developed foliation parallel to the sole thrust (Figures 2.3B and 2.3C; Banded Ultramafic unit of Searle and Malpas (1980)). Along this shear zone, fabrics related to the obduction have been superimposed on original mantle fabrics (Nicolas et al., 1980). Chapter 3 of this thesis, demonstrates that olivine grains size decreases towards the base of the ophiolite and is controlled by the abundance of volumetrically minor phases (pyroxene and hornblende). Farther up the section, dunite occurs within harzburgite as meter to tens of metres bands roughly parallel to the Moho (Figure

2.3D). The proportion of dunite is generally higher near the top of the mantle section.

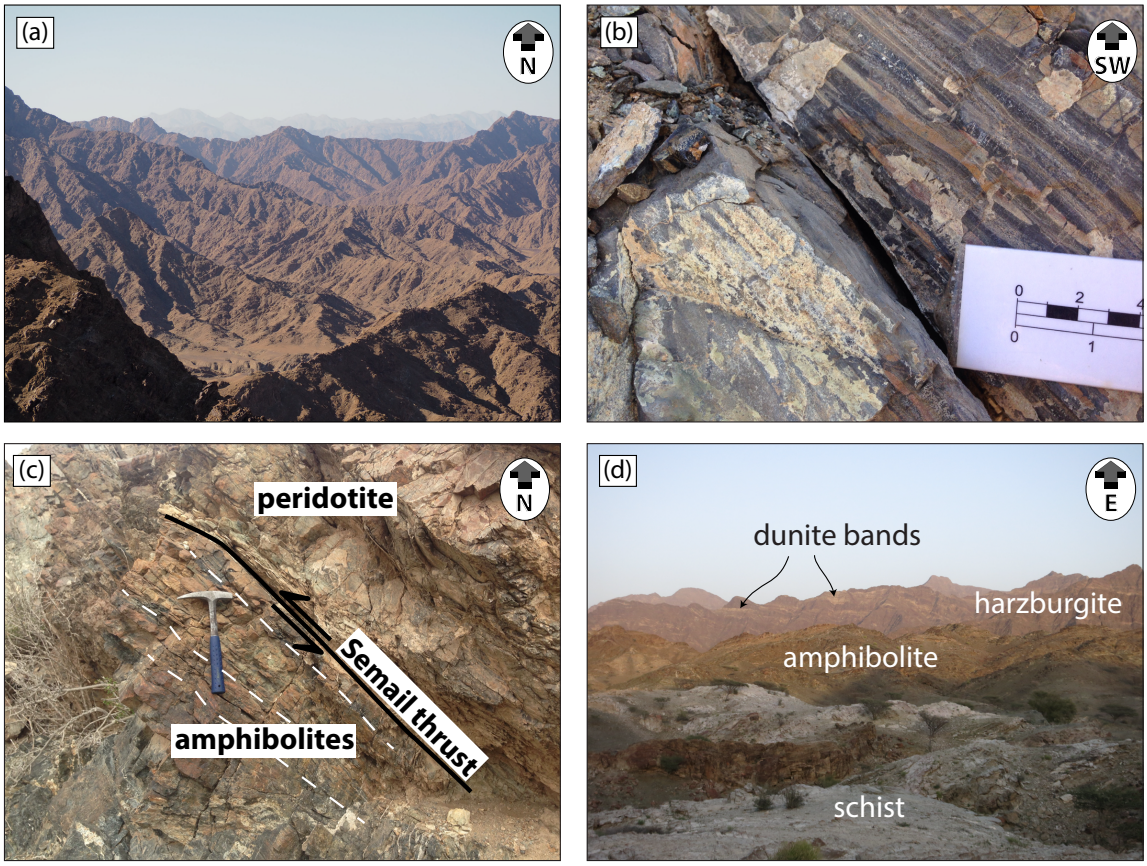


Figure 2.3: Field photographs of the mantle section. (a) Mountains of generally featureless mantle harzburgites in the northern UAE. (b) West-dipping mylonitized harzburgite exposed near the western margin of the Masafi window. (c) East-dipping Semail thrust exposed along the eastern margin of the Masafi window. (d) Quartz-schists and amphibolites of the sole in the Masafi window with the overlying mantle peridotites in the background. Note the horizontal dunite bands within the harzburgite.

2.4.2 Moho Transition Zone

The crust and mantle sections of the ophiolite are separated by the Moho Transition Zone (MTZ), which comprises a thickness of 10s to 100s of meters of mixed mafic and ultramafic lithologies (Boudier and Nicolas, 1995). The base of the MTZ, marked by the first appearance of gabbro, is the petrologic Moho, and the top, marked by a sharp decline of ultramafic lithologies and faster P-wave velocities, is the seismic Moho. The exact location of where the boundaries are drawn can be subjective as the boundaries are gradational and laterally inconsistent. In the UAE, the MTZ includes the Mixed Unit of the BGS (e.g., Goodenough et al., 2010) as well as the stratigraphically higher interlayered gabbro and wehrlite.

The base of the MTZ, located ∼2 km east of the first mantle peridotites along the road section, is marked by the first appearance of gabbro (Fig. 2.4A). The base of the MTZ is generally shallowly dipping and clearly observed in the field separating the more competent overlying rock, from the rubbly peridotite below (Fig. 2.4B). Across the mountains, the high peaks are capped by gabbro, whereas peridotite of the mantle sequence and MTZ is exposed in topographic lows (Figure 2.4A).

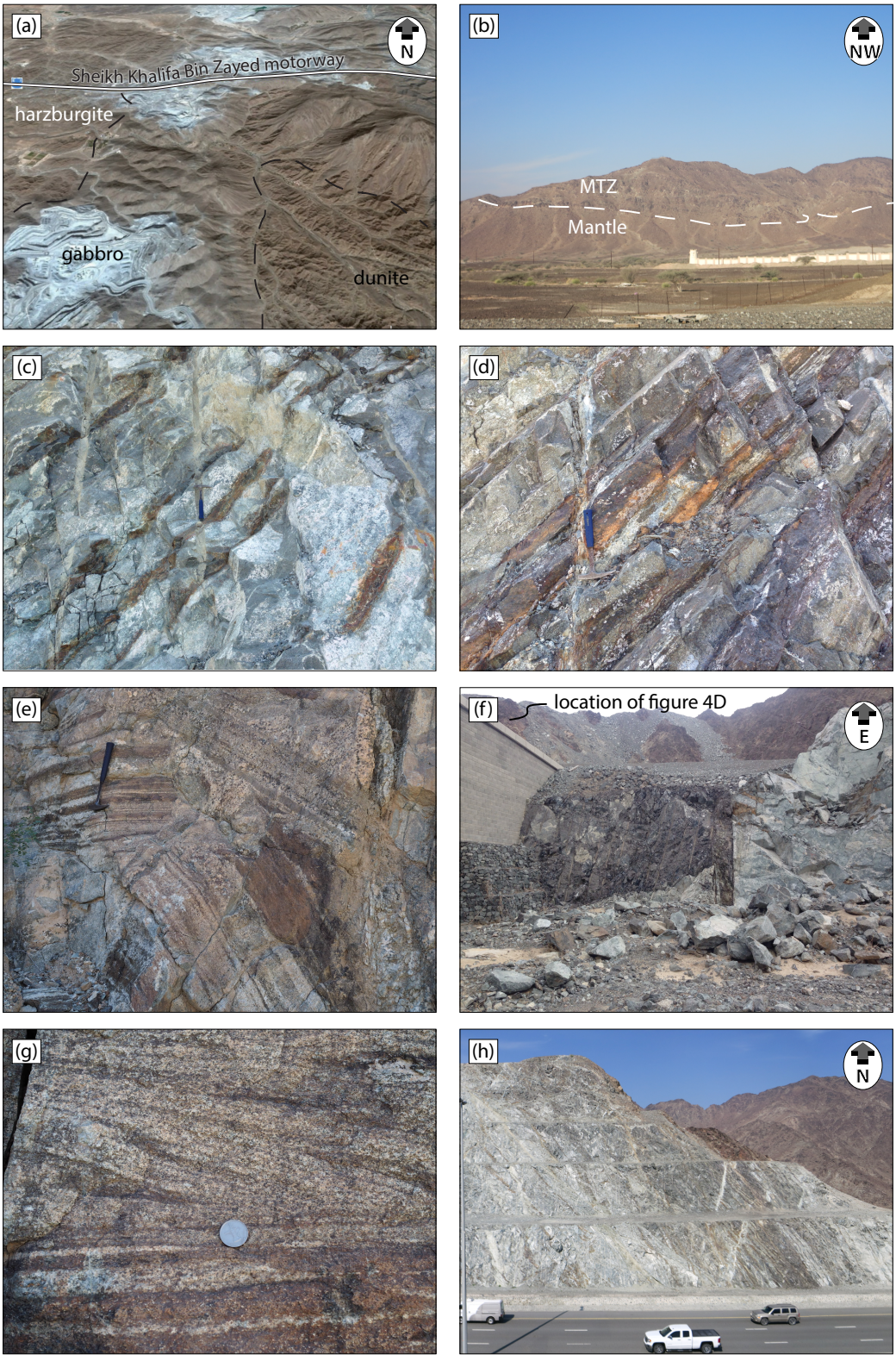

(a)
N
Sheikh Khalifa Bin Zayed motorway
harzburgite
gabbro
dunite
(b)
NW
MTZ
Mantle
(c)
(d)
(e)
(f)
location of figure 4D
E
(g)
(h)
N

Figure 2.4 ***(preceding page)*****:** (a) Inclined Google Earth image showing the first exposures of gabbro from the west along the road section. Gabbros, marked by the quarries, occur on topographic highs whereas dunite and harzburgite occur in topographic lows, consistent with a shallow MTZ. (b-h) Field photographs of the Moho Transition Zone (MTZ). (b) Shallowly dipping contact separating rubbly ultramafic rocks from the overlying mixed gabbro and ultramafic lithologies of the MTZ. (c) Oxidized olivine-rich gabbro pods in less olivine rich gabbro. (d) Interlayered wehrlite and gabbro. (e) Multiple orientations of modal layering within the gabbros. (f) Outcrop of wehrlite that feeds up into layered wehrlite and gabbro shown in 2.4D. (g) Sedimentary-like cross-bedding in gabbro. (h) Steeply dipping interlayered wehrlite and gabbro.

In general, the proportion of ultramafic lithologies decreases up section through the MTZ. The lower part of the MTZ is dominated by wehrlite and clinopyroxenite sills and dykes, dunite pods and dykes, and layered olivine-gabbro (Figure 2.4 and 2.5). Ultramafic intrusions and xenoliths can be over a kilometre in size (Figure 2.1). Gabbro textures and composition can be highly variable over small distances, with grain size ranging from very fine to pegmatitic. Aside from late cross-cutting plagiogranite dykes (e.g., Figures 2.5A and 2.5C), magmatism with a large range in compositions appears to have occurred synchronously, or over a very short time span (Figures 2.5A–C). Ultramafic-gabbro contacts are commonly irregular and lack chilled margins, consistent with intrusion of melts into a still hot and ductile host rock (Figures 2.5A and 2.5C). Multiple magmatic episodes are seen with peridotite xenoliths in gabbro (Figures 2.5A–D), gabbro dykes cutting peridotite (Figure 2.5C), wehrlite intrusions cross-cutting earlier gabbros (Figures 2.5A and 2.5C), and wehrlite interlayered with gabbro (Figures 2.4D, 2.4H and 2.5D).

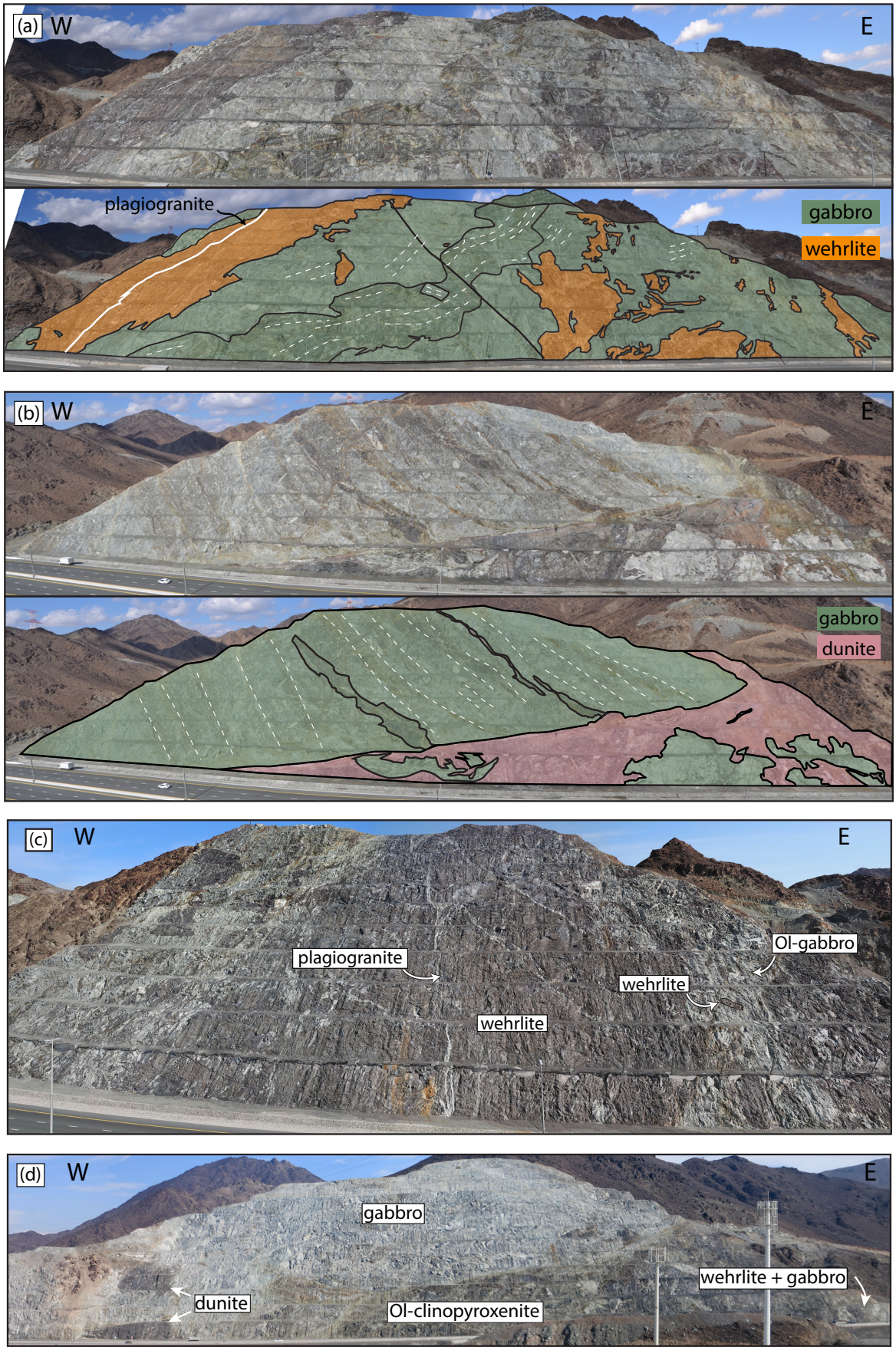

(a)
W
E
plagiogranite
gabbro
wehrlite
(b)
W
E
gabbro
dunite
(c)
W
E
plagiogranite
Ol-gabbro
wehrlite
wehrlite
(d)
W
E
gabbro
dunite
Ol-clinopyroxenite
wehrlite + gabbro

Figure 2.5 ***(preceding page)*****:** Panoramas of a ∼50 m high road cuts along the Sheikh Khalifa Bin Zayed motorway that expose the MTZ. The mineral abundances, textures, and development of layering within the gabbro is highly variable. See Figure 2.1 for photo localities. (a) A darker, relatively olivine rich, section of layered gabbro cuts across the middle of the road cut. A several-metre-size block in the centre of the photo has rotated and fallen into the rest of the olivine rich layer. Wehrlite not only cuts and includes xenoliths of gabbro, but is also cut by and included within gabbro, suggesting that both phases of magmatism were synchronous. (b) Layering in the gabbro is well developed and defined by the modal abundance of olivine. Gabbro occurs in both intrusive and fault contact with dunite. (c) Wehrlite both intruded and was intruded by gabbro. Here, most of the gabbro postdates the wehrlite, as indicated by the abundant xenoliths of wehrlite. A near vertical, late plagiogranite dyke cuts the entire section. (d) Olivine-clinopyroxenite and dunite in both fault and intrusive contact with gabbro.

Gabbro layering in the MTZ is defined by changes in the modal abundance of olivine, clinopyroxene, and plagioclase. The most obvious layering is the result of interlayered gabbro and wehrlite (Figures 2.4D and 2.4H). In places, larger wehrlite intrusions (Figure 2.4F) can be observed feeding upwards into interlayered wehrlite and gabbro (Figure 2.4D). Layering, which is common but not always present or obvious within the MTZ, occurs on the decametre scale and generally dips moderately to the northeast. The orientation, however, can be highly variably at the outcrop scale (Figures 2.4E), and in places dips to the west (Figure 2.5A). In some places, there are examples of sedimentary-like structures such as graded bedding and cross-bedding (Figure 2.4G), which we interpret as representing magmatic flow and crystal-settling along the base of a small magma chamber or sill. Olivine-rich gabbro commonly forms conspicuous oxidized pods that are parallel to modally layered, less olivine-rich gabbro (Figure 2.4C).

2.4.3 Crustal Sequence

The upper boundary of the MTZ and base of the crustal section is marked by a general lack of ultramafic rocks (Figures 2.6A–D). Up-section (towards the east), the modal abundance of olivine in gabbro decreases and layering becomes less common (Figure 2.6E). Along our profile, the base of the crustal section is located just east of the village of Farfar (Figures 2.1 and 2.2) and coincides with spectacular exposure of 'vinaigrette' (Goodenough et al., 2010), a unit that cuts layered olivine gabbro, and consists of tonalitic melt that has intruded diorite that appears to have been brittle in some places but ductile elsewhere (Figures 2.6A–D and 2.7). The diorite is relatively fine grain and consists of roughly equal portions of biotite, amphibole, quartz, and feldspar. The tonalite is coarser and consists of quartz, plagioclase, and amphibole. The 'vinaigrette' unit was also observed near the upper section of the crustal unit, although less commonly and in smaller volumes. 'Vinaigrette' dykes near the base of the crust that feed up into sills that spread laterally (Figures 2.6A–D and 2.7) coincide with a change from the primarily horizontal flow of the gabbros below, to the primarily

vertical flow above, including the sheeted dyke complex. Mafic dykes become increasingly abundant up section. Vertical sheeted dykes are exposed along the coast south of Fujairah (Figure 2.6E) and the higher pillow lavas crop out further south in Oman. The near vertical orientation of the sheeted dykes near Fujairah indicates the ophiolite pseudostratigraphy is likely near horizontal.

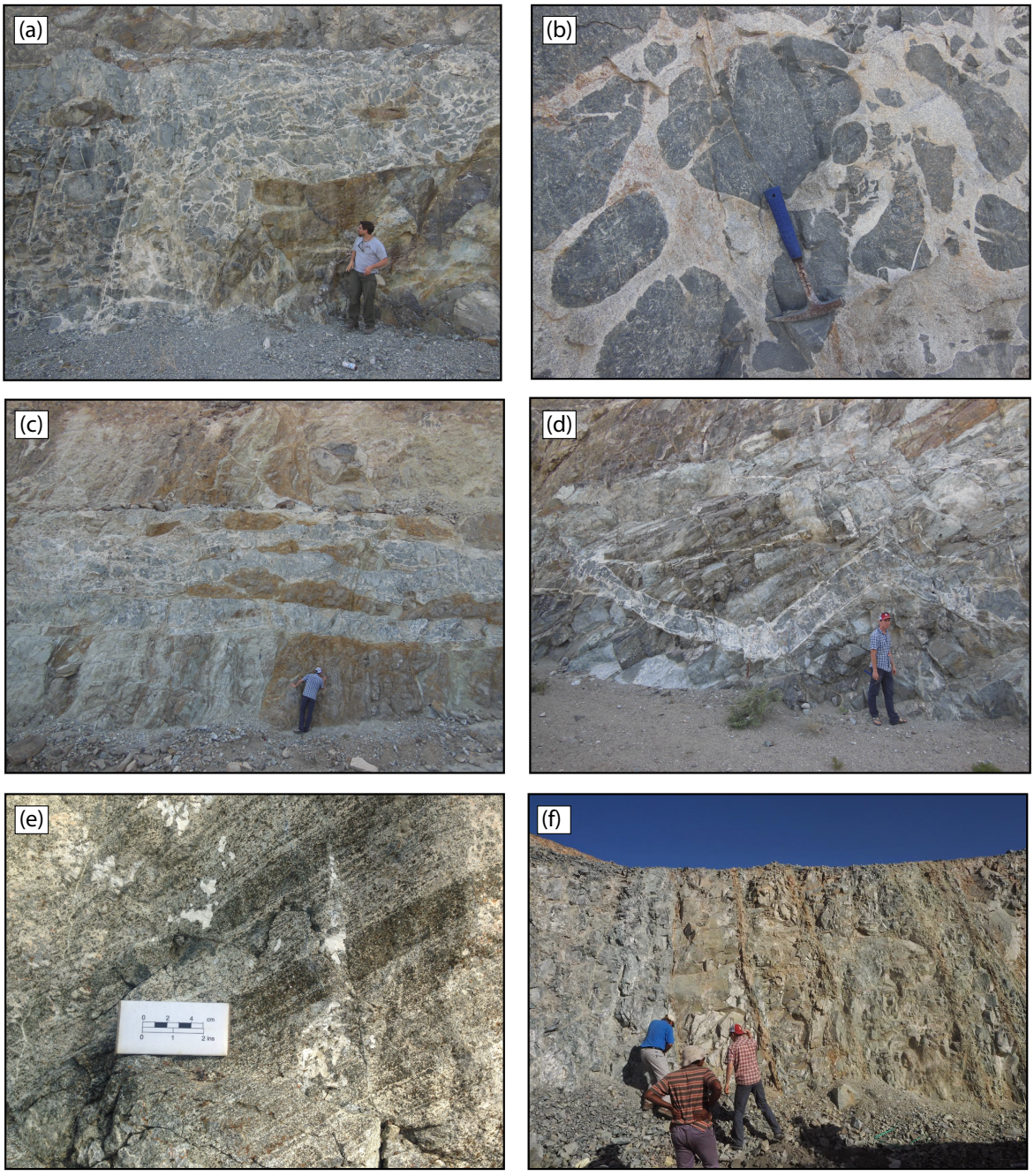


Figure 2.6: Field photographs of the crustal section in the southern UAE. (a-d) Dykes comprising light coloured plagiogranite and darker coloured diorite, commonly referred to as 'vinaigrette', intruded into olivine gabbro. In places the diorite appears to have been ductile during intrusion of the tonalite, whereas in elsewhere it deformed brittlely. (e) Fine-scale modal layering, defined by varying abundance of plagioclase and pyroxene, in crustal gabbros. (f) Vertical sheeted dykes south of Fujairah City.

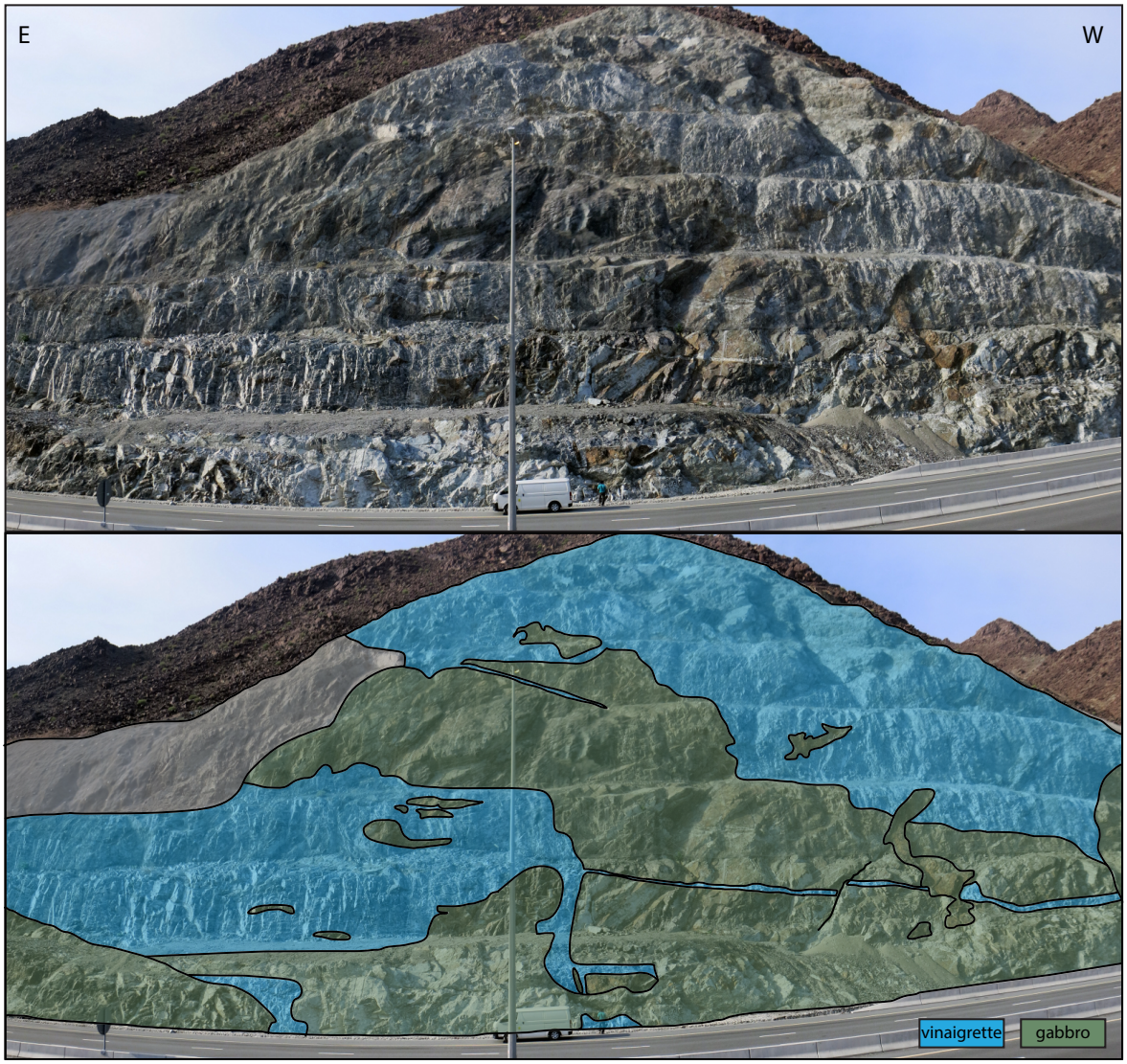


Figure 2.7: An ∼50 m high road cut showing 'vinaigrette' dykes that cut layered olivine-gabbro. This outcrop is near the base of the crustal section, as defined by the general lack of ultramafic lithologies. See Figure 2.1 for location.

2.4.4 Metamorphic Sole

The metamorphic sole is a thrust bound package of highly sheared amphibolites and metasedimentary rocks including quartzite and marble located immediately beneath the ophiolite (Figures 2.3C–D). In the UAE, the metamorphic sole is exposed in the Masafi window, along the northern margin of the ophiolite, and at Bani Hamid (Figures 2.1 and 2.2). Metamorphic grade in the sole is inverted, with progressively lower grade rocks exposed at deeper structural levels (Searle and Malpas, 1980, 1982; Gnos, 1998; Cowan et al., 2014). The top ∼100 m of the sole consists of garnet-clinopyroxene amphibolites that pass down section through bimineralic- and epidote- amphibolites (Figures 2.8A–B). The amphibolites gradually transition down structural section to isoclinally folded greenschist facies metasedimentary rocks that consist of piemontite (manganese rich epidote) bearing quartzites (Figure 2.8C, and quartz+mica schists (Figure 2.8), as well as occasional carbonate and ash layers.

Sub-ophiolitic metamorphic rocks are also exposed in the Bani Hamid thrust slice (Figure 2.1). Unlike the Masafi sole, the metamorphic sequence at Bani Hamid preserves granulite facies assemblages throughout the ∼1 km thick package of calc-silicates, two-pyroxene quartzites, and amphibolites (Searle et al., 2015). Rocks from the metamorphic sole in Masafi, which are similar to the Sumeini and Wadi Tayyin localities in Oman, record peak pressures and temperatures of 11–13 kbar and 770–900 °C (Gnos, 1998; Cowan et al., 2014), while rocks from Bani Hamid record similarly high temperatures of ∼850 °C, but considerably lower pressures of only ∼6 kbar (Searle et al., 2015). Whereas the normal metamorphic sole is interpreted to represent thrust-slices of oceanic basalts and sediments subducted beneath the newly forming ophiolite (e.g., Searle and Malpas, 1980, 1982; Hacker, 1990b), the much thicker Bani Hamid granulites are thought to be Haybi thrust sheet units stacked up in the lower crust during the later stages of obduction (Searle et al., 2015).

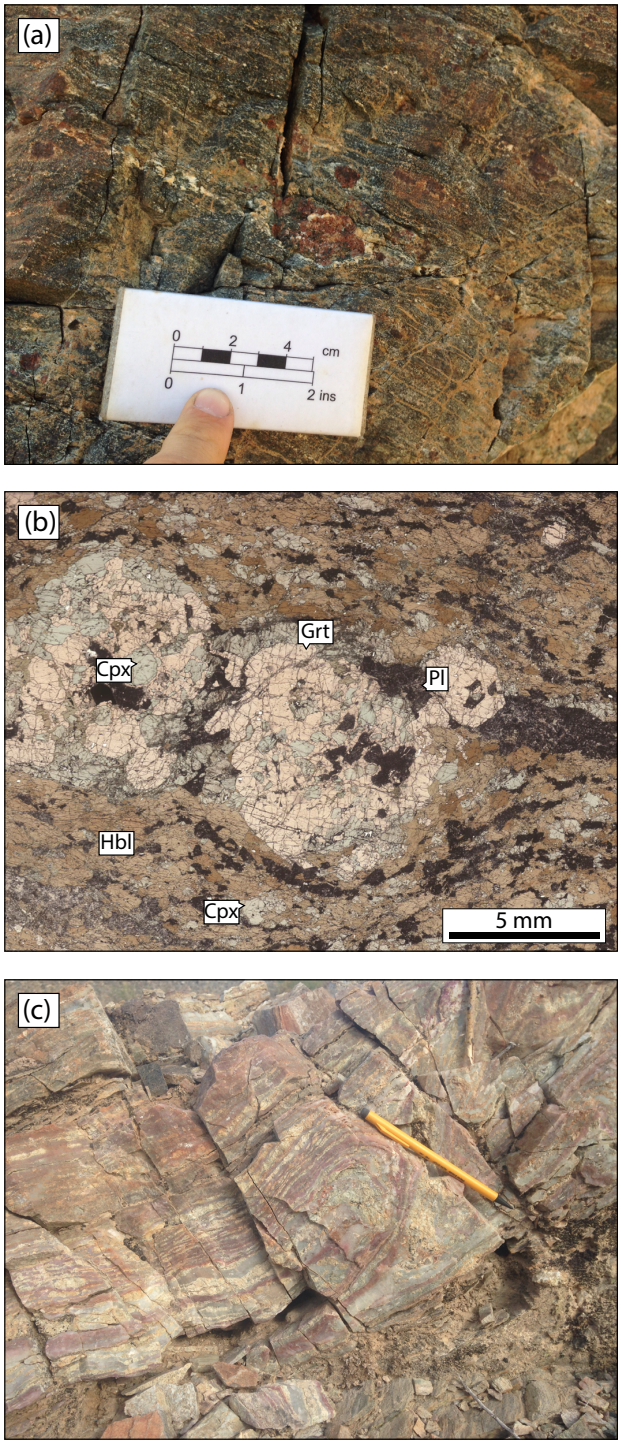


Figure 2.8: Field photographs and a photomicrograph of the metamorphic sole. (a) Garnet-clinopyroxene amphibolite near the top of the sole. (b) Photomicrograph of garnet-clinopyroxene amphibolite. Clinopyroxene occurs as inclusions in garnet, rimming garnet, and in the amphibolite and plagioclase matrix. The main foliation, defined by the alignment of amphibole, wraps around and hence post-dates the garnet. (c) Isoclinally folded piemontite bearing quartzite in the metamorphic sole.

2.5 Discussion

2.5.1 Is the ophiolite in the UAE different from Oman?

Recent studies have suggested that the magmatic, structural, and tectonic evolution of the ophiolite in the UAE are considerably different from Oman (Styles et al., 2006; Goodenough et al., 2010, 2014; Nicolas and Boudier, 2017). The BGS team (Styles et al., 2006; Goodenough et al., 2010, 2014) proposed that widespread mantle-rooted ductile faulting during ophiolite formation exerted a primary control on the architecture of the ophiolite in the UAE, but not in Oman. The BGS team suggested that the widespread ductile shear zones and associated magmatism were related to subduction initiation and post-dated an early mid-ocean ridge phase. Nicolas and Boudier (2017) speculated that, unlike in Oman, the UAE portion of the ophiolite formed at a ridge-trench junction within an embayment along the Arabian continental margin. Constraining geological evolution of the UAE portion of the ophiolite and its relationship to Oman has implications for regional tectonics as well as ophiolite emplacement, subduction initiation, and sea-floor spreading in general. Here we combine our field observations with previously published BGS maps to constrain the large-scale structure and internal architecture of the ophiolite in the UAE.

2.5.2 Regional structure of the ophiolite in the UAE

Figure 2.2 presents the regional structure of the ophiolite in the UAE as constrained by our field observations. The eastward progression from the mantle sequence through to structurally higher levels of the ophiolite indicates that, on a regional scale, the ophiolite pseudostratigraphy dips to the east. The exposure of gabbro on topographic highs, and MTZ and mantle sequence rocks in topographic lows (Figures 2.4A and B), as well as the near-vertical orientation of the sheeted dykes south of Fujairah (Figure 2.6) indicate that the ophiolite pseudostratigraphy dips gently.

At the Masafi window, the Semail thrust is folded into a roughly north-south trending anticline and erosion through the base of the ophiolite has exposed the metamor-

phic sole. The closure of the window to the south indicates that the anticline axis plunges south (Figures 2.2A–C). A southward plunge is also consistent with exposure of the metamorphic sole beneath the northern extent of the ophiolite (Figure 2.2C). Folding and (late-stage) exhumation of the metamorphic sole was related to the post-Oligocene–early-Miocene west-vergent thrusting and culmination of the Musandam shelf carbonates to the north and the subsequent Miocene onset of the Zagros orogeny (Searle et al., 2014). Thus, folding post-dates ophiolite emplacement (Searle et al., 2014), which requires that the ophiolite is also folded.

From the Masafi window, where present-day thickness of the ophiolite thins to zero, and assuming a dip of 20° for the Semail thrust, the ophiolite thickens to ∼6 km along the coast to the east (Figure 2.2B), consistent with (albeit speculative) geophysical constrains (Tarapoanca et al., 2010). Note, however, that the measured dip of the Semail thrust at the surface is variable and often much steeper that 20° (Figure 2.3C). As the ophiolite pseudostratigraphy dips shallowly, 6 km also approximates the pseudostratigraphy thickness of the present-day ophiolite along the coast to the east of the Masafi window. Since this portion of the ophiolite primarily consists of the mantle section, an additional ∼5 km or so must be added to account for the original ophiolite thickness, including the crustal section. The resulting ∼11 km thickness for the complete ophiolite section is in agreement with estimates from Oman (e.g., Nicolas et al., 2000).

The Bani Hamid granulite sequence is exposed in the hanging-wall of the Bani Hamid thrust (Figures 2.1 and 2.2; Searle et al., 2015). Two lines of evidence indicate that the Bani Hamid Thrust was out-of-sequence: (1) it structurally offsets the older Semail Thrust (Searle et al. 2015), and (2) cooling ages indicate that it was exhumed later than the normal sole (Hacker, 1994; Hacker and Mosenfelder, 1996; Searle et al., 2015; Roberts et al., 2016). The Bani Hamid metamorphic sequence is distinct from the rest of the sole exposures in that it is uniformly granulite facies, and contains a much higher proportion of meta-carbonate and two-pyroxene quartzites (Gnos and Nicolas, 1996; Searle et al., 2015). Searle et al., (2015) interpreted the

Bani Hamid granulites to be the metamorphosed equivalent of the Haybi thrust sheet (Triassic Oman exotics, cherts and minor alkali basalts) which, due to the low-density carbonates and quartzites, jammed the subduction zone and initiated out-of-sequence thrusting. The lithologies and metamorphic conditions of the Bani Hamid thrust slice are unique to this occurrence in the UAE. However, it is possible and rather likely that similar granulite-facies Haybi equivalents are located at depth beneath the rest of the ophiolite to the south. We speculate that Bani-Hamid-like thrusts may tip-line at depth elsewhere (Figure 2.2).

2.5.3 Architecture of the ophiolite in the UAE

Our large-scale constraints on the structure of the ophiolite provide the basis to decipher its architecture. In general, the Oman-UAE ophiolite can be considered a classic Penrose-type ophiolite, consisting of mantle harzburgites and dunites overlain by layered and isotropic gabbros, sheeted dykes, and finally basaltic flows, pillow basalts, and pelagic sediments (Figure 2.9A; Anonymous, 1972). In detail, however, the ophiolite architecture is considerably more complex. Contacts are gradational over 10s to 1000s of metres: layering in the gabbros becomes less pronounced up section and slowly gives way to isotropic gabbros as the proportion of olivine and wehrlite decreases. Likewise, mafic dykes gradually increase in abundance up-section until they comprise 100% of the section and eventually transition into pillow basalts and lava flows. At the outcrop scale, contacts are complex and in the absence of 3-dimensional exposures, are difficult to interpret (Figures 2.4–2.7). The gradational and complex nature of contacts make placing lines on a map difficult and highly subjective.

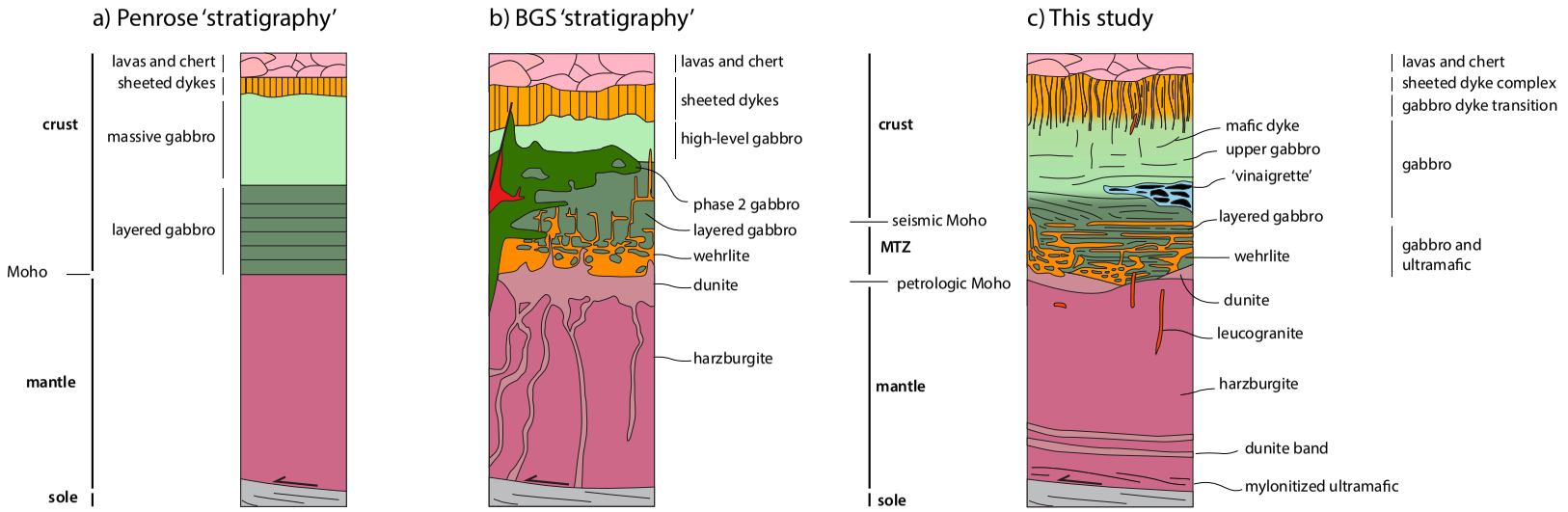


Figure 2.9: Pseudostratigraphy of the ophiolite as proposed by different authors. (a) The classic Penrose ophiolite (Anonymous, 1972). (b) Pseudostratigraphy of the ophiolite as proposed by the British Geological Survey. Note the dark green gabbro on the left that cuts from the mantle through to the sheeted dykes. (c) Pseudostratigraphy of the ophiolite as per this study. The key difference between this study and the BGS study is the lack of cross-cutting gabbro. Also note that dunite bands are always observed to be roughly parallel to the Moho, as shown in Figure 2.3. See text for discussion.

The BGS team attributed the map pattern in the southern UAE, and in particular the extensive gabbro and MTZ (Figure 2.1), to reflect a major phase of cross-cutting magmatism related to subduction initiation and associated ductile shear zones that routed in to the mantle (Styles et al., 2006; Goodenough et al., 2010; Farrant et al., 2012; Goodenough et al., 2014). The BGS presented a pseudostratigraphy specific to the ophiolite in the UAE that exhibits several differences from the classic Penrose ophiolite (e.g., Goodenough et al., 2014; reproduced in Figure 2.9B). The BGS pseudostratigraphy illustrates the complex and gradational nature of contacts. It is also worth noting the proposed vertical dunite bands (Figure 2.9B), which are commonly inferred to be the remnants of conduits that transported melt from the mantle up to the crustal section during ophiolite formation (e.g., Kelemen et al., 1995). Throughout our investigation of the ophiolite in both the UAE and Oman, dunite bands were almost always observed to be parallel to the Moho and near the base of the ophiolite, rather than vertical (Figure 2.3D). The feature we wish to highlight is the proposed late cross-cutting gabbro, illustrated intruding along a shear zone in Figure 2.9B. Note that in Figures 2.1 and 2.2 we have kept the BGS subdivision of late gabbro for reference, although we argue against it in the following paragraph. The BGS speculated that the cross-cutting gabbros and associated ultramafic rocks (e.g., wehrlite) cut the entire mantle section of the ophiolite (Figure 2.10A; also see Figure 5 in Goodenough et al. (2010) and Figure 5 in Goodenough et al. (2014)). Based on the revised pseudostratigraphy specific to the UAE, the BGS proposed that northern blocks of the ophiolite underwent a separate evolution.

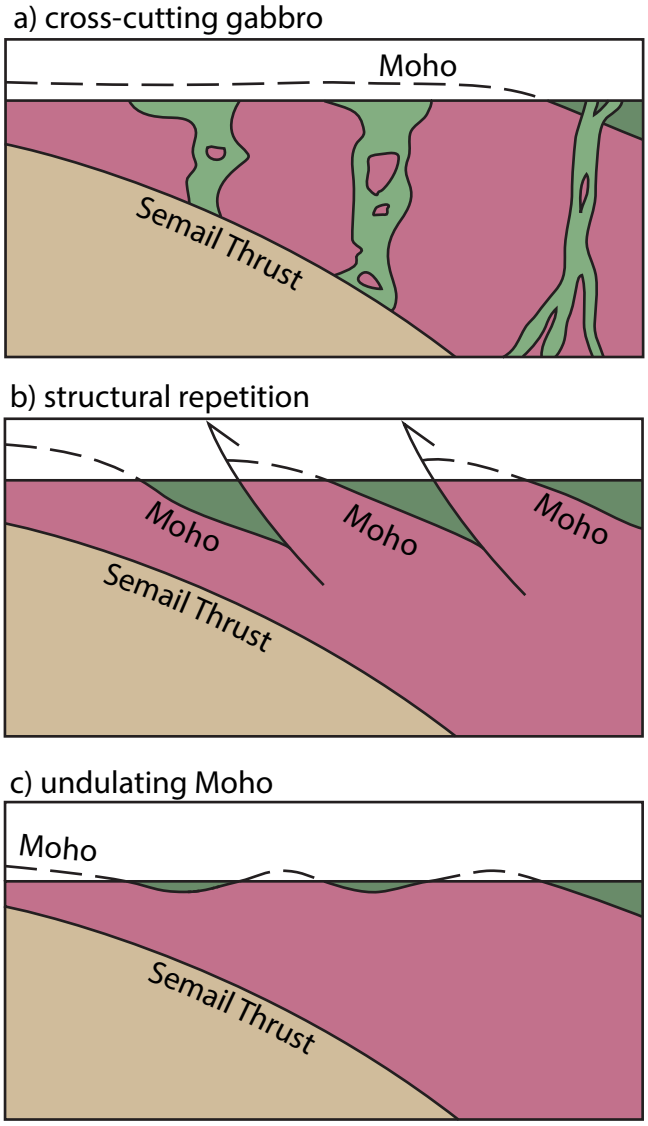


Figure 2.10: Schematic diagrams summarizing 3 different models for the map pattern, and in particular the extensive crustal section, of the ophiolite in the southern UAE. All three models result in the same repetition of gabbro (green) and ultramafic (burgundy). (a) The BGS model, with an early (darker green) and later cross cutting phase of gabbro (lighter green). (b) Model in which the extensive gabbro results from out-of-sequence-thrusts that cut the ophiolite and repeat the crustal section. (c) Model preferred by the authors in which the ophiolite is near horizontal and undulating, and present erosion levels coincide with the MTZ.

However, the BGS interpretation of the architecture in the UAE is inconsistent with our field observations as well as recent geochemical and geochronological data. First, major-element fractionation trends for the V1 (Geotimes) volcanics (MacLeod et al., 2013), and overlapping dates for peak-metamorphism of the metamorphic sole (i.e, downgoing slab) with crystallization ages from the crustal-section of the ophiolite(Rioux et al., 2016), both indicate that the entire ophiolite formed above a subduction zone. As such, there is no inherent need to invoke two distinct phases of magmatism that correspond to different tectonic settings. Second, high-resolution U-Pb zircon dates reveal that the entire crustal-section of the ophiolite was formed in only ∼1 Myr (Rioux et al., 2012, 2015, 2016), a much shorter time-span than previously thought. Goodenough et al., (2010) concluded that the early (mid-ocean ridge) phase of magmatism must be older than ∼96.4 Ma, the oldest age obtained for the late magmatic suite. Rioux et al. (2012, 2015, 2016), however, demonstrated that both phases of magmatism occurred between ∼96.5 and ∼95.5 Ma. As such, what were previously interpreted as early and late phases of magmatism were evidently coeval. Ambiguous and highly-varied cross-cutting relationships, a lack of chilled margins, and irregular contacts, are all consistent with short-lived and simultaneous mafic–ultramafic magmatism. Third, although the geochemical signatures of the early and later suites can be distinguished on some discrimination diagrams, the transition between the two is gradational (Goodenough et al., 2010, 2014). Geochemical variation across the ophiolite, interpreted to reflect a range in the degree of subduction input, can be explained by an evolving subduction zone, as previously proposed by Whattam and Stern (2011). In addition to the complex cross-cutting relationships and gradational nature of contacts, the fact that the transition in geochemical signatures between the early- and late-magmatic phases is gradational precludes any chance of consistently mapping such contacts. Finally, the BGS model predicts that large volumes of gabbro cut the mantle section of the ophiolite. Aside from metre-scale gabbroic and granitic dykes, we observed no major intrusions in the mantle section. Within the mantle section there are a number of gabbro outcrops surrounded by harzburgite (Figure 2.1). In each instance,

however, the contacts are near horizontal, there is no evidence that the gabbro cutting across the mantle, and the relationship is more easily explained as marking the base of the MTZ.

Given the lack of evidence for major late-stage cross-cutting magmatism, some other explanation is needed to explain the large extent of gabbro and MTZ lithologies in the southern UAE. It is conceivable that out-of-sequence-thrusts have structurally repeated the MTZ and lower crust (Figure 2.10B). However, our observations indicate that the ophiolite is largely intact and only gently folded. The map pattern results from the interplay between relatively simple structure, topography, complicated magmatic relationships (e.g., synchronous ultramafic through to mafic and felsic magmatism), and highly subjective contacts. This interplay commonly produces localities on the map that appear to be major structures (i.e., shear-zones or faults). Such a case is illustrated by Figure 2.5B, which reveals the gradational contact between gabbro to the west, and dunite to the east (see Figure 1 for location). The BGS interpreted the contact in Figure 2.5B to be part of a major (10s of km long), vertical, north-south shear zone related to intrusion of a late gabbro (Styles et al., 2006). Following this contact to the north, the BGS has mapped a shear zone that separates layered gabbro to the east from late (Phase 2) gabbro to the west (Figure 2.1). However, the road cut reveals no evidence for such for large-scale shearing, but rather a gently west-dipping MTZ as presented in Figures 2.2B and C. Another example of an apparent structural contact is illustrated by Figure 2.4A (see Figure 2.1 for location). Here, the road passes through gabbro interpreted by the BGS to be a late intrusion that cuts the mantle section (Figure 2.1). Yet the contacts are shallow, with gabbro on topographic highs and peridotite in topographic lows.There is no evidence that the gabbro cuts up through the mantle section.

We propose that the apparently large volume of gabbro and MTZ lithologies exposed in the southern UAE results from an undulating and nearly horizontal MTZ that coincides with present-day erosion levels (Figure 2.10C). In other words, relative to Oman, the ophiolite in the southern UAE exposes an apparent but not actual high

level of gabbro and MTZ lithologies. An undulating/folded MTZ also explains along-strike structures in the ophiolite (Figure 2.2C). For example, north of the villages of Esfini and Mamdooh, the ophiolite passes from crustal gabbros and MTZ rocks to mantle sequence harzburgite (Figure 2.1). Goodenough et al. (2010) interpreted this to be another major ductile shear zone, with sufficient importance to require a name: the Siji shear zone. Upon investigation, however, the proposed shear zone lacks any obvious deformation. The contact, however, can explained by a southward dipping MTZ (Figure 2.2C), consistent with the presence of wehrlite and other MTZ lithologies along the contact, and the southward plunge of the folded Semail thrust at the Masafi window. Even the bulge of the contact directly north of Mamdooh is elucidated by projecting the gentle synform revealed along the road cut (Figure 2.2B).

Figure 2.9C presents our revised pseudostratigraphy for the ophiolite in the UAE. The key difference between our proposed pseudostratigraphy and that previously proposed by BGS (Figure 2.9B) is the lack of a distinct cross-cutting phase of magmatism. Our models for both the regional structure (Figure 2.2) and pseudostratigraphy (Figure 2.9C) of the ophiolite mark a considerable simplification compared to several recent studies. However, our interpretations are backed-up by extensive field observations, and in better agreement with recently published geochronological and geochemical data.

Our proposed pseudostratigraphy for the ophiolite in the UAE (Figure 2.9C) is broadly similar to that of Juteau et al. (1988) for Oman. Given the consistency, we see no reason to infer a unique tectonic evolution for the UAE sector of the ophiolite as proposed by both the BGS team as well as Nicolas and Boudier (2017). There is undoubtedly small-scale structural and magmatic complexity beyond what is presented in Figure 2.2. However, there is little evidence to support the large-scale faulting and ductile shear-zones (aside from the Bani Hamid out-of-sequence thrust and Wadi Ham vertical fault), nor the associated late-phase intrusions, proposed by the BGS (Styles et al., 2006; Goodenough et al., 2010, 2014). There is also no evidence to support the highly-speculative and perplexing model involving the interaction between ridge-trench junctions, mantle diapirs, slab-windows, transform faults, and pull-apart basins,

as recently proposed by Nicolas and Boudier (2017) for the UAE.

The BGS subdivided the gabbro into seven different units that correspond to the interpreted timing of intrusion, geographic location, and perceived abundance of mafic dykes. The BGS maps have been valuable to our research and, in general, the distribution of lithologies on the maps is consistent with our field observations. However, subdividing the units based on genetic interpretations is highly subjective and potentially misleading, especially considering that such genetic interpretations are largely inconsistent with recent studies.

2.5.4 The Oman-UAE ophiolite as an analogue for mid-ocean ridges

Despite the evidence for a SSZ setting, the Oman-UAE ophiolite continues to be used as an analogue for large-scale, mid-ocean ridges such as the East Pacific Rise (e.g., Nicolas, 1989; Boudier et al., 1997; Nicolas and Boudier, 2015, 2017). While ophiolites provide valuable insight into seafloor spreading and lithospheric structure, there are a number of key differences between the formation of the Oman-UAE ophiolite and mid-ocean ridges. Although a detailed review is beyond the scope of this paper, we highlight some of the key geochemical, petrological, geodynamical, thermal, and rheological differences between open ocean mid-ocean ridges and SSZ settings that may have influenced the structure of the ophiolite. Recognizing these distinctions is necessary to evaluate the suitability of the ophiolite as an analogue and when interpreting data from mid-ocean ridges.

1. Fractionation trends for the lavas and dykes required concentrations of water considerably higher than expected for mid-ocean ridges (MacLeod et al., 2013). The presence of water during ophiolite formation influenced petrological processes from melting through to crystallization. The volcanic stratigraphy of the ophiolite includes evolved lithologies from basaltic-andesites, through to andesites, dacites and even rhyolites (Pearce et al., 1981; Alabaster et al., 1982). In places the

volcanic rocks are boninitic (Pearce et al., 1981; Ishikawa et al., 2002).

2. Beneath mid-ocean ridges upwelling mantle decompresses and partially melts from depths greater than 100 km (The Melt Seismic Team, 1998). On either side of mid-ocean ridges the mantle advects horizontally away from the axis. In contrast, advection during crystallization of the ophiolite was within a mantle wedge, similar to a backarc basin (Taylor and Martinez, 2003).

3. The thermal structure of the mantle during ophiolite formation would have evolved rapidly as cold oceanic lithosphere was subducted. In contrast, the thermal structure beneath mid-ocean ridges is constant over considerably longer timescales.

4. The ophiolite formed rapidly over only ∼1 million years (Rioux et al., 2016). In contrast, mid-ocean ridges such as the East Pacific Rise have been spreading for tens to hundreds of millions of years (Muller et al., 2008). Feedback loops that control processes such as melt migration and strain localization may not have had sufficient time to reach steady state during formation of the ophiolite.

5. The released water into the mantle wedge may have also had a rheological effect. Water could have potentially weakened the lithosphere by (1) reducing the viscosity of olivine in the mantle (Mei and Kohlstedt, 2000a, 2000b) and gabbro in the crust (Getsinger et al., 2013), (2) stabilizing secondary phases that pin grain boundaries, limit grain size, and promote diffusion creep and associated rheological weakening (Herwegh et al., 2011; Chapter 3), (3) stabilizing inherently weak phases such as serpentine, and (4) lowering the melting temperature.

2.5.5 How was seafloor spreading accommodated during ophiolite formation?

Regardless of the precise tectonic setting, the thick crustal section of the Oman-UAE ophiolite is consistent with formation at a fast spreading centre (Reid and Jackson,

1981). Onshore, the ophiolite is as wide (across strike) as ∼120 km, which corresponds to a full spreading-rate of 120 km/Myr, or 120 mm/yr, comparable to the fastest modern spreading rates along the East Pacific Rise of 120–145 mm/yr (DeMets et al., 2010). However, 120 mm/yr is a minimum estimate as the offshore extent of the ophiolite is unknown. Furthermore, our estimate assumes that a spreading-rate of 120 mm/yr was reached instantaneously and at a single spreading axis. In other words, immediately following subduction initiation, an East Pacific Rise type spreading centre developed. If the initial spreading rate was zero, and acceleration was constant, a final velocity of 240 mm/yr is required to generate 120 km of spreading in 1 Myr, considerably faster than anywhere on Earth. An alternate hypothesis to rapid development of a single spreading axis is that extension was more broadly distributed, perhaps across multiple more diffuse centres. In addition to the unrealistically fast spreading-rates required, several lines of evidence are inconsistent with localized spreading: (1) There is no trend in crystallization ages collected across the strike of the ophiolite (Rioux et al., 2012). The dates indicate that magmatism was broadly synchronous rather localized at a single axis. (2) A large-range of magmatic compositions were intruded synchronously and there are no obvious trends in magma evolution, as might be expected as the seafloor is transported away from the axis (e.g., Boudier and Nicolas, 1995). (3) The widespread distribution of melting and presence of water indicate the lithosphere was weaker than typical of oceanic-lithosphere. Since extension, at least within the gabbros, was primarily accommodated within partially molten layers (VanTongeren et al., 2015), it seems unlikely that spreading would quickly localize. (4) No topographic spreading centres (sensu stricto) have been mapped in the ophiolite. In contrast, mapping of the Lasail (V2) arc volcanic rocks revealed isolated and chemically distinct seamounts above the ubiquitous V1 lavas (Pearce et al., 1981; Alabaster et al., 1982).

The East African rift provides some insight into the dynamics of early-stage extension, albeit in a continental break-up setting. The Main Ethiopian Rift of the East African Rift system records different stages in the evolution of rifting, from early continental rifting in the south, to seafloor spreading in the north (Corti, 2009). Along

the southern extent of the Main Ethiopian Rift, where rifting is in the early stages, extension and magmatism is distributed (Ebinger, 2005). Further north spreading is more advanced and deformation and magmatism become progressively more localized (Ebinger, 2005). Despite obvious difference between continental and oceanic rifting, it is reasonable to assume that some period of time is also required to localize strain and magmatism during the onset of extension in the ocean. Whether or not 1–2 million years was sufficient to develop a mature spreading centre during formation of the ophiolite is uncertain, but the evidence outlined above suggests it may not have been.

2.6 Conclusion

Several recent studies have suggested that the structural and magmatic architecture of the ophiolite in UAE is considerably different from Oman (Styles et al., 2006; Goodenough et al., 2010, 2014; Nicolas and Boudier, 2017). These studies have led to the suggestion that the UAE portion of the ophiolite underwent a separate tectonic history (Goodenough et al., 2010; Nicolas and Boudier, 2017). Determining whether or not the UAE portion of the ophiolite, which compromises approximately one-fifth the total length, is fundamentally different from Oman is critical to elucidating not just the regional tectonic evolution, but to subduction initiation, ophiolite formation, and ophiolite emplacement in general. We have demonstrated that the architecture (i.e., pseudostratigraphy) of the ophiolite in the UAE is broadly similar to Oman (e.g., Lippard et al., 1986; Juteau et al., 1988). Thus, there is no indication that the ophiolite in the UAE underwent a distinct tectonic history, as recently suggested (Goodenough et al., 2010, 2014; Nicolas and Boudier, 2017). Although our interpretation of the ophiolite in the UAE is a simplification of previous models, it is more consistent with our field-observations as well as recent geochemical and geochronological data. Based on our findings we make the following further conclusions:

- The ophiolite is largely intact, and gently folded. Aside from the Bani Hamid thrust and Wadi Ham fault, we found no evidence of the large-scale ductile shear-

zones mapped by the BGS team.

- In the southern UAE, the MTZ is gently folded, nearly horizontal, and coincident present-day erosion levels, giving the appearance of anomalously large volumes of magma. We found no evidence for anomalously high-volumes of late-stage magmatism associated with mantle-rooted ductile shear-zones, as proposed by the BGS team.

- Road cuts reveal ambiguous magmatic contacts that span a large-range of rock-types, consistent with the U-Pb geochronological evidence indicating the whole sequence formed in a very short (1 Myr) time (Rioux et al., 2012, 2013, 2016).

- At the regional scale, the map pattern is controlled by the interplay between topography, complex and irregular magmatic relationships, gradational (and hence subjective) contacts, and relatively simple regional-scale structures.

- Based on the evidence for wide-spread and short-lived magmatism, as well as the isolated distribution of volcanic centres in Oman (Pearce et al., 1981; Alabaster et al., 1982) we speculate that extension was broadly distributed during formation of the ophiolite, rather than concentrated at a single East-Pacific-Rise type spreading centre.

Chapter 3

Controls on the rheological properties of peridotite at a palaeosubduction interface: a transect across the base of the Oman-UAE ophiolite

3.1 Introduction

Earths lithosphere consists of highly viscous tectonic plates with deformation localized within less viscous material at plate boundaries (e.g., Bercovici and Karato, 2003). However, the processes that control the development of plate boundary-scale shear zones remain poorly constrained. Generating strain localisation in plate-tectonic models has proven challenging, primarily due to a lack of clarity on the best rheological parameterization (e.g., Tackley, 2000). An often proposed mechanism for localized weakening is localized grain-size reduction, as exemplified by the occurrence of mylonites in ductile shear zones (e.g., Rutter and Brodie, 1988). Studies of small-scale natural shear zones (Hansen and Warren, 2015; Herwegh et al., 2011; Toy et al., 2010;

Warren and Hirth, 2006) and experimentally deformed rocks (Hiraga et al., 2010; Farla et al., 2013) have demonstrated that volumetrically minor phases in polyphase rocks can control strain localisation by limiting grain-growth, enhancing and maintaining grain-size reduction, and thereby promoting grain-size sensitive creep. These observations from the field and laboratory have been used to inspire and constrain theoretical descriptions of grain-size evolution in two-phase rocks (e.g., Bercovici and Skemer, 2017). During shearing, increased intracrystalline strain drives dynamic recrystallization and grain-size reduction (e.g., Poirier and Guillopé, 1979). Sufficient grain-size reduction can promote grain-size sensitive deformation mechanisms and associated rheological weakening (e.g., Drury, 2005). However, grain-size reduction is opposed by surface energy-driven grain growth, which increases with decreasing grain size (de Bresser et al., 1998, 2001). The steady state grain size depends on the relative contributions of grain-size reduction and grain growth (Austin and Evans, 2009; Derby and Ashby, 1987). In monophase rocks, the resulting equilibrium grain size tends to fall near the transition between the dislocation creep and diffusion creep fields, thus limiting the magnitude of rheological weakening possible through increased activity of grain-size sensitive deformation mechanisms (de Bresser et al., 1998, 2001). In polyphase rocks, however, an even finer grain size can be maintained by a well-mixed (i.e., dispersed) minor phase that pins grain boundaries, limiting grain-boundary migration and grain growth (e.g., Cross and Skemer, 2017; Toy et al., 2010). As such, by promoting and maintaining a finer grain size than would be expected in a monophase rock at a given stress, the presence of minor phases appears critical in promoting grain-size sensitive deformation and thus the dynamic rheological weakening necessary for strain localisation. This concept has been successfully implemented in geodynamic analyses of plate boundary formation and stability with encouraging results (Bercovici and Ricard, 2014). However, while observations of the role of minor phases in strain localisation have been made from the thin-section to the outcrop scale, it remains to be tested with direct observation whether this process is applicable to strain localisation at an actual plate boundary.

Here we test the hypothesis that minor phases control strain localisation at plate boundaries by examining mantle rocks at a palaeosubduction interface. We analysed peridotite samples collected across a basal section of the Oman-United Arab Emirates (UAE) ophiolite. The ophiolite formed above a subduction zone during the late Cretaceous (MacLeod et al., 2013; Pearce et al., 1981; Rioux et al., 2016). The base of the ophiolite is bound by the Semail thrust, which represents the fossilised contact between subducted Tethyan crust and overlying mantle wedge (e.g., Cowan et al., 2014; Searle and Malpas, 1980, 1982). We used electron backscatter diffraction (EBSD) to quantify trends and relationships in grain size, modal mineral abundance, and crystallographic preferred orientation (CPO). Our results support microstructural and rheological models in which minor phases hinder olivine grain growth, which promotes diffusion creep, and thereby strongly influences strain localisation at plate boundaries.

3.2 Geologic Setting

The Oman-UAE ophiolite (Figure 3.1) is a thrust-bound slice of oceanic lithosphere formed at ca. 96.4–95.5 Ma in the hanging wall of a newly initiated, northeast dipping, intraoceanic subduction zone (MacLeod et al., 2013; Pearce et al., 1981; Rioux et al., 2012, 2013, 2016). The ophiolite consists of upper-mantle peridotite overlain by a crustal section of gabbros, sheeted dykes, basaltic flows and pillows, and pelagic sediments (e.g.,,Glennie et al., 1973. Following subduction initiation, tholeiitic basalts, gabbros, and sediments were subducted beneath the newly forming ophiolite to form the metamorphic sole (Searle and Malpas, 1980, 1982; Gnos, 1998; Cowan et al., 2014) (Searle and Malpas 1980, 1982; Gnos, 1998; Cowan et al., 2014). Burial, accretion to the base of the ophiolite, and the onset of exhumation of the sole occurred within about one million years of subduction initiation (Hacker et al., 1994; Rioux et al., 2016). Following exhumation of the sole, deformation stepped to shallower levels in the foreland as convergence was accommodated by in-sequence stacking of rise, slope, and shelf sedimentary packages (e.g.; Searle, 1988). By ca. 79 Ma, the continental margin reached

the subduction zone and was subducted to eclogite facies in the southeastern part of the ophiolite in Oman (Warren et al., 2005). The obduction process was complete by ∼70 Ma and is marked by the return of shallow-marine passive margin sedimentation (Glennie et al. 1973).

For the most part, the mantle section of the ophiolite does not exhibit any obvious structure (Figure 3.2A). However, the basal few hundred metres of the ophiolite exhibits a mylonitic fabric, with grain size that is smaller and foliation that is more pronounced towards the base of the ophiolite (Figures 3.2A–D). The base of the ophiolite is marked by the Semail thrust, which placed the ophiolite over the metamorphic sole, a thrust slice of highly sheared amphibolite, quartz schist, and metachert that was scraped off the downgoing slab and accreted to the base of the mantle wedge (Figure 3.1).

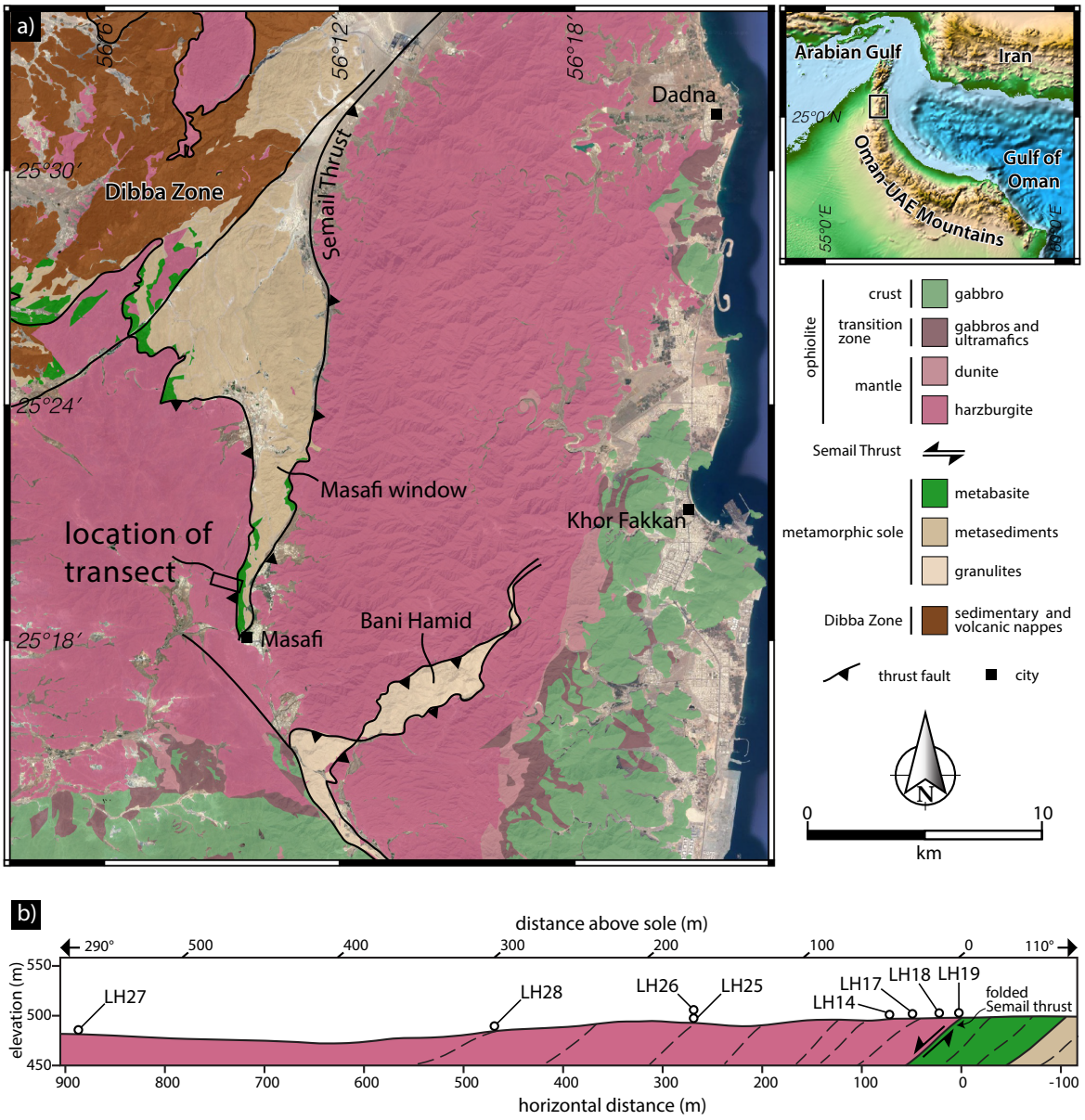


Figure 3.1: (a) Simplified geological map of the northern United Arab Emirates (modified after Farrant et al. (2012)) and elevation model showing the map location on the northeast margin of the Arabian peninsula. (b) Cross-section across the uppermost sole and basal peridotites with locations of analysed samples. Along the western margin of the Masafi window the Semail thrust has an apparent normal sense because the transport direction is to the west and the Semail thrust has been affected by later (post-emplacement) folding. Foliation is indicated by dashed lines. Distance above the sole was estimated using the average foliation of the upper sole and banding in peridotites, which approximate the orientation of the thrust contact. Horizontal distance is taken from the sole-peridotite contact.

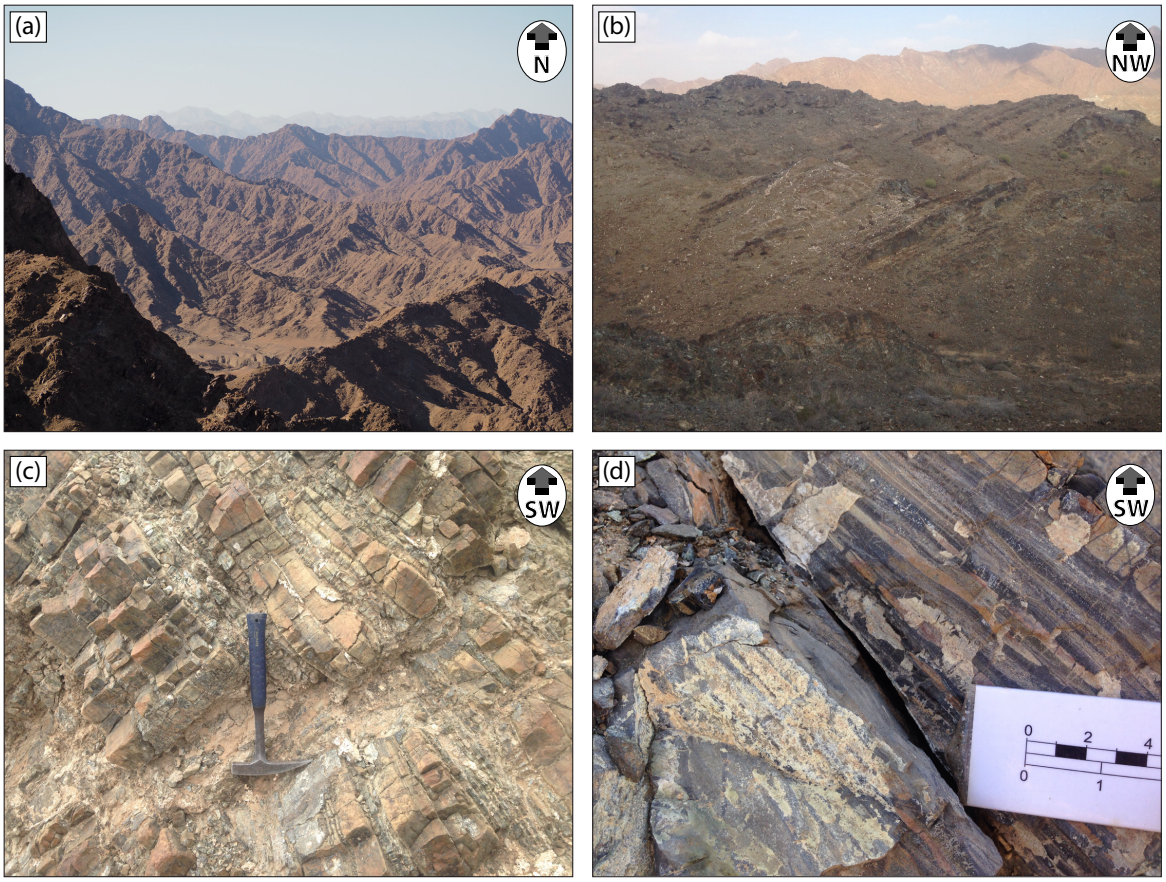


Figure 3.2: Field photos of the Oman-UAE ophiolite mantle section. (a) Most of the mantle section lacks obvious lineations and foliation. (bc) The basal kilometre of the mantle peridotites displays a foliation that increases in intensity towards the base. (d) The lowermost few metres of the ophiolite exhibit a well developed mylonitic fabric.

Several structural and petrological characteristics suggest that the mylonitic fabric in the peridotites adjacent to the Semail thrust is related to the early high-temperature history of subduction. (1) Deformation was ductile and distributed over hundreds of meters. (2) In addition to olivine and orthopyroxene, the mylonitic peridotites also contain clinopyroxene and hornblende, which have previously been interpreted to be related to fluids released from the downgoing slab (Prigent et al., 2014, 2015). Microstructural evidence (discussed in more detail in Section 3.4.1) indicates that these phases were present during deformation at temperatures in excess of 650 °C. (3) Although the mineral assemblage of the peridotites is not suitable for thermobarometry, thermobarometric estimates for garnet–clinopyroxene amphibolites from the metamorphic sole immediately beneath the Semail Thrust in Oman provided peak metamorphic conditions of 770–900 °C and 10–13 kb (Cowan et al., 2014). U-Pb zircon ages of ca. 96 and 94 Ma (Rioux et al., 2016) that date peak metamorphism of the sole overlap with crystallization of the crustal section of the ophiolite at ca. 96.4–95.5 Ma (Rioux et al., 2012, 2013). Thus, it seems reasonable to assume that peridotites in the adjacent hanging-wall were deformed at similarly high temperatures.

While many studies have investigated the pressure, temperature, and deformation history of the metamorphic sole (e.g., Searle and Malpas, 1980, 1982; Hacker, 1990b, 1991, 1994; Hacker and Mosenfelder, 1996; Hacker et al., 1996; Gnos, 1998; Cowan et al., 2014; Rioux et al., 2016) and shear zones within the mantle section (e.g., Dijkstra and Drury, 2002; Michibayashi and Mainprice, 2004; Michibayashi et al., 2006; Linckens et al., 2011), relatively few have focused on the banded ultramafic unit in the hanging-wall. In a review of ophiolitic mantle sections, Nicolas et al. (1980) differentiate between an upper section with a coarse-grained porphyroclastic to granular texture, and a lower section with a fine-grained porphyroclastic to mylonitic texture. They interpret the upper peridotites as preserving high-temperature asthenospheric flow beneath an oceanic spreading centre, that is overprinted by the mylonitic and porphyroclastic textures related to lower-temperature thrusting during emplacement of the ophiolite. Boudier and Coleman (1981) conducted a microstructural analysis of peridotites from

a ∼12 km transect across the mantle section of the ophiolite at Wadi Tayin, Oman. Olivine CPOs from this transect are characterized by [100] dominantly sub-parallel to the lineation and are interpreted to indicate slip on (010)[100] and $0kl$[100]. Boudier and Coleman (1981) additionally reported that the strength of the CPOs did not display any obvious trends with structural position. Subsequently, Boudier et al. (1988) mapped the distribution of fabrics related to either high-temperature asthenospheric flow or lower-temperature emplacement at several locations in Oman and the UAE. Unlike the previous study at Wadi Tayin, olivine CPOs weaken towards the sole and disappear in the basal mylonites (Boudier et al., 1988). In addition to harzburgite and dunite, which comprise the majority of the mantle sequence, several occurrences of lherzolite have also been described. Geochemical trends from the lherzolites have previously been interpreted to indicate some combination of melt extraction, interaction with a fluid or melt, and primary mantle heterogeneity (Takazawa et al., 2003; Khedr et al., 2013; Yoshikawa et al., 2015).

3.3 Methods

3.3.1 Sample collection and preparation

The study area is located in the northern UAE where the ophiolite is folded and erosion has exposed the Semail thrust and underlying metamorphic sole in the Masafi window (Figure 3.1). Eight oriented peridotite samples were collected along a ∼900 m transect oriented perpendicular to the strike of the foliation of the peridotite and metamorphic sole (Figure 3.1). The structurally lowest (easternmost) sample was located within a metre of the metamorphic sole. The transect spans a structural thickness of ∼490 m in the direction normal to the mean orientation of foliation of the peridotite and metamorphic sole, which corresponds to a horizontal distance of nearly 900 m (Figure 3.1B). As the strength and orientation of the foliation in the peridotites was variable and no lineation was observed, samples were cut with reference to the average orientation of foliation in the metamorphic sole (187°/39°), which is similar to the ori-

entation of banding in the peridotite. Although a lineation was not observable in hand samples of peridotite or in amphibolites in the adjacent sole, a well-developed north-south trending mineral-stretching lineation that is parallel to fold-axes was observed in metasedimentary units further down the section in the metamorphic sole. Thin sections and billets were oriented perpendicular to orientation of the average foliation and parallel to the average dip direction. All analyses were on polished billets, aside from LH14 and LH19, which were performed on thin sections. All specimens were polished with progressively finer diamond slurry from 30 μm to 0.25 μm and finished with either 0.05 μm diamond or 0.03 μm colloidal silica.

3.3.2 Microstructural analysis

Mineral abundances, CPO, and grain sizes were quantified with electron backscatter diffraction (EBSD) data. These data were collected using an FEI Quanta 650 scanning electron microscope (SEM) with a field emission gun and an Oxford Instruments AZtec acquisition system and NordlysNano EBSD camera. Uncoated samples were mapped in low-vacuum mode (50 Pa) at 30 kV accelerating voltage with a step size of 5 μm (15 μm for LH19). Data were processed using Oxford Instruments Channel5 software and the MTEX toolbox (e.g., Hielscher and Schaeben, 2008) for MATLAB. Channel5 was used to remove isolated pixels (wildspikes), and non-indexed points surrounded by $\geq$ 5 neighbours within the same grain were filled with the average of their neighbour orientations. After processing, $\sim$10–80% of the map consisted of non-indexed pixels (Table 3.1), with increasing amount of non-indexing reflecting the degree of serpentinization. Estimates of mean grain size and subgrain size were calculated in Channel5 using the line-intercept method (see Appendix A in Hansen et al. (2011)). The method was applied parallel (X-direction) and perpendicular (Z-direction) to the foliation. Grain and subgrain boundaries were defined as having misorientation angles >10 $^\circ$ and 1–10 $^\circ$, respectively. A geometric correction factor of 1.5 was applied to convert mean intercept-length to estimates of mean grain size and mean subgrain size for use in flow laws (Underwood (1970) pp. 80–93). For a material with significant

regions of unindexed pixels, as is the case for some samples in this study, the line intercept method is better suited to determining (sub)grain sizes than methods based on grain area (Humphreys, 2001). Intercept lengths are measured with the line continuing uninterrupted, ignoring unindexed pixels (e.g., in a serpentine vein), until it reaches an indexed pixel with a misorientation angle relative to the last indexed pixel greater than the set threshold. This method may, however, overestimate the grain size in samples with high enough degrees of serpentinization such that entire grains are missing.

Table 3.1: Results from microstructural analysis

Sample	Position (m)	Modal abundances (%)							Olivine grain size (µm)	Minor phases grain size (µm)	Olivine subgrain size (µm)	Stress in olivine (Mpa)	Olivine J-index
		Olivine	Cpx	Opx	Hbl	Sp	Non-indexed	Minor					
LH19	1	44	2.4	8.2	10	0.3	35	20.9	142	103			1.2
LH18	22	47	3.3	12	0.33	0.6	36	16.2	114	79	43.3	33.8	1.2
LH17	51	68	3.1	14	3.3	0.7	10	21.1	98	61	58.7	24.9	1.3
LH14	80	29	2.8	9		0.2	59	12.0	162	129	53.2	27.5	1.4
LH25	266	17	0.61	3.5	0.46	0.0	78	4.6	307	223			1.4
LH26	266	15	0.35	3.3	0.14	0.3	81	4.1	350	214			2.1
LH28	469	34	0.9	11	21	0.1	33	33.0	162	120	56.6	25.8	1.1
LH27	888	37	1.4	7.8	0.042	0.1	53	9.3	245	161	47.8	30.6	2.6

EBSD data are used to estimate palaeostresses experienced by our samples. In monomineralic rocks, experimentally derived grain-size piezometers can be used to estimate differential stress (for olivine see: Karato et al., 1980; Van der Wal et al., 1993). In polymineralic rocks, however, pinning due to minor phases may lead to overestimation of differential stress if grain size is maintained below that which would be attained in a monomineralic rock (Herwegh et al., 2011; Tasaka et al., 2014). Therefore, following the protocol outlined by Hansen and Warren (2015), we used the olivine subgrain-size piezometer of Toriumi (1979) to estimate differential stresses. For each set of orientations, an orientation distribution function was determined using the automatic halfwidth algorithm in MTEX (Hielscher and Schaeben, 2008). Each orientation distribution function was calculated using one-point-per-grain for over 1000 grains. Unlike for grain-size measurements, grains were iteratively dilated in Channel5 using the orientation of adjacent pixels so that no non-indexed pixels remained. This minimized the likelihood of more than one point being included per grain due to grains being dissected by serpentine veins. Pole figures (i.e., graphical presentations of orientation distribution functions) are oriented in a geographic reference frame relative to the average foliation of the metamorphic sole (187°/39°) immediately beneath the ophiolite. All pole figures are plotted with the same colour-scale, as multiples of uniform distribution (M.U.D.) ranging from 0–2.5, to facilitate comparison among them. uniform distribution of orientations to infinity for a single crystal.The strength of the CPO was quantified using the J-index (Bunge, 1982), which ranges from 1 for a uniform distribution of orientations to infinity for a single crystal.

3.3.3 Mineral abundances

Mineral abundances were calculated from the processed EBSD data using MTEX. Isolated porphyroclasts of orthopyroxene were excluded from modal abundance estimates as we are primarily interested in the volumetrically more significant matrix, which we assume controlled the rheological properties. Indexing ranged from ∼20–90% and is primarily a reflection of the amount of serpentinization. Most of the serpentiniza-

tion observed in the samples is interpreted to have resulted from surface processes, consistent with seismic velocities (Christensen and Smewing, 1981), as well as phase equilibria modelling, serpentine chemistry, and δO^{18} values for carbonate veins and ground water (Streit et al., 2012). Although pyroxenes can be serpentinized, olivine alters more rapidly (Wicks, 1969). As such, assuming that the other minerals were preserved and indexed, the non-indexed pixels are interpreted to have been primarily olivine prior to serpentinization. Unindexed pixels are not included as a minor phase in our analyses, but instead considered to be composed of olivine when calculating modal proportions.

3.4 Results

3.4.1 Petrography

Modal abundances of different mineral phases determined from EBSD maps are presented in Table 1. Olivine is the most abundant phase in all samples, even when only considering the indexed regions. Minor phases comprise 4–33% of the mapped regions, and consist primarily of orthopyroxene, with less abundant clinopyroxene, hornblende, and spinel (Table 1).

Examples of the spatial distribution of different mineral phases are presented as photomicrographs in Figures 3.3A–C and EBSD maps in Figures 3.4A–C (EBSD phase maps, band contrast maps, orientation maps, and local misorientation maps for all samples are provided in the appendix). Orthopyroxene occurs both as porphyroclasts (Figures 3.3A , 3.4A and C) and as finer-grained material mixed within the matrix (Figures 3.4B–C). Clinopyroxene occurs both as a fine-grained and well mixed phase throughout the matrix (Figure 3.2B), as well as exsolution lamellae and inclusions within orthopyroxene (Figure 3.2A). Hornblende is colourless in thin section and occurs both as a well-mixed, fine-grained phase in the matrix (Figures 3.3B–C), as well as replacement rims around and within orthopyroxene (Figures 3.4A and C). Several lines of evidence indicate that hornblende was present during high-temperature defor-

mation, rather than having formed after deformation and/or at lower temperatures. First, hornblende is cut by serpentine veins and hence predates the low-temperature serpentinization (Figure 3.3b). Lizardite and chrysotile, the polymorphs of serpentine present in the ophiolite (e.g., Streit et al., 2012), are both unstable above about 400 °C (Evans, 2004), which places a minimum temperature limit for hornblende crystallization. Second, hornblende exhibits lattice curvature indicative of crystal plasticity by dislocation motion (Figure 3.4D), consistent with deformation temperatures in excess of 650–700 °C (Berger and Stünitz, 1996). Third, asymmetrical overgrowths of hornblende on orthopyroxene (Figure 3.4C) indicate that deformation occurred in the stability field of hornblende, which does not overlap with that of serpentine.

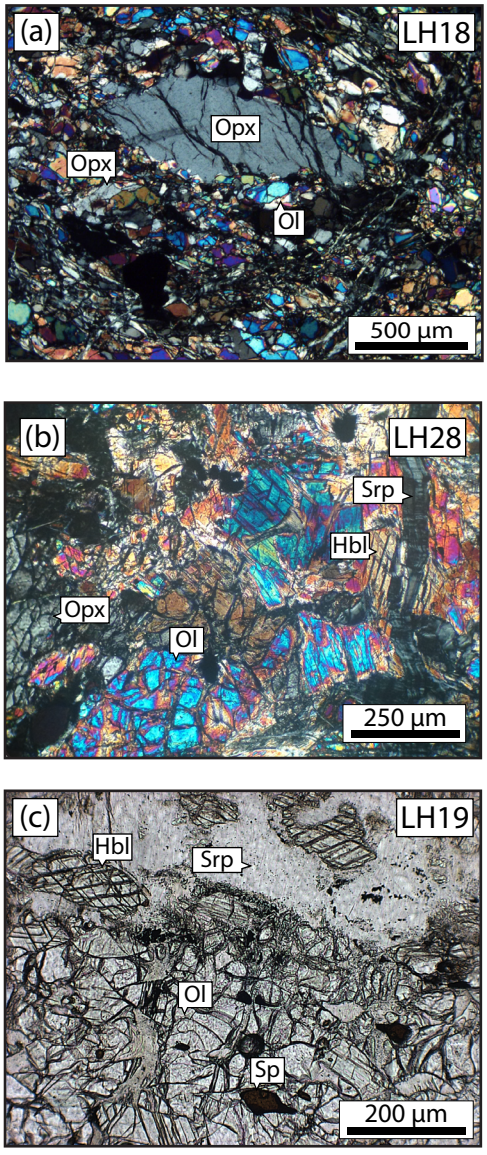


Figure 3.3: Representative photomicrographs displaying: (a) an orthopyroxene porphyroclast surrounded by a fine-grained olivine matrix in sample LH18, (b) orthopyroxene, olivine, and hornblende cut by serpentine in sample LH28, and (c) olivine, hornblende, spinel, and serpentine in sample LH19. Ol (olivine), Opx (orthopyroxene), Cpx (clinopyroxene), Hbl (hornblende), Sp (spinel), Srp (serpentine).

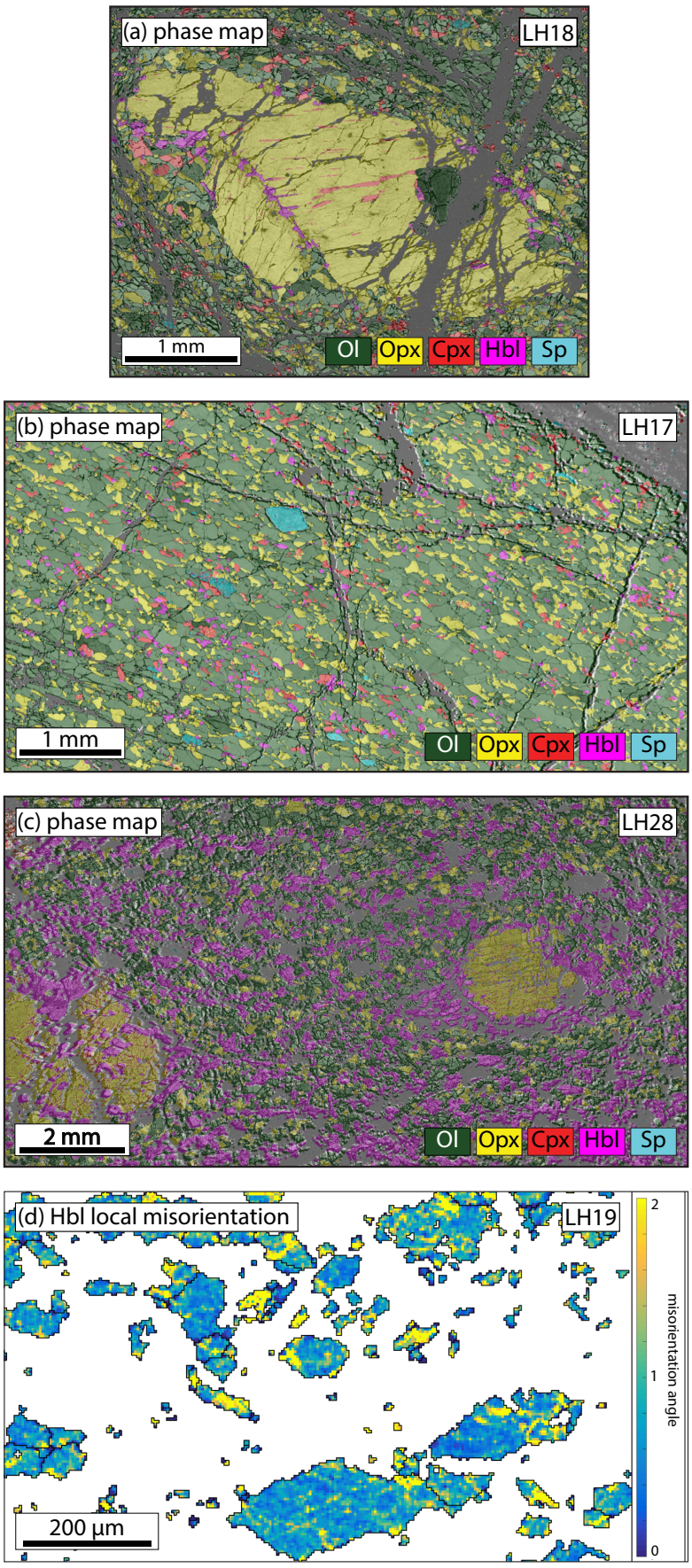

(a) phase map
LH18
1 mm
Ol
Opx
Cpx
Hbl
Sp
(b) phase map
LH17
1 mm
Ol
Opx
Cpx
Hbl
Sp
(c) phase map
LH28
2 mm
Ol
Opx
Cpx
Hbl
Sp
(d) Hbl local misorientation
LH19
200 µm
2
1
0
misorientation angle

Figure 3.4 *(preceding page)*: EBSD maps. (a) Phase map overlain on band contrast map of sample LH18 displaying an orthopyroxene porphyroclast with clinopyroxene exsolution lamellae and hornblende replacement along fractures. Olivine appears to have penetrated and mixed with orthopyroxene along the bottom of the porphyroclast. (b) Phase map overlain on band contrast map of sample LH17 displaying olivine with well-mixed (dispersed) minor phases (orthopyroxene, clinopyroxene, and hornblende). (c) Phase map overlain on band contrast of map LH28 displaying porphyroclasts of orthopyroxene overgrown by hornblende and a finer-grained matrix of olivine, orthopyroxene, and hornblende. (d) Map of local misorientation in hornblende averaged within 3x3 pixel kernels. Abbreviations: Ol (olivine), Opx (orthopyroxene), Cpx (clinopyroxene), Hbl (hornblende), Sp (spinel). Gray pixels are mostly serpentine that was not indexed during EBSD analysis.

3.4.2 Grain size and subgrain size

Figure 3.5 presents distributions of intercept lengths used to estimate mean olivine grain size and mean olivine subgrain size. Estimates of the mean olivine grain sizes range from 98–350 μm (Figure 3.5, Table 3.1). Three samples (LH19, LH25, LH26) were not sufficiently indexed to allow for an accurate estimate of the mean olivine subgrain size. Estimates of the mean olivine subgrain size of the remaining five samples range from 43–58 μm (Figures 3.5, Table 3.1). The subgrain-size piezometer of Toriumi (1979) predicts corresponding differential stresses of 25–34 MPa. Estimates of the mean grain size of minor phases (excluding large and isolated porphyroclasts of orthopyroxene) range from 61–223 μm (Table 3.1).

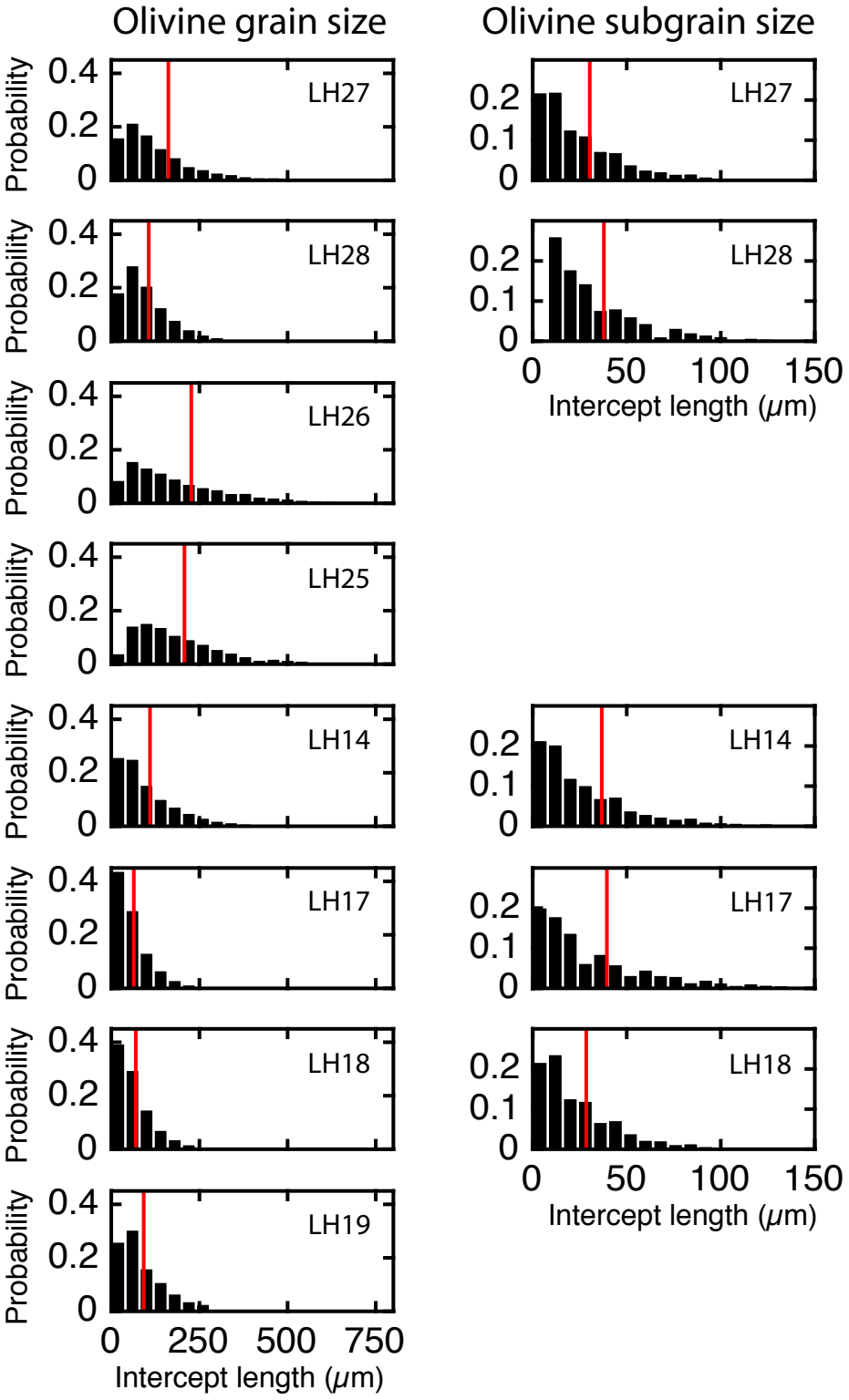


Figure 3.5: Histograms of olivine grain size (left column) and subgrain size (right column) from intercepts measured parallel (x-direction) and perpendicular (z-direction) to foliation. Samples are ordered according to distance from the sole. The average grain sizes in Figures 3.7, 3.8, and 3.9A, Table 1 are an average of the x- and z-direction. A geometric correction factor of 1.5 was applied to convert intercept length to grain size.

3.4.3 Crystallographic preferred orientations

Olivine CPOs vary in strength but have similar shapes (Figure 3.6). J-index values range from 1.1 for the weakest fabrics, to 2.6 for the strongest. Aside from LH28, all samples exhibit olivine CPOs characterized by [100] point maxima that are approximately parallel to the average foliation of the metamorphic sole, and [010] and [001] orientation distributions that range from diffuse girdles to point maxima approximately perpendicular to the average foliation of the metamorphic sole. The orientations of [100] point maxima are remarkably consistent across the transect, indicating a broadly similar deformation geometry throughout the sampled region. Furthermore, [100] point maxima are oriented roughly perpendicular to the dip direction and have a similar orientation to the mineral stretching lineation observed in the metamorphic sole (Figure 3.6).

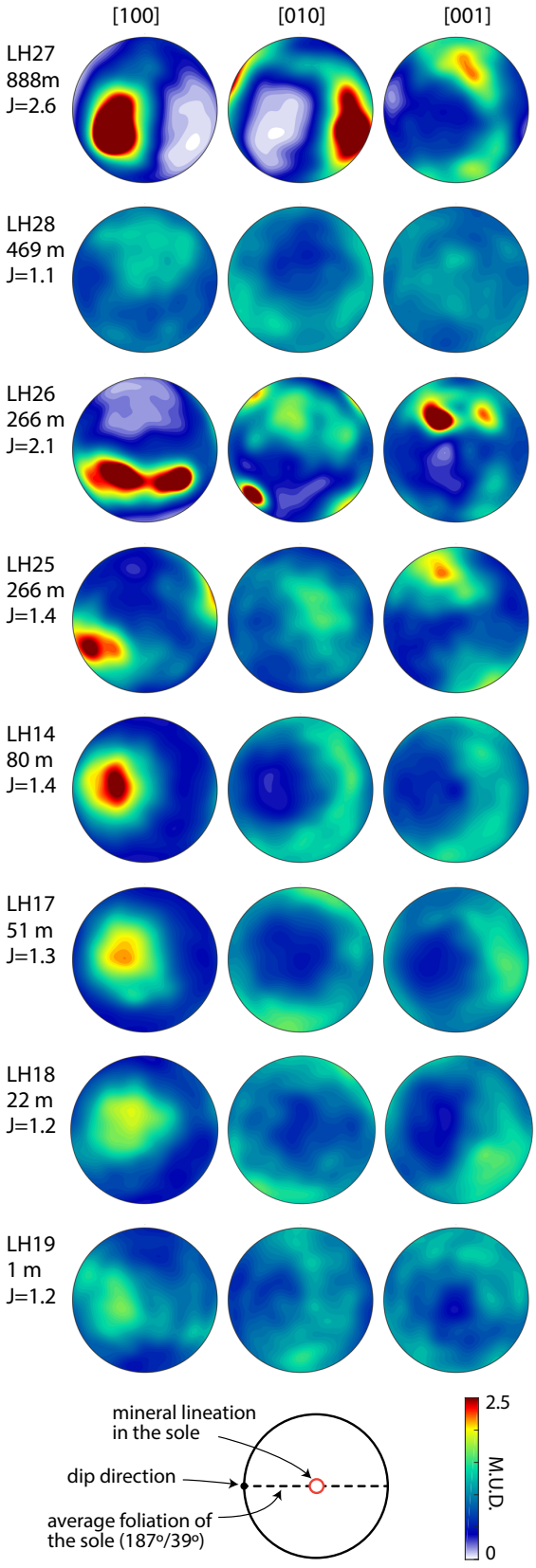

[100]
[010]
[001]
LH27
888m
J=2.6
LH28
469 m
J=1.1
LH26
266 m
J=2.1
LH25
266 m
J=1.4
LH14
80 m
J=1.4
LH17
51 m
J=1.3
LH18
22 m
J=1.2
LH19
1 m
J=1.2
mineral lineation
in the sole
dip direction
average foliation of
the sole (187º/39º)
2.5
M.U.D.
0

Figure 3.6 ***(preceding page)*****:** Olivine pole figures for all samples illustrating the change in CPO from with distance from the sole. Distance from sole and J-index value are included for reference. Pole figures are oriented within a geographic reference frame, as schematically shown at the bottom. All figures are contoured for multiples of uniform distributions (M.U.D.) ranging from 0 to 2.5.

3.4.4 Microstructure as a function of position

Microstructural characteristics described above are presented as a function of position along the transect in Figures 3.7A–D. Throughout this figure, sample LH28 is singled out with a red square because it exhibits an anomalously high proportion of minor phases that are primarily made up of hornblende. Mean olivine grain size generally decreases towards the sole (Figure 3.7A). However, the mean olivine grain size in sample LH28 (red squares in Figure 3.7) is only 162 μm, which is fine relative to adjacent samples. In contrast, mean olivine subgrain size, and hence stress estimates from subgrain-size piezometry (e.g., Toriumi, 1979), remain reasonably constant along the length of the transect (Figure 3.7B).

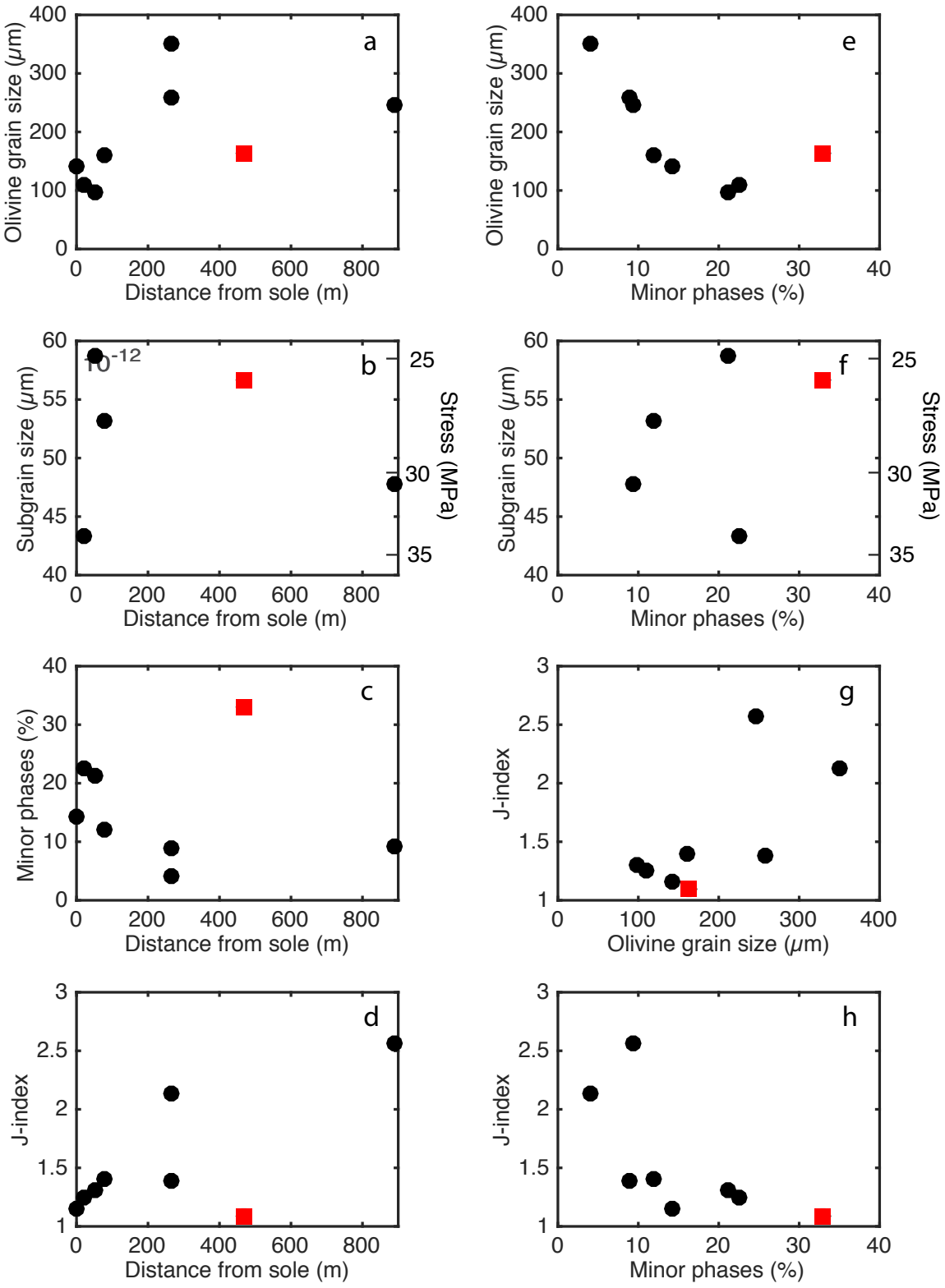


Figure 3.7: Microstructural relationships. Subgrain sizes were not calculated for 3 samples due to insufficient indexing. In all plots, the red square corresponds to LH28.

Minor phases exhibit a linear increase in abundance towards the sole from about 260 m (Figure 3.7C). Sample LH27, located furthest from the sole has a similar minor-phase content as the samples located at 266 m from the sole. However, sample LH28, collected 413 m from the sole, contains the highest minor-phase content of all samples, due primarily to the high hornblende content. If sample LH28 is ignored due to the anomalously high hornblende content, the minor phase fraction remains reasonably constant beyond 260 m (Figure 3.7C). The strength of the olivine CPO gradually decreases towards the sole, with J-index values of 2.6 furthest from the sole, and 1.2 immediately adjacent to the sole (Figures 3.6 and 3.7D). Sample LH28 (red squares in figure 3.7D), however, has a weak CPO relative to adjacent samples and a J-index value of just 1.1, the lowest of any of the samples. Despite similar mineralogy, low degree of indexing (i.e., high degree of serpentinization), and location along the transect, LH25 has a considerably weaker CPO than LH26, which was collected from the same location.

3.4.5 Relationships among grain size, minor-phase abundance, and texture strength

Although general trends can be observed with distance from the sole, there is significant covariance among microstructural characteristics. Figure 3.7E demonstrates that mean olivine grain size and minor-phase abundance are inversely related. If sample LH28 (red squares) is ignored, the decrease in mean olivine grain size with increasing minor-phase content is roughly linear. In contrast, no relationship is evident between mean olivine subgrain size and minor-phase abundance (Figure 3.7F). Mean olivine grain size and texture strength exhibit a rough positive relationship (Figure 3.7G). Samples with a mean olivine grain size less than 200 μm display reasonably constant and relatively low J-index values ranging from 1.1–1.4, whereas the three coarser samples exhibit a larger range but generally stronger texture strength, with J-index values between 1.4 and 2.6 (Figure 3.7G). Sample LH28 has a somewhat weak texture strength relative to other samples with similar mean olivine grain sizes, but nonetheless is not an obvious outlier in Figure 3.7G. Minor-phase abundance and texture strength exhibit an inverse

relationship (Figure 3.7H). For minor-phase abundance below ∼10%, there is a large range in the texture strength, with J-index values ranging from 1.4–2.6. However, for samples with a minor-phase abundance greater than ∼10%, texture strength decreases linearly with minor-phase abundance with J-index values ranging from 1.4–1.1. In contrast to being an obvious outlier in Figures 3.7A, 3.7C, 3.7D and 3.7E, sample LH28 lies along (albeit at the end) of the trend between texture strength and minor-phase abundance (Figure 3.7G).

3.5 Discussion

3.5.1 Controls on strain localisation along the base of the Oman-UAE ophiolite

Studies of experimentally deformed rocks and outcrop-scale natural shear zones indicate that minor phases can control strain localisation (Farla et al., 2013; Hansen and Warren, 2015; Herwegh et al., 2011; Hiraga et al., 2010; Toy et al., 2010; Warren and Hirth, 2006; Tasaka et al., 2014, 2017). These small-scale studies are often used to infer the importance of minor phases in the formation of lithospheric-scale shear zones, and theoretical models have suggested that minor phases are crucial in the formation of tectonic plate boundaries (Bercovici and Ricard, 2014; Bercovici and Skemer, 2017). The Oman-UAE ophiolite provides a unique opportunity to directly examine strain localisation at the larger and more relevant scale of a former plate boundary. In this section, we discuss the trends and relationships among minor-phase abundance, olivine grain size, and CPO strength from the mantle section at the base of the Oman-UAE ophiolite. As olivine is the most abundant and generally weakest phase in the upper mantle, it is often presumed to control the macroscopic rheology (Karato and Wu, 1993; Zimmerman and Kohlstedt, 2004). Furthermore, the recent experiments of Tasaka et al. (2013) demonstrate that, if olivine grain size is kept constant, even an increase in pyroxene fraction of 30% (roughly the maximum observed here) only modifies the

macroscopic viscosity in diffusion creep by a factor of ∼2 (see Figure 10 in (Tasaka et al., 2013)). As presented below, this difference is insignificant compared to the changes in viscosity associated with changing the olivine grain size. The following discussion therefore focuses on olivine rheology, and in particular, the effect of minor-phases in moderating the strength of olivine.

3.5.2 The influence of minor phases on olivine grain size

Our results resolve an interplay between minor-phase content and olivine grain size along the base of the Oman ophiolite. Based on our initial observation in Figure 3.7E, we suggest the inverse relationship between olivine grain size and minor-phase content is a result of minor phases pinning olivine grain boundaries. If true, our microstructural data should follow the general Zener equation, $olivine\ grain\ size = c \times minor\text{-}phase\ grain\ size/(fraction\ of\ minor\ phases)^m$, where c is a constant of order 1 and m is a factor related to the spatial distribution of the dispersed phase (for reviews, see Evans et al., 2001; Herwegh et al., 2011). Based on theoretical development and computer simulation, m is predicted to take on values of 0.33 to 1. Figure 3.8 presents our results using a value of $m = 0.52$, following the empirical determination by Tasaka et al. (2014) for olivine-pyroxene mixtures. Our data are consistent with this form of the Zener equation and in agreement with previous observations from natural peridotites (Linckens et al., 2011; Tasaka et al., 2013, 2014; Hansen and Warren, 2015), supporting our hypothesis that the presence of minor phases controlled olivine grain size along the base of the mantle wedge.

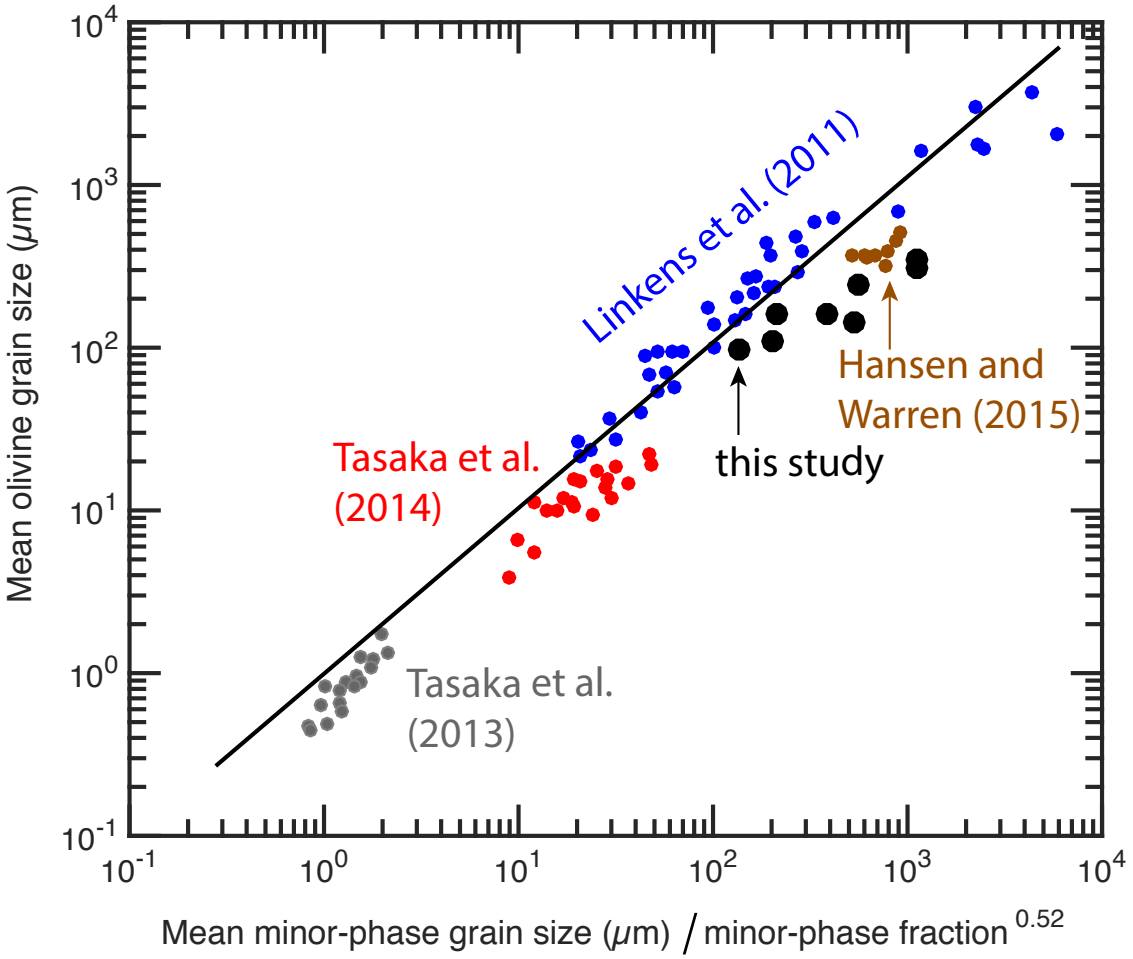


Figure 3.8: Mean olivine grain size as a function of mean minor-phase grain size and minor-phase volume fraction. Following Tasaka et al. (2014), we use a value of $m = 0.52$ for the minor phase volume fraction. Our samples are plotted along with data from synthetic olivine-pyroxene aggregates (Tasaka et al. 2013), as well as data from natural shear zones in Oman (Linckens et al., 2011, 2015; Tasaka et al., 2014) and the Josephine peridotite (Hansen and Warren, 2015). The solid line is the best fit derived by Tasaka et al. (2014).

While the role of minor phases in limiting grain size is fairly well understood, the mechanism by which minor phases become mixed (i.e., dispersed) is still somewhat enigmatic. Hypotheses that have been proposed to explain mixing include nucleation of one phase in regions dominated by another phase as a result of stress-induced chemical potential gradients (Tasaka et al., 2017), nucleation of phases from a fluid in cavities opened by grain-boundary sliding (Précigout and Stünitz, 2016), or mechanical production of new grains that are transported along grain boundaries of another phase as a result of surface tension and local stresses at the boundaries (Bercovici and Skemer, 2017). It is possible that multiple mechanisms were responsible for phase mixing in our samples. Clinopyroxene and hornblende, on the one hand, are interpreted to be produced from metasomatic fluids associated with the subducting slab (Prigent et al., 2014, 2015; Yoshikawa et al., 2015). Considering these phases are not generally seen as porphyroclasts and are primarily observed in well-mixed regions (Figures 3.4B and C), it is possible they were generated by a mechanism similar to that proposed by Précigout and Stünitz (2016). Orthopyroxene, on the other hand, does occur as porphyroclasts, and small olivine grains appear to penetrate into the larger orthopyroxene grains (Figure 3.4A). The location of these olivine grains does not appear to be controlled by orthopyroxene grain or subgrain boundaries, which is in better agreement with the model of Tasaka et al. (2017).

3.5.3 Deformation mechanisms and rheology of the subduction interface

We suggest that the grain-size reduction described above leads to weakening through a transition in deformation mechanism. We first use CPO strength to qualitatively assess variations in the relative contributions of dislocation creep and diffusion creep to the total strain rate. Deformation accommodated largely by the motion of dislocations typically leads to development of a CPO (e.g., Karato, 1988). In contrast, diffusion creep is presumed to produce a random or weak CPO (Fliervoet et al., 1999; Rutter et al., 1994). Although some questions remain regarding the effectiveness of diffusion

creep in modifying an existing CPO (Wheeler, 2009), recent experiments on olivine-pyroxene mixtures by Tasaka et al. (2017) demonstrated that CPO strength decreases with increasing contributions of grain-size sensitive deformation to the strain rate. Therefore, the positive relationship between texture strength and mean olivine grain size in our samples (Figure 3.7G) indicates that a mechanism other than dislocation creep was promoted by fine grain sizes. Given the influence of minor phases on olivine grain size (Figures 3.7E and 3.8), this provides an explanation for the inverse correlation between minor-phase content and texture strength (Figure 3.7H).

An increase in the fraction of strain produced by grain-size sensitive deformation at a given stress can result in rheological weakening and provide a mechanism for strain localisation (e.g., Drury, 2005; Warren and Hirth, 2006). To constrain the activity of different deformation mechanisms, we constructed deformation mechanism maps using the experimentally derived flow laws for wet olivine deforming by diffusion creep and dislocation creep as given by (Hirth and Kohlstedt, 2003; Figure 3.9A). Hirth and Kohlstedt (2003) argued that dislocation-accommodated grain-boundary sliding (disGBS) is not important under hydrous conditions. Alternatively, Ohuchi et al. (2015) have more recently developed a flow law for disGBS in olivine under hydrous conditions based on high-pressure experiments. Their results, however, indicate that the contribution of disGBS to the total strain rate is insignificant at the deformation conditions expected along the base of the mantle wedge (low temperature and low stress). As such, we have not included disGBS in our calculations. Strain rates were calculated using a temperature of 800 °C and a confining pressure of 600 MPa. This pressure and temperature roughly correspond to peak temperature and intermediate pressure estimates from the hanging wall metamorphic sole (Cowan et al., 2014). The wet flow laws also include a term for hydrogen concentration (or water fugacity). Although the water content has not been precisely constrained in our dataset, the presence of hornblende is consistent with water-saturated conditions. At 800 °C and 600 MPa, the solubility of hydrogen in olivine is $\sim$300 $H/106Si$ (Kohlstedt et al., 1996; Zhao et al., 2004). To assess the effect of water on strain rate, Figures 3.9B and 3.9C present

predicted strain rates using both the wet (Hirth and Kohlstedt, 2003) and dry (Hirth and Kohlstedt, 2003; Hansen et al., 2011) flow laws. Unlike the wet flow law of Hirth and Kohlstedt (2003), the dry flow laws of Hansen et al. (2011) and Hirth and Kohlstedt (2003) include a contribution from disGBS in addition to dislocation and diffusion creep. The wet flow law for water saturated olivine predicts an increase in strain rate of approximately two orders of magnitude relative to the dry flow laws (Figure 3.9B). Importantly, the strain rate increases along the transect towards the sole, a feature that is apparent regardless of the water content used (Figures 3.9B and 3.9C). Given the presence of hornblende, which suggests that significant amounts of water were present during deformation, and that the overall trends are not drastically affected by varying the water content, we have used a water concentration of 300 $H/10^6Si$ in the flow laws for all samples (Figure 3.9). It is worth noting, however, that the heterogeneous distribution of hornblende (Figure 3.3) is consistent with channelized flow of a hydrous fluid (e.g., Plümper et al., 2016). Thus, it is possible that hydration of olivine varied along the section.

Our calculated deformation mechanism map is presented in Figure 3.9A. The map is coloured by the fraction of the total strain rate due to dislocation creep to emphasize that the transition from dislocation creep to diffusion creep is gradational and does not reflect an abrupt switch in deformation mechanism (e.g., Skemer and Hansen, 2016). Dislocation creep continues to operate at the same strain rates for a given stress in the diffusion creep field in stress-grain-size space. However, the proportion of the total strain rate due to dislocation creep decreases with decreasing grain size as the efficiency of diffusion creep increases. Our samples are plotted in Figure 3.9A using measured olivine grain sizes and stress estimates from subgrain-size piezometry. All samples fall to the left of the nominal boundary between deformation mechanisms (50% diffusion creep and 50% dislocation creep). Aside from LH27, which was located furthers from the sole thrust, all of our samples are finer grained than predicted by grain-size piezometry (white dashed line; Van der Wal et al., 1993). The predicted percent of the total strain rate due to dislocation creep ranges from 3–46% and generally decreases

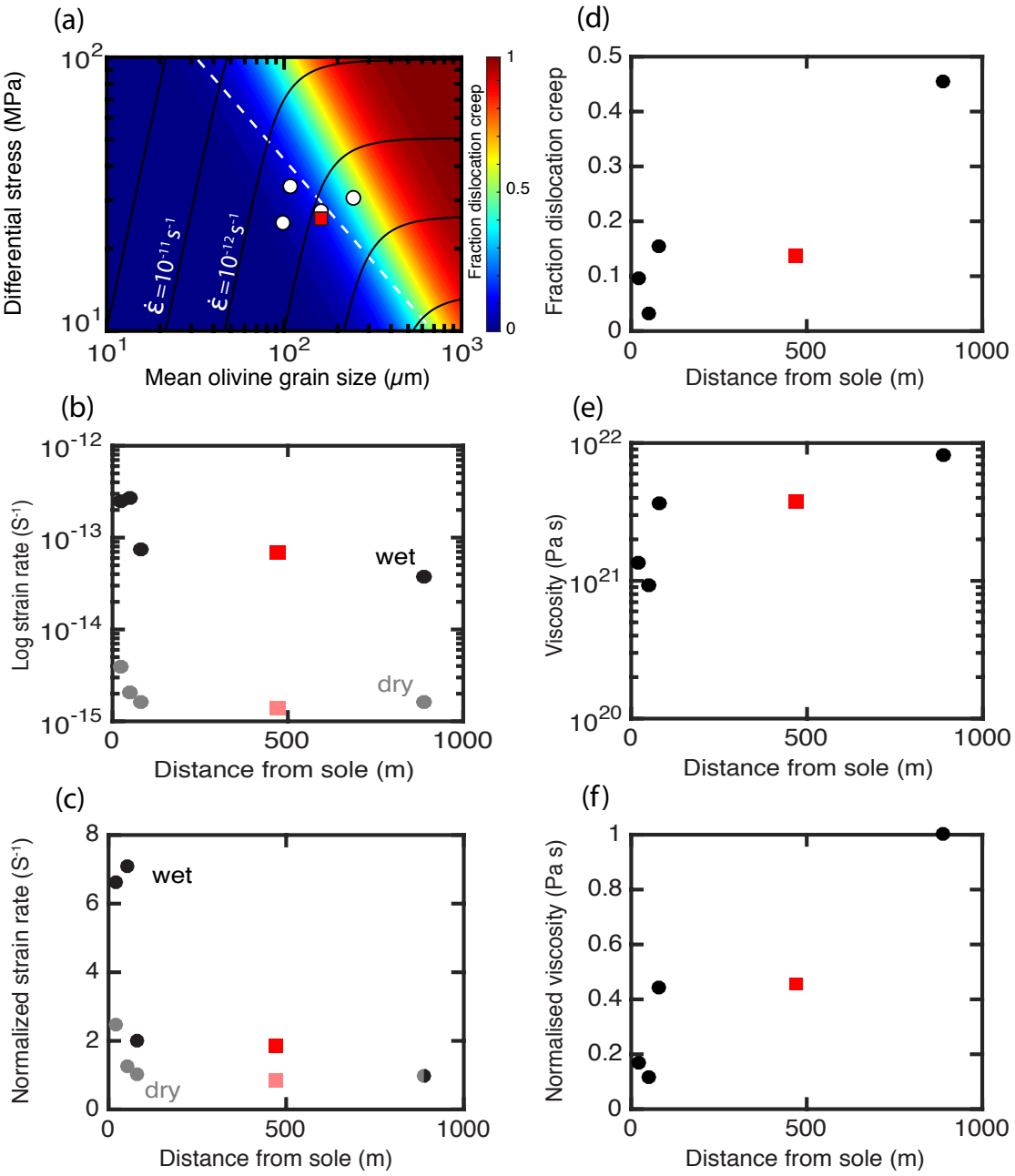


Figure 3.9: (a) Deformation mechanism map for olivine using the wet flows law for diffusion creep and dislocation creep (Hirth and Kohlstedt, 2003). Our samples are plotted using the measured grain size, and stress estimates from subgrain-size piezometry. The colour scale corresponds to the fraction of the total strain rate produced by dislocation creep. Flow laws were calculated using 800 °C, a confining pressure of 600 MPa, and $300H/10^6Si$. Black lines are contours for constant strain-rate. White dashed line is the grain-size piezometer of Van der Wal et al. (1993). (b) Predicted strain rates and (c) strain rates normalized to sample LH27 using the flow laws for wet olivine (black circles) and dry olivine (gray circles) as a function of distance from the sole. (d) Fraction of dislocation creep for wet olivine as a function of distance from the sole. (e) Predicted viscosities and (f) viscosities normalized to sample LH27 for wet olivine as a function of distance from the sole. Sample LH28 is displayed as a red square in all panels.

towards the sole (Figure 3.9D). Despite similar estimated stresses, this increase in diffusion creep is associated with an increase in predicted strain rates by a factor of ∼7.5 ($4x10^{-14} - 3x10^{-13}s^{-1}$) towards the metamorphic sole (Figures 3.9D and 3.9C). We also calculate that apparent viscosities decrease by a factor of ∼10 ($10^{22} - 10^{21} Pa\ s$) within ∼100 m of the metamorphic sole (Figures 3.9E and 3.9F).

Our estimated strain rates are reasonably consistent with geochronological constraints for both the ophiolite and metamorphic sole, as well as pressure estimates from the sole. Geochronology (Rioux et al., 2012, 2013, 2016) thermochronology (Hacker, 1994) of the crustal sequence and metamorphic sole indicate that high-temperature deformation along the base of the ophiolite lasted approximately 1 Myr. The subducting slab reached depths of ∼40 km (Gnos, 1998; Cowan et al., 2014). For a dip of 45° and perpendicular convergence, these constraints correspond to ∼56 km of movement along the subduction interface and an upper bound for the strain rate of $\sim 10 - 12\ s^{-1}$ for a 1 km wide shear zone.

The results from our microstructural analysis are consistent with the hypothesis that minor phases pinned olivine grain boundaries and limited grain-boundary migration, which hindered olivine grain growth and promoted diffusion creep. This transition in deformation mechanism had a weakening effect on olivine (Figure 3.9A). As such, we suggest it was ultimately the distribution of minor phases that controlled the rheological weakening at the base of the mantle section. Similarly, Linckens et al. (2011) demonstrated a correlation between minor-phase abundance, grain size, and the rheological properties of peridotite from the vertical, strike-slip Hilti shear zone located within the middle of the mantle section in Oman. Here, we have demonstrated that minor phases also influenced strain localization during subduction-related deformation along the base of the ophiolite.

Although generally stronger than olivine (e.g., Hansen and Warren, 2015), the net effect of increasing pyroxene content along our transect was a viscosity reduction. This conclusion is in contrast to the results of Hansen and Warren (2015). They examined a shear-zone formed under relatively dry conditions with a significant portion

of the deformation occurring by disGBS. In the disGBS regime, they suggested the intrinsic strength of pyroxene roughly offsets any grain-size related weakening due to the relatively small grain-size sensitivity of disGBS. Thus, the hydrous conditions in the mantle section indirectly promoted significant weakening because diffusion creep is enhanced relative to disGBS (at this temperature and stress).

3.5.4 Orientation of CPOs and strain geometry at the subduction interface

For the deformation conditions expected along the subduction interface, it is expected that olivine would have [100] axes aligned approximately parallel to the transport direction (see Figure 4 in Skemer and Hansen, 2016). However, Figure 3.6 demonstrates that olivine CPOs exhibit [100] axes at a high angle to the dip direction and more closely aligned with the stretching lineation in the metamorphic sole, particularly for the lower most sample. Four possible explanations can account for the difference between the orientation of the alignment of [100] axis and that of the dip direction. (1) It is possible that formation of the olivine CPOs predated deformation along the subduction interface. However, the high degree of olivine recrystallization, systematic trends in the olivine CPO towards the metamorphic sole, orientation of the foliation parallel to the subduction interface, and evidence of deformation in the presence of hornblende all indicate that deformation and development of the CPO resulted from shearing along the subduction interface. (2) Another explanation is that the CPOs developed during high-stress and wet deformation conditions (Jung and Karato, 2001; Jung et al., 2006), which has been demonstrated to produce CPOs with [100] axes aligned perpendicular to the shear direction and the shear-plane normal (B-type fabric). However, the development of a B-type fabric requires significantly higher stresses than those estimated here by subgrain-size piezometery, even if the relatively low temperature of deformation is taken into account (Karato et al., 2008). (3) It is possible that the CPO developed during oblique convergence. However, the strain rates required to subduct the sole to 40 km in only 1 million years if subduction had a dominant strike-slip component

are unrealistically high. Furthermore, thrusts, axial planes, and fold axes generally trend north-south, indicating that shortening was oriented east-west. (4) Our preferred explanation is that deformation was constrictional during (near) perpendicular convergence with a strong component of trench-parallel extension. Constrictional deformation is consistent with the well developed mineral stretching lineation in observed metasedimentary rocks in the metamorphic sole.

3.5.5 Tectonic Implications

The role of minor phases in localising strain at the base of the mantle wedge has important implications for subduction zone processes. Orthopyroxene was the most abundant minor phase in seven of eight samples. The large-scale spatial distribution of orthopyroxene is most easily explained by pre-existing mantle heterogeneity. In contrast, hornblende, the most abundant minor phase in one sample, and clinopyroxene have previously been interpreted to form during metasomatism of the mantle wedge by slab derived fluids (Prigent et al., 2014, 2015; Yoshikawa et al., 2015). Therefore, fluid transfer can yield additional localized weakening through crystallization of minor phases that limit olivine grain growth and enhance diffusion creep. These fluids may additionally weaken the mantle through 1) the reduction of the crystal plastic strength of nominally anhydrous minerals, such as olivine, through incorporation of intracrystalline hydrogen (e.g., Mei and Kohlstedt, 2000b;Mei and Kohlstedt, 2000a) or 2) crystallization of weaker phases such as serpentine and chlorite. Thus, weakening and localization in the mantle near the subduction interface appears controlled by both pre-existing heterogeneity and infiltration of fluids from the slab.

In contrast to weakening of the mantle wedge, concomitant dehydration of the slab would have had a strengthening effect. The magnitude of the strengthening in the slab, however, is uncertain as there is a paucity of experimental data on the rheological influence of dehydration of metabasites. Fluid infiltration and amphibolitisation of gabbro (i.e., approximately the reverse reaction to that observed in the sole) has been demonstrated to have a significant weakening effect, primarily from the hydra-

tion of plagioclase (Getsinger et al., 2013). The contrasting rheological evolution of the mantle wedge and downgoing slab has previously been proposed to control the progressive deepening of the subduction interface and associated accretion of slices of the downgoing slab (i.e., the future metamorphic sole) to the hanging-wall peridotites (e.g, Hacker, 1990b; Agard et al., 2016). Agard et al. (2016) suggested that strain localizes where there is a large contrast in rheologies. In the model of Agard et al. (2016), the downgoing slab is initially stronger than the serpentinized mantle wedge and strain localizes at the interface between the two. However, with increasing depth and temperature the mantle wedge becomes less serpentinized and stronger, whereas the slab becomes hotter and weaker. At some critical point the downgoing slab and mantle wedge have similar viscosities and the locus of highest strain migrates into the slab. Here we have demonstrated that the abundance of minor phases exerts an additional and significant rheological control along the base of the mantle wedge not accounted for in previous models. Thus, dehydration and strengthening of the slab and concomitant metasomatism and weakening of the mantle wedge would enhance the strength contrast across the subduction interface, thereby limiting coupling to greater depths. While our results demonstrate that the heterogenous distribution of minor phases influences plate boundary development, they also raise questions as to the origin and extent of petrological heterogeneities in the mantle. Further insight would be gained by grid sampling (at the mm through to the km scale) across the mantle section of the ophiolite in bog-standard peridotite and characterizing the distributions of grain size, composition, water, CPO, and modal mineral abundances on each scale.

3.6 Conclusions

Models of strain localisation at plate boundaries rely on the extrapolation of data from experimentally deformed rocks and small-scale natural shear zones. Direct observation of the strain localization at plate boundaries is difficult due to the paucity of suitable exposure. We examined samples of peridotite collected across the base of the Oman-

UAE ophiolite to elucidate the rheological controls on a palaeosubduction interface and use laboratory-based constraints to identify strain localization. Microstructural analyses reveal systematic changes in olivine grain size, minor-phase content, and olivine CPO. We demonstrate that minor phases pinned olivine grain boundaries and limited grain growth. The resultant finer grain size promoted diffusion creep and led to rheological weakening. We calculate that viscosity and strain rate respectively decrease and increase by approximately an order of magnitude towards the base of the ophiolite. Our data indicate that this rheological weakening was the result of more abundant minor phases near the base of the ophiolite. Orthopyroxene is the most abundant minor phase in all samples. The distribution of orthopyroxene is interpreted to reflect compositional heterogeneity that predates deformation. Unlike orthopyroxene, hornblende and clinopyroxene are interpreted to have crystallised during metasomatism of the mantle wedge by fluids from dehydration of the downgoing slab. Thus, in addition to hydrating and weakening olivine, metasomatic fluids released from the downgoing slab indirectly influenced strain localization by promoting the crystallization of minor phases that limited olivine grain size and promoted grain-size sensitive deformation mechanisms. Furthermore, based on our microstructural evidence and recent laboratory deformation experiments, we suggest that the presence of a hydrous fluid promoted diffusion creep relative to disGBS, enhancing the grain-size sensitivity and associated weakening. While observed in experimentally deformed rocks and at the outcrop scale, this is the first demonstration that minor phases controlled strain localisation at a plate boundary. Moreover, our interpretations are consistent with theoretical models that suggest the distribution of minor phases strongly influence strain localisation along plate boundaries.

Chapter 4

Burial, accretion, and exhumation of the Oman-UAE metamorphic sole

4.1 Introduction

Metamorphic soles are thin thrust-bound sheets of highly sheared, granulite through subgreenschist grade, metabasic and metasedimentary rocks found immediately beneath Tethyan-type ophiolites (e.g., Jamieson, 1980, 1986; Searle and Malpas, 1980; Searle and Malpas, 1982; Williams and Smyth, 1973; Spray, 1984). Metamorphic soles comprise detached sheets of the downgoing slab that were accreted to the base of the hanging-wall mantle immediately following subduction initiation (e.g., Dewey and Bird, 1971; Searle and Malpas, 1980; Searle and Malpas, 1982; Dewey and Casey, 2013). Thus, metamorphic soles provide the unique opportunity to directly study rocks that have been buried, deformed, metamorphosed, and exhumed along the subduction interface. Studies of metamorphic soles can provide valuable insight into initiation and the early stages of subduction by constraining the pressure-temperature-time-deformation history of the downgoing slab. Despite the potential of metamorphic soles to elucidate fundamental geological processes, there is still considerable uncertainty regarding

their evolution. In particular, two major problems remain unsolved: (1) What controls detachment of metamorphic soles from the downgoing slab and accretion to the hanging-wall mantle, and (2) how are metamorphic soles exhumed?

4.1.1 Burial of metamorphic soles

The first step in the evolution of a metamorphic sole is the burial of oceanic crust and interlayered quartz-rich sediments. Remarkably, the highest-grade section of most metamorphic soles record similar peak pressure-temperature conditions of 10–12 kbar, corresponding to depths of 30–40 km, and 800–900 °C (see Figure 2 in van Hinsbergen et al. (2015)). The high geothermal-gradient and absence of blueschists indicate that burial occurred during the earliest stages of subduction and before the mantle wedge had cooled, though the details of subduction initiation remain debated (e.g., Stern and Bloomer, 1992; Casey and Dewey, 1984; Dewey and Bird, 1970; Maffione et al., 2015; Spray and Spray, 1983; Boudier et al., 1988). The characteristic steep inverted metamorphic gradient of metamorphic soles, from granulite down section to subgreenschist facies (Searle and Malpas, 1980; Ghent and Stout, 1981), suggests that heat for metamorphism came from the overlying mantle wedge (Jamieson, 1986). However, metamorphic soles also exhibit an inverted pressure gradient, indicating accretion at different depths (Gnos, 1998). As emphasized by Hacker (1990b), the metamorphic field gradient does not preserve the original thermobarometric gradient during metamorphism. Rather, soles comprises a series of slices that were metamorphosed at different pressures, temperatures, and times and subsequently juxtaposed (Spray, 1984; Gnos and Nicolas, 1996; Hacker and Mosenfelder, 1996; Searle and Cox, 1999; Searle et al., 2015).

4.1.2 Accretion of metamorphic soles

Although peak metamorphic conditions are reasonably well constrained, the mechanisms by which metamorphic soles detached from the downgoing slab and accreted to the hanging-wall mantle remains unclear. The similar metamorphic conditions and

ubiquity beneath Tethyan-type ophiolites indicate the development of metamorphic soles is governed by some fundamental process. Malpas (1976) suggested that the sole of the Bay of Islands ophiolite was accreted as the subduction interface migrated downwards into the slab. Jamieson (1980) inferred the same process for the St. Anthony Complex to the north. Based on numerical simulations partially constrained by observations from the Oman-UAE ophiolite, Hacker (1990b, 1991) proposed that displacement is initially located within the hot and thereby weak basal peridotites of the mantle wedge. With continued subduction and cooling, strain progressively localizes towards the base of the mantle wedge. Concomitantly, conductive heating of the initially cold strong slab has a weakening effect. The key insight by Hacker (1990b, 1991) is that, at some point, the downgoing slab becomes weaker than the peridotite, causing deformation to migrate downward into the slab. A consequence of this downward migration is the accretion of a slice of the uppermost slab to the base of the hanging wall mantle. Similar models, with key differences regarding controls on the rheological properties across the subduction interface, have recently been proposed by other researchers (e.g., Plunder et al., 2015; Plunder et al., 2016; Agard et al., 2016; Soret et al., 2017).

4.1.3 Exhumation of metamorphic soles

Following burial and accretion, metamorphic soles must be exhumed. Pressure estimates from garnet-clinopyroxene amphibolites are typically 10–12 kbar (see Figure 2 in van Hinsbergen et al. (2015) and Figure 3 of Agard et al. (2016)), consistent with depths of 30–40 km. Such depths are considerably deeper than can be accounted for by the thickness of the overlying ophiolites, implying that metamorphic soles are exhumed relative to the ophiolite (Jamieson, 1980; Casey and Dewey, 1984; Hacker and Gnos, 1997; Cowan et al., 2014). Two models have been proposed for the exhumation of the sole: (1) buoyancy-driven ductile extrusion along the subduction interface (Searle and Cox, 2002; Cowan et al., 2014), and (2) extrusion of the mantle wedge above a flattening slab (Casey and Dewey, 1984; Dewey and Casey, 2013). Differentiating

between the two models has proven difficult, as determining pressures in peridotite is notoriously difficult. Ductile extrusion predicts lower pressures for the peridotite immediately adjacent the sole. In contrast, if the sole was exhumed along a flattening slab the adjacent peridotite would presumably record similar pressures. Ductile return flow is difficult to reconcile with three key observations: (1) the limited partial melting necessary for ductility, (2) the small buoyancy contrast between the amphibolites and adjacent peridotite, and (3) the small thickness and total mass of amphibolites. On the other hand, it also difficult to comprehend how and why a slab would shallow from 40 km to less than 20 km, especially given the short time frame of just 1–2 Myr (Hacker, 1994; Hacker et al., 1996; Rioux et al., 2016).

4.1.4 Focus of this study

The Oman-UAE metamorphic sole is the largest and most intensely studied on Earth. Previous studies have paid little attention to the retrograde evolution and generally focussed on attaining pressure-temperature conditions of peak metamorphism. Here we document the textural evolution of the metamorphic sole from burial, through to accretion, and finally exhumation. We pay particular attention to retrograde textures that persisted from granulite down to greenschist facies. Our observations indicate that the extent of retrogression has been significantly underestimated. Our investigation of retrograde textures provides clues about peak conditions. We suggest that granulite formation was far more pervasive than previously considered. Based on our findings, we propose that granulite formation significantly increased the viscosity of the downgoing slab, causing deformation to migrate into the slab and thus accrete the future sole. Shortly following accretion, fluids released from underplated lower-grade amphibolites and metasedimentary rocks led to rehydration and weakening of the sole that facilitated exhumation.

4.2 Oman-UAE metamorphic sole

The metamorphic sole is present beneath the entire Oman-UAE ophiolite, but most studies have focussed on three of the best exposed localities: the Masafi (or Asimah) window in the northern UAE, Jebel Sumeini in northern Oman, and Wadi Tayyin to the south of Muscat. The metamorphic sole is bound at the top by the Semail thrust, which separates the overlying banded ultramafics along the base of the ophiolite (Figures 4.2 and 4.3A; Reinhardt, 1969; Allemann and Peters, 1972; Glennie et al., 1974). Underlying the metamorphic sole are unmetamorphosed thrust sheets of the Haybi complex (Searle et al., 1980; Searle and Malpas, 1980). The sole is characterized by a steep inverted metamorphic field gradient that passes from garnet-clinopyroxene amphibolites at the structurally highest levels, down through epidote-amphibolite, amphibolite, and greenschist facies metabasic and metasedimentary rocks (Searle and Malpas, 1980; Hacker and Mosenfelder, 1996; Gnos, 1998). Pressure-temperature estimates of garnet-clinopyroxene amphibolites from the Oman-UAE sole are consistently between 10–12 kbar (30–40 km) and 750–900 °C (Searle and Malpas, 1980; Ghent and Stout, 1981; Hacker and Gnos, 1997; Gnos, 1998; Cowan et al., 2014; Soret et al., 2017). As discussed in Chapter 2, the original (i.e., pre-erosion) thickness of the ophiolite was likely ∼12 km, which implies that the sole formed about three times deeper than can be accounted for by the preserved thickness of the ophiolite. U-Pb zircon dates demonstrate that metamorphism of the sole was synchronous with crystallization of the crustal sequence of the overlying ophiolite (Rioux et al., 2016). Ar/Ar cooling ages from amphibole indicate rapid exhumation to below ∼550 °C in only 1–2 Myr following crystallization of the crustal section of the ophiolite (Hacker, 1994; Hacker et al., 1996).

As opposed to the 'normal' metamorphic sole, the Bani Hamid sole is a slice of uniformly granulite facies metasediments and minor metabasic rocks that has been exposed by out-of-sequence thrusting (Figure 4.1; Gnos and Kurz, 1994; Gnos and Nicolas, 1996; Searle et al., 2015). Searle et al. (2015) suggested that Bani Hamid is the metamorphosed equivalent of dolomitic cherts, calcareous turbidites, and alkali volcanics of the Haybi complex. Despite similarly high-temperatures of 850 ± 60 °C,

thermobarometry estimates from Bani Hamid indicate considerably lower pressures of just 5.6 ± 0.5kbar (Searle et al., 2015). The high-temperatures and low pressures of Bani Hamid is enigmatic, especially given that metamorphism post dates that of the normal sole by ∼2–3 million years (Searle et al., 2015), by which point the isotherms would have been expected to have relaxed.

4.2.1 Study area

The Masafi window exposes the metamorphic sole in the core of a south-plunging antiform (Figure 4.1; Chapter 2). Detailed geological mapping and sample collection was conducted near the southern extent of the Masafi window, immediately adjacent to the peridotite transect of Chapter 3 (Figure 4.2). The top ∼60 m of the sole consists solely of amphibolite with varying abundances of garnet and clinopyroxene (Figure 4.3A). The amphibolites exhibit a gneissic foliation, defined by discontinuous, alternating plagioclase and amphibole rich layers (Figures 4.3B and C), that is parallel with the Semail thrust and mylonitic fabric of the adjacent banded ultramafic unit (Chapter 3). Small amounts of coarse leucosome are associated with garnet-clinopyroxene porphyroclasts (Figure 4.3B). Down section, amphibolites become finer-grained and the foliation becomes schistose or even phyllitic. In contrast to descriptions from other localities (e.g., Ghent and Stout, 1981; Hacker and Mosenfelder, 1996; Gnos, 1998), partial melting was not restricted to the uppermost few metres of the sole. Judging from the abundance of leucosome, the most extensive melting occurred further down the section in schistose, epidote- and bi-mineralic (i.e., amphibole + plagioclase) amphibolites interlayered with metasediments. Figure 4.3C presents a field photograph of sample locality TA94 (∼200 m below the peridotites), which contains abundant coarse-grained trondhjemitic leucosomes that exhibit pinch and swell structures.

Metasedimentary rocks—primarily impure quartzites with piemontite (Mn-epidote), muscovite, biotite, feldspar, amphibole, garnet, and rarely kyanite—first appear interlayered with amphibolite at ∼60 below the peridotite contact (Figures 4.3D–H, 4.2). The abundance of metasedimentary rocks increases down section until they be-

come dominant. Schistose amphibolite occurs as centimetre to several metre thick, discontinuous, layers and boudins within the metasedimentary rock (Figures 4.3D–E). Metasediments also occurs as boudins within amphibolite. The metasedimentary rocks and less commonly bi-mineralic and epidote amphibolites exhibit centimetre to tens of metre scale, isoclinal folds with roughly N-S trending fold-axis (Figures 4.3G and H). A well-developed lineation defined by quartz stretching and rodding is parallel to fold axes. The eastern margin of the mapped area marks the beginning of a several kilometer thick section of folded and faulted, (sub)greenschist facies metasedimentary rocks with occasional metabasic ash layers (Fig 4.1).

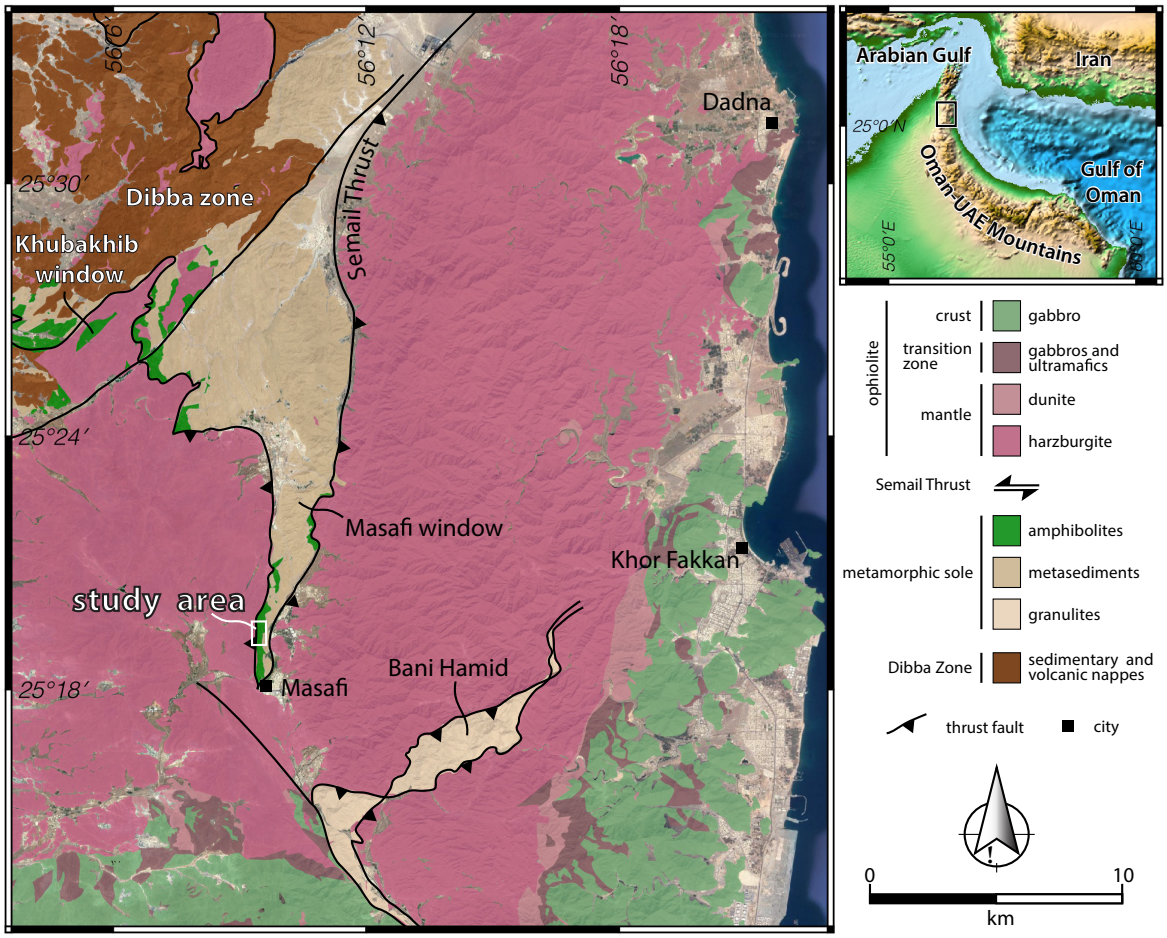


Figure 4.1: Simplified geological map of the northern UAE showing the location of the study area. Location on the Arabian peninsula is shown on the inset. Modified after British Geological Survey maps (Farrant et al., 2012)

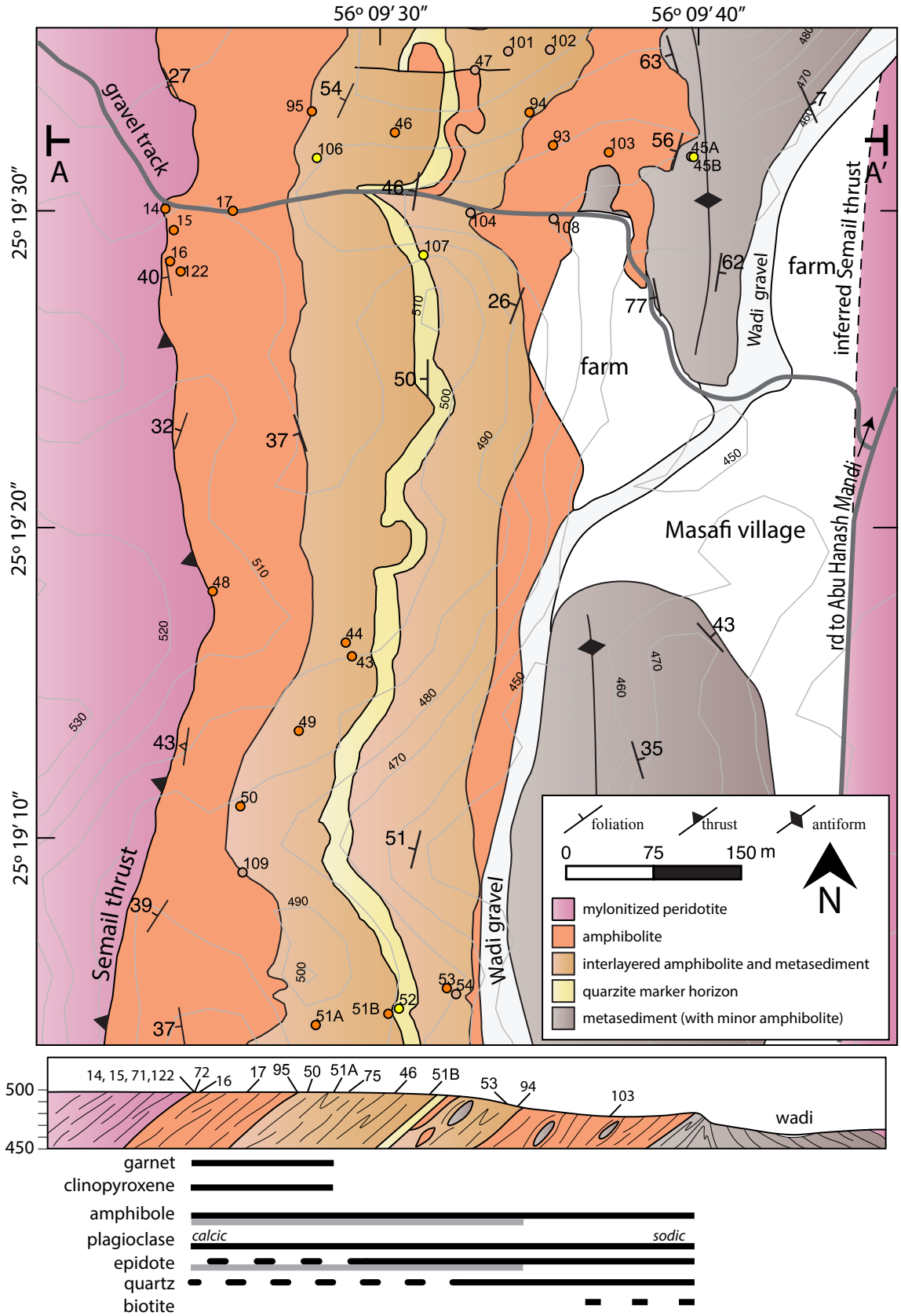


Figure 4.2: Geological map and cross-section of the study area. Samples locations are projected on to the section line, commonly with the help of the quartzite marker horizon. Mineral distributions are shown beneath the cross-section. See Figure 4.1 for location.

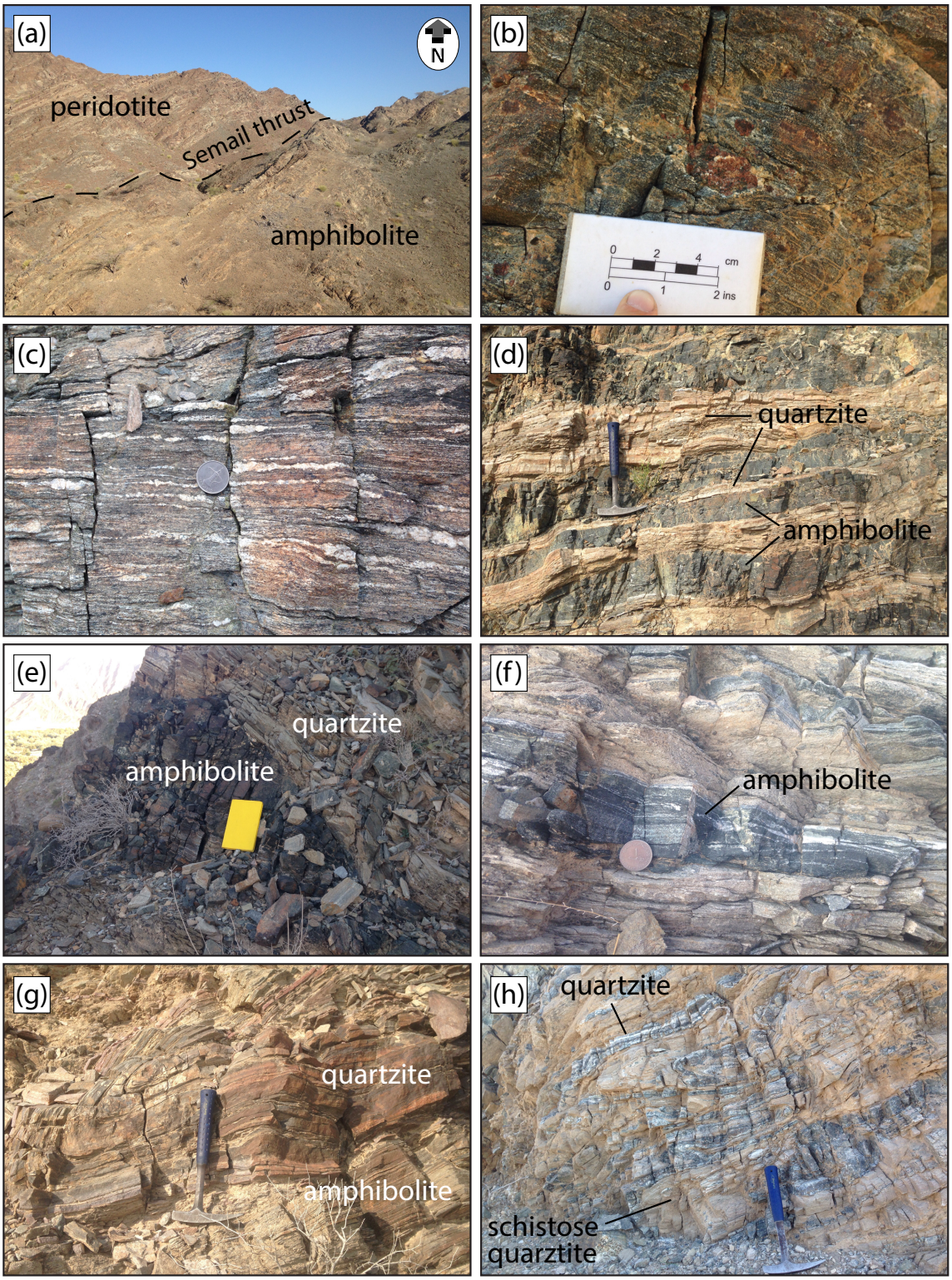


Figure 4.3: Field photographs demonstrating key textures and relationships.

4.3 Petrography and mineral chemistry

4.3.1 Sampling strategy and analytical methods

Sixteen thin sections were made from samples collected along a transect spanning 250 m of structural thickness. Petrographic descriptions of these samples are presented in Table 4.1. Sample locations and the spatial distribution of minerals are presented in Figure 4.2. Of the sixteen thin sections, ten were selected for more detailed petrological analyses. Major element chemistry of minerals that exhibit solid solutions were measured using a Cameca SX-5 field emission electron microprobe with a 5 μm spot size, 30 s count time per element, 15KeV, and 20 nA. The following standards were used: andradite (Fe, Ca), faylite (Mn), albite (Si, Al, Na), MgO (Mg), sanidine (K), TiO_2 (Ti). Representative mineral analysis are presented in Table 4.2. This section provides a summary of key mineral associations, textures, and petrological trends.

Table 4.1: Sample descriptions

Sample	lat.	long.	metres below peridotite	peak assemblage	textures
TA122	25.3243	56.1567	float	grt cpx amp pl qz ilm	cpx → dark-brown amp trondjhemitic segregations
TA14	25.3249	56.1565	float	grt cpx amp pl ilm	relict ep in amp cpx → brown amp cpx → green amp brown amp → green amp (minor) cpx --> ep + ab ilm → ttn
TA15	25.3247	56.1566	float	grt cpx amp pl	grt → ep ± green amp brown amp → green amp cpx → brown amp pl? → ab + ep
TA71	25.3122	56.1574	1	grt cpx amp pl qz	cpx → brown amp grt → ep ± green amp pl → ep brown amp → green amp
TA72	25.3114	56.1572	1	grt cpx amp pl qz ilm	cpx → brown amp brown amp → green amp (minor) trondhjemitic segregation
TA16	25.3244	56.1566	5	grt cpx amp pl ilm	brown amp → green amp cpx → brown amp pl → spongy ep/czo + ab symplectic kfs+ep
TA17	25.3248	56.1571	30	grt cpx amp pl ilm	brown amp → green amp brown amp → brown amp + ep grt → ep ± green amp cpx → brown amp cpx → green amp rt in titanite core
TA95	25.3257	56.1578	63	grt cpx amp pl ru ilm	cpx → brown amp rt in ttn cores ep veins
TA50	25.3198	56.1572	69	grt cpx amp pl ep? Ilm ru	cpx → brown amp brown amp → green amp (replacement) brown amp → green amp (diffusional) grt → ep ± green amp pl → ep rt in ttn cores amp in cpx in grt
TA51A	25.3179	56.1579	85	grt cpx amp pl qz ilm	cpx → brown amp brown amp → green amp(minor) trondhjemitic leucosome
TA75	25.3113	56.1587	99	ep amp pl qz	intergrown ep-amp
TA46	25.3255	56.1585	122	amp pl ep ttn	brown amp → green amp (replacement)
TA51B	25.3180	56.1585	141	ep pl amp ilm	-
TA53	25.3182	56.1590	187	amp pl ep qz ru ttn?	pl → qz + ep symplectite brown amp → green amp brown amp → green amp + ep green amp → ep + ab/kfs/qz? rt included in Ttn
TA94	25.3257	56.1597	197	amp ep pl qz ilm	act-ep intergrowths trondhjemitic segregation
TA103	25.3253	56.1604	250	ep pl amp qz bt ilm ttn	-

Table 4.2: Mean composition of clustered analyses as oxide wt% and c.p.f.u..

	TA14					TA16					TA17					TA95			
Min	grt	grt	cpx	amp	FeTiOx	grt	grt	cpx	amp	FeTiOx	grt	grt	cpx	amp	FeTiOx	grt	grt	cpx	amp
Note	low-Ca	high-Ca	mean	mean	mean	core	rim	mean	mean	mean	core	rim	mean	pro	1-spot	high Ca	low Ca	mean	pro
SiO2	38.0	38.0	49.6	42.2	0.3	39.1	39.3	49.5	41.4	0.0	38.1	37.8	49.4	41.2	0.1	37.8	37.8	47.6	41.0
TiO2	0.1	0.1	0.4	1.8	48.0	0.2	0.1	0.6	1.9	49.7	0.2	0.1	0.6	1.9	52.7	0.2	0.1	0.5	1.5
Al2O3	21.2	21.6	4.5	12.6	0.2	21.1	21.2	5.1	12.7	0.0	20.4	20.5	5.0	12.6	0.0	21.8	22.2	5.5	14.1
Fe2O3	0.0	0.0	0.0	0.0	0.0	0.0	0.0	0.0	0.0	0.0	0.0	0.0	0.0	0.0	0.0	0.0	0.0	0.0	0.0
FeO	24.9	23.4	10.6	16.1	46.2	23.2	24.9	11.0	16.8	44.8	21.7	23.8	10.4	15.8	38.9	21.7	23.3	10.0	15.4
MnO	1.5	1.4	0.2	0.2	0.7	1.2	1.5	0.2	0.1	1.9	1.5	1.3	0.2	0.2	3.7	1.2	2.4	0.2	0.1
MgO	5.5	4.6	10.7	10.0	0.0	4.5	4.7	10.3	9.1	0.1	4.4	5.1	10.5	9.5	0.0	4.3	4.4	10.9	10.1
CaO	8.2	10.4	20.9	11.1	0.5	11.9	9.6	22.1	12.0	0.1	12.7	10.1	21.7	11.7	0.1	12.9	10.3	21.8	11.8
Na2O	0.0	0.0	1.2	2.2	0.1	0.0	0.1	1.1	2.0	0.0	0.0	0.0	1.2	2.3	0.0	0.1	0.1	0.9	1.7
K2O	0.0	0.0	0.0	0.6	0.0	0.0	0.0	0.0	0.8	0.0	0.0	0.0	0.0	0.8	0.0	0.0	0.0	0.0	1.0
Totals	99.6	99.4	98.1	96.7	96.0	101.2	101.3	99.8	96.8	96.6	99.1	98.6	98.8	96.0	95.7	99.9	100.7	97.4	96.7
Oxygens	12	12	6	23	3	12	12	6	23	3	12	12	6	23	3	12	12	6	23
Si	2.97	2.97	1.89	6.34	0.01	3.01	3.03	1.86	6.30	0.00	2.99	2.98	1.87	6.30	0.00	2.94	2.92	1.83	6.17
Ti	0.01	0.01	0.01	0.20	0.94	0.01	0.00	0.02	0.22	0.97	0.01	0.01	0.02	0.22	1.03	0.01	0.01	0.02	0.16
Al	1.96	1.99	0.20	2.23	0.01	1.91	1.92	0.23	2.28	0.00	1.89	1.91	0.22	2.27	0.00	2.00	2.03	0.25	2.51
Fe3	0.09	0.06	0.08	0.22	0.10	0.00	0.00	0.00	0.00	0.00	0.11	0.12	0.09	0.02	0.00	0.12	0.12	0.14	0.26
Fe2	1.54	1.47	0.26	1.80	0.91	0.04	0.02	0.10	0.02	0.05	1.32	1.45	0.24	2.00	0.85	1.29	1.39	0.18	1.69
Mn	0.10	0.09	0.01	0.02	0.02	1.45	1.58	0.25	2.11	0.93	0.10	0.09	0.01	0.02	0.08	0.08	0.16	0.01	0.02
Mg	0.64	0.53	0.61	2.24	0.00	0.08	0.10	0.01	0.02	0.04	0.51	0.60	0.59	2.17	0.00	0.49	0.51	0.62	2.25
Ca	0.69	0.87	0.85	1.79	0.01	0.51	0.54	0.58	2.05	0.00	1.07	0.85	0.88	1.91	0.00	1.07	0.86	0.90	1.89
Na	0.00	0.00	0.09	0.65	0.00	0.98	0.79	0.89	1.95	0.00	0.00	0.00	0.09	0.68	0.00	0.01	0.01	0.06	0.49
K	0.00	0.00	0.00	0.11	0.00	0.00	0.01	0.08	0.59	0.00	0.00	0.00	0.00	0.16	0.00	0.00	0.00	0.00	0.20
Sum	8	8	4	16	2	8	8	4	16	2	8	8	4	16	2	8	8	4	16

	TA50				TA51A					TA46		TA53		TA103			
Min	grt	grt	cpx	amp	grt	grt	cpx	amp	FeTiOx	amp	ep	amp	ep	amp	ep	bt	FeTiOx
Note	rim	core	mean	pro	rim	core	mean	mean	mean	retro	mean	mean	mean	mean	mean	mean	spot 1
SiO2	38.6	38.6	49.0	41.5	38.5	38.1	48.7	41.7	0.0	53.0	37.5	43.6	37.8	44.3	38.1	37.7	2.1
TiO2	0.2	0.2	0.6	1.4	0.2	0.2	0.5	1.6	18.7	0.1	0.2	1.0	0.3	0.7	0.1	2.3	14.0
Al2O3	20.6	20.5	5.6	13.4	20.8	20.7	6.3	13.3	0.4	3.3	25.6	12.8	26.3	11.8	24.2	15.8	0.2
Fe2O3	0.0	0.0	0.0	0.0	0.0	0.0	0.0	0.0	0.0	0.0	14.2		10.8	0.0	15.1	0.0	0.0
FeO	23.0	22.6	10.6	15.6	21.1	22.8	8.9	12.9	71.0	11.1	0.0	12.7	0.0	13.6	0.0	13.8	70.4
MnO	1.1	1.3	0.2	0.2	2.3	1.9	0.3	0.2	0.1	0.3	0.2	0.2	0.1	0.3	0.3	0.2	0.1
MgO	4.9	4.4	9.9	9.3	5.6	4.8	11.0	11.5	0.0	16.4	0.0	11.6	0.1	12.1	0.0	14.8	0.0
CaO	11.3	12.2	22.5	12.0	11.0	10.9	22.3	12.0	0.0	12.2	22.9	11.9	24.2	11.6	23.9	0.3	1.7
Na2O	0.0	0.0	1.0	1.7	0.0	0.0	1.1	1.6	0.0	0.5	0.0	1.6	0.0	2.0	0.0	0.1	0.0
K2O	0.0	0.0	0.0	1.3	0.0	0.0	0.0	1.3	0.0	0.2	0.0	0.4	0.0	0.8	0.0	8.3	0.0
Totals	99.8	99.8	99.4	96.5	99.4	99.3	99.0	96.0	90.2	96.9	100.6	95.9	99.5	97.2	101.6	93.3	88.4
Oxygens	12	12	6	23	12	12	6	23	3	23	12.5	23	12.5	23	12.5	11	3
Si	3.01	3.01	1.85	6.31	2.99	2.98	1.83	6.26	0.00	7.61	2.91	6.49	2.94	6.54	2.94	2.84	0.06
Ti	0.01	0.01	0.02	0.16	0.01	0.01	0.02	0.18	0.38	0.01	0.01	0.11	0.02	0.07	0.01	0.13	0.29
Al	1.90	1.89	0.25	2.41	1.91	1.91	0.28	2.35	0.01	0.56	2.33	2.25	2.41	2.06	2.20	1.40	0.01
Fe3	0.08	0.07	0.09	0.00	0.10	0.10	0.11	0.13	1.23	0.18	0.83	0.13	0.63	0.22	0.88	0.01	1.31
Fe2	1.42	1.40	0.25	1.99	1.27	1.39	0.17	1.49	0.38	1.16	0.00	1.46	0.00	1.46	0.00	0.86	0.29
Mn	0.07	0.09	0.01	0.02	0.15	0.13	0.01	0.03	0.00	0.03	0.01	0.03	0.01	0.04	0.02	0.01	0.00
Mg	0.57	0.51	0.56	2.11	0.65	0.56	0.62	2.59	0.00	3.50	0.01	2.57	0.01	2.67	0.00	1.66	0.00
Ca	0.95	1.02	0.91	1.95	0.92	0.92	0.90	1.94	0.00	1.87	1.90	1.90	2.01	1.84	1.98	0.03	0.05
Na	0.00	0.00	0.07	0.51	0.01	0.00	0.08	0.47	0.00	0.14	0.00	0.47	0.00	0.57	0.00	0.02	0.00
K	0.00	0.00	0.00	0.25	0.00	0.00	0.00	0.24	0.00	0.04	0.00	0.08	0.00	0.14	0.00	0.79	0.00
Sum	8	8	4	16	8	8	4	16	2	15	8	15	8	16	8	8	2

4.3.2 Garnet

Garnet is present in samples from immediately beneath the contact with peridotites to ∼85 m down the section (Figure 4.2, 4.1). However, garnet is not ubiquitous across this distance and becomes less common with increasing distance from the peridotites. Samples with garnet visible in hand sample were preferentially selected. Garnet and clinopyroxene always occur within the same section. Garnet typically occurs as large porphyroblasts or aggregates with subrounded inclusions and intergrowths of clinopyroxene (Figure 4.4). Garnet, clinopyroxene and plagioclase form centimeter-scale ovoid enclaves that are wrapped by the gneissic foliation (Figures 4.4A–B and G). Garnet grains are typically anhedral, but some euhedral faces are preserved (Figure 4.5A). In some samples, such as TA51, garnet occurs as skeletal grains associated with quartz and plagioclase, indicating crystallization during melting. Garnet also commonly contains inclusions of Ti-oxides, plagioclase, apatite, and less commonly amphibole. In about half the thin sections of garnet-clinopyroxene amphibolites, garnet is partially replaced by epidote and/or intergrowths of epidote and actinolite (Figures 4.5A–D).

Compositional profiles from garnet grains are presented in Figure 4.6. Garnet consist primarily of the almandine end-member. Garnet zoning is generally patchy and weak, but there are some consistent trends. Ca exhibits the strongest zoning and, aside from TA51A, decreases towards the rims and clinopyroxene inclusions. A grain from TA95 displays a remarkable zoning profile that is flat across the core (0.8 cations per formula unit (c.p.f.u)), rises sharply through the mantle (1.1 c.f.p.u.), and then drops to ∼ 0.9 c.p.f.u. at the outermost rim. TA95 is also the the only sample to retain prograde zoning, characterized by a high-Mn core and low Mn-rim. In the remaining samples, Mn shows little variation across most of the grains and only minor spikes near some rims. Mg# ($Mg/Mg + Fe^{2+}$) is either constant or increases by up to a few percent across most garnet grains. Garnet in TA14 and TA51A, the structurally highest and lowest garnet-bearing samples, respectively, display the largest increases in Mg# towards the rim. The relatively small variation in Mg# is present despite changes in both Fe^{2+} and Mg. This suggests that Fe^{2+} and Mg are similarly compensating for

variation in Ca, rather than directly reflecting changes in pressure and temperature. A nice examples of this is demonstrated by compositions nears the rim of a garnet grain in TA17 (Figure 4.6), where a sharp decrease in Ca reflects an increase in both Mg and Fe^{2+}, thus maintaining the Mg#. A sharp decrease in Mg# near the outermost rim of some grains (e.g., TA16, TA50) indicates some extent of retrograde Fe-Mg exchange took place.

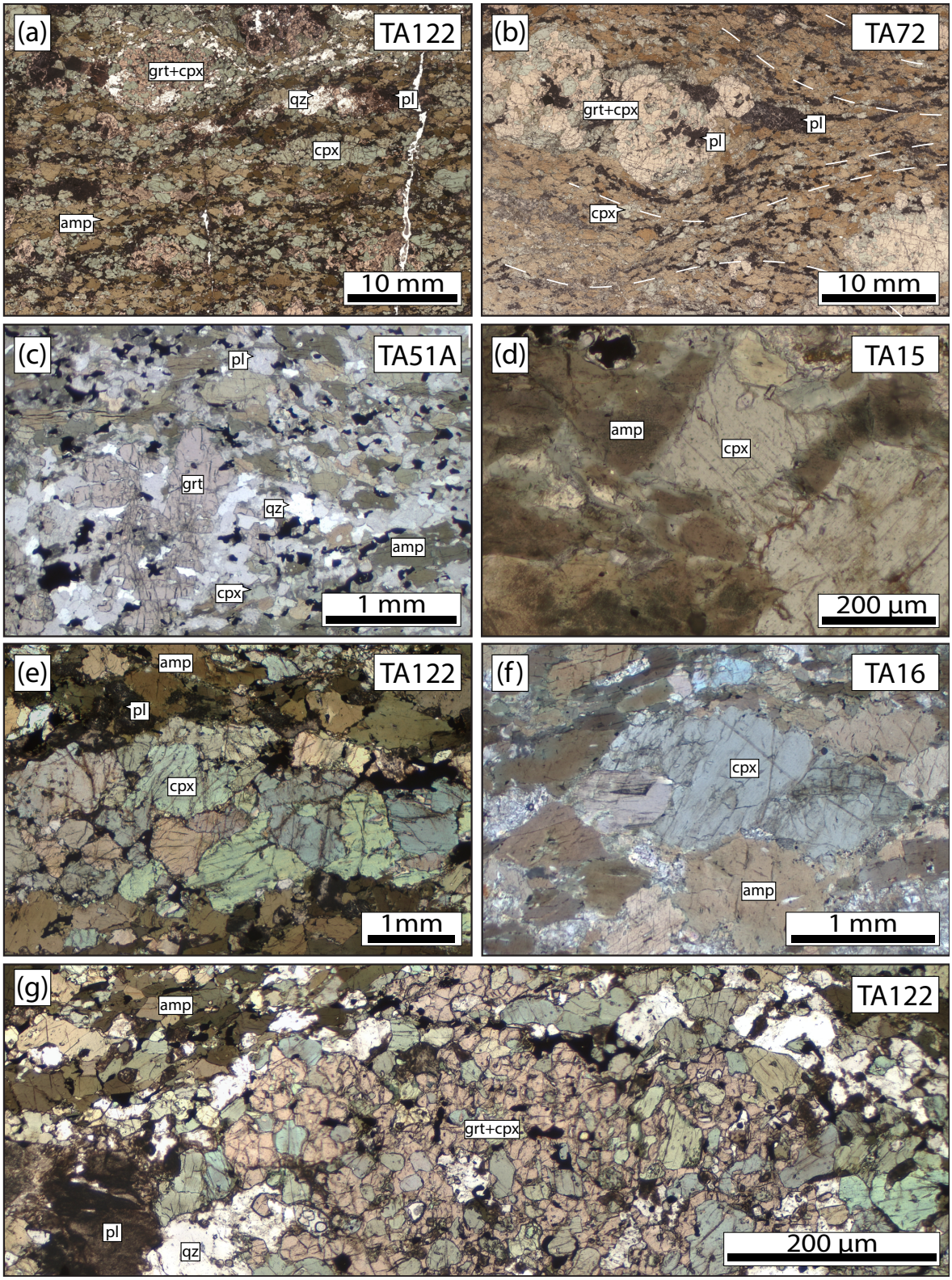


Figure 4.4: Photomicrographs of key textures from garnet-clinopyroxene amphibolites. See text for discussion.

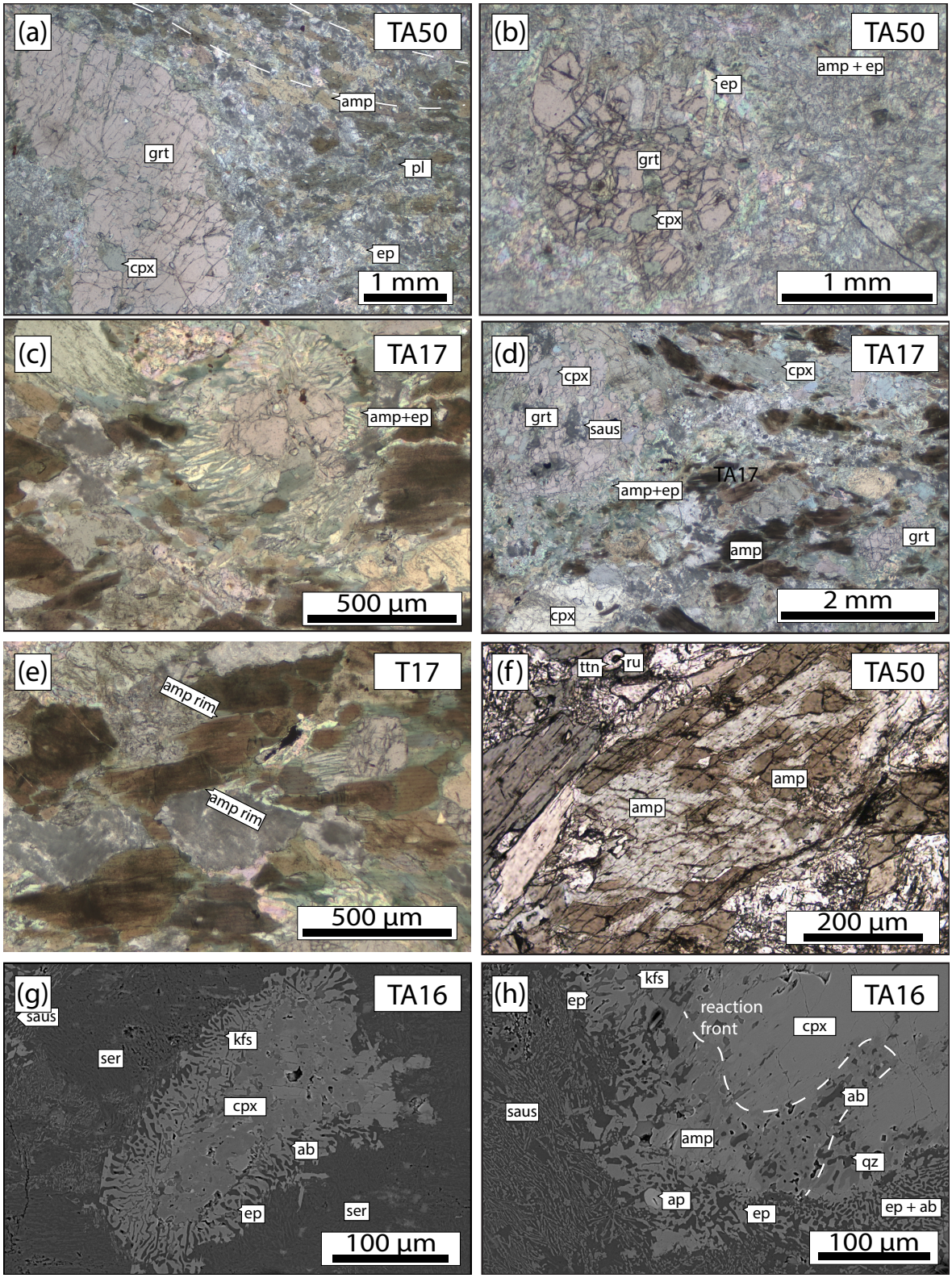


Figure 4.5: Photomicrographs and BSE images of retrograde textures from Grt-Cpx amphibolites. See text for discussion.

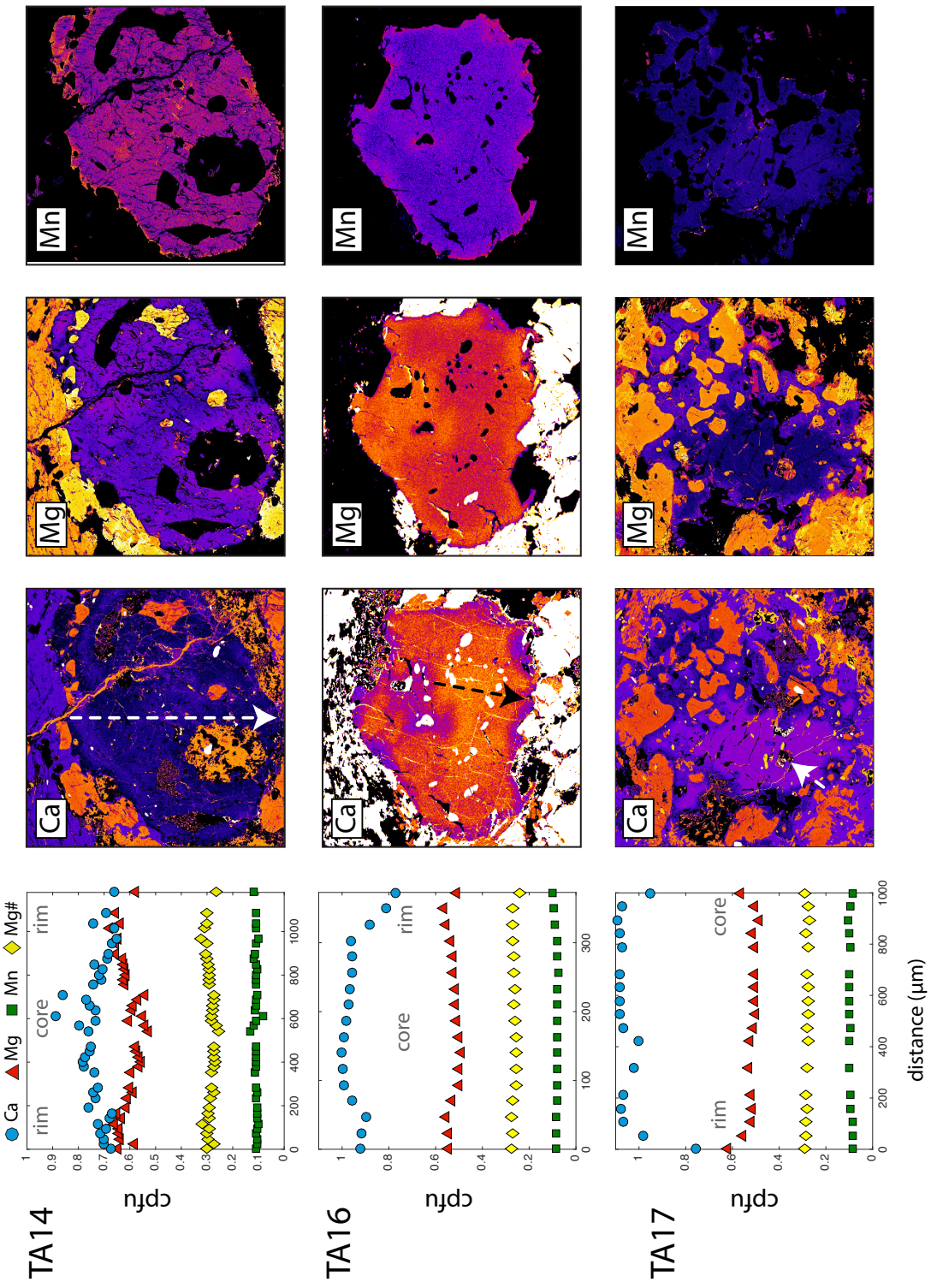


Figure 4.6: Garnet compositional profiles and elemental maps.

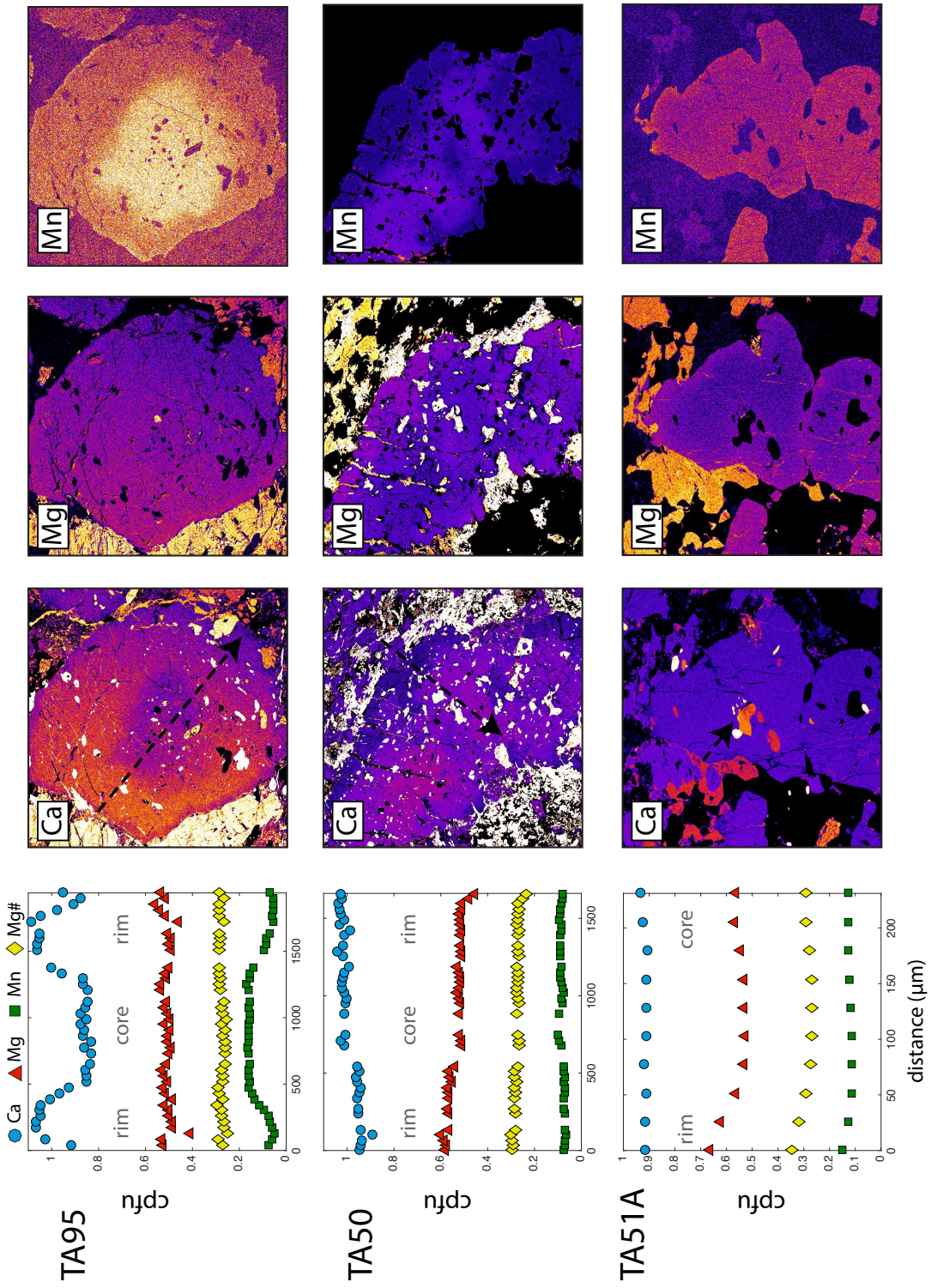


Figure 4.6: Garnet compositional profiles and elemental maps *(continued)*.

4.3.3 Clinopyroxene

Clinopyroxene only occurs in thin sections that also contain garnet (Figure 4.2). Clinopyroxene occurs as inclusions in and intergrowths with garnet (Figure 4.4A–C and G). Clinopyroxene also occurs as lenticular grains or more commonly as granoblastic aggregates surrounded by amphibole (Figures 4.4D–G). Clinopyroxene grains commonly exhibit exsolution lamellae that are clearly visible with a petrographic microscope. Most clinopyroxene has undergone some extent of retrograde breakdown to amphibole (Table 4.1). Clinopyroxene is typically replaced by dark brown amphibole along grain boundaries and fractures (Figures 4.4D–F). Rarely, clinopyroxene has been replaced by pale-green amphibole. Clinopyroxene is best preserved within larger enclaves with garnet, although some inclusions have been partially replaced by amphibole.

Mean clinopyroxene compositions are presented in Table 4.3. Clinopyroxene grains are unzoned aside from a minor increase in Mg# near some rims. Between samples, clinopyroxene compositions are similar and exhibit no correlation with structural position (Table 4.3 and Figure 4.7).

Table 4.3: Amphibole, plagioclase, and clinopyroxene compositions. Blue rows are for retrograde associations.

		amphibole							plagioclase						clinopyroxene						
Sample	meters below peridotite	mean total ts	σ	mean total ed	σ	mean Ti (wt %)	σ	n	mean An fresh	σ	n	mean An saussurite	σ	n	Ca (c.p.f.u.)	σ	Al + Na (c.p.f.u.)	σ	Mg#	σ	n
TA14	1	1.05	0.05	0.606	0.04	1.77	0.27	88				0.36	0.01	10	0.85	0.02	0.29	0.04	0.70	0.02	53
TA16	5	1.00	0.06	0.70	0.05	1.92	0.26	28				0.43	0.05	10	0.89	0.03	0.30	0.03	0.70	0.02	60
TA17	30	0.96	0.08	0.75	0.03	1.93	0.26	13				0.38	0.03	9	0.88	0.03	0.30	0.05	0.71	0.02	30
TA17	30	0.54		0.49		0.36		2	0.08	0.01	4	-	-								
TA95	63	1.20	0.04	0.63	0.03	1.41	0.32	15				0.52	0.04	10	0.90	0.04	0.31	0.04	0.78	0.04	30
TA50	69	1.00	0.06	0.70	0.03	1.42	0.22	21				0.49	0.02	11	0.91	0.01	0.32	0.02	0.69	0.02	31
TA50	69	0.37	0.16	0.29	0.12	0.28	0.19	15	0.07	0.05	8	-	-								
TA51A	85	1.07	0.03	0.67	0.04	1.57	0.22	11	0.49	0.04	14	0.44	0.05	8	0.90	0.01	0.36	0.02	0.78	0.03	29
TA46	122	0.80	0.08	0.44	0.08	0.62	0.18	5													
TA46	122	0.27	0.07	0.11	0.04	0.06	0.03	15	0.07	0.02	13										
TA53	187	1.02	0.06	0.48	0.04	0.96	0.10	13	0.44	0.03	7	0.49	0.03	6							
TA94	197	1.10	0.03	0.62	0.03	0.59	0.07	21	0.36	0.03	10										
TA103	250	0.86	0.02	0.61	0.02	0.65	0.03	13	0.20	0.02	15										

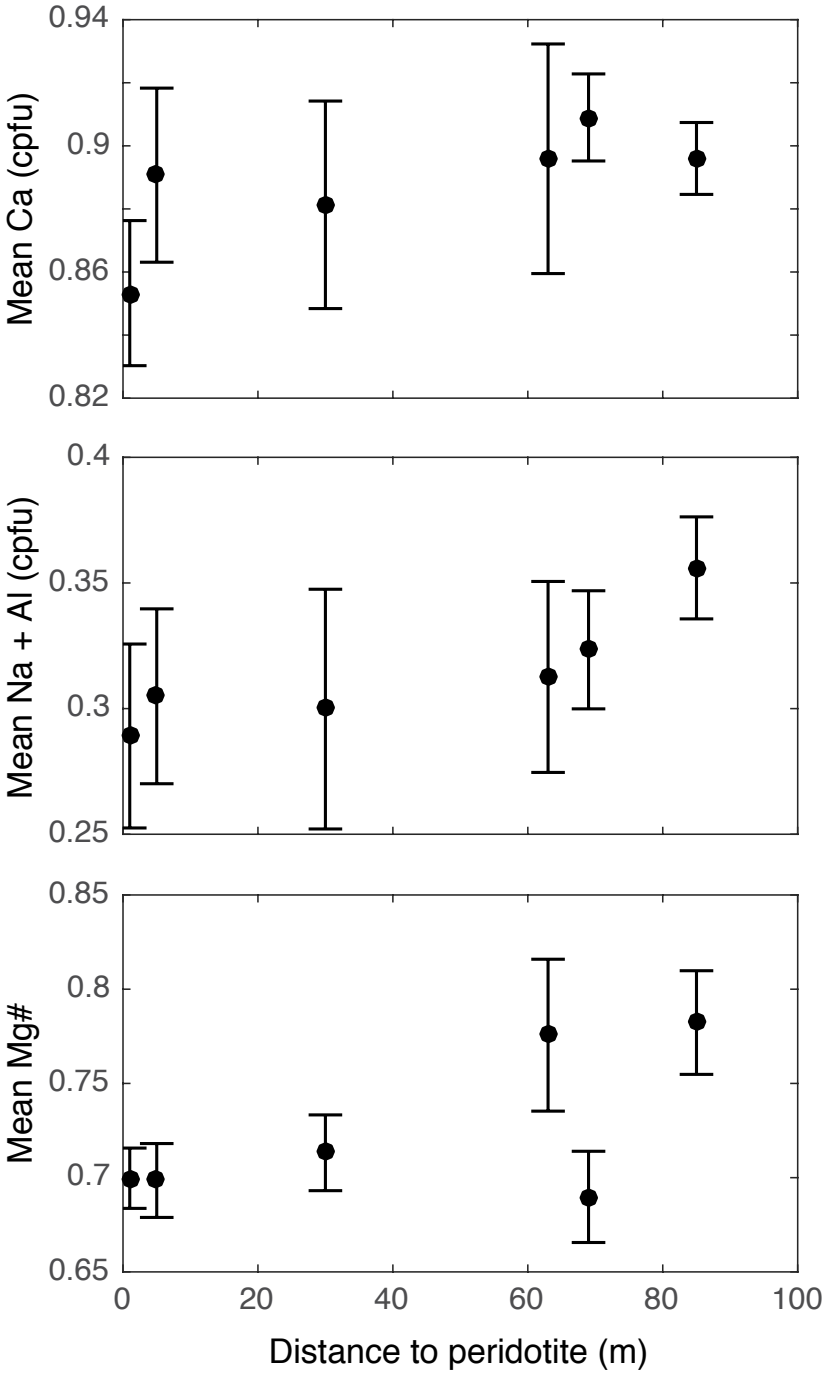


Figure 4.7: Mean clinopyroxene compositions against structural distance below the peridotites. Error bars represent variation (1 σ) within a population and do not include analytical error.

4.3.4 Amphibole

Amphibole is the dominant mineral in all of the samples analysed and occurs in several different textural settings. Most amphibole occurs as sub-equant to lozenge-shaped, well aligned crystals (Figures 4.4 and 4.8B and H). A compositional foliation is define by alternating amphibole-rich and either plagioclase-rich or clinopyroxene rich layers. The foliation wraps around garnet-clinopyroxene enclaves and garnet porphyroblasts, indicating that the fabric development post-dates the crystallization of garnet and clinopyroxene. Occasionally, amphibole occurs within garnet-clinopyroxene enclaves as either inclusions, intergrowths, or a replacement product of clinopyroxene. In sample TA51, amphibole occurs as an inclusion in clinopyroxene that is included in garnet. With increasing distance from the peridotites, amphibole becomes finer grained and, under plane-polarized light, transitions from dark brown to pale green.

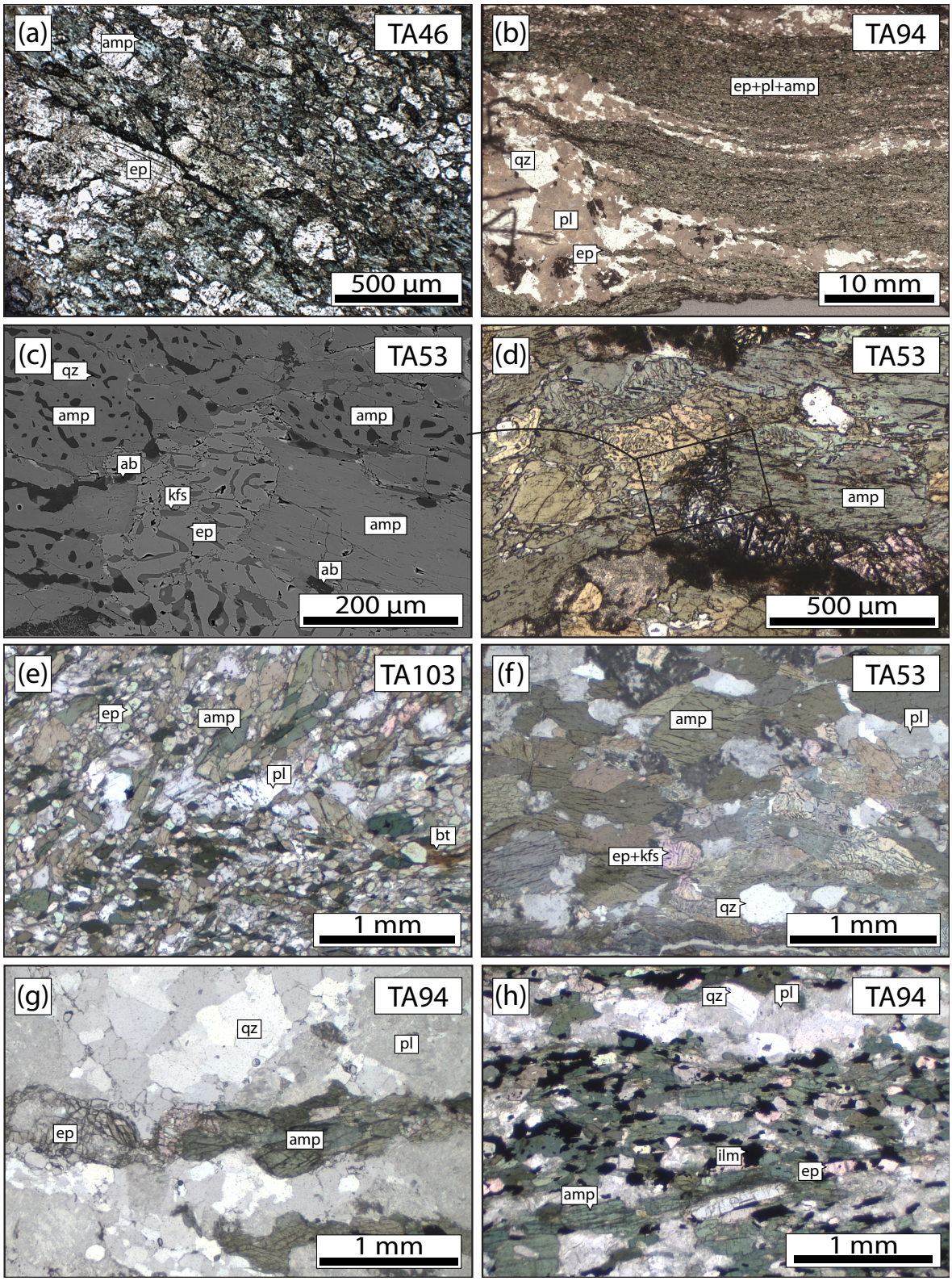


Figure 4.8: Photomicrographs and BSE images of key textures of epidote- and bi-mineralic amphibolites. See text for discussion.

In the garnet-clinopyroxene amphibolites, a considerable amount of amphibole occurs as a replacement product of clinopyroxene, earlier amphibole, and garnet. Amphibole replaces clinopyroxene along fractures and grain boundaries (Figure 4.4). The extent to which amphibole has replaced clinopyroxene is lowest within garnet-clinopyroxene enclaves. Amphibole that has replaced clinopyroxene is usually dark brown and rarely a pale green, presumably lower-temperature amphibole. Dark-brown amphibole is commonly replaced by a later greenish to colourless amphibole. This replacement occurs as either an apparently gradational front along grain boundaries (Figure 4.4A) and as a relatively high-temperature replacement within amphibole grains (Figure 4.5F). In TA17, a pale-blue amphibole occurs as an overgrowth on a dark-brown grain (Figure 4.5E). Pale-green amphibole commonly occurs as intergrowths with epidote and as replacement product of garnet. The extent of replacement ranges from minimal to nearly complete (Figure 4.5A–D) .

The structurally lower epidote- and bimineralic amphibolites exhibit less extensive replacement textures. In general, the amphibole is in textural equilibrium with plagioclase and epidote (Figure 4.8). Sample TA53 contains some nice symplectic ingrowths of K-feldspar and epidote that have replaced amphibole and plagioclase (Figure 4.8C, D and F).

Representative amphibole compositions from each sample are presented in Table 4.3. Figure 4.9 presents all of the amphibole compositions plotted using the classification scheme of Hawthorne et al. (2012). Amphibole compositions from TA14, TA16 and TA51A, TA53 and TA94 display relatively little intrasample variation and aside from TA53, which is slightly less edenitic and plots in the hornblende field, are pargasitic. In contrast, amphibole in TA17, TA95, TA50, TA46 and TA103, display a range in compositions along a trend between pargasite and tremolite. Actinolitic amphiboles are generally lighter brown to pale-green replacement products after garnet, clinopyroxene, and darker amphibole. Thus, this trend is interpreted to reflect the incomplete retrograde overprinting of the more pargasitic amphibole. However, it is interesting that the relatively pale-green primary amphibole in the structurally lower

garnet-clinopyroxene-free samples also plot within the pargasite field.

Figure 4.10 presents mean amphibole compositions with distance from the peridotites. Amphibole compositions in TA17, TA46 an TA50 have been separated into populations corresponding to the dark-brown high-temperature amphibole, and light-brown to pale-green lower-temperature populations. Neither tschermakite nor the edenite component of darker-brown amphiboles display a correlation with structural distance below the peridotites. In contrast, both the tschermakite and edenite component of the pale-green amphibole display an inverse correlation with structural distance below the peridotites. The Ti wt.% of the pale-green retrograde amphibole in samples TA17, TA46, and TA50 is lower than the dark-brown amphibole in the corresponding sample. Titanium wt% is inversely correlated with structural distance from the peridotites, consistent with the transition from brown- to green-amphibole down the section. Experimental data has demonstrated that the TiO_2 content of Ca-amphibole is inversely correlated with temperature (Ernst and Liu, 1998). Thus, the amphibole compositions data indicate a gradual decrease in temperature with increasing distance from the peridotites of both the high-temperature and retrograde populations. The lower TiO_2 content of the more actinolitic amphibole populations of TA17, TA46, and TA50 is consistent with late-stage replacement.

4.3.5 Plagioclase

The modal abundance of plagioclase ranges from ∼5–30%. Discontinuous amphibole-rich and plagioclase-rich layers define the foliation. Plagioclase is variably altered to intergrowths of clinozoisite + albite and/or white-mica + albite, known as saussuritization and sericitization, respectively. Both types of alteration can occur in the same sample and it is common for the same grain of plagioclase to exhibit both types of alteration. In thin section, saussuritized plagioclase is spongy and dark brown to almost black whereas sericitized plagioclase is light and spongy. In some samples, plagioclase is also replaced by symplectic intergrowths of epidote with either albite or K-feldspar (Figure 4.5G and H). Plagioclase alteration is generally less extensive in the

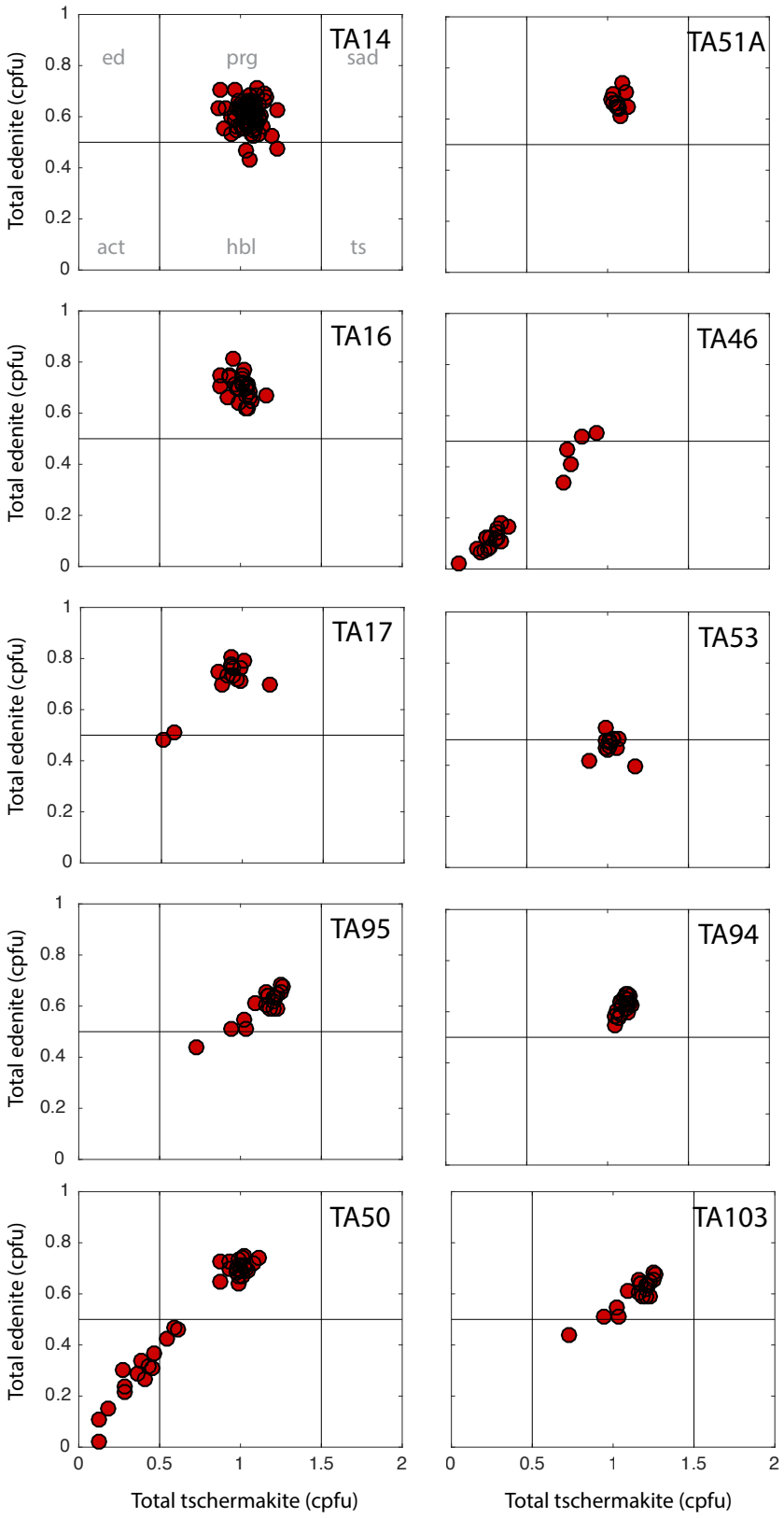


Figure 4.9: Amphibole compositions plotted as the total edenite component ($Na+K$ in the A site) against total tschermakite component ($Al+Fe^{3+}+Ti$ in the C) site after Hawthorne et al. (2012). Top right panel shows labels for edenite, pargasite, sadanagaite, actinolite, hornblende, and tschermakite.

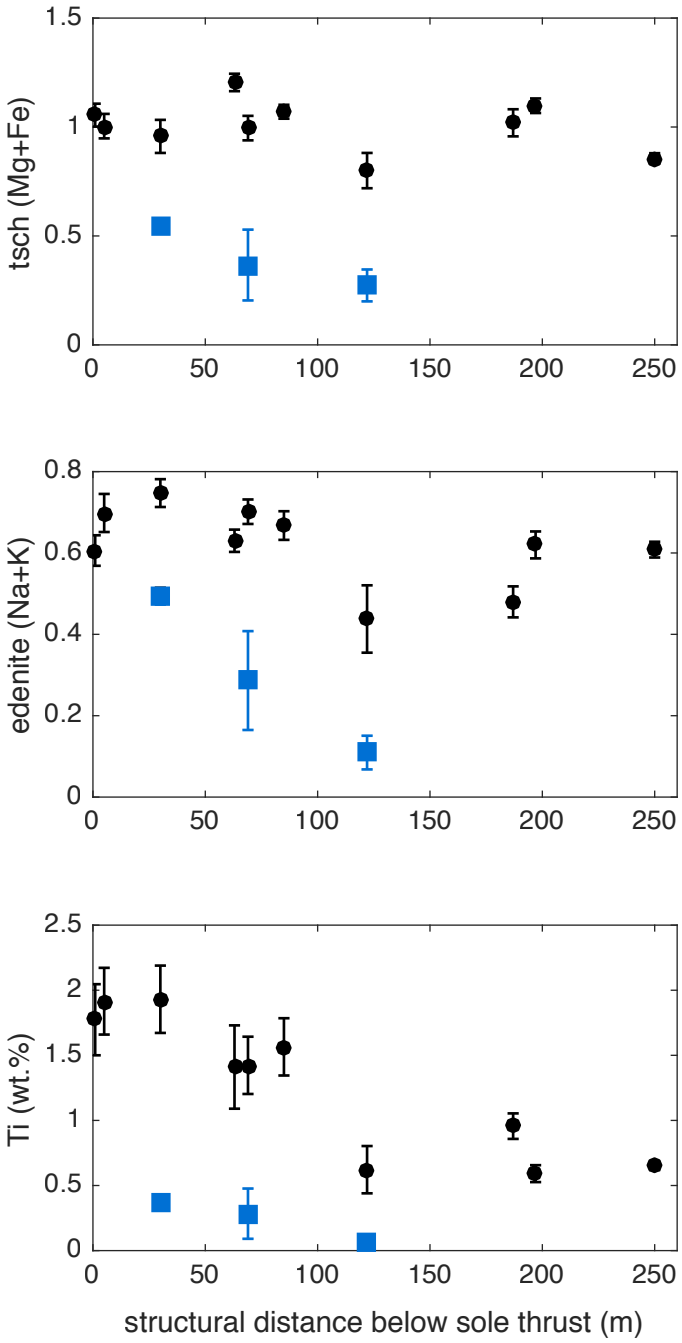


Figure 4.10: Mean amphibole compositions against distance below the peridotites. Error bars represent variation (1 σ) within a population and do not include analytical error. Blue squares are for pale green amphibole interpreted as retrograde.

structurally-lower, bi-mineral and epidote amphibolites.

Determining the plagioclase composition, and specifically the An content ($Ca/(Ca+Na+K)$), is necessary for thermobarometry and estimating bulk-rock composition for use in phase equilibria modelling. Also using samples from the Masafi sole, Cowan et al. (2014) demonstrated that even though the alteration disturbed Ca-Na-K ratios, the intergrowths retained the original Al-Si ratios. Cowan et al. (2014) found that there was less scatter in the compositions of saussuritized as compared to sericitized plagioclase, presumably reflecting a more open chemical system. From the Al-Si ratio, the original Ca-Na ratio can be recalculated. Following the method described by Cowan et al. (2014), we rastered regions of saussurite and based on the Al-Si ratios recalculated the original An content (Table 4.3). Samples TA51A and TA53 contain both fresh and altered plagioclase and therefore provide a test of the accuracy of the recalculation. The mean An of fresh plagioclase in TA51A and TA53 is $49 \pm 4\%$ and $44 \pm 3\%$, respectively, which is statistically indistinguishable for 44 ± 5% and 49 ± 3% for the saussurite regions. Thus, this method is also suitable for these samples.

Figure 4.11 presents the An content with distance from the sole thrust. An content from fresh plagioclase is presented in black, recalculated from saussurite in gray, and retrograde albite in blue. Note the overlap between fresh plagioclase and recalculated saussurite for samples TA51A (85 m) and TA53 (187 m). Aside from sample TA103, the An content of prograde plagioclase ranges between 36% and 52% and shows no correlation with structural position. Plagioclase in sample TA103, the structurally lowest sample, contains a considerably lower An content of only 20%. Retrograde plagioclase (ı.e., albite) in three samples has an An content of 7–8%.

4.3.6 Epidote

Epidote occurs in as an alteration product, a relict, vein material, or as part of the stable assemblage (Table 4.1). The modal abundance of epidote increases down section. In the epidote amphibolites (below ∼150 m) epidote is present as fine to coarse euhedral grains (Figure 4.8). Epidote commonly forms elongate grains that are parallel

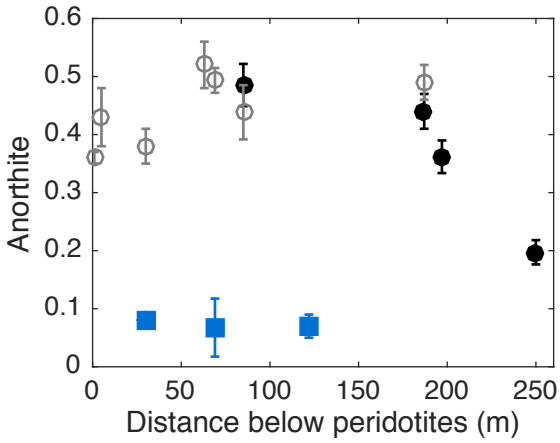


Figure 4.11: Anorthite content of plagioclase plotted against distance below peridotites for: fresh (black circles), recalculated saussurite (gray circles), and retrograde albite (blue squares). Error bars represent variation (1 σ) within a population and do not include analytical error.

to the foliation (Figures 4.8A and H). In garnet and clinopyroxene bearing samples, epidote occurs as: 1) a retrograde breakdown product of garnet, sometimes intergrown with green amphibole (Figure 4.5A–E), 2) monomineralic veins, 3) rare (presumably relict) grains trapped within amphibole, 4) as symplectic intergrowths with albite or K-feldspar replacing plagioclase (Figures 4.5G and H), and 5) as symplectic intergrowths with albite or K-feldspar replacing amphibole (Figures 4.8C, D, and F). In sample TA94, coarse epidote and amphibole grains occur within trondhjemitic leucosome, suggesting crystallization from melt. Epidote cores commonly exhibit higher birefringence, indicative of higher ferric iron.

4.3.7 Other minerals

Quartz is present in some of the samples and occurs as 1) coarse grains with plagioclase in leucosome, 2) as thin discontinuous layers between amphibole, plagioclase, and epidote, and 3) as fine grains within the matrix. All samples contain some combination of Ti-oxides in the form of titanite, ilmenite, hematite, rutile, titano-hematite, or pyrophanite. Rutile was most commonly observed in the cores of titanite grains. Ilmenite occurs as inclusions and along grain boundaries of of phases. Titanite is a common

inclusion and also occurs as a breakdown or exsolution product from ilmenite. Biotite occurs heterogeneously dispersed throughout TA103. In a few instances, chlorite was observed as an alteration phase. Carbonate occurs as rare veins. Apatite is a common accessory phase throughout the plagioclase-amphibole matrix and as inclusions within garnet. Zircon grains up to a few tens of microns in diameter are not uncommon. K-feldspar was observed as symplectic intergrowths with either epidote or clinozoisite in a few of the samples. Muscovite was present only as an alteration product of plagioclase.

4.4 Thermobarometry

Pressure and temperature estimates of all of the amphibolite samples were calculated using conventional and multi-equilibrium thermobarometry. Unlike phase equilibria models, these methods do not rely on estimating the bulk-rock composition, which, as discussed below (see Section 4.5), is problematic.

4.4.1 Amphibole-plagioclase thermometry

Table 4.4 presents new temperature estimates calculated with the Holland and Blundy (1994) calibration of the amphibole-plagioclase (edenite-tremolite) thermometer. Mean plagioclase compositions were used from both fresh and/or recalculated saussurite. Using the mean plagioclase compositions, a different temperatures was calculated for every amphibole. Thus, in Table 4.4, n equals both the number of amphiboles as well as temperatures calculated. The uncertainty does not include analytical or calibration error (typically ± 50) °C and only reflects the variation of amphibole composition within the population.

Table 4.4: Results from amphibole-plagioclase thermometry and garnet clinopyroxene thermometry. Two different calibrations for the garnet-clinopyroxene thermometer (Powell, 1985 and Ravna, 2000) are presented. For brevity, only temperatures from the Ravna (2000) are used in the text. The presented uncertainties are for variation within a population and do not include analytical error.

		Amp-Pl T (°C)			Grt-Cpx T (°C)			
Sample	meters to peridotite	Holland and Blundy (1994)	σ	n	Powell (1985)	σ	Ravna (2000)	σ
TA14	1	727	15	88	790	50	762	57
TA16	5	763	20	28	805	61	763	78
TA17	30	757	22	13	904	62	867	69
TA17	30	583		2				
TA95	63	804	23	15	823	59	770	70
TA50	69	764	17	21	795	62	746	67
TA50	69	534	53	15				
TA51A	85	780	16	11	733	67	693	73
TA46	122	-	-					
TA46	122	459	55	15				
TA53	187	678	11.7	13				
TA94	197	698	11.2	21				
TA103	250	645	4.2	13				

Calculated temperatures for pargasitic amphibole range between 645 °C, for the structurally lowest sample, and 804 °C from a garnet-clinopyroxene amphibolite near the top of the section. For three samples (TA17, TA50, and TA46), temperatures were calculated using the compositions from the actinolitic population with albite. As that the actinolitic amphibole compositions define a trend rather than a single population (Figure 4.9), the mean amphibole composition used for thermometry reflects some point along the cooling path. Thus, there is a large uncertainty associated with the temperature estimates as it is not possible to determine which plagioclase and amphibole were in equilibrium. Nonetheless, the results of 459–583 °C demonstrate the assemblage equilibrated at lower temperatures, consistent with the lower TiO_2 content and typical occurrence as replacement of dark-brown pargasitic amphibole.

Figure 4.12 presents the temperatures calculated from amphibole-plagioclase thermometry with respect to distance below the peridotites. Temperatures calculated from pargasitic amphibole form two distinct populations. The 6 samples nearest the peridotite record similar temperatures of between 727 and 804 °C and display no correlation with structural position. The 3 samples most distal from the peridotite record significantly lower temperatures of between 645 and 698 °C and also display no correlation with structural position.

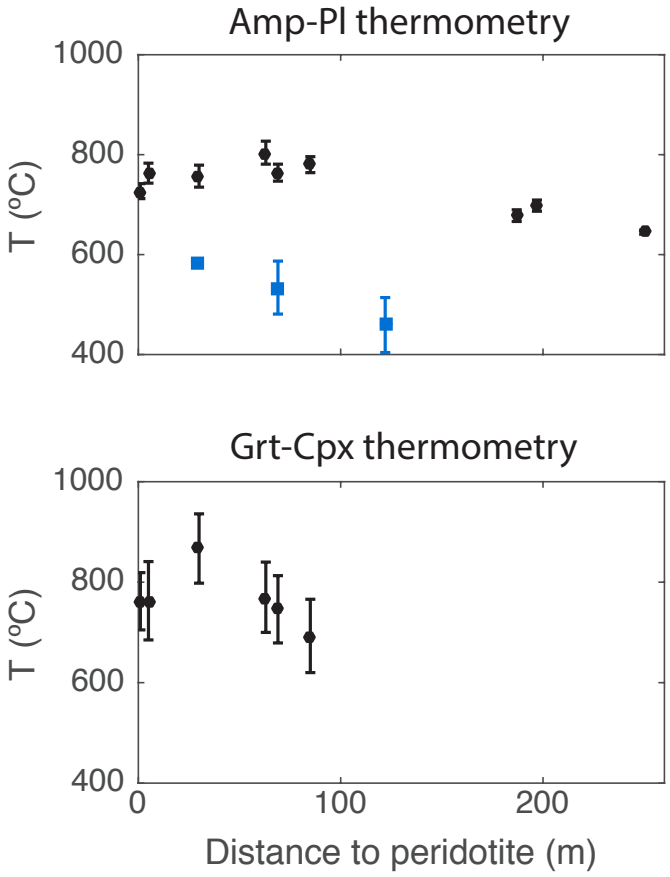


Figure 4.12: New temperature estimates from amphibole-plagioclase (Holland and Blundy, 1994) and garnet-clinopyroxene (Ravna, 2000) thermometry plotted against structural distance below the peridotites. Blue squares are calculated from retrograde amphibole and albite.

4.4.2 Garnet-clinopyroxene thermometry

Temperatures were calculated using both the Powell (1985) and Ravna (2000) calibrations of the garnet-clinopyroxene Fe^{2+}-Mg thermometer. The Powell (1985) calibration consistently calculated temperatures ∼20–50 °C higher than the Ravna (2000) calibration. For brevity, only temperatures from the Ravna (2000) calibration are discussed from here on. Fe^{3+} was calculated using the method of Droop (1987).To investigate the influence of analytical error on temperature estimates, a Monte Carlo simulation (n =100; 1% relative error on oxides) was applied to clinopyroxene and garnet compositions. Using the resulting compositions, calculated temperatures range between 693 ± 73 and 867 ± 69 °C and display no significant correlation with structural position (Figure 4.12). In most cases (aside from some retrograde rims and the prograde zoning of TA95) the influence of garnet zoning on temperature calculations is less than 20 °C.

4.4.3 Multi-equilibrium thermobarometry

Pressure-temperature conditions were further constrained from multi-equilibrium thermobarometry using Thermocalc (average-P and average-PT mode; Powell and Holland, 1994.) End-member activities were calculated from measured oxide wt% using the software-package AX (*www.esc.cam.ac.uk/research/research-groups/research-projects/tim-holland-softwarepages/ax*). Pure phases, such as titanite and quartz, were also included. All calculations included pure water as a fluid phase. Pressure-estimates from average-P were calculated using temperatures from either garnet-clinopyroxene or amphibole-plagioclase thermometry.

Table 4.5 and Figure 4.13 present the results from average-P and average-PT calculations. Samples TA46 and TA53 did not contain mineral assemblages suitable for generating sufficient equilibria and hence no pressures and temperatures were calculated. However, sample TA54 (a metasediment) was sampled immediately adjacent to TA53 and contains kyanite. Using the temperature of 678 ± 12 °C calculated with the amphibole-plagioclase thermometer for TA53, this suggests pressures of at least

7 kbar for TA54. Pressures and temperatures for the remaining samples fall within a fairly narrow range of 10–12 kbar and ∼800-900 °C. Estimated pressures and temperatures display no correlation with structural position (Figures 4.13A and B). Note that average-PT was only used to calculated temperatures for the garnet-clinopyroxene amphibolites.

Table 4.5: Results from average-P and average-PT. For garnet-clinopyroxene amphibolites, average-pressures were calculated using temperatures from both the Powell (1985) and Ravna (2000) calibrations. For samples the samples lacking garnet and clinoyproxene, pressures were calculated using temperature estimates from the amphibole-plagioclase thermometer of Holland and Blundy (1994). Samples TA46 and TA53 did not have mineral assemblages suitable for either average-PT and average-P.

			avPT (kbar, °C)				avP (kbar)						
sample	meters to peridotite	garnet association	P	σ	T	σ	P at H&B	σ	P at Powell	σ	P at Ravna	σ	no. of reactions
TA14	1	high-Ca core	11.1	2	839	78			10.3	1.4	9.9	1.5	7
TA16	5	high-Ca core	10.8	2.1	837	87			11.8	1.2	9.6	1.2	7
TA16	5	low-Ca rim	10.6	1.9	852	82			9.9	1.4	9.3	1.5	7
TA17	30	high-Ca core	11.6	1.3	853	82			12.1	0.8	11.8	0.8	7
TA17	30	low-Ca rim	12.2	1.3	906	84			12.1	0.8	11.8	0.7	7
TA95	63	high-Ca mantle	10.6	1.7	789	67			11.1	1.2	10.3	1.1	5
TA50	69	low-Ca rim	10.1	1	856	74			9.5	0.7	9.1	0.7	7
TA51A	85	high-Mg rim	11	0.9	832	53			10.2	0.9	9.9	1.0	8
TA46	122												0
TA53	187												0
TA94	197						9.8	0.8					1
TA103	250						10.3	0.9					1

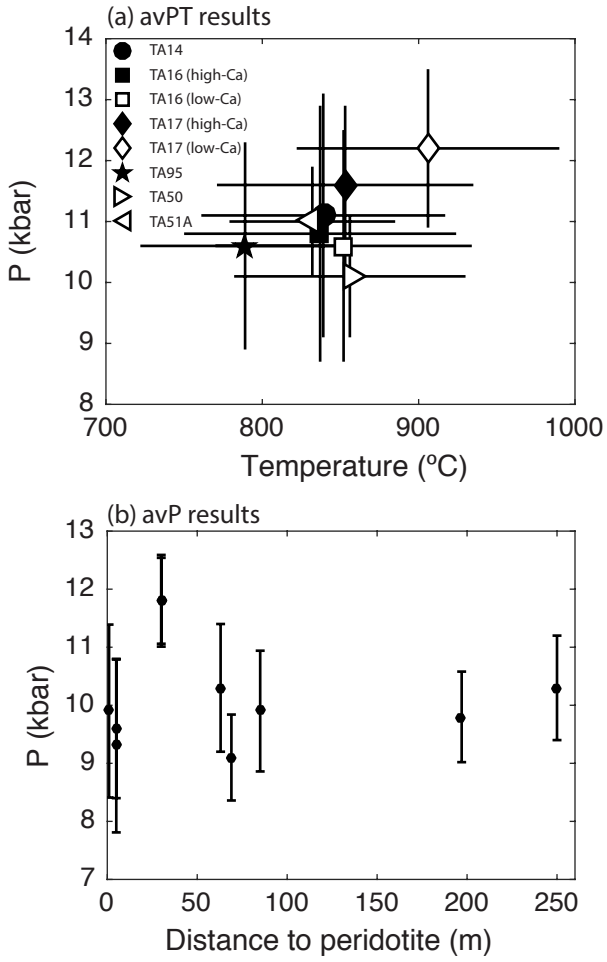


Figure 4.13: (a)Results of average-PT. (b) Estimated pressures (average-P) against distance from the peridotites using temperatures from garnet-clinopyroxene thermometry (garnet-clinopyroxene amphibolites) and amphibole-plagioclase thermometry (epidote- and bi-mineralic amphibolites).

4.5 Phase Equilibria Modelling

4.5.1 Model system and bulk rock composition

To further constrain the pressure-temperature and textural evolution of the sole, phase equilibria models (also known as pseudosections) were constructed for two garnet-clinopyroxene amphibolites (TA14 and TA95) and one epidote-amphibolite (TA46). Phase equilibria models were calculated in the system NCKFMASHTO using Thermocalc version 3.45 with dataset-62. The following activity-composition models were used: melt, amphibole, clinopyroxene (Green et al., 2016); epidote (Holland and Powell, 2011); ilmenite (White et al., 2000); garnet, muscovite, biotite, and chlorite (White et al., 2014); plagioclase (Holland and Powell, 2003). As TA14 and TA94 extend above the solidus, the augite (calcic) model was used (Green et al., 2016). For TA46, which equilibrated at lower-temperatures, the diopside (sodic-calcic) model produced better results (Green et al., 2016).

Modal mineral abundances were estimated by point counting on full slide scans (Table 4.6). Bulk compositions were estimated by integrating modal mineral abundances with mineral compositions measured from the electron microprobe (Table 4.7). For TA14, the garnet-clinopyroxene enclaves were omitted from bulk-rock calculations. For TA14 and TA95, a water content was selected that saturated the solidus at the pressure of interest. Water was set to excess for TA46.

Table 4.6: Modal mineral abundances (area %) used for calculating bulk-rock composition.

Sample	Grt	Amp	Cpx	Pl	Ti-oxide	Ep
TA14	3	49.8	13	33.2	1	0
TA46	0	46.6	0	5.4	0.5	47.9
TA95	3	47.5	0.2	48.4	0.9	0

4.5.2 Uncertainty in phase equilibria models

Phase equilibria models are affected by random and systematic error (see Palin et al. (2015) and references therein for a review). The most important systematic error relates

Table 4.7: Bulk-rock compositions used for phase diagram construction (mol.% oxide).

Sample	H_2O	SiO_2	Al_2O_3	CaO	MgO	FeO	K_2O	Na_2O	TiO_2	O
TA14	4.8	47.7	9.4	12.5	10.1	9.9	0.2	3.3	1.4	0.6
TA46	excess	47.1	9.2	19.6	11.1	9.2	0.1	0.8	0.2	2.8
TA95	5.2	47.1	13.1	13.7	8.2	7.8	0.4	2.8	1.0	0.9

to uncertainties in (1) activity-composition relationships and (2) thermodynamic data (Worley and Powell, 2000). Systematic error is applied evenly to multiple samples with the same mineral assemblage. Thus, if the same activity-composition models and thermodynamic dataset are used, the relative errors should be small (Worley and Powell, 2000). In contrast to systematic error, random errors influences the relative calculations between samples. The most important source of random error arises from estimating the bulk rock composition (Stuwe, 1997; Palin et al., 2015).

For the samples modelled below, selecting the water content is particularly problematic as there is evidence for both dehydration on the prograde path (i.e., granulite formation), and rehydration (i.e., retrogression of the granulite-facies assemblage) on the retrograde path. In other words, the water content contained in hydrous phases does not reflect peak conditions, but rather more hydrous conditions somewhere along the retrograde path. Thus, the water-content calculated from hydrous-phases will tend to overestimate the amphibolite-facies overprint at the expense of the granulite-facies peak assemblage. Another source of geological error results from sampling bias, and in particular the tendency to select samples and thin sections with the largest garnet-clinopyroxene enclaves (Forshaw, 2017). This represents a trade off between having garnet available for thermobarometric calculations, and calculating a bulk composition from a representative sample. This is especially true for the structurally lower garnet-clinopyroxene amphibolites, where garnet is sparse. An added complication is that the garnet-clinopyroxene enclaves were stronger and therefore less deformed and less likely to retrogress, thereby preferentially preserving the granulite-facies assemblage in more Fe-Mg rich domains (Forshaw, 2017). Thus, in practice the enclaves have not only a distinct assemblage, but also a different bulk composition. Nonetheless, with

these caveats in mind, phase equilibria models can provide context and aid in the interpretation of textures.

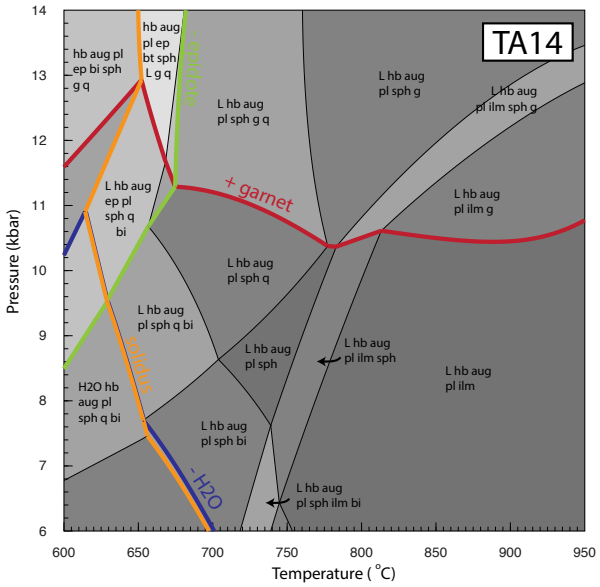
4.5.3 Results and discussion

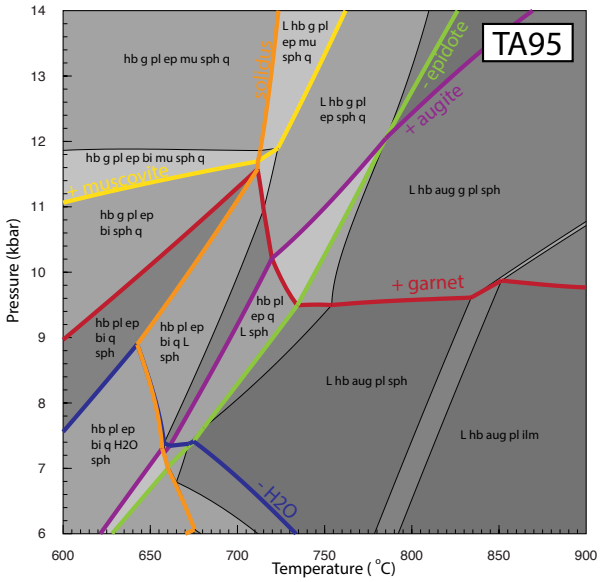
The pseudosections for TA14 and TA95 exhibit similar topologies characterized by a steep solidus (∼600–700 °C), and a nearly horizontal garnet-in line between ∼10.5–13 kbar for TA14 and slightly lower pressures of ∼9–11 kbar for TA95 (Figure 4.14). Clinopyroxene is predicted to be stable across the entire pressure-temperature range for TA14. In contrast, the clinopyroxene-in line for TA95 has a positive slope that cuts across the centre of the pressure-temperature range. This is consistent with the higher observed modal abundance of clinopyroxene in TA14 (13%) as opposed to less than 1% for TA95 (Table 4.6). A suprasolidus epidote-bearing assemblage is predicted for both TA14 and TA95. Ti-oxides are only present in low quantities (observed and calculated) and thus their predicted stabilities are not suitable for constraining pressures and temperatures. A similar argument can be made for the small amount of quartz predicted in each of the pseudosections.

The observed assemblage for TA14 and TA95 falls in the top right (high-PT) quadrant of the pseudosection. As with most of the garnet-clinopyroxene amphibolites, no evidence of melting is preserved in either TA14 nor TA95. However, given the consistently high-temperature estimates it is likely that some fraction of partial melt was present at peak temperatures, as predicted by the pseudosections. The garnet-in line provides a minimum estimate for peak pressures of TA14 and TA95. For TA14, minimum estimate on peak-temperature is constrained by the appearance of epidote at ∼675 °C. The occurrence of epidote included in dark-brown amphibole, and interpreted as relict, suggest that an earlier assemblage was not completely overprinted during prograde metamorphism. For TA95, the augite-in and epidote-out lines indicate temperatures above ∼740–870 °C, depending on pressure. Given these temperature constraints, the occurrence of garnet indicates peak-pressures in excess of ∼10.5–11.5 kbar for TA14 and ∼9.5 kbar for TA95. Thus, both pseudosections, and the corre-

sponding observed assemblage, are in general agreement with pressure-temperature estimates from conventional and multi-equilibrium modelling.

The pseudosection for TA46 is generally characterized by steep lines, reflecting the difficulty in pressure determinations (Figure 4.14). A minimum temperature of ∼475 °C is constrained by the chlorite-out line. Clinopyroxene, which was not observed in this sample, is predicted to be stable at temperatures above ∼500 °C, which seems unreasonably low and may reflect the tendency of the activity-composition models to overestimate the Al-content of amphibole (Forshaw, 2017). However, it may also result from the relatively high-Ca content of the bulk composition, potentially the result of Ca enrichment of a pillow margin (Holland, 1979). A very small amount ($< 0.01\%$) of biotite is predicted in all the fields, presumably accounting for the K_2O in the bulk. Actinolite and hornblende are predicted to coexist across a temperature interval of ∼100 °C, consistent with the range of measured amphibole compositions in this sample (Figure 4.9), though not necessarily indicative of a miscibility gap (e.g., Grapes and Graham, 1978). The maximum temperature for TA46 is best constrained by the disappearance of actinolite at ∼550 °C. Thus, the equilibrium assemblage falls somewhere around 500 °C. For comparison, a temperature of 459 ± 55 °C was calculated with the amphibole-plagioclase thermometer (Table 4.4). This slightly lower-temperature does not include compositions from the pargasitic amphibole, which would be expected to return higher temperatures.


TA14
hb aug pl ep bt sph L g q
hb aug pl ep bi sph g q
- epidote
L hb aug pl sph g q
L hb aug pl sph g
L hb aug pl ilm sph g
+ garnet
L hb aug ep pl sph q bi
L hb aug pl ilm g
L hb aug pl sph q
L hb aug pl sph q bi
- biotite
L hb aug pl sph
L hb aug pl ilm sph
L hb aug pl ilm
H2O hb aug pl sph q bi
L hb aug pl sph bi
- H2O
L hb aug pl sph ilm bi
Pressure (kbar)
Temperature (°C)


TA95
hb g pl ep mu sph q
- solidus
L hb g pl ep mu sph q
- epidote
+ augite
L hb g pl ep sph q
hb g pl ep bi mu sph q
+ muscovite
L hb aug g pl sph
hb g pl ep bi sph q
+ garnet
hb pl ep q L sph
hb pl ep bi q sph
hb pl ep bi q L sph
L hb aug pl sph
hb pl ep bi q H2O sph
L hb aug pl ilm
- H2O
Pressure (kbar)
Temperature (°C)

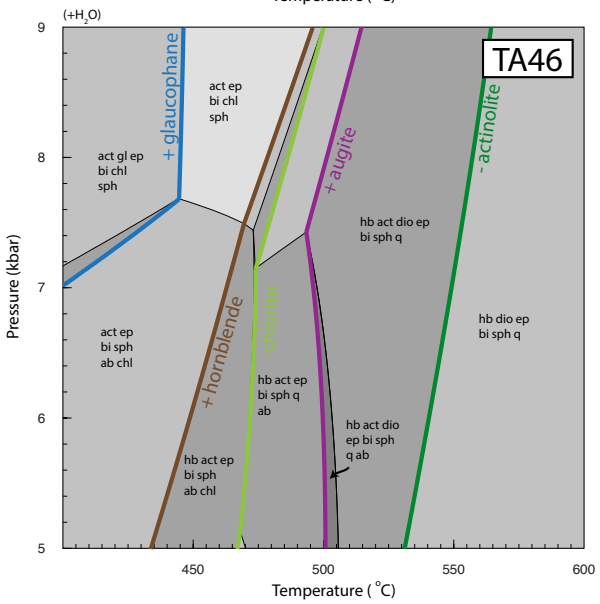

(+H2O)
TA46
+ glaucophane
act ep bi chl sph
act gl ep bi chl sph
+ augite
- actinolite
hb act dio ep bi sph q
+ hornblende
- chlorite
hb dio ep bi sph q
act ep bi sph ab chl
hb act ep bi sph q ab
hb act dio ep bi sph q ab
hb act ep bi sph ab chl
Pressure (kbar)
Temperature (°C)

Figure 4.14 ***(preceding page)*****:** Pressure-temperature pseudosections for two garnet-clinopyroxene amphibolites (TA14 and TA95) and an epidote amphibolite (TA46). Panels are organized according to structural position. Clinopyroxene is labelled according to the model used (see text for explanation). Amphibole is separated into actinolite (act), hornblende (hb), and glaucophane (gl).

4.6 Discussion

4.6.1 Metamorphic conditions

Pressure-temperature conditions of garnet-clinopyroxene amphibolites from the Oman-UAE metamorphic sole are consistently estimated to be ∼10–12 kbar and ∼700–900 °C (e.g., Searle and Malpas, 1980; Ghent and Stout, 1981; Hacker and Mosenfelder, 1996; Gnos, 1998; Cowan et al., 2014; Soret et al., 2017). Unsurprisingly the results presented above fall within this range. What is surprising, though, is the thickness over which these conditions occur at Masafi, and the lack of pressure and temperature gradients.

The structurally lowest garnet-clinopyroxene amphibolite sample (TA51A) is from 85 m beneath the peridotites (Figure 4.2). The Ravna (2000) calibration of the garnet-clinopyroxene thermometer returned a temperature of 693 ± 73 °C, which is statistically indistinguishable from all but one of the structurally higher samples (Figure 4.12). An even higher temperature of 832 ± 53 °C was calculated with average-PT (Table 4.5). In addition to the occurrence of garnet and clinopyroxene, the high temperature calculated for TA51A is supported by the presence of tonalitic melt pods and (peritectic?) skeletal garnet that indicate temperatures were sufficient for fluid-present melting (Figure 4.4C). For TA51A, Average-P and average-PT returned pressures of 9.9 ± 1.0 and 11 ± 0.9 kbar, respectively, consistent with the presence of garnet.

Partial melting was not limited to the garnet-clinopyroxene amphibolites. Surprisingly, evidence for the most extensive partial melting was not observed near the peridotites, but nearly 200 m below at the sample locality of TA94 (Figure 4.3C). Sample TA94 is a fine-grained epidote-amphibolite with abundant tonalitic melt pods that pinch and swell up to several cm in size (Figures 4.8B, G and H). A temperature of 698 ± 11.2 °C was calculated for TA94 with the amphibole-plagioclase thermometer. Although a pseudosection was not constructed for TA94, the pseudosection for TA95 predicts a melt-bearing, garnet- and clinopyroxene-free field around 9 kbar and 675 °C (Figure4.14).

Pressure-temperature gradient of the sole

The sole clearly exhibits an inverted pressure-temperature gradient over several kilometers. However, determining the precise values of the gradient and whether pressures and temperatures decrease linearly, exponentially, or stepwise has proven difficult. Gnos (1998) suggested a temperature gradient between 1000–4000 °C/km, but stated that these estimates are statistically insignificant. Hacker and Mosenfelder (1996) suggested that although on average the temperature gradient is ∼1000°C/km, the decrease is exponential, with temperatures decreasing by > 4000 °C/km across the uppermost sole.

Along the Masafi transect, the highest temperature calculated with the Ravna (2000) calibration of the garnet-clinopyroxene thermometer was 867 ± 69 °C for sample TA17, located 30 m below the peridotites. A temperature of 645 ± 4 °C was calculated for sample TA103, which was was collected at 250 m below the peridotite. These values result in an average gradient of ∼900 °C/Km over 250 m. If the slightly higher temperature of 904 ± 62 °C from the Powell (1985) calibration of the garnet-clinopyroxene thermometer is used, the estimated gradient is ∼1000 °C/km.

These temperature gradients discussed are averages across the 250 m transect. Our data, however, reveal two distinct populations. Temperatures calculated for garnet-clinopyroxene amphibolites, from both the amphibole-plagioclase and garnet-clinopyroxene thermometers, display no significant correlation with structural position (Figures 4.12 and 4.13). In the epidote and bi-mineralic amphibolites, the calculated temperatures also show no correlation with structural position, but are significantly lower than the garnet-clinopyroxene amphibolites. As discussed above, the standard deviation on these temperatures was calculated from the population without considering analytical error or error in the calibration. The combined error is typically thought to be about ±50 °C. Considering this, the calculated temperatures for epidote and bimineralic amphibolites are indistinguishable from each other, and although generally lower are also indistinguishable from the garnet-clinopyroxene amphibolites. Nonetheless, as analytical and calibration error is systematic, and thus affects the different analysis equally, the epidote and bimineralic amphibolites do seem to record lower

temperatures.

Pressures calculated from multi-equilibrium thermometry (average-P and average-PT) range between $\sim 10-12$ kbar and exhibit no significant correlation with structural position (Table 4.5 and Figure 4.13). Thus, although the amphibolites exhibit a temperature gradient, there is no significant pressure gradient for at least 250 m. The lack of garnet in the structurally lower part of the transect is the result of lower temperatures rather than pressures, as is perhaps more intuitive.

The pressure and temperature trends (or lack thereof) are consistent with clinopyroxene and amphibole compositions that exhibit no correlation with structural position (Figure 4.10A, B and 4.7). However, it is interesting that the Ti-component of amphibole displays an inverse correlation with distance from the peridotites, consistent with a thermal gradient (Figure 4.10C; Ernst and Liu, 1998). Thus, it seems reasonable to assume a small thermal gradient beyond the resolution of the empirical thermometers.

4.6.2 Thickness of the garnet-clinopyroxene amphibolites

Previous studies from other localities have described a much thinner extent of garnet, clinopyroxene, and partial melting. Ghent and Stout (1981) and Hacker and Mosenfelder (1996) reported garnet within a few metres of the peridotite contact and sporadic clinopyroxene up to 80 m below the peridotites at Wadi Tayyin and Jebel Sumeini. Cowan et al. (2014) reported a slighly thicker sequence of 10 m of garnet-clinopyroxene bearing amphibolites at Wadi Tayyin and Sumeini. Cowan et al. (2014) also noted the occurrence of melt-pods within a few metres of the peridotite contact at Tayyin, but as far as 30 m down section at Sumeini. Gnos (1998) reported a thickness of 70 m for garnet bearing amphibolites at the Wadi Khubakhib locality, a small window to the west of the Masafi window. Along the same transect clinopyroxene, was limited to the uppermost 40 m. Soret et al. (2017) reported the distribution of garnet and clinopyroxene from Sumeini and Wadi Khubakhib. Soret et al. (2017) describe garnet within 35 m and clinopyroxene within 55 m of the peridotite at Sumeini, whereas at Wadi Khubakhib, garnet was observed within the top 70 m, and clinopyroxene within

the top 28 m.

The 85 m section of garnet-clinopyroxene amphibolites and correspondingly high pressure-temperature conditions that we have documented at Masafi is considerably thicker than any other locality of the sole. Here, we discuss several possibilities that can explain why this section is anomalously thick.

The influence of bulk rock composition on the distribution of garnet and clinopyroxene

To some extent, the occurrence of garnet and clinopyroxene is controlled by intersample variation in the bulk-rock composition. An example is the shift of the clinopyroxene-in line to higher temperature for the relatively aluminous sample TA95 (Al_2O_3 = 13.1%) as opposed to TA14 ($Al_2O_3 = 9.4\%$). The influence of Al concentration can be visualized with an ACF-ternary diagram (Figure 4.15). A more aluminous bulk-rock composition plots further from the bottom (C–F) edge along which clinopyroxene lies and is thus (for the same pressures and temperatures) expected to contain a lower modal abundance of clinopyroxene. Similarly, more Fe^{2+}–Mg rich samples plot nearer the composition of garnet. Ishikawa et al. (2005) reported bulk-rock compositions for 25 amphibolite samples from Wadi Tayyin, spanning from 0 to >255 m below the peridotite. The Al_2O_3 content of these, which ranges from 13–21%, are relatively aluminous compared to the 3 samples from Masafi for which bulk rock data is available (Figure 4.15). However, even the sample with 21% Al_2O_3, located immediately beneath the peridotite, contains clinopyroxene. Yet, other samples from the same structural level that contain both garnet and clinopyroxene have as little as 14% Al_2O_3. Figure 4.15 also presents the bulk-rock composition of mostly garnet-free amphibolites from Gnos (1998). Although variations in bulk-rock composition can explain some of the sporadic occurrence of garnet and clinopyroxene, it is insufficient to account for the lack of garnet beyond the upper most few metres of the sole at Wadi Tayyin. The appearance of greenschist minerals such as epidote, chlorite, albite, and actinolitic amphibole at distances much nearer the peridotites at the other sole localities clearly

indicate a lower-grade assemblage.

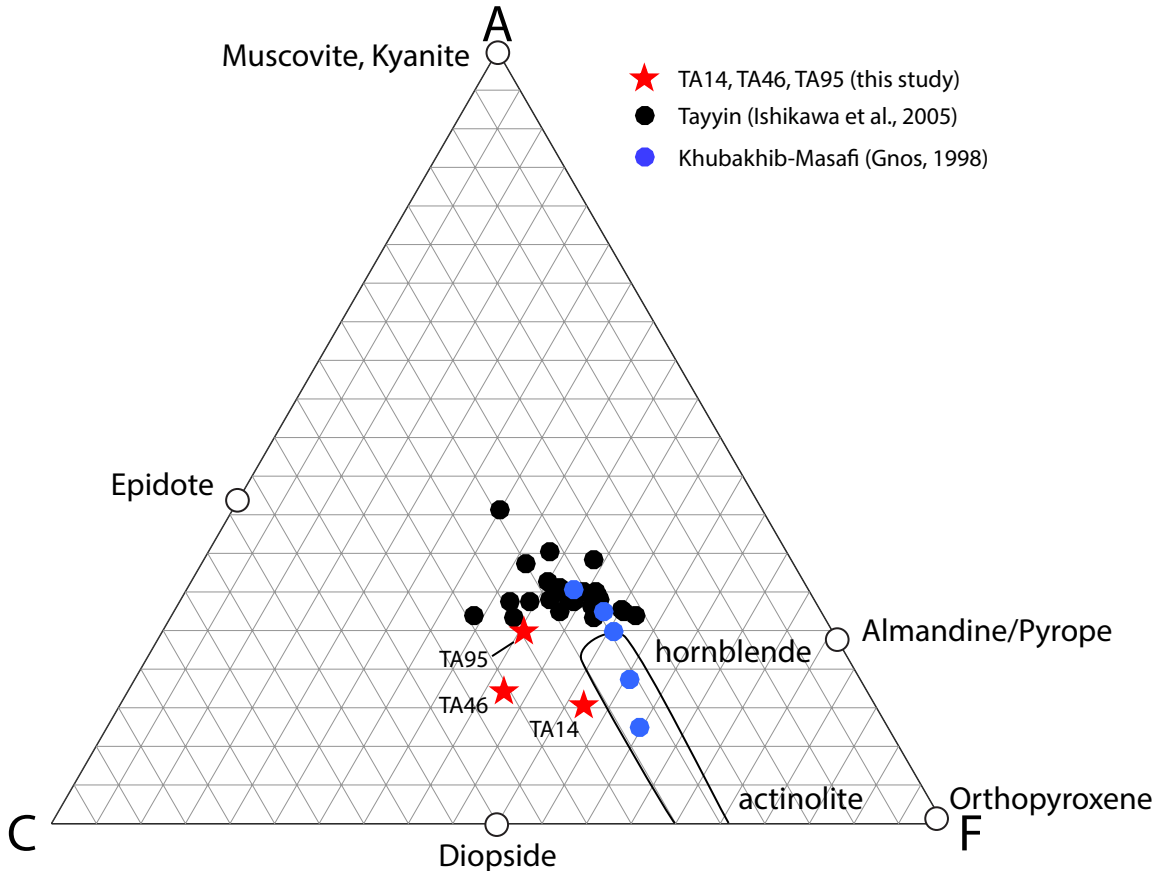


Figure 4.15: ACF ternary diagram displaying bulk-rock compositions from this study, Ishikawa et al. (2005), and Gnos (1998). As the Fe^{2+}/Fe^{3+} ratio is unknown, $F = Fe^{total} + Mg$ and $A = Al2O3 - Na_2O + K_2O$). Thus, A is slightly underestimated and F overestimated. $C = CaO - 3.33P_2O_5$

.

Structural controls on thickness

Another possible explanation for the large thickness of high-grade amphibolites across the described transect is that the section has been structurally thickened by late imbricate faulting. Based on mapped fabric discordances, Cowan et al. (2014) proposed that the sole at Wadi Tayyin and Sumeini had been imbricated. Interestingly, both of these localities have a relatively thin package of garnet-clinopyroxene amphibolites. Based on petrological and pressure-temperature discontinuities, Soret et al. (2017) interpreted several ductile shear zones within the sole at Sumeini, Wadi Tayyin, and Khubahib, although there was no field evidence to support their existence. Hacker and Mosenfelder (1996) noted that at Wadi Tayyin and Sumeini, the sole is only rarely cut by faults that exhibit no more than 10s of metres of offset. Similarly, only minor faults were identified through detailed mapping at Masafi. It is possible that the metamorphic sole at other localities has undergone a higher-degree of attenuation. To some extent the metamorphic sole has been either dismembered or was heterogeneously constructed, as demonstrated by patchy distribution of amphibolites along the margin of the Masafi window; it is not uncommon for peridotite to directly overly the metasediments. In general though and at all of the sole localities, amphibolites lie immediately beneath the peridotite. In contrast to the amphibolite section, the dominantly metasedimentary sole is intensely folded and has been structurally thickened, though at what pressure-temperature conditions is unknown.

4.6.3 Retrogression of the amphibolites

As discussed in section 4.3, all of the garnet-clinopyroxene amphibolites have been partially retrogressed. Textural evidence indicates progressive retrogression along the return path from granulite to greenschist facies. During cooling through amphibolite-facies temperatures, garnet was replaced by epidote (Figures 4.5A–D) and clinopyroxene was replaced by pargasitic dark brown Ti-rich amphibole (Figures4.4D and F). As cooling continued through epidote-amphibolite and down to greenschist temperatures,

dark-brown amphibole was replaced by pale-green to colourless Ti-poor actinolitic amphibole. Initially, temperatures were sufficient for direct replacement within the lattice of the higher-T amphibole (Figure 4.5F). At lower temperatures, the replacement of the dark-brown amphibole was restricted to grain boundaries (Figures 4.4D, 4.5C and 4.5E). In some instances, pale-green amphibole was replaced by intergrowths of epidote and K-feldspar (Figure 4.8C). At similar conditions some of the clinopyroxene was also replaced by actinolitic amphibole and garnet was replaced by epidote-actinolite intergrowths (Figure 4.5A–E). Throughout the cooling path, plagioclase was replaced by saussurite, albite, sericite, and epidote. Chlorite was only identified in a few thin sections, though at the nearby Khubakhib window Gnos (1998), noted chlorite pseudomorphs of garnet.

At Wadi Tayyin and Sumeini, Hacker and Mosenfelder (1996) noted an up-section increase in greenschist facies minerals and inferred the retrogressive fluids originated in the overlying mantle wedge. At Masafi, the extent of retrogression of the garnet-clinopyroxene amphibolites does not correlate with structural position. However, the epidote- and bimineralic-amphibolites are less retrogressed and appear to be in textural equilibrium. This suggests that the retrogressive fluids were in equilibrium with these lower-grade rocks but not the garnet-clinopyroxene amphibolites. Thus, the fluids that retrogressed garnet-clinopyroxene amphibolites likely originated from lower-grade amphibolites and metasedimentary rocks beneath. As discussed in Chapter 3 and in more detail below, these same fluids also infiltrated and metasomatised the overlying mantle wedge,

Though no correlation was observed with structural position, the extent of regression varies considerably. The common occurrence of symplectites in some of the amphibolites at Masafi (Figures 4.5 and 4.8) indicate that, for these samples, hydration was limited. At the same time, however, there is also evidence for hydration not just within the uppermost sole but also for hydration of the mantle wedge, as discussed in Chapter 3. This suggests that fluid flow through the metamorphic sole was channelized, as was also inferred for the mantle wedge (Chapter 3; Plümper et al., 2016).

The key question that arises is: how extensive was the granulite-facies assemblage prior to retrogression? Granulites have been described from other sole localities, such as the Bay of Islands ophiolite (Malpas, 1976; Dewey and Casey, 2013) and St Anthony Complex (Jamieson, 1980) in Newfoundland. Cowan et al. (2014) first raised the possibility that the higher-grade parts of the Oman-UAE metamorphic sole may have been granulites (i.e., dominated by garnet and clinopyroxene), rather than just amphibolite with sporadic garnet and clinopyroxene. Using garnet-core and clinopyroxene compositions, Cowan et al. (2014) calculated pressures several kbar higher when amphibole was excluded from the equilibrium assemblage—as opposed to most previous studies that assume amphibole was stable at peak metamorphic conditions. Unfortunately, because of the high error in the calculations, the difference in pressure was not statistically significant. The observation that the highest-temperature amphibole wraps around the garnet-clinopyroxene enclaves requires that much of the amphibole postdates peak conditions (Figures 4.4A and B). The rarity of amphibole inclusions in garnet further supports the hypothesis that amphibole was uncommon at peak. Thus, it seems reasonable that at peak conditions the upper part of the sole was dominantly garnet, clinopyroxene, and plagioclase with only minor amphibole. The best glimpse into the rock prior to retrogression is provided by the larger enclaves such as in TA122 (Figures 4.4A and G).

We considered the possibility that the inverted temperature gradient and the small thickness of garnet-clinopyroxene amphibolites at other localities resulted from variable degrees of retrogression. In other words, thick sections of garnet-clinopyroxene amphibolites (e.g., Masafi) underwent relatively little retrogression compared to thinner sections (e.g., Wadi Tayyin). Thus, the metamorphic field gradient could simply reflect a balance between prograde metamorphism from the overlying mantle wedge, and retrograde reactions driven by fluid released from the under-plated metasediments. This is unlikely though given the textural equilibrium exhibited by the lower amphibolites and a lack of evidence for an earlier higher-grade history.

4.6.4 Fabric evolution in the amphibolites

Textural evidence reveals 3 main stages of fabric development in the garnet-clinopyroxene amphibolites. During burial, the amphibolites would have developed a schistose–gneissic foliation, similar to the epidote- and bimineralic-amphibolites (e.g., Figures 4.3C, F and 4.8). This early prograde foliation was subsequently destroyed during granulite formation. Thus, the amphibolites must have reached sufficiently high-temperatures for a long enough time and with limited strain to the erase foliation. The amphibolite-facies gneissic foliation, defined by the modal abundance of plagioclase and dark-brown amphibole, wraps around and hence post-dates the garnet-clinopyroxene enclaves. In other words, the dominant foliation exhibited by the garnet-clinopyroxene amphibolites must be retrogressive.

During exhumation and cooling, garnet acted as a mechanical barrier that limited the amount of deformation and thus retrogression. This explains why the best preserved clinopyroxene is typically associated with garnet. There is, however, also evidence of pervasive retrogression despite the presence of garnet. A nice example is presented in Figures 4.5A and B, which shows two different garnets in sample TA50. In this sample, as with the others, clinopyroxene occurs as inclusions in garnet indicative that it was previously abundant. There is no evidence of clinopyroxene in the matrix, which has been pervasively retrogressed to dark-brown amphibole and, at lower-temperatures, fine-grained epidote, pale-green amphibole, and albite. With more time and/or fluids, the garnet would be completely replaced and the evidence of a former higher-grade assemblage lost. Fe-Mg rich layers would tend to have more garnet and thereby preferentially preserve the granulite facies mineral assemblage. As noted in Section 4.5.1, this tendency to preserve the granulite-facies assemblage in Fe-Mg rich domains leads to uncertainty in calculating the bulk-rock composition and ultimately phase equilibria modelling.

4.6.5 Tectonic implications

Granulite formation (i.e., the crystallization of garnet and clinopyroxene and the destruction of the earlier fabric) and the subsequent rehydration of the metamorphic sole has implications for burial, accretion, and exhumation. We have demonstrated that the extent of granulite formation has likely been underestimated. As pointed out by Cowan et al. (2014), the amphibolite facies assemblage commonly used to infer peak pressures and temperature lies along on the decompression path. Thus, the depths at which the metamorphic sole accreted may be underestimated by several kbar (Cowan et al., 2014). The key questions and the focus of this section, however, regard the influence of granulite formation on accretion and subsequent exhumation of the sole.

Previous models for sole accretion

Models for accretion of the sole to the base of the ophiolite involve relative changes in the rheological properties across the subduction interface (Hacker, 1990b, 1991; Agard et al., 2016), though what controls the rheological properties of the mantle wedge and downgoing slab remains unclear. Hacker (1990b, 1991) proposed that following subduction initiation, displacement is initially limited to peridotite at the base of the mantle wedge. As the isotherms relax, the mantle wedge peridotite cools and strengthens, and the slab heats and weakens. This causes displacement to progressively localize towards the base of the mantle wedge and, at some critical temperature, eventually migrate down into the slab, thus accreting the sole (Hacker, 1990b, 1991).

Agard et al. (2016) presented a model similar to Hacker (1990 and 1991), but with several key differences (also see Plunder et al., 2015 and Soret et al., 2017). In the model of Agard et al. (2016), the metamorphic sole is accreted at about twice the depth of Hacker (1990b, 1991). Until the discovery of kyanite bearing amphibolites by Gnos (1998), it was thought that pressures did not exceed 0.6 GPa. Agard et al. (2016) also considered the weakening effect of serpentinization in the mantle wedge. Agard et al. (2016) proposed a four-stage model based on rheological coupling to explain the accretion of metamorphic soles during nascent subduction. (1) Below ∼400 °C, the

mantle wedge is serpentinized and therefore weaker than the downgoing slab. The slab and mantle are uncoupled and strain localizes at the slab-mantle interface. (2) Further down-dip, increasing temperatures destabilize serpentine and strengthen the mantle wedge peridotites, whereas continued heating of the slab causes it to weaken. At ∼800 °C, the viscosities of the slab and the mantle wedge intersect and the locus of highest strain rate migrates into the slab, which causes a slice of the slab to detach and accrete (i.e., underplate) to the base of the mantle wedge. It is this detached slice that becomes the high-temperature (granulite and amphibolite) metamorphic sole. High-temperature metamorphic soles are mostly mafic material, indicating that there was little sediment cover during the earliest stages of subduction. (3) As the subduction zone evolves, the mantle wedge cools, the depth of serpentinization deepens, and an increasing amount of sediment reaches the trench. The metamorphosed sediments are initially stronger than the serpentinized mantle wedge and strain is localized at the contact between the two. With increasing depth, the mantle becomes less serpentinized and stronger, while the metasedimentary rock become hotter and weaker. At ∼600 °C the mantle peridotites and metasedimentary rocks have a similar rheology, which causes the subduction interface to deepen and accrete the low-temperature (greenschist) sole to the base of the mantle wedge. (4) At depths below the detachment of the high-temperature sole, the slab and mantle remain uncoupled. Agard et al. (2016) also note that the role of coupling explains why accretion and/or exhumation is limited to the onset of subduction. As the subduction-zone cools and a steady-state thermal structure is established, serpentinization extends to greater depths and a rheological contrast is preserved that prevents coupling (Agard et al., 2016).

Granulite formation as a mechanism for sole accretion

Previous models for sole accretion have not considered the influence of metamorphic reactions in the rheological evolution of the slab. This is likely due to (1) the paucity of data from experimentally deformed metabasites (e.g., Hacker and Christie, 1990; Rushmer, 1995; Soret et al., 2016), and (2) the assumption that granulite formation

was limited to small enclaves. It is remarkable that the highest-grade portions of most metamorphic soles record similar pressure-temperature conditions of 10–12 kbar and 700–900 °C (see Figure 2 of van Hinsbergen et al. (2015) and Figure 3 of Agard et al. (2016)). Previous models for sole accretion invoke a critical viscosity reduction in the downgoing slab and concomitant viscosity increase in the mantle wedge. In the models of Hacker (1990b, 1991) this was the result of the influence of temperature on flow-laws, while Agard et al. (2016) also considered the degree of serpentinization in the mantle wedge. Here we propose that accretion was controlled by granulite formation and strengthening of the downgoing slab(Figure 4.16).

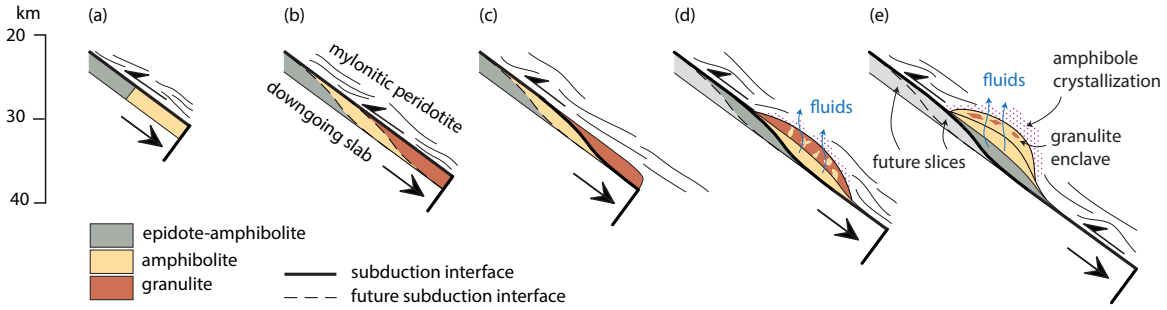


Figure 4.16: Schematic tectonic evolution of the metamorphic sole through time. (a) Following subduction initiation, mafic igneous rocks and interlayered deep-sea sediments are buried to amphibolite facies P-T conditions. (b)Temperatures in the mantle wedge are initially hot enough for the upper-part of the slab to pass through granulite facies conditions. (c) Granulite formation and related strengthening caused the subduction interface to step down and accrete/underplate to the hanging-wall mantle. This initial slice is the garnet-clinopyroxene amphibolite section of the sole (d) Subsequent slices were accreted/underplated at the same depths but did not reach granulite facies conditions as the hanging-wall mantle had cooled. Fluids released from these lower-grade slices retrogressed the overlying granulite sheet. The same fluids also metasomatised the mantle peridotites and led to amphibolite crystallization. As these lower-grade sheets also record pressures of ∼10 kbar, it is likely that the amphibole crystallized at 30-40 km. (e) Fluids released from further underplated sheets continued to retrogress the overlying granulite assemblage and metasomatize the mantle wedge.

Several aspects of granulite formation would have had a strengthening affect. (1) Amphibole and clinopyroxene have similar rheological properties (Hacker, 1990a). However, limited experimental data have demonstrated that garnet leads to strengthening in amphibolites Soret et al. (2016). (2) Granulite formation is associated with an increase in grain size that may have limited grain-size sensitive deformation mechanism (see Chapter 3), particularly in plagioclase. (3) Fluid infiltration and amphibolitisation of gabbro (i.e., approximately the reverse reaction to that observed in the sole) has been demonstrated to have a significant weakening effect, primarily from the hydration of plagioclase (Getsinger et al., 2013). Thus, dehydration of plagioclase would have had a strengthening effect. (4) Granulite formation destroyed the foliation and thereby the interconnectivity of weak plagioclase layers and alignment of amphibole that would have acted as preferential slip surfaces.

Our analysis of the sole has revealed 85 m of garnet-clinopyroxene amphibolites, the thickest reported from any locality. Our results also reveal that the entire 250 m thick section was subducted to similarly high pressures of 10–12 kbar, corresponding to depths of 30–40 km. The garnet-clinopyroxene amphibolites record temperatures ∼100 °C higher than the epidote and bimineralic amphibolites. We propose that the uppermost 85 m of the section was accreted when granulite formation caused a viscosity increase in the slab and downward migration of the subduction interface (Figure 4.16C–D). In contrast to previous models for sole accretion (Hacker, 1990b, 1991; Agard et al., 2016), we suggest that strengthening, as opposed to weakening, of the downgoing slab caused the subduction interface to migrate downwards. Precisely how far the interface migrated is difficult constrain, but the simplest explanation is that it stepped down to the first regionally extensive horizon of metasedimentary rock. In the described section, the break is probably just below the base of the garnet-clinopyroxene amphibolites, which coincides with a step in temperatures (Figure 4.12) and is just below the structural level at which metasedimentary rocks appear. This next sheet was accreted at similar depths but lower temperatures (Figure 4.16D–E), inconsistent with previous models (Plunder et al., 2015; Agard et al., 2016; Soret et al.,

2017), that inferred the detachment and accretion at progressively shallower depths. As these lower thrust sheets did not reach granulite facies, their accretion may have been controlled through the mechanisms suggested by Hacker (1990b, 1991) and Agard et al. (2016).

Retrogression and exhumation

Soon after accretion, the uppermost amphibolites were retrogressed by fluids originating in the underplated sheets (Figure 4.16D–E). Just as granulite formation strengthened the sole, rehydration would have again weakened it Getsinger et al. (2013). Weakening led to to increased strain and the development of a retrograde fabric that now comprises the dominant foliation of the amphibolites. This fabric, defined by alternating amphibolite and plagioclase rich layers, wraps around the granulite-enclaves, which are all that remains of an earlier assemblage. Rehydration and the development of retrograde fabric from amphibolite through to greenschist temperatures is inferred to be related to exhumation.

As discussed above, constraining the exhumation mechanism of the sole is difficult because pressures from the mantle peridotite are unknown. The results presented herein can, together with the results of Chapter 3, provide some insight into the exhumation mechanism. There are two potential sources for the hydrous-fluids in the mantle wedge that crystallized amphibole (Chapter 3). It is possible that the fluids were released during granulite formation of the uppermost amphibolites. However, given the large volume of fluids necessary to retrogress both the sole and mantle wedge, and the small thickness of granulites, the fluids were more likely derived from the lower-grade amphibolites and metasedimentary rocks (Figure 4.16D–E). In this case, hydration of the mantle wedge and uppermost amphibolites were concomitant. We have demonstrated that much of the retrogression of the sole occurred in the upper amphibolite facies, not long after peak metamorphism, which implies that hydration of the mantle wedge occurred at depths of 30–40 km. Thus, the base of the ophiolite and metamorphic sole both record similarly deep pressures, consistent with exhumation along a flattening

slab as previously proposed by (Casey and Dewey, 1984; Dewey and Casey, 2013).

4.7 Conclusion

To constrain the evolution of the Oman-UAE metamorphic sole, we investigated samples collected across a 250 m sequence of amphibolites near Masafi. The analysed samples range from upper-amphibolite with enclaves of garnet-clinopyroxene immediately beneath peridotites of the Oman-UAE ophiolite, down to lower-amphibolite facies further down section. Our investigation reveals the thickest section (∼85 m) of garnet-clinopyroxene bearing amphibolites and correspondingly high pressure-temperature conditions from any metamorphic sole. Garnet-clinopyroxene amphibolites were pervasively retrogressed during cooling but still retain clues of a granulite-facies assemblage. Thermobarometry and phase equilibria modelling reveal reasonably constant pressures of 10–12 kbar for the entire section. In contrast, calculated temperatures are ∼100 °C higher for the garnet-clinopyroxene amphibolites than the structurally lower epidote- and bi-mineralic amphibolites. However, the Ti-content of amphibole decreases continuously down section, which suggests that some temperature gradient does exist beyond the resolution of the thermometry (∼± 50 °C).

We propose three key stages in the evolution of the metamorphic sole. (1) Following subduction initiation, oceanic crust and associated sediments were buried to $10 - 12$ kbar and 700–900 °C. During burial, a schistose–gneissic foliation, like the one preserved in garnet-clinopyroxene free amphibolites, was developed. (2) At peak conditions, pervasive granulite formation increased the viscosity of the uppermost slab, causing the subduction interface to migrate downwards and accrete a slice (i.e., the metamorphic sole) to the hanging-wall mantle. (3) As rocks in the subduction zone cooled, continued underplating of metabasites and metasedimentary sheets occurred at similar pressures but colder temperatures. The lower temperatures resulted from the advection of heat by retrogressive fluids and the large-scale relaxation of isotherms as the subduction zone matured. Hydration resulted in a viscosity reduction and the

development of a gneissic but retrogressive foliation. We speculate that retrogression of the granulite assemblage was synchronous with hydration of the mantle wedge peridotites (as presented in Chapter 3). This suggests that the base of the ophiolite and the metamorphic sole were juxtaposed at depths of 30–40 km and later exhumed along a flattening slab. However, the driving force behind slab flattening remains enigmatic.

Chapter 5

Conclusion

5.1 Summary of results and conclusions

This thesis explored a range in spatial scales, from the plate-boundary to the crystal lattice, and different structural and stratigraphic levels, from the crust, through the mantle, and into the underlying sole. Each chapter focussed on the northern Oman-UAE ophiolite and metamorphic sole, but has implications for the entire Oman-UAE ophiolite as well as other Tethyan-type ophiolites and modern processes, such as sea-floor spreading, subduction, and strain localization. Part of the evolution of thesis was determining what questions needed to be asked. In the introduction, I narrowed each chapter down to a single question.

- **Chapter 2: Is the architecture and tectonic evolution of the ophiolite in the UAE distinct from Oman?** In Chapter 2, I demonstrated that the architecture of ophiolite in the UAE is similar to Oman. Thus, there is no reason to infer a different tectonic history. I presented 3-dimensional geological models of UAE that are simplified, yet more consistent with geochemical and geochronological data. In the southern UAE, the MTZ is gently folded, nearly horizontal, and coincides with present-day erosion levels, giving the appearance of anomalously large volumes of gabbro. It was this large expanse of gabbro and MTZ lithologies that led previous researchers to suggest the the UAE portion

of the ophiolite is distinct from Oman. My results indicate that the ophiolite sequence is gently folded but largely intact. Road cuts reveal ambiguous magmatic contacts that span a large-range of rock-types, consistent with the U-Pb geochronological evidence indicating the whole sequence formed in a very short (1 Myr) time (Rioux et al., 2012, 2013, 2016). Based on the evidence for widespread and short-lived magmatism, as well as the isolated distribution of volcanic centres in Oman (Pearce et al., 1981; Alabaster et al., 1982), I speculated that extension was broadly distributed during formation of the ophiolite, rather than concentrated at a single East-Pacific-Rise type spreading centre.

- **Chapter 3: What controls strain localization at plate boundaries?** In Chapter 3, I demonstrated that volumetrically minor phases controlled strain localization along the base of the ophiolite. As the base of the ophiolite is as palaeosubduction interface, I inferred that minor phases also exert a control on the development of plate boundaries. Microstructural analyses revealed systematic changes in olivine grain size, olivine CPO, and minor-phase content. I demonstrated that minor phases pinned olivine grain boundaries and limited grain growth. The resultant finer grain size promoted diffusion creep and led to rheological weakening. Similar observations have been made from experimentally deformed rocks, small-scale natural shear zones, and shear zones within the mantle section of the peridodite, but this is the first time these processes have been shown to operate at an actual plate boundary. I calculated that viscosity and strain rate respectively decrease and increase by approximately an order of magnitude towards the base of the ophiolite. My data indicate that this rheological weakening was the result of more abundant minor phases near the base of the ophiolite. Orthopyroxene is the most abundant minor phase in all samples. The distribution of orthopyroxene is interpreted to reflect compositional heterogeneity that predates deformation. Unlike orthopyroxene, hornblende and clinopyroxene are interpreted to have crystallised during metasomatism of the mantle wedge by fluids from dehydration of the downgoing slab.

- **Chapter 4: What controlled accretion of the metamorphic sole, and how was it exhumed?** In Chapter 4, I considered three different stages in the evolution of the metamorphic sole: burial, accretion, and exhumation. My results reveal reasonably constant pressures of ∼10–12 kbar (30–40 km) across the uppermost 250 m section of sole. In contrast, calculated temperatures are ∼100 °C higher for garnet-clinopyroxene amphibolites (∼700–900 °C) than for the structurally lower epidote- and bi-mineralic amphibolites (∼600-700 °C). Textural and petrological evidence indicate that granulite formation of the sole was more pervasive than typically considered. I proposed three key stages for the evolution of the metamorphic sole. (1) Following subduction initiation, oceanic crust and associated sediments were buried to 30–40 km. (2) At peak conditions, granulite formation increased the viscosity of the slab, which caused the subduction interface to migrate downwards and accrete a slice (i.e., the metamorphic sole) to the hanging-wall mantle. (3) As rocks in the subduction zone cooled, continued underplating of lower-grade rocks occurred at similar pressures but colder temperatures. The garnet-clinopyroxene amphibolites were retrogressed by hydrous fluids originating in these underplated sheets. Retrogression of the granulite-facies assemblage was likely synchronous with hydration of the mantle wedge and crystallization of high-temperature amphibole, as presented in Chapter 2. This requires that the base of the ophiolite and metamorphic sole were juxtaposed at 30–40 km, consistent with exhumation along a flattening slab.

5.2 Further questions and future work

Each chapter has resulted far more questions than answers. I conclude this thesis by summarizing the key questions to arise from each chapter, making suggestions for future work.

Structure and extent of the ophiolite

New road cuts along the highway to the west of Fujairah, provide the best exposure of the entire ophiolite and allowed for the structural models presented in Chapter 2. However, extrapolation of surface features from even the best exposure, is limited. Three fundamental questions remain. (1) How thick is the ophiolite?; (2) How far offshore does the ophiolite extend; and (3) Is the ophiolite continuous with Gulf of Oman oceanic crust? Despite the geological importance of the UAE ophiolite, these fundamental question persists. The models presented in Chapter 2 make testable predictions on ophiolite thickness and regional structure. Fortunately, this thesis was paired with on- and offshore geophysical surveys that collected magnetic, gravity, and seismic data. At the time of writing, processing of the geophysical data is incomplete, but the results are eagerly awaited and should help constrain the structure of the ophiolite.

Rheological properties of the basal peridotites

The key question to arise from Chapter 3 is why the abundance of minor phases (pyroxene and amphibole) increases towards the base of the ophiolite. An increase in amphibole and potentially clinopyroxene could reflect higher concentrations of hydrous fluids near the downgoing slab or fluid pathways. However, the most abundant minor phase is orthopyroxene, which is best explained by a pre-existing mantle heterogeneity. Characterizing the distribution of rock types in the mantle section of the ophiolite is a logical first step that would provide insight into mantle heterogeneity. The interpretations of Chapter 3 have implications for a wide range of geological processes, but are derived from only 8 samples. Further insight would be gained by grid sampling (at the mm through to the km scale) across the mantle section of the ophiolite in bog-standard peridotite and characterizing the distributions of grain size, composition, water, CPO, and modal mineral abundances on each scale and at different localities (e.g., Wadi Tayyin, Sumeini). Clearly the number of samples required to undertake such a project would be substantial, as would the time and cost for analysis. A hyperspectral survey,

by either a drone or balloon, could potentially reveal variations in mineral abundances and aid in developing a sampling strategy (e.g., Clenet, 2010; Rajendran and Nasir, 2015).

In addition to further transects above the normal sole, it would be insightful to examine transects above and below the Bani Hamid sole. Bani Hamid records different pressure-temperature conditions, was buried several million years later than the normal sole, and consists of different lithologies. It would be interesting to see if the same processes are recorded in the peridotites at Bani Hamid as described in Chapter 3.

The identification of high-T amphibole (i.e., hornblende as opposed to actinolite) within the mantle section has implications for fluid recycling in subduction zones. As amphibole is a hydrous mineral, it can potentially be used as proxy for fluid flow through the mantle wedge. Thus, the distribution of high-temperature amphibole in the mantle section could reveal former fluid pathways. Both increased sampling and remote sensing would be beneficial to answering questions regarding the distribution of fluid pathways in the mantle wedge. Key to answering these questions is constraining the timing of amphibole crystallization and the source for the metasomatic fluids.

A detailed petrological investigation of the amphibole bearing peridotites would be provide insight into the origin of hydrous fluids and the textural/metasomatic evolution of the peridotites. Given that mineral orientation data and mineral abundance has already been acquired, it would be also worthwhile to calculate the seismic properties of the peridotites. This is especially attractive given the new seismic data collected across the ophiolite (as discussed in 5.2).

The Metamorphic sole

Chapter 4 demonstrated that fairly simple petrography can provide considerable insight, in this case the former presence of a granulite facies assemblage. The thickness of garnet-clinopyroxene amphibolites at Masafi are an ideal location for further studies. Future work should include increased sample density across the sole, from the uppermost garnet-clinopyroxene amphibolites down to and including the phyllitic am-

phibolites interlayered with metasedimentary rocks. The lower-grade amphibolites are often overlooked in favour of the garnet-clinopyroxene amphibolites. However, the surprising result of pressures of 10 kbar from as far as 250 m below the peridotite highlights the need more detailed analyses. It is also recommended that future studies pay close attention to the incredible variety of retrograde textures exhibited by the amphibolites from all structural levels.

Constraining the pressure of amphibolites is difficult, particularly for those without garnet. The metasedimentary rocks, especially the more aluminous garnet±kyanite bearing horizons, are a viable alternative that have received little attention. It would be worth conducting conventional, multi-equilibrium, and pseudosection thermobarometry on the metasedimentary rocks to see how the results compare to amphibolites from similar structural levels. The locality described in Chapter 4 is an ideal location due to the common occurrence of metasediments within garnet-clinopyroxene amphibolites.

The metasedimentary rocks also present an excellent opportunity for investigating quartz deformation temperatures (from c-axis opening angles) across the sole. Although no major thrust were identified in the field, discontinuities and trends in deformation temperatures could reveal cryptic structures. Moreover, deformation temperatures from metasedimentary rocks could be compared with those from quartz-bearing amphibolites. It is likely that deformation was localized in the weaker metasediments as opposed to the stronger amphibolites. Though this remains to be test.

Cowan et al. (2014) first inferred extensive granulite formation based for samples from Sumeini and Wadi Tayyin. Given the implications of granulite formation, it is necessary to reassess the evidence for a former granulite facies assemblage at other localities. Future models for sole accretion need to consider granulite formation. However, there is a paucity of experimental data on the deformation of metabasites, without even considering the influence of metamorphic reaction (e.g., Hacker and Christie, 1990; Soret et al., 2016). It would be insightful to perform a series of deformation experiments on metabasite samples of different metamorphic grade and with different water contents. In particular the influence of garnet on the viscosity of basalt would

be valuable for modelling the subduction interface and sole accretion.

The Oman-UAE ophiolite and sole are relatively well dated. However, recent geochronological studies, such as Rioux et al. (2016) that revealed synchronous metamorphic sole formation and ophiolite crystallization, demonstrate there is still much to learn. It is often assumed that zircon is associated with trondhjemitc melt pods and most studies have focussed on leocosome from the uppermost garnet-clinopyroxene amphibolites. Casual observations from several samples during this thesis found most of the zircon was not associated with melt segregations. Future work should integrate textural relationships with isotopic dates and trace element geochemistry. Given the high precision required, this would likely entail microdrilling and ID-TIMS. Future dating should also include the structurally lower epidote- and bi-mineralic amphibolites. Even if zircon does turn out to be more often associated with melting, Chapter 4 reveals that melt is present to far greater depths than previously thought. Models for sole evolution predict younger ages of metamorphism for the structurally lower thrust sheets.

Finally, dates from the sole can provide clues about subduction initiation. Keenan et al. (2016) interpreted U-Pb zircon dates from the sole beneath the Palawan ophiolite (Western Pacific) as the timing of igneous crystallization of the sole protolith. As these dates are nearly the same as crystallization of the ophiolite, the authors inferred subduction initiation at a spreading center, as opposed to a transform fault or fracture zone (e.g., Stern and Bloomer, 1992; Dewey and Casey, 2013). If igneous zircons were discovered from the Oman-UAE sole they could help elucidate the setting of subduction initiation.

References

Abily, B., Ceuleneer, G., and Launeau, P. (2011). Synmagmatic normal faulting in the lower oceanic crust: Evidence from the Oman ophiolite. *Geology*, 39(4):391–394.

Agard, P., Yamato, P., Soret, M., Prigent, C., Guillot, S., Plunder, A., Dubacq, B., Chauvet, A., and Monié, P. (2016). Subduction infancy: mantle resistance to slab penetration and metamorphic sole formation controlled by plate interface rheological switches. *Earth and Planetary Science Letters*, in rev.:208–220.

Alabaster, T., Pearce, J. A., and Malpas, J. (1982). The volcanic stratigraphy and petrogenesis of the Oman ophiolite complex. *Contributions to Mineralogy and Petrology*, 81(3):168–183.

Allemann, F. and Peters, T. (1972). The ophiolite-radiolarite belt of the North-Oman Mountains The Ophiolite-Radiolarite Belt of the North-Oman Mountains. *Eclogae Geologicae Helvetiae*.

Anonymous (1972). Penrose field conference on ophiolites. *Geotimes*, 17:24–25.

Arai, S., Kadoshima, K., and Morishita, T. (2006). Widespread arc-related melting in the mantle section of the northern Oman ophiolite as inferred from detrital chromian spinels. *Journal of the Geological Society*, 163(5):869–879.

Austin, N. and Evans, B. (2009). The kinetics of microstructural evolution during deformation of calcite. *Journal of Geophysical Research: Solid Earth*, 114(9):1–22.

Batty, S., Flint, R., and Cowan, D. (2004). Summary technical report on geophysical interpretation of airborne magnetic and spectral data, United Arab Emirates. Technical report, Fugro Airborne Surveys and Ministry of Petroleum and Mineral Resources, Abu Dhabi, UAE.

Bercovici, D. and Karato, S.-i. (2003). Theoretical Analysis of Shear Localization in the Lithosphere. *Reviews in Mineralogy and Geochemistry: Plastic Deformation of Minerals and Rocks*, 51:387–421.

Bercovici, D. and Ricard, Y. (2012). Mechanisms for lithospheric shear localization and the generation of plate tectonics by two-phase grain-damage and pinning. *Physics of the Earth and Planetary Interiors*, 14:12151.

Bercovici, D. and Ricard, Y. (2014). Plate tectonics, damage and inheritance. *Nature*, 508(7497):513–6.

Bercovici, D. and Skemer, P. (2017). Grain damage , phase mixing and plate-boundary formation. *Journal of Geodynamics*, 108(May):40–55.

Berger, A. and Stünitz, H. (1996). Deformation mechanisms and reaction of hornblende: examples from the Bergell tonalite (Central Alps). *Tectonophysics*, 257:149–174.

Boudier, F., Ceuleneer, G., and Nicolas, A. (1988). Shear zones, thrusts and related magmatism in the Oman ophiolite: Initiation of thrusting on an oceanic ridge. *Tectonophysics*, 151(1-4):275–296.

Boudier, F. and Coleman, R. G. (1981). Cross section through the peridotite in the Samail Ophiolite, southeastern Oman Mountains. *Journal of Geophysical Research*, 86(B4):2573.

Boudier, F., Godard, M., and Armbruster, C. (2000). Significance of gabbronorite occurrence in the crustal section of the Semail ophiolite. *Marine Geophysical Researches*, 21(3-4):307–326.

Boudier, F. and Nicolas, A. (1988). The ophiolites of Oman. *Tectonophysics [Special Volume]*, 151(1-4).

Boudier, F., Nicolas, A., and Ildefonse, B. (1996). Magma chambers in the Oman ophiolite: fed from the top and the bottom. *Earth and Planetary Science Letters*, 144(96):239–250.

Boudier, F., Nicolas, A., Ildefonse, B., and Jousselin, D. (1997). EPR microplates, a model for the Oman ophiolite. *Terra Nova*, 9(2):79–82.

Casey, J. F. and Dewey, J. F. (1984). Initiation of subduction zones along transform and accreting plate boundaries, triple-junction evolution, and forearc spreading centres - implications for ophiolitic geology and obduction. *Geological Society, London, Special Publications*, 13:269–290.

Christensen, N. and Smewing, J. D. (1981). Geology and seismic structure of the Northern section of the Oman ophiolite. *Journal of Geophysical Research*, 86(B4):2545–2555.

Clenet, H. (2010). Thick sections of layered ultramafic cumulates in the Oman ophiolite revealed by an airborne hyperspectral survey: Petrogenesis and relationship to mantle diapirism. *Lithos*, 114(3-4):265–281.

Coleman, R. G. (1971). Plate tectonic emplacement of upper mantle peridotites along continental edges. *Journal of Geophysical Research*, 76(5).

Coleman, R. G. (1981). Tectonic setting for ophiolite obduction in Oman. *Journal of Geophysical Research: Solid Earth*, 86(B4):2497–2508.

Coleman, R. G. and Bailey, E. H. (1974). Mineral deposits and geology of Northern Oman as of 1974. Technical report, United States Geological Survey.

Coleman, R. G. and Hopson, C. A. (1981). Introduction to the Oman Ophiolite Special Issue. *Journal of Geophysical Research: Solid Earth*, 86(B4):2495–2496.

Corti, G. (2009). Continental rift evolution: From rift initiation to incipient break-up in the Main Ethiopian Rift, East Africa. *Earth-Science Reviews*, 96(1-2):1–53.

Cowan, R. J., Searle, M., and Waters, D. J. (2014). Structure of the metamorphic sole to the Oman Ophiolite, Sumeini Window and Wadi Tayyin: implications for ophiolite obduction processes. *Geological Society, London, Special Publications*, 392(1):155–175.

Cox, J., Searle, M., and Pedersen, R. (1999). The petrogenesis of leucogranitic dykes intruding the northern Semail ophiolite, United Arab Emirates: Field relationships, geochemistry and Sr/Nd isotope systematics. *Contributions to Mineralogy and Petrology*, 137:267–287.

Cross, A. J. and Skemer, P. (2017). Ultramylonite generation via phase mixing in high strain experiments. *Journal of Geophysical Research*, pages 1–16.

Dare, S. A. S., Pearce, J. A., McDonald, I., and Styles, M. T. (2009). Tectonic discrimination of peridotites using fO2-Cr# and Ga-Ti-Fe3 systematics in chrome-spinel. *Chemical Geology*, 261(3-4):199–216.

de Bresser, J. H. P., Peach, C. J., Reijs, J. P. J., and Spiers, C. J. (1998). On dynamic recrystallization during solid state flow: Effects of stress and temperature. *Geophysical Research Letters*, 25(18):3457–3460.

de Bresser, J. H. P., Ter Heege, J. H., and Spiers, C. J. (2001). Grain size reduction by dynamic recrystallization: Can it result in major rheological weakening? *International Journal of Earth Sciences*, 90(1):28–45.

DeMets, C., Gordon, R. G., and Argus, D. F. (2010). Geologically current plate motions. *Geophysical Journal International*, 181(1):1–80.

Derby, B. and Ashby, M. F. (1987). On dynamic recrystallisation. *Scripta Metallurgica*, 21(6):879–884.

Dewey, J. F. and Bird, J. (1971). Origin and Emplacement of the ophiolite suite: Appalachian Ophiolites in Newfoundland. *Journal of Geophysical Research*, 76(14):2120–2121.

Dewey, J. F. and Bird, J. M. (1970). Moutain Belts and the New Global Tectonics. *Journal of Geophysical Research*, 75(14):2625–2646.

Dewey, J. F. and Casey, J. F. (2013). The sole of an ophiolite: the Ordovician Bay of Islands Complex, Newfoundland. *Journal of the Geological Society, London*, 170(5):715–722.

Dietz, R. S. (1963). ALPINE SERPENTINES AS OCEANIC RIND FRAGMENTS. *Geological Society of America Bulletin*, 74(July):947–952.

Dijkstra, A. and Drury, M. (2002). Microstructures and lattice fabrics in the Hilti mantle section (Oman Ophiolite): Evidence for shear localization and melt weakening in the crustmantle transition zone? *Journal of Geophysical Research-Solid Earth*, 107(b11):2270.

Dilek, Y. and Flower, M. F. J. (2003). Arc-trench rollback and forearc accretion: 2. A model template for ophiolites in Albania, Cyprus, and Oman. *Geological Society, London, Special Publications*, 218(1):43–68.

Dilek, Y. and Furnes, H. (2011). Ophiolite genesis and global tectonics: Geochemical and tectonic fingerprinting of ancient oceanic lithosphere. *Bulletin of the Geological Society of America*, 123(3-4):387–411.

Droop, G. (1987). A General Equation for Estimating Fe3+ Concentrations in Ferromagnesian Silicates and Oxides from Microprobe Analyses, Using Stoichiometric Criteria. *Mineralogical Magazine*, 51(361):431–435.

Drury, M. (2005). Dynamic recrystallization and strain softening of olivine aggregates in the laboratory and the lithosphere. *Geological Society London Special Publications*, 243(2):143–158.

Ebinger, C. (2005). Continental break-up: The East African perspective. *A&G. The Bullerwell Lecture*, 46(April):1–6.

Ernewein, M., Pflumio, C., and Whitechurch, H. (1988). The death of an accretion zone as evidenced by the magmatic history of the Sumail ophiolite (Oman). *Tectonophysics*, 151(1-4):247–274.

Ernst, W. G. and Liu, J. (1998). Experimental phase- equilibrium of Al- and Ti-contents of calcic amphibole in MORB- A semiquantitative thermobarometer. *American Mineralogist*, 83:952–969.

Evans, B., Renner, J., and Hirth, G. (2001). A few remarks on the kinetics of static grain growth in rocks. *International Journal of Earth Sciences*, 90(1):88–103.

Evans, B. W. (2004). The Serpentinite Multisystem Revisited: Chrysotile Is Metastable. *International Geology Review*, 46(March):479–506.

Farla, R. J. M., Karato, S.-i., and Cai, Z. (2013). Role of orthopyroxene in rheological weakening of the lithosphere via dynamic recrystallization. *Proceedings of the National Academy of Sciences of the United States of America*, 110(41):16355–60.

Farrant, A., Ellison, R. A., Thomas, R. J., Goodenough, K. M., Arkley, S. L., Burke, H. F., Carney, J. N., Finlayson, A., Jordan, C. J., Lee, J. R., Leslie, A. B., Merritt, J. E., Merritt, J., Newell, A. J., Phillips, E. R., Pickett, E., Price, S. J., Schofield, D. I., Smith, R., Stephenson, D., Styles, M. T., and Warrak, M. (2012). *Geological map of the United Arab Emirates*. British Geological Survey, Keyworth, Nottingham.

Fliervoet, T. F., Drury, M., and Chopra, P. N. (1999). Crystallographic preferred orientations and misorientations in some olivine rocks deformed by diffusion or dislocation creep. *Tectonophysics*, 303(1-4):1–27.

Forshaw, J. (2017). *Testing Thermodynamic Models for High-Temperature Metabasite Mineral Assemblages*. Mearthsci thesis, University of Oxford.

Gass (1968). Is the Troodos Massif of Cyprus a Fragment of Mesozoic Ocean Floor? *Nature*, 220(5162):39–42.

Getsinger, A. J., Hirth, G., Stünitz, H., and Goergen, E. T. (2013). Influence of water on rheology and strain localization in the lower continental crust. *Geochemistry, Geophysics, Geosystems*, 14(7):2247–2264.

Ghent, E. and Stout, M. Z. (1981). Metamorphism at the base of the Samail Ophiolite, southeastern Oman Mountains. *Journal of Geophysical Research*, 86(B4):2557.

Glennie, K., Boeuf, M., Hughes Clarke, M., Mood-Stuart, M., Pilaar, W., and Reinhardt, B. (1973). Late Cretaceous Nappes in Oman Mountains and Their Geologic Evolution. *AAPG Bulletin*, 57(1):5–27.

Glennie, K., Boeuf, M., Hughes-Clarke, M., Mood-Stuart, M., Pilaar, W., and Reinhardt, B. (1974). Geology of the Oman Mountains. *Verhandelingen Koninklijk Nederlands geologisch mijnbouwkundidg Genootschap*, 31:423.

Gnos, E. (1998). Peak Metamorphic Conditions of Garnet Amphibolites Beneath the Semail Ophiolite: Implications for an Inverted Pressure Gradient. *International Geology Review*, 40(4):281–304.

Gnos, E. and Kurz, D. (1994). Sapphirine-quartz and sapphirine-corundum assemblages in metamorphic rocks associated with the Semail Ophiolite (United Arab Emirates). *Contributions to Mineralogy and Petrology*, 116:398–410.

Gnos, E. and Nicolas, A. (1996). Structural Evolution of the northern end of the Oman Ophiolite and enclosed granulites. *Tectonophysics*, 254:111–137.

Godard, M., Bosch, D., and Einaudi, F. (2006). A MORB source for low-Ti magmatism in the Semail ophiolite. *Chemical Geology*, 234(1-2):58–78.

Goodenough, K. M., Styles, M., Schofield, D., Thomas, R. J., Crowley, Q. C., Lilly, R. M., McKervey, J., Stephenson, D., and Carney, J. N. (2010). Architecture of the OmanUAE ophiolite: evidence for a multi-phase magmatic history. *Arabian Journal of Geosciences*, 3(4):439–458.

Goodenough, K. M., Thomas, R. J., Styles, M., Schofield, D. I., and MacLeod, C. J. (2014). Records of ocean growth and destruction in the Oman-UAE ophiolite. *Elements*, 10(2):109–114.

Grantham, G., Goedhart, M., Wipplinger, P., Thomas, R., Eglington, B., R.E., H., and F.J., H. (2004). The surface geology of the Emirate of Fujairah. Technical report, Department of Industry and Economy, Fujairah, UAE.

Grapes, R. H. and Graham, C. M. (1978). The actinolite-hornblende series in metabasites and the so-called miscibility gap: A review. *Lithos*, 11(2):85–92.

Green, E. C. R., White, R. W., Diener, J. F. A., Powell, R., Holland, T., and Palin, R. M. (2016). Activity-composition relations for the calculation of partial melting equilibria in metabasic rocks. *Journal of Metamorphic Geology*, 34(9):845–869.

Greenwood, J. E. and Loney, P. (1968). Geology and Mineral Resources of the Trucial Oman Range. Technical report, Institute of Geological Sciences, London.

Hacker, B. R. (1990a). Amphibolite-facies-to-granulite-facies reactions in experimentally deformed, unpowdered amphibolite. *American Mineralogist*, 75:1349–1361.

Hacker, B. R. (1990b). Simulation of the metamorphic and deformational history of the metamorphic sole of the Oman ophiolite. *Journal of Geophysical Research-Solid Earth*, 95(B4):2527–2544.

Hacker, B. R. (1991). The role of deformation in the formation of metamorphic gradients: ridge subduction beneath the Oman ophiolite. *Tectonics*, 10(2):455–473.

Hacker, B. R. (1994). Rapid emplacement of young oceanic lithosphere: argon geochronology of the oman ophiolite. *Science*, 265(5178):1563–1565.

Hacker, B. R. and Christie, J. M. (1990). Brittle\ductile and plastic\cataclastic transitions in experimentally deformed and metamorphosed amphibolite. In *The brittle ductile transition in rocks*. American Geophysical Union.

Hacker, B. R. and Gnos, E. (1997). The conundrum of Samail: explaining the metamorphic history. *Tectonophysics*, 279:215–226.

Hacker, B. R. and Mosenfelder, J. L. (1996). Metamorphism and deformation along the emplacement thrust of the Samail ophiolite, Oman. *Earth and Planetary Science Letters*, 144(3-4):435–451.

Hacker, B. R., Mosenfelder, J. L., and Gnos, E. (1996). Rapid emplacement of the Oman ophiolite: thermal and geochronological constrains. *Tectonics*, 15(6):1230–1247.

Hansen, L. N. and Warren, J. M. (2015). Quantifying the effect of pyroxene on deformation of peridotite in a natural shear zone. *Journal of Geophysical Research: Solid Earth*, 120:2717–2738.

Hansen, L. N., Zimmerman, M. E., and Kohlstedt, D. L. (2011). Grain boundary sliding in San Carlos olivine: Flow law parameters and crystallographic-preferred orientation. *Journal of Geophysical Research: Solid Earth*, 116(8):1–16.

Hawthorne, F. C., Oberti, R., Harlow, G. E., Maresch, W. V., Martin, R. F., Schumacher, J. C., and Welch, M. D. (2012). Ima report: Nomenclature of the amphibole supergroup. *American Mineralogist*, 97(11-12):2031–2048.

Herwegh, M., Linckens, J., Ebert, A., Berger, A. L., and Brodhag, S. H. (2011). The role of second phases for controlling microstructural evolution in polymineralic rocks: A review. *Journal of Structural Geology*, 33(12):1728–1750.

Hess, H. (1962). History of ocean basins. *Petrologic Studies (Buddington Volume)*, pages 599–620.

Hielscher, R. and Schaeben, H. (2008). A novel pole figure inversion method: specification of the MTEX algorithm. *Journal of Applied Crystallography*, 41(6):1024–1037.

Hiraga, T., Tachibana, C., Ohashi, N., and Sano, S. (2010). Grain growth systematics for forsterite enstatite aggregates: Effect of lithology on grain size in the upper mantle. *Earth and Planetary Science Letters*, 291(1-4):10–20.

Hirth, G. and Kohlstedt, D. L. (2003). Rheology of the upper mantle and the mantle wedge: a view from the experimentalists. In Eiler, J. M., editor, *Inside the Subduction Factory*, pages 83–105. American Geophysical Union.

Holland, T. (1979). Deformed pillow lavas from the central Hohe Tauern, Austria, and their bearing on the origin of epidote-banded greenstones. *Earth and Planetary Science Letters*, 43:397–405.

Holland, T. and Blundy, J. (1994). Non-ideal interactions in calcic amphiboles and their bearing on amphibole-plagioclase thermometry. *Contributions to Mineralogy and Petrology*, 116(4):433–447.

Holland, T. and Powell, R. (2003). Activity-composition relations for phases in petrological calculations: an asymmetric multicomponent formulation. *Contributions to Mineralogy and Petrology*, 145(4):492–501.

Holland, T. and Powell, R. (2011). An improved and extended internally consistent thermodynamic dataset for phases of petrological interest, involving a new equation of state for solids. *Journal of Metamorphic Geology*, 29(3):333–383.

Humphreys, F. J. (2001). Grain and subgrain characterisation by electron backscatter diffraction. *Journal of Materials Science*, 36(16):3833–3854.

Huntings Geology and Geophysics (1976). Geological map of the northern Emirates, 1:250,000 scale.

Ishikawa, T., Fujisawa, S., Nagaishi, K., and Masuda, T. (2005). Trace element characteristics of the fluid liberated from amphibolite-facies slab: Inference from the metamorphic sole beneath the Oman ophiolite and implication for boninite genesis. *Earth and Planetary Science Letters*, 240(2):355–377.

Ishikawa, T., Nagaishi, K., and Umino, S. (2002). Boninitic volcanism in the Oman ophiolite: Implications for thermal condition during transition from spreading ridge to arc. *Geology*, 30(10):899–902.

Jacobs, J., Thomas, R. J., Ksienzyk, A. K., and Dunkl, I. (2015). Tracking the Oman Ophiolite to the surface New fission track and (UTh)/He data from the Aswad and Khor Fakkan Blocks, United Arab Emirates. *Tectonophysics*, 644-645:68–80.

Jamieson, R. (1980). Formation of metamorphic aureoles beneath ophiolites- Evidence from the St. Anthony Complex, Newfoundland. *Geology*, 8(3):150–154.

Jamieson, R. (1986). P-T paths from high temperature shear zones beneath ophiolites. *Journal of metamorphic Geology*, 4(1):3–22.

Jung, H. and Karato, S.-i. (2001). Water-Induced Fabric Transitions in Olivine. *Science*, 293(5534):1460–1463.

Jung, H., Katayama, I., Jiang, Z., Hiraga, T., and Karato, S.-i. (2006). Effect of water and stress on the lattice-preferred orientation of olivine. *Tectonophysics*, 421(1-2):1–22.

Juteau, T., Ernewein, M., Reuber, I., Whitechurch, H., and Dahl, R. (1988). Duality of magmatism in the plutonic sequence of the Sumail Nappe, Oman. *Tectonophysics*, 151(1-4):107–135.

Karato, S.-i. (1988). The role of recrystallization in the preferred orientation of olivine. *Physics of the Earth and Planetary Interiors*, 51(1-3):107–122.

Karato, S.-i., Jung, H., Katayama, I., and Skemer, P. (2008). Geodynamic Significance of Seismic Anisotropy of the Upper Mantle: New Insights from Laboratory Studies. *Annual Review of Earth and Planetary Sciences*, 36(1):59–95.

Karato, S.-i., Toriumi, M., and Toshitsugu, F. (1980). Dynamic recrystallization of olivine single crystals during high-temperature creep. *Geophysical Research Letters*, 7(9):649–652.

Karato, S.-i. and Wu, P. (1993). Rheology of the upper mantle: a synthesis. *Science (New York, N.Y.)*, 260(5109):771–778.

Keenan, T. E., Encarnación, J., Buchwaldt, R., Fernandez, D., Mattinson, J., Rasoazanamparany, C., and Luetkemeyer, P. B. (2016). Rapid conversion of an oceanic spreading center to a subduction zone inferred from high-precision geochronology. *Proceedings of the National Academy of Sciences*, page 201609999.

Kelemen, P. B., Shimizu, N., and Salters, V. (1995). Extraction of mid-ocean-ridge basalt from the upwelling of mantle by focused flow of melt in dunite channels. *Nature*, 375:747–743.

Khedr, M. Z., Arai, S., and Python, M. (2013). Petrology and chemistry of basal lherzolites above the metamorphic sole from Wadi Sarami central Oman ophiolite. *Journal of Mineralogical and Petrological Sciences*, 108(1):13–24.

Kohlstedt, D. L., Keppler, H., and Rubie, D. C. (1996). Solubility of water in the α, β and γ phases of (Mg,Fe)2SiO4. *Contributions to Mineralogy and Petrology*, 123(4):345–357.

Lees, G. (1928). The Geology and Tectonics of Oman and of Parts of South-Eastern Arabia. *Quarterly Journal of the Geological Society*, 84(1-4):585–670.

Linckens, J., Herwegh, M., Mntener, O., and Mercolli, I. (2011). Evolution of a polymineralic mantle shear zone and the role of second phases in the localization of deformation. *Journal of Geophysical Research: Solid Earth*, 116(6):1–21.

Lippard, S. J. (1986). Chapter 2 Evolution of the Oman Tethys. *Geological Society, London, Memoirs*, 11(1):17–38.

Lippard, S. J., Shelton, A., and Gass, I. G. (1986). The ophiolite of the Northern Oman. *Geological Society, London, Memoirs*, 11(1):1–16.

MacLeod, C. J., Johan Lissenberg, C., and Bibby, L. E. (2013). "Moist MORB" axial magmatism in the Oman ophiolite: The evidence against a mid-ocean ridge origin. *Geology*, 41(4):459–462.

Maffione, M., Thieulot, C., van Hinsbergen, D. J. J., Morris, a., Plümper, O., and Spakman, W. (2015). Dynamics of intraoceanic subduction initiation: 1. Oceanic detachment fault inversion and the formation of supra-subduction zone ophiolites. *Geochemistry, Geophysics, Geosystems*, 16:1–18.

Malpas, J. (1976). *The petrology and petrogenesis of the Bay of Islands ophiolite suite, western Newfoundland*. PhD thesis, Memorial University of Newfoundland.

Mei, S. and Kohlstedt, D. L. (2000a). Influence of water on plastic deformation of olivine aggregates 1. Diffusion creep regime. *Journal of Geophysical Research*, 105(B9):21456–21469.

Mei, S. and Kohlstedt, D. L. (2000b). Influence of water on plastic deformation of olivine aggregates 2. Dislocation creep regime. *J. Geophys. Res.*, 105(B9):21471–21481.

Michibayashi, K., Ina, T., and Kanagawa, K. (2006). The effect of dynamic recrystallization on olivine fabric and seismic anisotropy: Insight from a ductile shear zone, Oman ophiolite. *Earth and Planetary Science Letters*, 244(3-4):695–708.

Michibayashi, K. and Mainprice, D. (2004). The Role of Pre-existing Mechanical Anisotropy on Shear Zone Development within Oceanic Mantle Lithosphere: an Example from the Oman Ophiolite. *Journal of Petrology*, 45(2):405–414.

Miyashiro, A. (1973). The Troodos ophiolitic complex was probably formed in an island arc. *Earth and Planetary Science Letters*, 19(2):218–224.

Moores, E. M. (1982). Origin and Emplacement of Ophiolites. *Reviews of Geophysics*, 20(4):735–760.

Moores, E. M., Kellogg, L. H., and Dilek, Y. (2000). Tethyan ophiolites, mantle convection, and tectonic "historical contingency": A resolution of the "ophiolite conundrum".

Moores, E. M. and Vine, F. J. (1971). The Troodos Massif, Cyprus and other Ophiolites as Oceanic Crust: Evaluation and Implications. *Philosophical Transactions of the Royal Society A: Mathematical, Physical and Engineering Sciences*, 268(1192):443–467.

Muller, R. D., Sdrolias, M., Gaina, C., and Roest, W. R. (2008). Age, spreading rates, and spreading asymmetry of the world's ocean crust. *Geochemistry, Geophysics, Geosystems*, 9(4):1–19.

Nicolas, A. and Boudier, F. (2015). Structural contribution from the Oman ophiolite to processes of crustal accretion at the East Pacific Rise. *Terra Nova*, 27(2):77–96.

Nicolas, A. and Boudier, F. (2017). Emplacement of Semail-Emirates ophiolite at ridge-trench collision. *Terra Nova*, 29(April 2016):127–134.

Nicolas, A., Boudier, F., and Bouchez, J.-L. (1980). Interpretation of peridotite structures from ophiolitic and oceanic environments.

Nicolas, A., Boudier, F., Ildefonse, B., and Ball, E. (2000). Accretion of Oman and United Arab Emirates ophiolite Discussion of a new structural map. pages 147–179.

Ohuchi, T., Kawazoe, T., Higo, Y., Funakoshi, K.-I., Suzuki, A., Kikegawa, T., and Irifune, T. (2015). Dislocation-accommodated grain boundary sliding as the major deformation mechanism of olivine in the Earth's upper mantle. *Science advances*, 1(9):e1500360.

Palin, R. M., Weller, O. M., Waters, D. J., and Dyck, B. (2015). Quantifying geological uncertainty in metamorphic phase equilibria modelling; a Monte Carlo assessment and implications for tectonic interpretations. *Geoscience Frontiers*, pages 1–17.

Pearce, J. A. (2003). Supra-subduction zone ophiolites: the search for modern analogues. *Geological Society of America Special Paper*, 373:269–293.

Pearce, J. A., Alabaster, T., Shelton, A., and Searle, M. (1981). The Oman Ophiolite as a Cretaceous Arc-Basin Complex: Evidence and Implications. *Philosophical transactions of the Royal Society of London*, 300(1454):299–317.

Pilgrim, G. (1908). Geology of the Persian Gulf and adjoining portions of Persia and Arabia. *Indian Geological Survey Memoir*, 34(4):1–177/.

Plümper, O., John, T., Podladchikov, Y. Y., Vrijmoed, J. C., and Scambelluri, M. (2016). Fluid escape from subduction zones controlled by channel-forming reactive porosity. *Nature Geoscience*, 1(December).

Plunder, A., Agard, P., Chopin, C., Pourteau, A., and Okay, A. I. (2015). Accretion, underplating and exhumation along a subduction interface: From subduction initiation to continental subduction (Tavsanli zone, W. Turkey). *Lithos*, 226:233–254.

Plunder, A., Agard, P., Chopin, C., Soret, M., Okay, A. I., and Whitechurch, H. (2016). Metamorphic sole formation, emplacement and blueschist facies overprint: early subduction dynamics witnessed by western Turkey ophiolites. *Terra Nova*, 28(5):329–339.

Poirier, J. P. and Guillopé, M. (1979). Deformation induced recrystallization of minerals. *Bulletin de Mineralogie*, 102:67–74.

Powell, R. (1985). Regression diagnostics and robust regression in geothermometer/geobarometer Calibration: the garnet-clinopyroxene geothermometer revisited. *Journal of Metamorphic Geology*, 3:231–243.

Powell, R. and Holland, T. (1994). Optimal geothermometry and geobarometry. *American Mineralogist*, 79(1994):120–133.

Précigout, J. and Stünitz, H. (2016). Evidence of phase nucleation during olivine diffusion creep: A new perspective for mantle strain localisation. *Earth and Planetary Science Letters*, 455:94–105.

Prigent, C., Guillot, S., Agard, P., and Godard, M. (2015). Mantle Wedge formation during Subduction Initiation : evidence from the refertilized base of the Oman ophiolitic mantle. In *EGU Abstracts*, volume 17.

Prigent, C., Guillot, S., Agard, P., Godard, M., and Chauvet, A. (2014). The basal part of the Oman ophiolitic mantle : a fossil Mantle Wedge ? In *EGU Abstracts*, volume 16, page 10266.

Python, M. and Ceuleneer, G. (2003). Nature and distribution of dykes and related melt migration structures in the mantle section of the Oman ophiolite. *Geochemistry, Geophysics, Geosystems*, 4(7):n/a–n/a.

Python, M., Ceuleneer, G., and Arai, S. (2008). Chromian spinels in mafic-ultramafic mantle dykes: Evidence for a two-stage melt production during the evolution of the Oman ophiolite. *Lithos*, 106(1-2):137–154.

Rabu, D., Nehlig, P., Roger, J., Béchennec, F., Beurrier, M., Le Métour, J., Bourdillon Jeudy-De-Grissac, C., Tegyey, M., Chauvel, J.-J., Cavelier, C., Al Azri, H., Juteau, T., Janjou, D., Lemière, B., Villey, M., and Wyns, R. (1993). Stratigraphy and structure of the Oman mountains. Technical report, Bureau of Geological and Mining Research, Orleans, Frane.

Rajendran, S. and Nasir, S. (2015). Mapping of Moho and Moho Transition Zone (MTZ) in Samail ophiolites of Sultanate of Oman using remote sensing technique. *Tectonophysics*, 657:63–80.

Ravna, E. (2000). The garnet clinopyroxene Fe 2 + Mg geothermometer : an updated calibration. *Journal of Metamorphic Geology*, 18(2):211–219.

Reid, I. and Jackson, H. R. (1981). Oceanic sreading and crustal thickness. *Marine Geophysical Researches*, 5:165–172.

Reinhardt, B. (1969). On the genesis and emplacement of ophiolites in the Oman Mountains geosyncline. *Geologie En Mijnbouw*, 49(2):161–163.

Rioux, M., Bowring, S., Kelemen, P. B., Gordon, S., Dudás, F., and Miller, R. (2012). Rapid crustal accretion and magma assimilation in the Oman-U.A.E. ophiolite: High precision U-Pb zircon geochronology of the gabbroic crust. *Journal of Geophysical Research*, 117(B7):B07201.

Rioux, M., Bowring, S., Kelemen, P. B., Gordon, S., Miller, R., and Dudás, F. (2013). Tectonic development of the Samail ophiolite: High-precision U-Pb zircon geochronology and Sm-Nd isotopic constraints on crustal growth and emplacement. *Journal of Geophysical Research: Solid Earth*, 118(5):2085–2101.

Rioux, M., Garber, J., Bauer, A., Bowring, S., Searle, M., Kelemen, P. B., and Hacker, B. R. (2016). Synchronous formation of the metamorphic sole and igneous crust of the Semail ophiolite: New constraints on the tectonic evolution during ophiolite formation from high-precision UPb zircon geochronology. *Earth and Planetary Science Letters*, 451:185–195.

Roberts, N. M., Thomas, R. J., and Jacobs, J. (2016). Geochronological constraints on the metamorphic sole of the Semail ophiolite in the United Arab Emirates. *Geoscience Frontiers*, pages 1–11.

Robertson, A. H., Blome, C., Cooper, D. J. W., Kemp, A., and Searle, M. (1990a). Evolution of the Arabian continental margin in the Dibba Zone , Northern Oman Mountains. *Geological Society London Special Publications*, 49.

Robertson, A. H., Searle, M., and Ries, A. (1990b). The geology and tectonics of the Oman region. *Geological Society, London, Special Publications*, 49.

Rollinson, H. (2009). New models for the genesis of plagiogranites in the Oman ophiolite. *Lithos*, 112(3-4):603–614.

Rollinson, H. and Adetunji, J. (2013). Mantle podiform chromitites do not form beneath mid-ocean ridges: A case study from the Moho transition zone of the Oman ophiolite. *Lithos*, 177:314–327.

Rollinson, H., Searle, M., Abbasi, I. a., Al-Lazki, a. I., and Al Kindi, M. H. (2014). Tectonic evolution of the Oman Mountains: an introduction. *Geological Society, London, Special Publications*, 392(1):1–7.

Rushmer, T. (1995). An experimental deformation study of partially molten amphibolite: Application to low-melt fraction segregation. *Journal Of Geophysical Research*, 100(B8):15681.

Rutter, E. H. and Brodie, K. H. (1988). The role of tectonic grain size reduction in the rheological stratification of the lithosphere. *Geologische Rundschau*, 77(1):295–307.

Rutter, E. H., Casey, M., and Burlini, L. (1994). Preferred crystallographic orientation development during the plastic and superplastic flow of calcite rocks. *Journal of Structural Geology*, 16(10):1431–1446.

Searle, M. (1988a). Structure of the Musandam culmination (Sultanate of Oman and United Arab Emirates) and the Straits of Hormuz syntaxis. *Journal of the Geological Society, London*, 145:831–845.

Searle, M. (1988b). Thrust tectonics of the Dibba zone and the structural evolution of the Arabian continental margin along the Musandam mountains (Oman and United Arab Emirates). *Journal of the Geological Society*, 145(1):43–53.

Searle, M. (2007). Structural geometry, style and timing of deformation in the Hawasina Window, Al Jabal al Akhdar and Saih Hatat culminations, Oman Mountains. *GeoArabia*, 12(2):99–130.

Searle, M., Cherry, A. G., Ali, M. Y., and Cooper, D. J. W. (2014). Tectonics of the Musandam Peninsula and northern Oman Mountains : From ophiolite obduction to continental collision. *GeoArabia*, 19(2):135–174.

Searle, M. and Cox, J. (1999). Tectonic setting , origin , and obduction of the Oman ophiolite. *GSA Bulletin*, 111(1):104–122.

Searle, M. and Cox, J. (2002). Subduction zone metamorphism during formation and emplacement of the Semail ophiolite in the Oman Mountains. *Geological Magazine*, 139:241–255.

Searle, M., Lippard, S. J., Smewing, J. D., and Rex, D. C. (1980). Volcanic rocks beneath the Semail Ophiolite nappe in the northern Oman mountains and their significance in the Mesozoic evolution of Tethys. *Journal of the Geological Society, London*, 137(January 2009):589–604.

Searle, M. and Malpas, J. (1980). Structure and metamorphism of rocks beneath the Semail ophiolite of Oman and their significance in ophiolite obduction. *Transactions of the Royal Society of Edinburgh: Earth Sciences*, 71:247–262.

Searle, M. and Malpas, J. (1982). Petrochemistry and origin of sub-ophiolitic metamorphic and related rocks in the Oman Mountains. *Journal of the Geological Society*, 139(3):235–248.

Searle, M., Warren, C. J., Waters, D. J., and Parrish, R. (2004). Structural evolution, metamorphism and restoration of the Arabian continental margin, Saih Hatat region, Oman Mountains. *Journal of Structural Geology*, 26(3):451–473.

Searle, M., Waters, D. J., Garber, J., Rioux, M., Cherry, A., and Ambrose, T. (2015). Structure and metamorphism beneath the obducting Oman ophiolite: Evidence from the Bani Hamid granulites, northern Oman mountains. *Geosphere*, 11(6):GES01199.1.

Sinton, J. and Detrick, R. S. (1992). Midocean ridge magma chambers. *Journal of Geophysical Research-Solid Earth*, 97(B1):197–216.

Skemer, P. and Hansen, L. N. (2016). Inferring upper-mantle flow from seismic anisotropy: An experimental perspective. *Tectonophysics*, 668-669:1–14.

Soret, M., Agard, P., Dubacq, B., Hirth, G., and Yamato, P. (2016). Metamorphic sole formation and early plate interface rheology : Insights from Griggs apparatus experiments. In *EGU Abstracts*, volume 18.

Soret, M., Agard, P., Dubacq, B., Plunder, A., and Yamato, P. (2017). Petrological evidence for stepwise accretion of metamorphic soles during subduction infancy (Semail ophiolite, Oman and UAE). *Journal of Metamorphic Geology*, (December 2016):1–30.

Spray, J. G. (1984). Possible causes of upper mantle decoupling and ophiolite displacement. *Ophiolites and oceanic lithosphere.*, 13(May 2007):255–268.

Spray, J. G. and Spray, J. G. (1983). Lithosphereasthenosphere decoupling at spreading centers and initiation of obduction.

Stern, R. J. (2004). Subduction initiation: Spontaneous and induced. *Earth and Planetary Science Letters*, 226(3-4):275–292.

Stern, R. J. and Bloomer, S. (1992). Subduction zone infancy: Examples from hte Eocene Izu-Bonin-Mariana and Jurassic California arc. *Geological Society of America Special Publications*, 104:1621–1636.

Streit, E., Kelemen, P. B., and Eiler, J. (2012). Coexisting serpentine and quartz from carbonate-bearing serpentinized peridotite in the Samail Ophiolite, Oman. *Contributions to Mineralogy and Petrology*, 164(5):821–837.

Stuwe, K. (1997). Effective bulk composition changes due to cooling: a model predicting complexities in retrograde reaction textures. *Contributions to Mineralogy and Petrology*, 129(1):43–52.

Styles, M., Ellison, R., Arkley, S., Crowley, Q. G., Farrant, A., Goodenough, K. M., McKervey, J., Pharaoh, T., Phillips, E., Schofield, D., and Thomas, R. J. (2006). *The geology and geophysics of the United Arab Emirates : Volume 2, Geology.* Ministry of Energy, Petroleum and Minerals Sector, Minerals Department, Abu Dhabi, United Arab Emirates.

Tackley, P. J. (2000). The Quest for Self-Consistent Generation of Plate Tectonics in Mantle Convection Models. In RIchards, M., Gordon, R., and van der Hilst, R., editors, *The History and Dynamics of Global Plate Motions, American Geophysical Union Monograph 121*, pages 47–72. American Geophysical Union, Washington, DC.

Takazawa, E., Okayasu, T., and Satoh, K. (2003). Geochemistry and origin of the basal lherzolites from the northern Oman ophiolite (northern Fizh block). *Geochemistry, Geophysics, Geosystems*, 4(2).

Tarapoanca, M., Andriessen, P., Broto, K., Chérel, L., Ellouz-Zimmermann, N., Faure, J.-L., Jardin, A., Naville, C., and Roure, F. (2010). Forward kinematic modelling of a regional transect in the Northern Emirates using geological and apatite fission track age constraints on paleo-burial history. *Arabian Journal of Geosciences*, 3(4):395–411.

Tasaka, M., Hiraga, T., and Michibayashi, K. (2014). Influence of mineral fraction on the rheological properties of forsterite + enstatite during grain size sensitive creep: 3. Application of grain growth and flow laws on peridotite ultramylonite. *Journal of Geophysical Research: Solid Earth*, 119(2):840–857.

Tasaka, M., Hiraga, T., and Zimmerman, M. E. (2013). Influence of mineral fraction on the rheological properties of forsterite + enstatite during grain-size-sensitive creep: 2. Deformation experiments. *Journal of Geophysical Research: Solid Earth*, 118(8):3991–4012.

Tasaka, M., Zimmerman, M. E., and Kohlstedt, D. L. (2017). Rheological Weakening of Olivine + Orthopyroxene Aggregates Due to Phase Mixing: Part 2. Microstructural Development. *Journal of Geophysical Research: Solid Earth*, pages 1–16.

Thomas, R. J. and Ellison, R. (2014). *Geological evolution of the United Arab Emirates: Over Six Hundred Million Years of Earth History*. British Geological Survey, Keyworth, Nottingham.

Toriumi, M. (1979). Relation between dislocation density and subgrain size of naturally deformed olivine in peridotites. *Contributions to Mineralogy and Petrology*, 68(2):181–186.

Toy, V. G., Newman, J., Lamb, W., and Tikoff, B. (2010). The role of pyroxenites in formation of shear instabilities in the mantle: Evidence from an ultramafic ultramylonite, Twin Sisters massif, Washington. *Journal of Petrology*, 51(1-2):55–80.

Tsuchiya, N., Shibata, T., Yoshikawa, M., Adachi, Y., Miyashita, S., Adachi, T., Nakano, N., and Osanai, Y. (2013). Petrology of Lasail plutonic complex, northern Oman ophiolite, Oman: An example of arc-like magmatism associated with ophiolite detachment. *Lithos*, 156-159:120–138.

Umino, S., Yanai, S., Jaman, A., Nakamura, Y., and Iiyama, J. (1990). The transition from spreading to subduction: Evidence from the Semail ophiolite, northern Oman

mountains. In Malpas, J., editor, *Ophiolites: Oceanic Crustal Analogues. Proceedings of the Symposium Troodos 1987.*, pages 375–395. Geological Survey Department, Ministry of Agriculture and Natural Resources, Nicosia Cyprus.

Underwood, E. (1970). *The Mathematical Foundations of Quantitative Stereology.* Addison-Wesley, Reading, Mass.

Van der Wal, D., Chopra, P., Drury, M., and Fitz Gerald, J. (1993). Relationships between dynamically recrystallized grain size and deformation conditions in experimentally deformed olivine rocks. *Geophysical Research Letters*, 20(14):1479–1482.

van Hinsbergen, D. J. J., Peters, K., Maffione, M., Spakman, W., Guilmette, C., Thieulot, C., Plümper, O., Gürer, D., Brouwer, F. M., Aldanmaz, E., and Kaymakc, N. (2015). Dynamics of intraoceanic subduction initiation: 2. Suprasubduction zone ophiolite formation and metamorphic sole exhumation in context of absolute plate motions. *Geochemistry, Geophysics, Geosystems*, 16(August):n/a–n/a.

VanTongeren, J., Hirth, G., and Kelemen, P. B. (2015). Constraints on the accretion of the gabbroic lower oceanic crust from plagioclase lattice preferred orientation in the Samail ophiolite. *Earth and Planetary Science Letters*, 427:249–261.

Wakabayashi, J. and Dilek, Y. (2003). What constitutes 'emplacement' of an ophiolite?: Mechanisms and relationship to subduction initiation and formation of metamorphic soles. *Geological Society, London, Special Publications*, 218(1):427–447.

Wakabayashi, J., Ghatak, A., and Basu, A. R. (2010). Suprasubduction-zone ophiolite generation, emplacement, and initiation of subduction: A perspective from geochemistry, metamorphism, geochronology, and regional geology. *Bulletin of the Geological Society of America*, 122(9-10):1548–1568.

Warren, C. J., Parrish, R. R., Searle, M., and Waters, D. J. (2003). Dating the subduction of the Arabian continental margin beneath the Semail ophiolite, Oman. *Geology*, 31(10):889–892.

Warren, C. J., Parrish, R. R., Waters, D. J., and Searle, M. (2005). Dating the geologic history of Oman's Semail ophiolite: Insights from U-Pb geochronology. *Contributions to Mineralogy and Petrology*, 150(4):403–422.

Warren, J. M. and Hirth, G. (2006). Grain size sensitive deformation mechanisms in naturally deformed peridotites. *Earth and Planetary Science Letters*, 248(1-2):423–435.

Wheeler, J. (2009). The preservation of seismic anisotropy in the Earth's mantle during diffusion creep. *Geophysical Journal International*, 178(3):1723–1732.

White, R. W., Powell, R., Holland, T., Johnson, T., and Green, E. C. R. (2014). New mineral activity-composition relations for thermodynamic calculations in metapelitic systems. *Journal of Metamorphic Geology*, 32(3):261–286.

White, R. W., Powell, R., Holland, T., and Worley, B. A. (2000). The effect of TiO2 and Fe2O3 on metapelitic assemblages at greenschist and amphibolite facies conditions : mineral equilibria calculations in the system K2OFeOMgOAl2O3SiO2H2OTiO2Fe2O3. *Journal of Metamorphic Geology*, 18:497–511.

Wicks, F. (1969). *X-ray and optical studies of serpentine minerals*. PhD thesis, University of Oxford.

Williams, H. and Smyth, W. R. (1973). Metamorphic aureoles beneath ophiolite suites and alpine peridotites; tectonic implications with west Newfoundland examples.

Worley and Powell, R. (2000). High-precision relative thermobarometry: theory and a worked example. *Journal of Metamorphic Geology*, 18(1):91–101.

Yamasaki, T., Maeda, J., and Mizuta, T. (2006). Geochemical evidence in clinopyroxenes from gabbroic sequence for two distinct magmatisms in the Oman ophiolite. *Earth and Planetary Science Letters*, 251(1-2):52–65.

Yoshikawa, M., Python, M., Tamura, A., Arai, S., Takazawa, E., Shibata, T., Ueda, A., and Sato, T. (2015). Melt extraction and metasomatism recorded in basal peridotites above the metamorphic sole of the northern Fizh massif, Oman ophiolite. *Tectonophysics*, 650:53–64.

Zhao, Y. H., Ginsberg, S. B., and Kohlstedt, D. L. (2004). Solubility of hydrogen in olivine: Dependence on temperature and iron content. *Contributions to Mineralogy and Petrology*, 147(2):155–161.

Zimmerman, M. E. and Kohlstedt, D. L. (2004). Rheological Properties of Partially Molten Lherzolite. *Journal of Petrology*, 45(2):275–298.

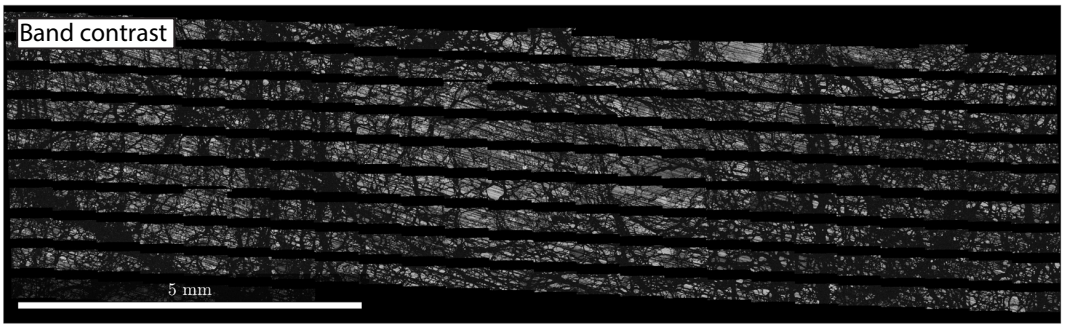
Appendices

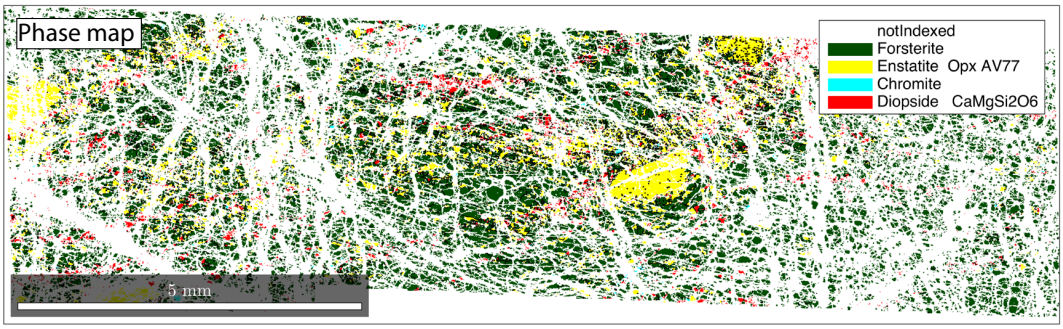
Appendix A

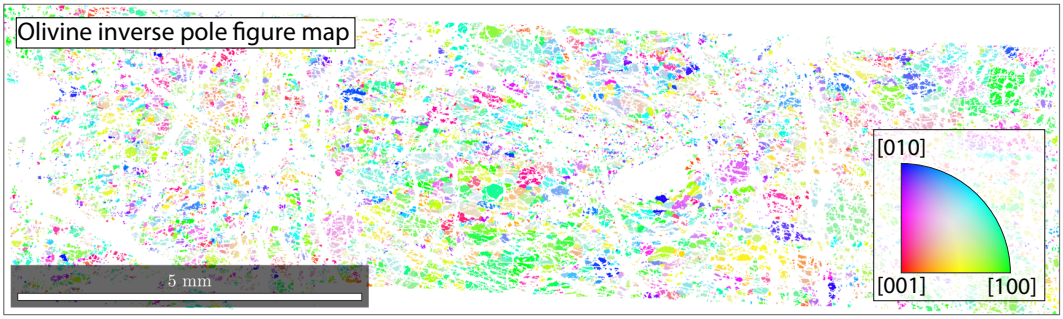
EBSD maps

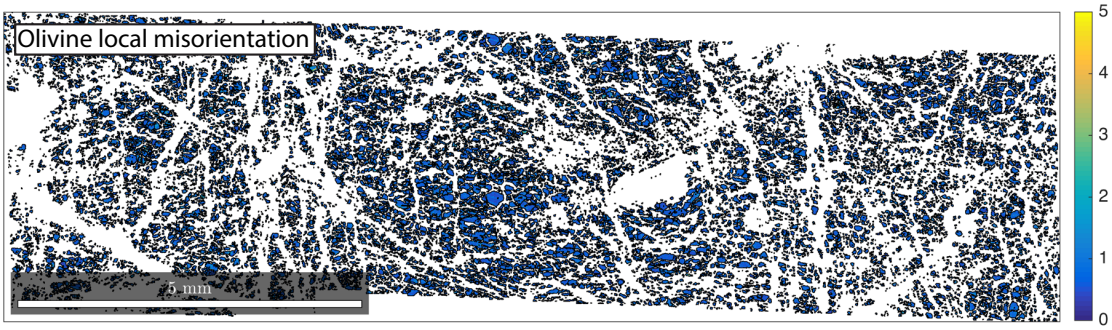
Band contrast, phase, olivine inverse pole figure, and olivine local misorientation maps for all samples.

LH14

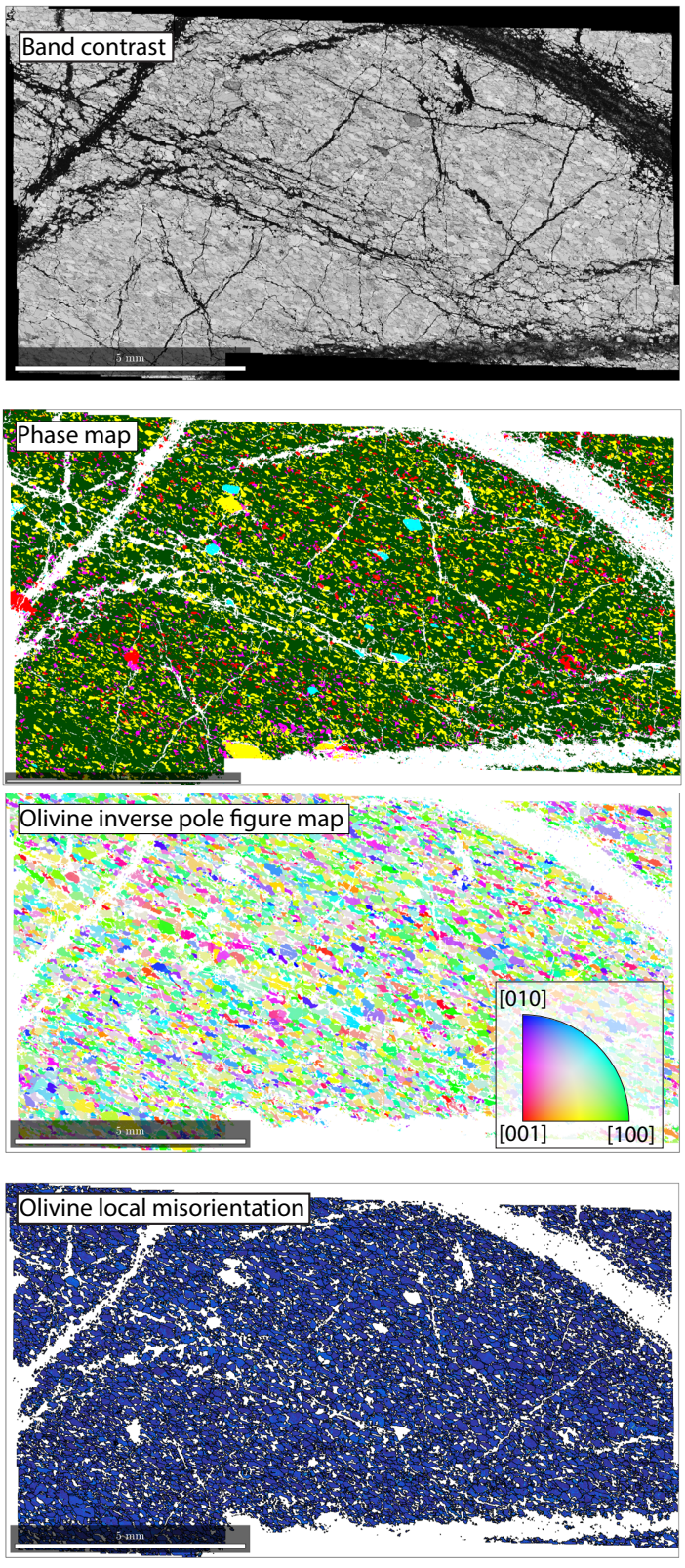

Band contrast
5 mm


Phase map
notIndexed
Forsterite
Enstatite Opx AV77
Chromite
Diopside CaMgSi2O6
5 mm

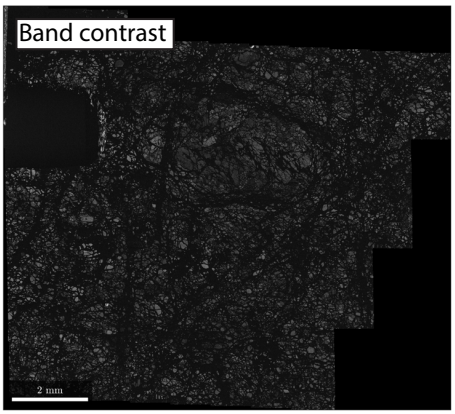

Olivine inverse pole figure map
[010]
[001]
[100]
5 mm

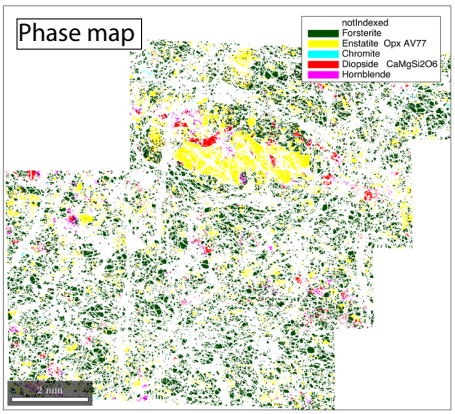

Olivine local misorientation
5 mm
5
4
3
2
1
0

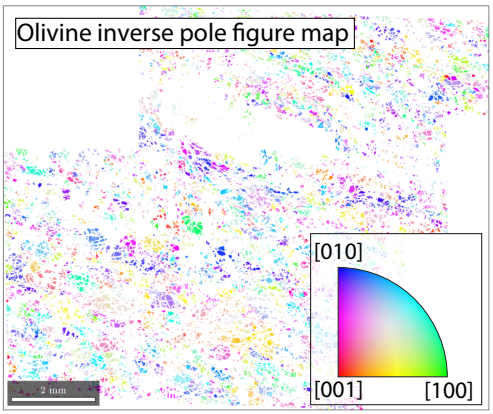
LH17

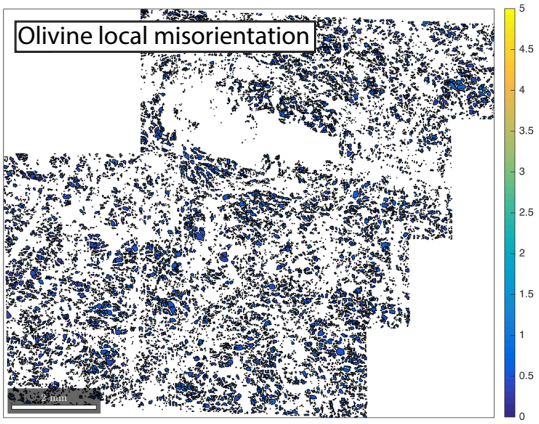

Band contrast
5 mm
Phase map
Olivine inverse pole figure map
[010]
[001]
[100]
5 mm
Olivine local misorientation
5 mm
5
4.5
4
3.5
3
2.5
2
1.5
1
0.5
0

LH25

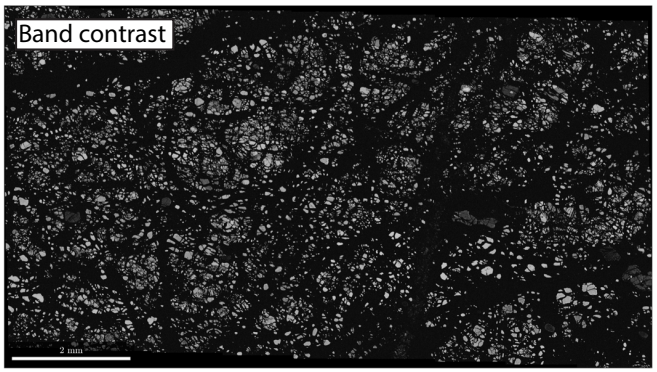

Band contrast
2 mm

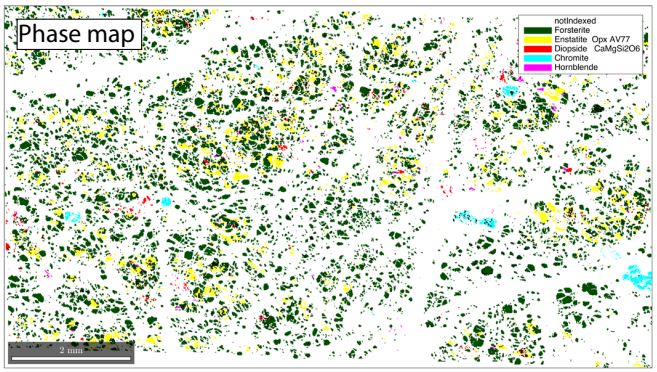

Phase map
notIndexed
Forsterite
Enstatite Opx AV77
Chromite
Diopside CaMgSi2O6
Hornblende
2 mm

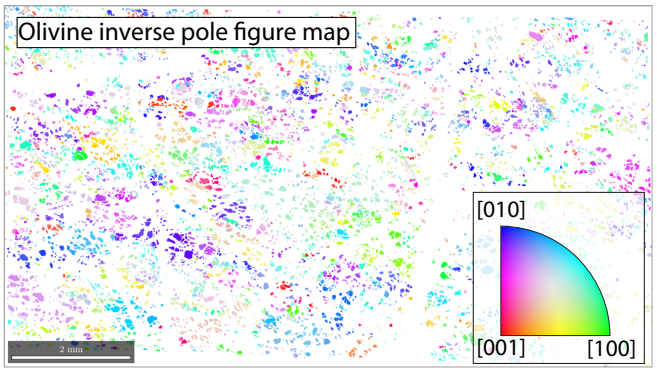

Olivine inverse pole figure map
[010]
[001]
[100]
2 mm

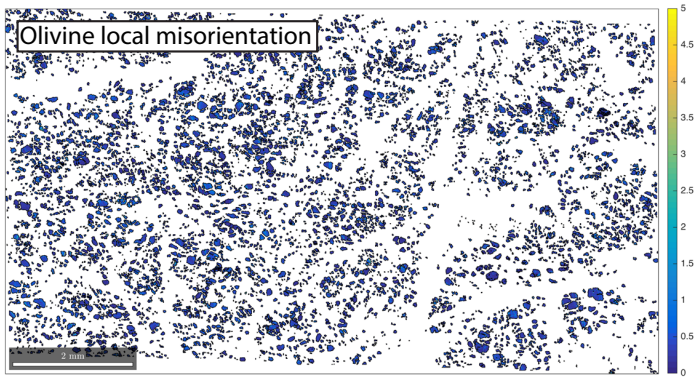

Olivine local misorientation
5
4.5
4
3.5
3
2.5
2
1.5
1
0.5
0
2 mm

LH26

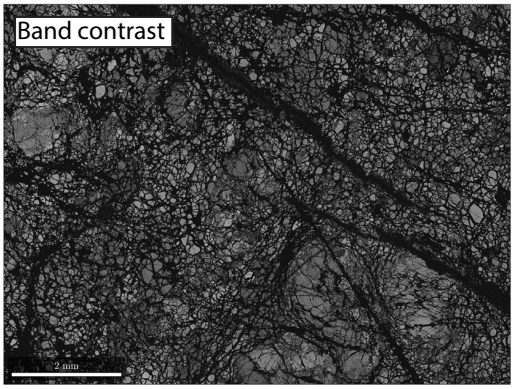

Band contrast
2 mm

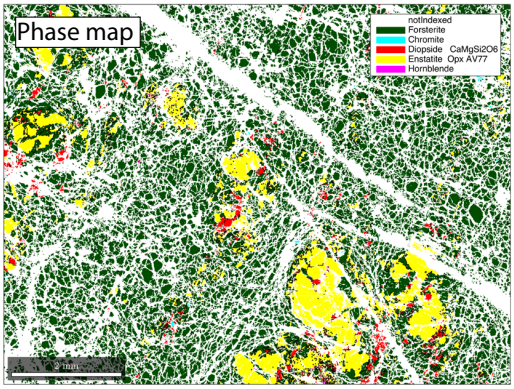

Phase map
notIndexed
Forsterite
Enstatite Opx AV77
Diopside CaMgSi2O6
Chromite
Hornblende
2 mm

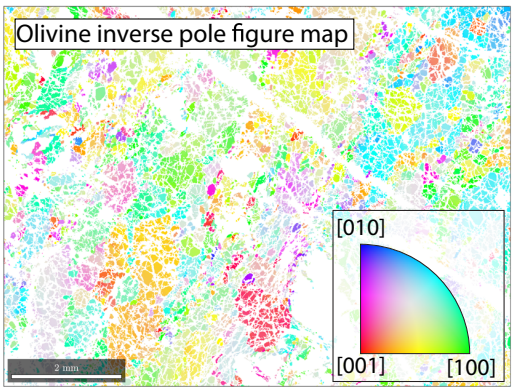

Olivine inverse pole figure map
[010]
[001]
[100]
2 mm

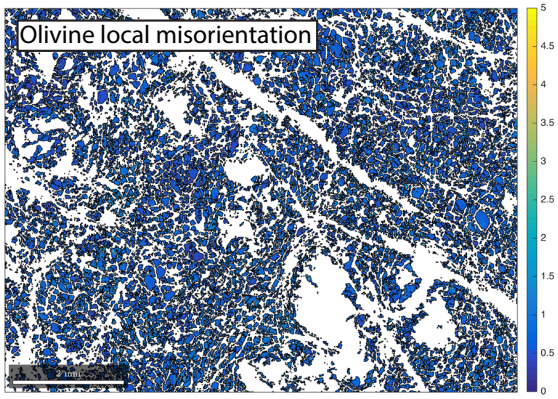

Olivine local misorientation
5
4.5
4
3.5
3
2.5
2
1.5
1
0.5
0
2 mm

LH27

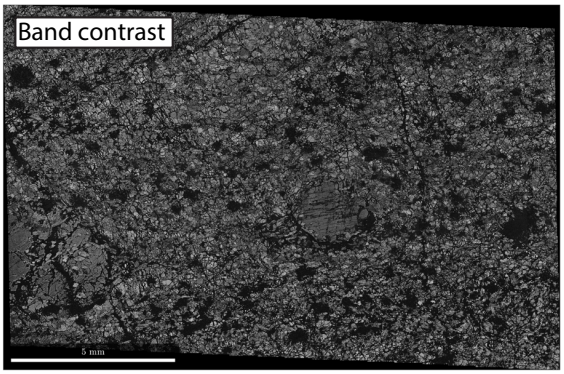

Band contrast
2 mm

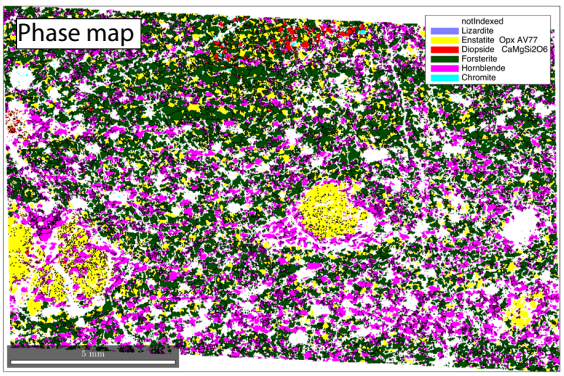

Phase map
notindexed
Forsterite
Chromite
Diopside CaMgSi2O6
Enstatite Opx AV77
Hornblende
2 mm

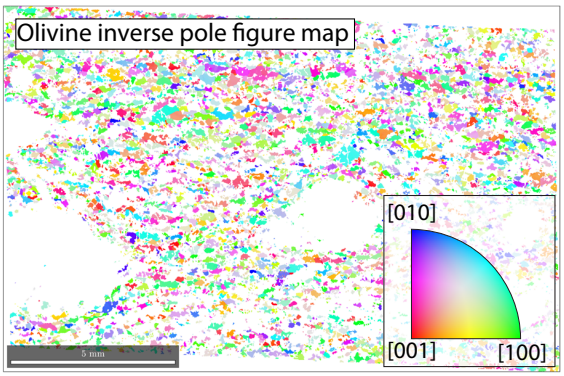

Olivine inverse pole figure map
[010]
[001]
[100]
2 mm

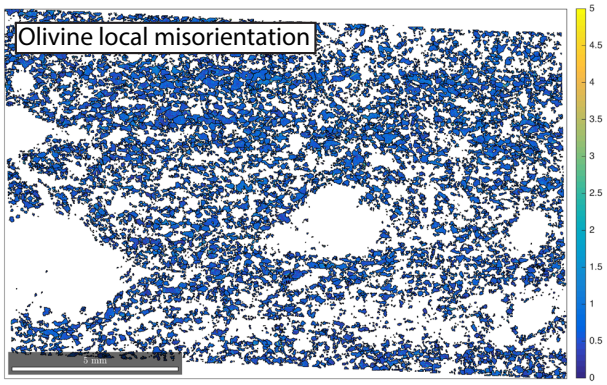

Olivine local misorientation
2 mm
5
4.5
4
3.5
3
2.5
2
1.5
1
0.5
0

LH28


Band contrast
5 mm

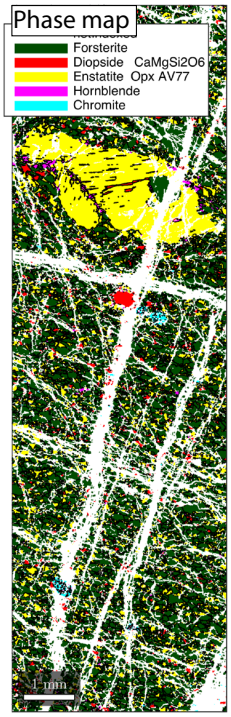

Phase map
notIndexed
Lizardite
Enstatite Opx AV77
Diopside CaMgSi2O6
Forsterite
Hornblende
Chromite
5 mm

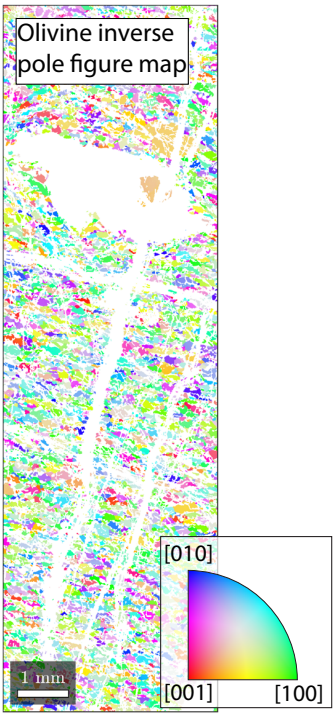

Olivine inverse pole figure map
[010]
[001]
[100]
5 mm

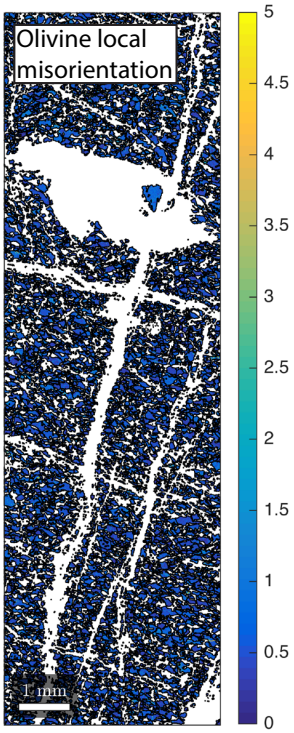

Olivine local misorientation
5
4.5
4
3.5
3
2.5
2
1.5
1
0.5
0
5 mm

LH18


Band contrast
1 mm

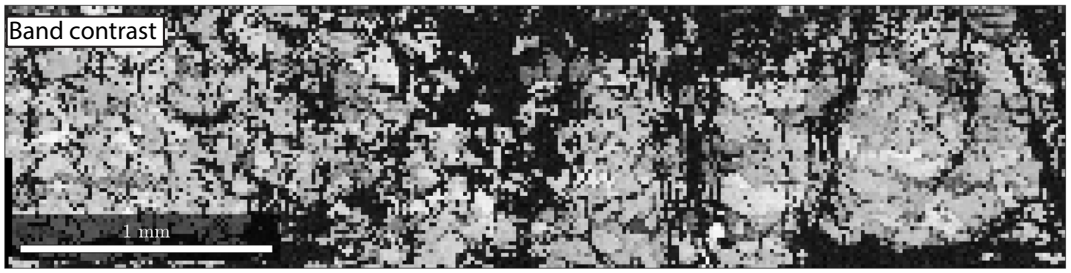

Phase map
Forsterite
Diopside CaMgSi2O6
Enstatite Opx AV77
Hornblende
Chromite
1 mm

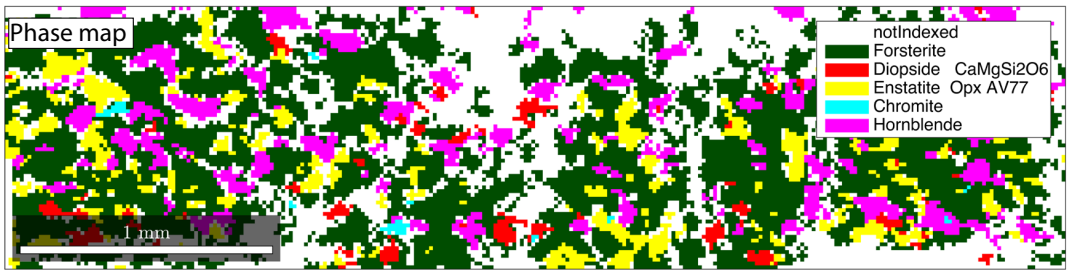

Olivine inverse pole figure map
[010]
[001]
[100]
1 mm

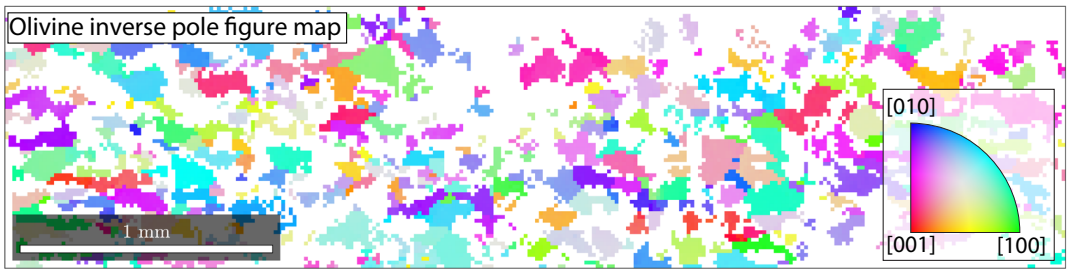

Olivine local misorientation
1 mm

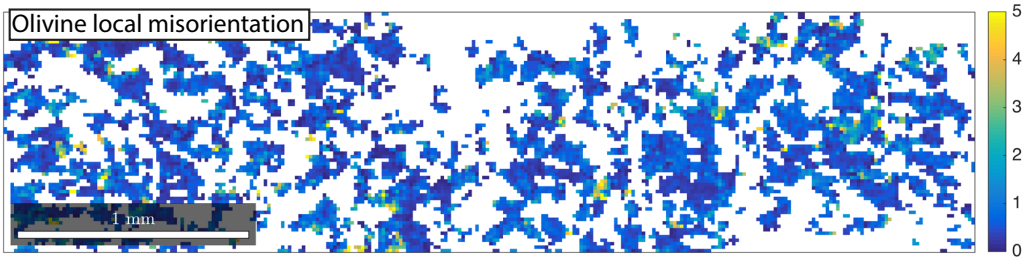
5
4.5
4
3.5
3
2.5
2
1.5
1
0.5
0

LH19


Band contrast
1 mm


Phase map
1 mm
notIndexed
Forsterite
Diopside CaMgSi2O6
Enstatite Opx AV77
Chromite
Hornblende


Olivine inverse pole figure map
1 mm
[010]
[001]
[100]


Olivine local misorientation
1 mm
5
4
3
2
1
0

Appendix B

Electron microprobe analyses

A complete table of electron microprobe analyses, as well as SEM-EDS results from rastering saussurite. The mineral is listed in the comments column. Excluded analyses are preceded by fx (fracture), mx (mixing), and $*$ (high total). Crosses mark closely spaced analyses that were excluded from statistical analysis. In some instances, minerals are followed by a second mineral in brackets. The second mineral was what was incorrectly labelled during spot selection, but was retained for 'book-keeping' purposes. Mineral abbreviations are amp (amphibole), cpx (clinopyroxene), bt (biotite), grt (garnet), pl (plagioclase), ep (epidote), ttn (titanite), ilm (ilmenite), ru (rutile), saus (saussurite). Some transects are identified by shaded rows, the specific colour of which has no meaning but is there for readability.

Sample	Point	SiO2	TiO2	Al2O3	FeO	MnO	MgO	CaO	Na2O	K2O	Total	Comment	Distance (µm)
TA14	5 / 1 .	38.30	0.06	21.52	24.57	1.61	5.40	8.20	0.02	0.00	99.76	Grt1	0
TA14	6 / 1 .	38.45	0.07	21.86	23.95	1.50	5.07	9.28	0.04	0.06	100.37	Grt2	221
TA14	7 / 1 .	38.01	0.20	21.23	23.77	1.43	5.26	9.50	0.03	0.02	99.45	Grt3	1045
TA14	8 / 1 .	38.13	0.07	21.84	24.28	1.49	5.44	8.59	0.03	0.03	99.94	Grt4	1431
TA14	9 / 1 .	37.86	0.12	21.40	24.50	1.56	5.60	8.30	0.02	-0.01	99.37	Grt5	2173
TA14	10 / 1 .	37.81	0.11	21.05	24.44	1.45	5.54	8.48	0.05	0.01	98.96	Grt6	2672
TA14	11 / 1 .	37.97	0.11	21.34	24.46	1.52	5.61	8.29	0.02	0.01	99.36	Grt7	3148
TA14	12 / 1 .	38.01	0.06	21.73	25.18	1.62	5.61	7.85	0.01	0.00	100.10	Grt8	4284
TA14	13 / 1 .	38.18	0.11	21.11	25.35	1.55	5.46	8.23	0.03	0.00	100.04	Grt9	4797
TA14	14 / 1 .	38.11	0.17	21.13	25.00	1.49	5.40	8.19	0.03	0.01	99.56	Grt10	5859
TA14	15 / 1 .	38.09	0.11	21.03	25.24	1.50	5.39	8.13	0.04	0.00	99.53	Grt11	6215
TA14	16 / 1 .	38.18	0.12	21.08	24.96	1.52	5.48	8.40	0.03	-0.01	99.78	Grt12	6487
TA14	17 / 1 .	38.28	0.09	21.74	23.92	1.49	5.40	9.01	0.02	0.01	100.00	Grt13	6997
TA14	18 / 1 .	37.89	0.10	21.41	23.26	1.47	4.75	10.32	0.04	0.00	99.24	Grt14	7359
TA14	19 / 1 .	38.13	0.08	21.78	23.97	1.44	4.40	10.69	0.00	0.02	100.51	Grt15	7675
TA14	20 / 1 .	37.85	0.08	21.40	23.22	1.38	4.04	11.14	0.01	0.00	99.18	Grt16	7850
TA14	21 / 1 .	38.01	0.09	21.47	23.66	1.44	4.56	10.05	0.04	0.01	99.40	Grt17	8049
TA14	22 / 1 .	37.87	0.08	21.62	23.58	1.41	4.64	10.10	0.01	0.01	99.34	Grt18	8096
TA14	23 / 1 .	37.97	0.08	21.78	22.86	1.43	4.98	10.08	0.02	0.00	99.24	Grt19	8172
TA14	24 / 1 .	37.86	0.09	21.80	23.53	1.42	5.28	9.24	0.02	0.00	99.29	Grt20	8195
TA14	25 / 1 .	38.00	0.10	21.57	24.26	1.46	5.47	8.35	0.01	0.00	99.28	Grt21	8220
TA14	26 / 1 .	37.54	0.07	21.46	25.82	1.94	4.54	7.54	0.01	0.01	98.96	Grt22	8271
TA14	27 / 1 .	49.15	0.38	4.81	10.60	0.21	10.53	20.87	1.23	-0.01	97.83	Cpx1	
TA14	28 / 1 .	49.87	0.29	3.88	10.51	0.22	10.93	20.61	1.27	0.00	97.66	Cpx2	
TA14	29 / 1 .	41.63	1.06	12.83	15.33	0.12	10.57	10.88	1.94	0.67	95.08	amp (Cpx3)	
TA14	30 / 1 .	49.19	0.50	4.98	10.65	0.19	10.56	20.69	1.36	0.01	98.17	Cpx4	
TA14	31 / 1 .	48.04	0.49	4.94	10.82	0.21	10.37	19.63	1.24	0.03	95.82	[fx]Cpx5	
TA14	32 / 1 .	47.48	0.42	4.95	10.24	0.17	10.57	19.90	1.27	0.03	95.05	[fx]Cpx5	
TA14	33 / 1 .	38.04	0.07	21.52	24.95	1.59	5.26	8.35	0.06	-0.01	99.85	grt profile ds33	0
TA14	33 / 2 .	37.98	0.06	21.56	24.69	1.60	5.15	8.47	0.03	0.00	99.59	grt profile ds33	11
TA14	33 / 3 .	38.05	0.07	21.35	24.54	1.55	5.16	8.63	0.00	0.00	99.39	grt profile ds33	22
TA14	33 / 4 .	37.80	0.09	20.58	23.43	1.41	4.81	10.51	0.08	0.10	98.84	grt profile ds33	32
TA14	33 / 5 .	36.85	0.08	20.89	21.66	1.18	4.17	12.95	-0.01	0.00	97.83	grt profile ds33	43
TA14	33 / 6 .	33.11	0.14	17.60	20.25	0.32	3.76	12.37	0.05	0.05	87.69	[fx]grt profile ds33	54
TA14	33 / 7 .	39.64	0.05	19.68	25.68	1.67	4.30	8.53	0.18	0.14	99.92	grt profile ds33	65
TA14	33 / 8 .	49.80	0.30	3.47	10.08	0.19	11.21	21.59	0.99	0.00	97.65	cpx profile ds33	76
TA14	33 / 9 .	49.75	0.42	4.58	10.65	0.23	10.58	21.25	1.18	0.00	98.66	cpx profile ds33	86
TA14	33 / 10 .	45.32	0.44	4.46	10.91	0.19	9.01	20.72	1.05	0.00	92.14	[fx]cpx profile ds33	97
TA14	33 / 11 .	49.54	0.47	4.83	10.97	0.25	10.33	20.65	1.28	0.01	98.35	cpx profile ds33	108
TA14	33 / 12 .	49.47	0.49	5.14	11.10	0.20	10.52	20.26	1.31	-0.01	98.52	cpx profile ds33	119
TA14	33 / 13 .	49.54	0.42	4.54	11.01	0.23	10.53	20.75	1.28	0.01	98.36	cpx profile ds33	130
TA14	33 / 14 .	49.58	0.46	4.78	11.29	0.21	10.48	20.54	1.24	0.01	98.63	cpx profile ds33	140
TA14	33 / 15 .	50.00	0.38	4.32	10.88	0.22	10.78	20.65	1.19	0.00	98.48	cpx profile ds33	151
TA14	33 / 16 .	49.45	0.42	4.70	10.83	0.20	10.49	20.63	1.25	0.00	97.99	cpx profile ds33	162
TA14	34 / 1 .	49.20	0.48	5.28	11.30	0.25	10.29	20.84	1.35	0.01	99.04	Cpx7	
TA14	35 / 1 .	41.67	1.95	12.92	16.14	0.19	9.86	11.38	2.26	0.59	96.98	amp1	
TA14	36 / 1 .	41.61	1.65	12.82	16.06	0.16	9.74	11.23	2.22	0.56	96.11	amp2	
TA14	37 / 1 .	49.05	0.46	5.08	10.48	0.23	10.31	21.25	1.22	0.01	98.11	Cpx7	
TA14	38 / 1 .	48.67	0.49	5.19	11.54	0.23	10.32	20.72	1.23	0.05	98.48	Cpx8	
TA14	39 / 1 .	41.39	1.87	12.86	16.90	0.15	9.46	11.31	2.33	0.59	96.92	amp3	
TA14	40 / 1 .	29.79	0.06	17.75	30.01	0.74	3.78	6.37	0.03	0.02	88.58	[fx]grt23	
TA14	41 / 1 .	38.09	0.06	21.60	24.69	1.38	5.56	8.02	0.02	0.00	99.44	grt24	
TA14	42 / 1 .	49.61	0.41	4.82	10.02	0.18	10.91	20.94	1.29	0.00	98.20	cpx9	
TA14	43 / 1 .	41.96	1.68	12.63	16.47	0.14	9.65	11.39	2.07	0.58	96.63	amp4	
TA14	44 / 1 .	41.62	1.93	13.17	16.32	0.15	9.47	11.37	2.21	0.57	96.84	amp5	
TA14	45 / 1 .	48.95	0.50	4.80	10.81	0.23	10.42	20.76	1.19	0.01	97.71	cpx10	
TA14	46 / 1 .	49.74	0.37	3.76	10.96	0.18	11.00	20.34	0.97	0.08	97.44	cpx (profile46)	0
TA14	46 / 2 .	49.73	0.39	4.11	10.63	0.19	10.64	21.63	1.15	0.00	98.52	cpx (profile46)	16
TA14	46 / 3 .	49.19	0.48	4.71	10.99	0.22	10.38	20.97	1.15	0.00	98.14	cpx (profile46)	32
TA14	46 / 4 .	49.65	0.39	4.26	10.77	0.17	10.61	21.82	1.07	-0.01	98.79	cpx (profile46)	48
TA14	46 / 5 .	49.37	0.46	4.43	10.70	0.22	10.48	21.32	1.15	0.01	98.18	cpx (profile46)	64
TA14	46 / 6 .	49.48	0.36	4.53	10.46	0.20	10.60	21.69	1.13	0.01	98.50	cpx (profile46)	80
TA14	46 / 7 .	49.71	0.34	4.61	10.48	0.21	10.49	21.68	1.20	0.00	98.75	cpx (profile46)	96
TA14	46 / 8 .	50.32	0.15	3.34	10.04	0.18	11.29	22.05	0.95	0.00	98.33	cpx (profile46)	112
TA14	46 / 9 .	38.07	0.73	19.83	5.28	0.09	1.25	31.61	0.18	0.07	97.17	[mx]boundary profile46	128
TA14	46 / 10 .	37.90	0.07	21.57	26.21	1.77	4.19	7.99	0.01	0.00	99.74	grt (profile46)	144
TA14	46 / 11 .	38.25	0.10	21.67	24.52	1.32	5.18	8.91	0.03	0.00	99.99	grt (profile46)	160
TA14	46 / 12 .	38.10	0.12	21.66	23.67	1.27	5.19	9.50	0.01	0.01	99.54	grt (profile46)	177
TA14	46 / 13 .	38.41	0.07	22.23	23.29	1.25	5.01	10.24	0.03	0.00	100.57	grt (profile46)	193
TA14	46 / 14 .	38.23	0.10	21.72	23.34	1.27	4.84	10.40	0.02	0.02	99.94	grt (profile46)	209
TA14	46 / 15 .	38.19	0.09	21.49	23.40	1.32	4.83	10.33	0.02	0.01	99.74	grt (profile46)	225
TA14	46 / 16 .	38.04	0.11	21.70	23.56	1.35	4.71	10.39	0.02	0.00	99.90	grt (profile46)	241
TA14	46 / 17 .	37.32	0.09	21.76	23.32	1.34	4.65	10.31	0.03	0.00	98.82	grt (profile46)	257
TA14	46 / 18 .	38.35	0.08	21.85	23.39	1.36	4.79	10.36	0.02	0.00	100.20	grt (profile46)	273

Sample	Point	SiO2	TiO2	Al2O3	FeO	MnO	MgO	CaO	Na2O	K2O	Total	Comment	Distance (µm)
TA14	46 / 19 .	38.30	0.12	21.59	23.32	1.39	4.79	10.25	0.03	0.00	99.81	grt (profile46)	289
TA14	46 / 20 .	38.14	0.07	21.84	23.48	1.36	4.99	10.27	0.05	0.01	100.21	grt (profile46)	305
TA14	47 / 1 .	49.64	0.51	5.20	10.44	0.22	10.44	21.12	1.35	0.00	98.96	cpx profile47	0
TA14	47 / 2 .	49.80	0.47	5.23	10.66	0.20	10.33	20.72	1.40	0.01	98.86	†cpx profile48	17
TA14	47 / 3 .	49.56	0.52	5.21	10.84	0.21	10.34	20.65	1.33	0.00	98.71	†cpx profile49	34
TA14	47 / 4 .	49.36	0.50	5.21	10.74	0.23	10.37	20.79	1.30	0.01	98.50	†cpx profile50	52
TA14	47 / 5 .	49.55	0.51	5.02	10.68	0.21	10.34	21.07	1.21	0.01	98.65	cpx profile51	69
TA14	47 / 6 .	49.93	0.47	4.81	10.55	0.21	10.35	21.36	1.19	0.01	98.90	†cpx profile52	86
TA14	47 / 7 .	49.56	0.44	5.06	10.41	0.21	10.45	21.15	1.34	0.01	98.65	†cpx profile53	103
TA14	47 / 8 .	50.00	0.38	4.30	10.38	0.23	10.75	21.44	1.07	0.01	98.59	†cpx profile54	120
TA14	47 / 9 .	50.84	0.31	3.50	9.98	0.20	11.24	21.97	0.97	0.02	99.06	cpx profile55	137
TA14	47 / 10 .	41.46	1.77	12.29	16.63	0.10	9.48	11.50	2.31	0.58	96.17	amp profile47	155
TA14	47 / 11 .	41.93	1.77	12.81	16.99	0.16	8.56	10.70	2.08	0.61	95.69	amp profile47	172
TA14	47 / 12 .	43.00	1.75	13.15	16.79	0.16	9.21	11.48	2.24	0.61	98.46	amp profile47	189
TA14	47 / 13 .	41.91	1.70	12.57	16.55	0.14	9.58	11.43	2.14	0.52	96.62	†amp profile47	206
TA14	47 / 14 .	42.38	1.70	12.47	16.45	0.15	9.85	11.47	2.11	0.52	97.17	†amp profile47	223
TA14	47 / 15 .	41.46	1.84	13.14	16.46	0.14	9.25	11.40	2.43	0.58	96.78	†amp profile47	240
TA14	47 / 16 .	41.19	1.91	13.16	16.73	0.16	9.08	11.35	2.31	0.63	96.60	†amp profile47	258
TA14	47 / 17 .	41.51	1.64	12.05	17.91	0.12	8.91	10.19	1.82	0.65	94.87	low total profile47	275
TA14	47 / 18 .	42.01	1.94	12.52	16.44	0.16	9.57	11.44	2.16	0.57	96.89	†amp profile47	292
TA14	47 / 19 .	42.18	1.74	12.42	16.47	0.15	9.60	11.38	2.21	0.54	96.75	†amp profile47	309
TA14	47 / 20 .	39.37	1.80	11.22	16.50	0.14	9.37	11.05	2.05	0.49	92.08	[fx]amp profile47	326
TA14	48 / 1 .	39.83	0.28	4.59	17.05	0.17	5.36	16.44	0.43	0.23	84.40	[fx]ds48	0
TA14	48 / 2 .	46.59	0.38	5.50	11.37	0.23	9.65	18.61	1.03	0.10	93.48	[fx]ds48	27
TA14	48 / 3 .	47.94	0.39	4.51	12.30	0.24	10.03	20.39	1.09	0.05	96.97	cpx ds48	54
TA14	48 / 4 .	50.03	0.35	4.19	10.57	0.27	10.66	21.58	1.23	0.00	98.91	cpx ds48	80
TA14	48 / 5 .	50.04	0.42	4.48	10.67	0.26	10.66	21.40	1.26	-0.01	99.24	cpx ds48	107
TA14	48 / 6 .	49.85	0.41	4.94	10.69	0.23	10.54	21.17	1.25	0.01	99.13	cpx ds48	134
TA14	48 / 7 .	24.31	0.41	2.74	12.55	0.25	4.45	17.03	0.43	0.06	62.28	[fx]cpx ds48	161
TA14	48 / 8 .	49.93	0.42	4.62	10.78	0.24	10.76	21.22	1.24	0.02	99.27	cpx ds48	188
TA14	48 / 9 .	42.95	1.22	11.42	17.03	0.18	10.16	11.67	1.99	0.43	97.07	amp ds48	215
TA14	48 / 10 .	42.32	1.43	11.81	17.20	0.19	9.87	11.51	2.10	0.49	96.95	amp ds48	241
TA14	48 / 11 .	42.81	1.34	11.15	16.87	0.19	10.30	11.66	2.09	0.43	96.84	amp ds48	268
TA14	48 / 12 .	42.72	1.43	11.26	17.75	0.14	9.76	10.96	2.04	0.48	96.62	amp ds48	295
TA14	48 / 13 .	43.70	1.56	11.15	16.35	0.20	10.21	11.41	2.06	0.43	97.13	amp ds48	322
TA14	48 / 14 .	42.86	1.60	11.69	16.53	0.19	10.21	11.46	2.14	0.45	97.17	amp ds48	349
TA14	48 / 15 .	41.90	1.92	12.73	16.50	0.17	9.60	11.46	2.21	0.58	97.11	amp ds48	376
TA14	48 / 16 .	41.71	1.89	12.66	16.72	0.19	9.57	11.31	2.20	0.56	96.83	amp ds48	402
TA14	48 / 17 .	42.09	1.95	12.96	16.80	0.20	9.56	11.51	2.20	0.58	97.89	amp ds48	429
TA14	48 / 18 .	2.16	0.64	0.88	28.76	0.08	2.18	2.37	0.61	0.16	37.86	[fx]amp ds48	456
TA14	48 / 19 .	41.76	1.91	13.06	16.64	0.18	9.55	11.37	2.26	0.56	97.34	amp ds48	483
TA14	48 / 20 .	41.82	1.97	13.03	16.41	0.17	9.46	11.39	2.31	0.63	97.25	amp ds48	510
TA14	48 / 21 .	41.92	2.02	12.95	16.23	0.18	9.56	11.40	2.30	0.58	97.18	amp ds48	537
TA14	48 / 22 .	34.68	1.09	13.82	22.86	0.17	10.16	7.78	1.85	0.43	92.88	[fx]amp ds48	563
TA14	48 / 23 .	42.42	1.94	12.31	16.19	0.19	9.89	11.39	2.24	0.58	97.21	amp ds48	590
TA14	48 / 24 .	42.52	1.93	11.98	16.08	0.16	10.26	11.67	2.13	0.49	97.28	amp ds48	617
TA14	48 / 25 .	43.04	1.87	11.73	15.95	0.17	10.32	11.56	2.08	0.50	97.27	amp ds48	644
TA14	48 / 26 .	42.45	1.89	12.23	16.09	0.19	10.21	11.63	2.22	0.49	97.46	amp ds48	671
TA14	48 / 27 .	43.14	1.83	11.84	15.49	0.20	10.54	11.59	2.08	0.51	97.26	amp ds48	698
TA14	48 / 28 .	50.40	0.45	4.29	10.20	0.24	10.92	21.50	1.07	-0.01	99.10	cpx ds48	724
TA14	48 / 29 .	47.19	0.70	5.14	11.82	0.20	11.02	18.04	1.12	0.16	95.41	[fx]cpx ds48	751
TA14	48 / 30 .	38.35	1.59	11.51	19.55	0.16	8.02	9.90	1.90	0.64	91.65	[fx]amp ds48	778
TA14	48 / 31 .	42.38	1.95	12.76	16.16	0.17	9.96	11.44	2.12	0.54	97.54	amp ds48	805
TA14	48 / 32 .	43.96	1.95	13.27	15.98	0.20	10.72	11.43	2.37	0.52	100.41	amp ds48	832
TA14	48 / 33 .	42.32	1.88	12.54	16.11	0.19	10.07	11.46	2.27	0.55	97.45	amp ds48	859
TA14	48 / 34 .	42.48	1.78	12.57	16.18	0.17	9.85	11.45	2.25	0.52	97.32	amp ds48	885
TA14	48 / 35 .	33.78	0.86	13.54	21.70	0.15	9.84	6.29	1.20	0.33	87.73	[fx]amp ds48	912
TA14	48 / 36 .	37.51	0.09	22.68	12.64	0.02	0.15	22.42	0.10	0.03	95.67	ep (ds48)	939
TA14	48 / 37 .	42.47	1.10	12.56	17.29	0.18	9.00	11.50	2.37	0.64	97.16	amp ds48	966
TA14	48 / 38 .	2.21	0.03	1.02	2.06	0.02	0.37	49.90	0.09	0.02	55.74	[fx]amp ds48	993
TA14	48 / 39 .	38.58	0.03	29.15	6.30	0.03	0.00	23.77	0.08	0.01	97.97	ep ds48	1020
TA14	48 / 40 .	38.67	0.01	30.02	4.84	0.05	-0.01	24.11	0.01	0.01	97.73	ep ds48	1046
TA14	1 / 1 .	38.14	0.08	31.12	3.30	0.07	0.00	24.38	0.01	0.01	97.12	Pl1	
TA14	2 / 1 .	63.71	0.00	21.75	1.00	0.01	0.08	3.85	10.68	0.10	101.18	Pl2	
TA14	3 / 1 .	51.20	-0.01	25.51	3.52	0.03	0.04	12.93	5.68	0.04	98.96	Pl3	
TA14	4 / 1 .	45.80	0.01	27.77	3.35	0.01	0.02	17.37	3.03	0.02	97.38	Pl4	
TA14	5 / 1 .	67.53	-0.01	20.42	0.01	-0.01	0.00	0.34	11.71	0.08	100.09	Pl5	
TA14	6 / 1 .	60.34	0.03	23.58	0.29	-0.02	-0.01	6.06	8.88	0.20	99.38	Pl6	
TA14	7 / 1 .	61.52	-0.03	23.92	0.16	0.02	-0.01	5.77	9.11	0.11	100.63	Pl7	
TA14	8 / 1 .	66.70	0.01	21.23	0.10	0.00	-0.01	1.06	11.13	0.12	100.35	Pl8	
TA14	9 / 1 .	57.49	0.01	24.99	0.64	-0.01	-0.01	8.78	7.49	0.07	99.47	Pl9	
TA14	10 / 1 .	57.59	0.02	25.44	0.29	0.00	-0.01	8.11	7.53	0.18	99.18	Pl10	
TA14	11 / 1 .	39.00	-0.03	31.70	3.15	0.04	-0.01	23.44	-0.01	0.01	97.36	Pl11	

Sample	Point	SiO2	TiO2	Al2O3	FeO	MnO	MgO	CaO	Na2O	K2O	Total	Comment	Distance (µm)
TA14	12 / 1 .	37.65	0.06	24.14	11.78	0.05	0.02	22.17	-0.01	0.01	95.88	fxPl12	
TA14	13 / 1 .	56.26	0.00	25.60	0.65	0.01	0.00	9.56	7.35	0.06	99.49	Pl13	
TA14	14 / 1 .	58.16	-0.01	24.60	0.48	0.02	0.00	8.04	7.83	0.10	99.23	Pl14	
TA14	15 / 1 .	60.88	0.01	26.20	0.11	0.00	0.02	0.69	8.46	3.71	100.10	Pl15	
TA14	16 / 1 .	39.22	-0.02	34.36	0.54	0.03	0.01	23.33	0.02	0.00	97.51	Pl16	
TA14	17 / 1 .	53.88	-0.01	26.23	1.20	0.00	-0.01	11.13	6.15	0.01	98.61	Pl17	
TA14	18 / 1 .	56.93	0.01	25.03	0.89	0.01	-0.01	8.72	7.42	0.05	99.06	Pl18	
TA14	19 / 1 .	42.09	1.94	12.74	15.83	0.19	9.89	10.64	2.18	0.53	96.16	amp6	
TA14	20 / 1 .	48.56	0.51	5.34	11.22	0.28	10.50	19.15	1.38	0.02	96.99	Cpx12	
TA14	21 / 1 .	38.16	0.09	21.80	23.39	1.66	4.81	9.36	0.02	0.02	99.34	Grt 25	
TA14	22 / 1 .	38.28	0.10	21.72	24.15	1.52	5.58	7.96	0.01	-0.01	99.39	Grt 26	
TA14	23 / 1 .	37.87	0.06	21.42	25.64	2.34	4.41	7.40	0.02	0.00	99.16	Grt 27	
TA14	24 / 1 .	51.19	0.20	3.20	9.74	0.21	11.54	20.85	1.05	0.00	98.01	Cpx 13	
TA14	25 / 1 .	50.28	0.37	4.22	9.99	0.21	10.87	20.78	1.04	-0.01	97.79	Cpx 14	
TA14	26 / 1 .	0.00	43.64	0.00	50.68	0.50	0.05	0.02	-0.03	-0.01	94.96	Ilm1	
TA14	27 / 1 .	0.03	47.83	0.00	47.24	0.70	0.01	0.20	-0.02	0.02	96.08	Ilm2	
TA14	28 / 1 .	42.93	1.62	12.81	15.46	0.18	10.26	10.93	2.09	0.54	96.87	amp7	
TA14	29 / 1 .	49.61	0.39	4.72	11.18	0.25	10.50	20.09	1.19	0.05	98.03	Cpx15	
TA14	30 / 1 .	49.27	0.48	4.94	11.23	0.26	10.69	19.50	1.14	0.04	97.59	Cpx16	
TA14	31 / 1 .	50.73	0.26	3.03	10.37	0.20	11.09	21.21	0.91	0.00	97.83	cpx Grt profile ds31	0
TA14	31 / 2 .	50.94	0.21	2.91	10.05	0.21	11.48	21.21	0.91	0.01	97.99	cpx Grt profile ds31	24
TA14	31 / 3 .	50.15	0.28	3.79	10.33	0.23	10.96	21.13	1.06	0.00	97.93	cpx Grt profile ds31	47
TA14	31 / 4 .	55.19	0.25	5.90	12.10	0.16	11.38	18.67	1.53	0.18	105.40	*profile ds31	71
TA14	31 / 5 .	49.42	0.45	4.48	10.94	0.18	10.67	21.45	0.88	0.01	98.52	cpx Grt profile ds31	94
TA14	31 / 6 .	48.15	0.38	4.88	10.29	0.20	10.09	21.05	0.96	0.00	96.02	cpx Grt profile ds31	118
TA14	31 / 7 .	49.90	0.43	4.54	9.51	0.18	10.96	21.33	1.02	0.01	97.90	cpx Grt profile ds31	142
TA14	31 / 8 .	51.15	0.17	3.03	9.92	0.19	11.46	21.38	1.04	0.00	98.34	cpx Grt profile ds31	165
TA14	31 / 9 .	38.25	0.85	14.70	19.84	0.22	7.64	10.29	1.73	0.49	94.05	mxGrt profile ds31	189
TA14	31 / 10 .	41.12	0.10	14.09	19.80	0.27	6.80	10.33	2.29	0.79	95.59	mxGrt profile ds31	212
TA14	31 / 11 .	39.78	0.22	14.44	16.42	0.33	5.57	16.69	2.27	0.44	96.20	mxGrt profile ds31	236
TA14	31 / 12 .	39.44	0.09	22.53	24.40	1.59	5.46	8.41	0.04	0.02	102.03	*Grt profile ds31	260
TA14	31 / 13 .	43.80	0.10	20.59	13.34	0.74	2.13	16.97	4.28	0.00	101.95	*Grt profile ds31	283
TA14	31 / 14 .	38.27	0.08	21.53	24.20	1.66	5.39	8.39	0.02	0.01	99.57	Grt profile ds31	307
TA14	31 / 15 .	27.48	0.03	18.12	30.21	0.21	11.72	0.22	0.22	0.06	88.30	fxprofile Grt ds31	330
TA14	31 / 16 .	40.78	0.02	16.65	11.03	0.12	3.31	0.59	4.74	0.32	77.58	fxprofile Grt ds31	354
TA14	31 / 17 .	29.88	0.06	17.82	16.44	0.55	2.44	16.00	1.39	0.14	84.75	fxprofile Grt ds31	377
TA14	31 / 18 .	37.98	0.07	21.82	24.29	1.66	5.57	8.04	0.06	0.00	99.50	Grt profile ds31	401
TA14	31 / 19 .	37.49	0.13	21.31	24.25	1.59	4.92	8.27	0.11	0.01	98.09	Grt profile ds31	425
TA14	31 / 20 .	37.98	0.07	21.09	24.46	1.60	5.45	8.32	0.06	0.01	99.06	Grt profile ds31	448
TA14	31 / 21 .	38.52	0.07	21.48	24.27	1.63	5.58	8.63	0.05	0.01	100.25	Grt profile ds31	472
TA14	31 / 22 .	38.28	0.10	21.46	24.16	1.60	5.52	8.29	0.02	0.01	99.43	Grt profile ds31	495
TA14	31 / 23 .	36.42	0.12	21.64	23.50	1.46	5.57	8.51	0.06	0.01	97.28	Grt profile ds31	519
TA14	31 / 24 .	38.21	0.07	21.69	24.40	1.61	5.45	8.13	0.03	0.02	99.63	Grt profile ds31	543
TA14	31 / 25 .	37.99	0.06	21.64	24.62	1.59	5.60	8.02	0.02	0.00	99.56	Grt profile ds31	566
TA14	31 / 26 .	38.82	0.10	21.93	23.73	1.61	5.36	9.22	0.08	0.00	100.86	Grt profile ds31	590
TA14	31 / 27 .	39.44	0.11	22.62	24.71	1.67	5.43	8.49	0.05	-0.02	102.59	*Grt profile ds31	613
TA14	31 / 28 .	38.18	0.09	21.24	24.49	1.62	5.25	8.79	0.03	-0.01	99.73	Grt profile ds31	637
TA14	31 / 29 .	38.29	0.09	21.16	24.60	1.61	5.04	8.88	0.05	-0.01	99.73	Grt profile ds31	661
TA14	31 / 30 .	38.16	0.09	21.53	24.49	1.63	5.19	8.68	0.06	0.00	99.85	Grt profile ds31	684
TA14	31 / 31 .	34.43	0.08	20.01	24.20	1.64	4.43	8.71	0.24	0.07	93.84	fxprofile Grt ds31	708
TA14	31 / 32 .	28.29	0.07	14.45	16.77	1.17	5.03	6.70	3.84	0.72	77.06	fxprofile Grt ds31	731
TA14	31 / 33 .	38.12	0.09	21.79	24.06	1.72	5.12	8.84	0.02	0.02	99.80	Grt profile ds31	755
TA14	31 / 34 .	38.13	0.09	21.55	24.54	1.66	4.88	9.35	0.07	0.00	100.29	Grt profile ds31	779
TA14	31 / 35 .	38.19	0.14	21.59	24.36	1.66	4.78	9.42	0.07	0.00	100.24	Grt profile ds31	802
TA14	31 / 36 .	38.12	0.12	21.45	24.29	1.63	4.86	9.28	0.06	0.02	99.84	Grt profile ds31	826
TA14	31 / 37 .	38.14	0.12	21.60	24.35	1.68	4.92	9.08	0.04	0.00	99.95	Grt profile ds31	849
TA14	31 / 38 .	38.16	0.08	21.68	24.28	1.63	4.98	9.02	0.03	0.00	99.86	Grt profile ds31	873
TA14	31 / 39 .	40.44	0.07	23.24	23.78	1.61	6.14	8.61	0.12	0.00	104.06	*Grt profile ds31	897
TA14	31 / 40 .	28.45	0.10	16.52	23.69	1.50	3.28	8.67	0.57	0.06	82.86	fxprofile Grt ds31	920
TA14	31 / 41 .	37.92	0.06	21.45	24.67	1.99	4.51	9.05	0.04	0.00	99.69	Grt profile ds31	944
TA14	31 / 42 .	38.10	0.12	21.22	24.75	1.76	4.65	9.57	0.04	0.00	100.21	Grt profile ds31	967
TA14	31 / 43 .	38.36	0.09	21.73	24.67	1.67	5.25	8.82	0.01	-0.01	100.61	Grt profile ds31	991
TA14	31 / 44 .	39.68	0.07	21.81	21.82	1.29	4.82	10.83	0.33	0.02	100.67	Grt profile ds31	1014
TA14	31 / 45 .	38.06	0.10	21.47	24.66	1.69	5.08	8.75	0.04	0.01	99.87	Grt profile ds31	1038
TA14	31 / 46 .	38.17	0.12	21.56	24.13	1.64	5.07	9.04	0.04	0.01	99.81	Grt profile ds31	1062
TA14	31 / 47 .	38.16	0.10	21.42	24.61	1.66	4.90	9.25	0.05	0.00	100.16	Grt profile ds31	1085
TA14	31 / 48 .	38.38	0.11	21.74	23.91	1.58	4.73	10.40	0.05	0.00	100.91	Grt profile ds31	1109
TA14	31 / 49 .	37.06	0.10	19.17	23.13	1.24	4.01	7.11	0.73	0.05	92.65	fxprofile Grt ds31	1132
TA14	31 / 50 .	38.32	0.07	21.44	24.65	1.69	5.36	8.92	0.02	-0.01	100.51	Grt profile ds31	1156
TA14	31 / 51 .	38.43	0.06	22.19	24.13	1.64	5.40	8.59	0.02	0.00	100.47	Grt profile ds31	1180
TA14	31 / 52 .	38.20	0.11	21.93	24.24	1.65	5.33	8.66	0.04	0.01	100.18	Grt profile ds31	1203
TA14	31 / 53 .	37.59	0.03	21.62	24.51	1.59	5.31	8.40	0.06	0.00	99.10	Grt profile ds31	1227
TA14	31 / 54 .	37.52	0.03	21.89	23.90	1.66	5.33	8.78	0.01	-0.01	99.15	Grt profile ds31	1250

Sample	Point	SiO2	TiO2	Al2O3	FeO	MnO	MgO	CaO	Na2O	K2O	Total	Comment	Distance (µm)
TA14	31 / 55 .	36.88	0.03	21.39	24.29	1.76	5.30	8.07	0.14	0.00	97.87	Grt profile ds31	1274
TA14	31 / 56 .	38.04	0.03	21.65	24.49	1.72	5.67	8.17	0.03	-0.01	99.81	Grt profile ds31	1298
TA14	31 / 57 .	33.12	0.07	20.28	23.62	1.36	4.37	8.62	0.43	0.04	91.91	fxprofile Grt ds31	1321
TA14	31 / 58 .	38.45	0.09	22.15	24.51	1.66	5.72	8.12	0.04	0.01	100.78	Grt profile ds31	1345
TA14	31 / 59 .	36.90	0.08	22.54	23.94	1.50	5.54	7.78	0.43	0.03	98.75	Grt profile ds31	1368
TA14	31 / 60 .	27.01	0.03	18.42	28.95	0.70	7.86	2.92	0.20	0.09	86.19	fxprofile Grt ds31	1392
TA14	31 / 61 .	38.05	0.08	21.72	24.73	1.67	5.87	7.92	0.02	0.00	100.04	Grt profile ds31	1416
TA14	31 / 62 .	38.09	0.14	21.37	24.21	1.66	5.49	8.87	0.01	-0.01	99.86	Grt profile ds31	1439
TA14	31 / 63 .	46.54	0.11	19.93	23.62	1.42	3.86	7.57	0.24	0.04	103.33	*Grt profile ds31	1463
TA14	31 / 64 .	38.28	0.10	21.64	24.31	1.64	5.67	8.32	0.03	0.01	100.03	Grt profile ds31	1486
TA14	31 / 65 .	35.49	0.03	27.60	7.75	0.07	0.43	21.39	0.02	0.00	92.80	fxprofile Grt ds31	1510
TA14	31 / 66 .	37.79	0.17	28.20	7.55	0.07	0.31	22.66	0.02	0.01	96.80	ep Grt profile ds31	1534
TA14	31 / 67 .	38.25	0.18	28.54	6.99	0.05	0.01	23.27	0.05	-0.01	97.36	ep Grt profile ds31	1557
TA14	31 / 68 .	38.30	0.06	21.76	25.35	1.79	4.99	7.89	0.06	-0.01	100.20	Grt profile ds31	1581
TA14	31 / 69 .	42.16	0.97	12.85	17.55	0.18	8.52	11.70	2.41	0.49	96.88	mx(Grt profile ds31)	1604
TA14	31 / 70 .	44.09	1.03	11.73	16.23	0.15	10.50	11.42	2.11	0.43	97.75	mx(Grt profile ds31)	1628
TA14	31 / 71 .	25.02	24.55	7.98	22.76	0.79	5.32	10.76	1.25	0.23	98.77	mxGrt profile ds31	1651
TA14	31 / 72 .	50.65	0.30	3.58	9.77	0.20	11.91	21.55	0.98	0.01	98.95	mx(Grt profile ds31)	1675
TA14	31 / 73 .	50.22	0.38	4.01	9.90	0.24	11.44	21.37	1.05	0.01	98.66	mx(Grt profile ds31)	1699
TA14	31 / 74 .	43.50	1.42	11.95	14.63	0.13	10.86	11.37	2.43	0.42	96.74	amp (Grt profile ds31)	1722
TA14	31 / 75 .	42.89	1.59	12.49	15.22	0.14	10.40	11.30	2.06	0.49	96.61	amp (Grt profile ds31)	1746
TA14	31 / 76 .	42.58	1.60	12.68	15.57	0.16	10.07	11.27	2.07	0.53	96.57	amp (Grt profile ds31)	1769
TA14	31 / 77 .	43.13	1.37	12.11	15.40	0.13	10.43	11.26	2.04	0.47	96.41	amp (Grt profile ds31)	1793
TA14	31 / 78 .	29.92	1.25	6.76	16.29	0.14	11.25	8.93	1.86	0.33	76.74	fxprofile Grt ds31	1817
TA14	31 / 79 .	43.59	1.42	11.27	15.39	0.15	10.92	11.07	2.03	0.48	96.37	amp (Grt profile ds31)	1840
TA14	31 / 80 .	41.62	1.68	12.81	16.37	0.15	9.79	10.91	2.29	0.57	96.25	amp (Grt profile ds31)	1864
TA14	31 / 81 .	41.88	1.77	12.49	16.52	0.18	9.92	10.93	2.36	0.60	96.70	amp (Grt profile ds31)	1887
TA14	31 / 82 .	45.30	1.57	17.66	16.05	0.15	12.42	9.18	3.35	0.47	106.18	*Grt profile ds31	1911
TA14	31 / 83 .	41.46	1.73	11.98	16.08	0.20	9.91	10.88	2.26	0.50	95.06	amp (Grt profile ds31)	1935
TA14	31 / 84 .	36.32	1.01	16.02	14.87	0.13	9.11	11.21	3.19	0.45	92.34	fx amp Grt profile ds31	1958
TA14	31 / 85 .	41.88	1.82	12.11	16.43	0.14	9.86	10.96	2.43	0.54	96.20	amp (Grt profile ds31)	1982
TA14	31 / 86 .	41.81	1.77	12.35	16.56	0.17	9.89	10.99	2.33	0.54	96.46	amp (Grt profile ds31)	2005
TA14	31 / 87 .	40.40	1.39	13.82	18.10	0.18	4.27	10.06	0.90	0.46	89.64	fx amp Grt profile ds31	2029
TA14	31 / 88 .	42.23	1.80	13.59	16.58	0.18	9.65	10.95	2.06	0.54	97.61	amp (Grt profile ds31)	2053
TA14	31 / 89 .	43.31	1.56	13.59	15.08	0.14	8.75	11.03	1.92	0.53	96.00	amp (Grt profile ds31)	2076
TA14	31 / 90 .	42.56	1.75	11.96	15.67	0.15	10.26	11.10	2.12	0.51	96.16	amp (Grt profile ds31)	2100
TA14	31 / 91 .	41.69	1.74	13.97	16.22	0.19	8.86	10.78	1.93	0.51	95.93	amp (Grt profile ds31)	2123
TA14	31 / 92 .	40.61	2.00	13.55	16.51	0.18	9.43	10.95	2.40	0.59	96.29	amp (Grt profile ds31)	2147
TA14	31 / 93 .	40.28	1.98	13.19	16.66	0.20	9.17	10.68	2.60	0.59	95.37	amp (Grt profile ds31)	2171
TA14	31 / 94 .	40.45	1.60	14.31	16.85	0.16	8.93	10.85	2.21	0.62	96.04	amp (Grt profile ds31)	2194
TA14	31 / 95 .	40.86	1.74	14.24	16.55	0.16	9.19	11.10	2.42	0.66	97.00	amp (Grt profile ds31)	2218
TA14	31 / 96 .	42.41	1.07	11.39	18.04	0.13	8.81	9.90	1.98	0.61	94.43	fx amp Grt profile ds31	2241
TA14	31 / 97 .	41.51	1.25	13.91	16.97	0.15	8.98	11.24	2.42	0.59	97.06	amp (Grt profile ds31)	2265
TA14	31 / 98 .	37.86	0.74	14.56	21.17	0.13	9.68	7.75	2.04	0.46	94.42	fxGrt profile ds31	2288
TA14	31 / 99 .	44.71	1.17	13.17	15.43	0.16	10.63	11.10	2.27	0.49	99.17	mxGrt profile ds31	2312
TA14	31 / 100 .	50.20	0.01	32.24	1.42	0.00	0.24	0.19	2.56	9.07	95.95	Kfs Grt profile ds31	2336
TA14	32 / 1 .	41.57	0.40	5.21	11.89	0.17	8.27	17.86	0.85	0.07	86.33	low total Cpx17	
TA14	33 / 1 .	38.03	0.08	21.69	24.42	1.70	5.24	8.95	0.05	0.00	100.18	Grt profile ds33	0
TA14	33 / 2 .	38.04	0.11	21.49	24.64	1.68	5.16	8.93	0.08	-0.01	100.16	Grt profile ds33	16
TA14	33 / 3 .	38.22	0.08	21.65	24.56	1.66	5.27	8.85	0.02	0.00	100.34	Grt profile ds33	32
TA14	33 / 4 .	38.16	0.10	21.69	24.48	1.62	5.32	8.78	0.03	-0.01	100.21	Grt profile ds33	49
TA14	33 / 5 .	37.92	0.06	21.67	24.66	1.73	5.20	8.86	0.02	0.00	100.12	Grt profile ds33	65
TA14	33 / 6 .	38.05	0.06	21.79	24.31	1.70	5.29	8.70	0.05	0.00	99.95	Grt profile ds33	81
TA14	33 / 7 .	37.87	0.12	21.00	22.33	1.48	4.65	10.51	0.39	0.01	98.35	inclGrt profile ds33	97
TA14	33 / 8 .	38.04	0.09	21.42	24.46	1.71	5.32	8.71	0.02	0.00	99.80	Grt profile ds33	114
TA14	33 / 9 .	38.08	0.07	21.75	24.49	1.66	5.16	8.89	0.01	0.01	100.12	Grt profile ds33	130
TA14	33 / 10 .	24.88	0.07	18.05	29.19	0.75	3.00	4.02	0.19	0.06	80.20	fxGrt profile ds33	146
TA14	33 / 11 .	37.48	0.08	21.56	24.26	1.64	5.28	8.62	0.05	0.01	98.98	Grt profile ds33	162
TA14	33 / 12 .	38.01	0.13	21.78	24.71	1.71	5.25	8.84	0.04	0.00	100.47	Grt profile ds33	178
TA14	33 / 13 .	37.76	0.08	21.96	24.25	1.69	5.21	8.71	0.05	-0.01	99.70	Grt profile ds33	195
TA14	33 / 14 .	37.96	0.06	22.08	24.29	1.66	5.35	8.63	0.07	0.01	100.11	Grt profile ds33	211
TA14	33 / 15 .	37.63	0.08	21.52	24.20	1.75	5.27	8.72	0.11	0.03	99.32	Grt profile ds33	227
TA14	33 / 16 .	37.36	0.07	23.03	23.44	1.47	5.69	8.93	0.56	0.06	100.61	inclGrt profile ds33	243
TA14	33 / 17 .	38.07	0.10	21.96	24.28	1.72	5.25	8.65	0.08	0.00	100.11	Grt profile ds33	260
TA14	33 / 18 .	37.98	0.04	22.05	24.64	1.73	5.27	8.69	0.05	0.01	100.49	Grt profile ds33	276
TA14	33 / 19 .	37.79	0.05	21.98	24.39	1.73	5.20	8.65	0.03	0.00	99.81	Grt profile ds33	292
TA14	33 / 20 .	37.89	0.08	21.85	24.25	1.59	5.14	8.77	0.86	0.02	100.49	inclGrt profile ds33	308
TA14	33 / 21 .	30.00	0.08	16.94	24.12	1.62	3.43	8.63	0.45	0.05	85.33	fxGrt profile ds33	324
TA14	33 / 22 .	27.21	0.12	20.81	19.23	1.06	4.67	6.33	1.57	0.15	81.16	fxGrt profile ds33	341
TA14	33 / 23 .	38.02	0.07	21.94	24.29	1.62	5.17	9.16	0.03	0.03	100.33	Grt profile ds33	357
TA14	33 / 24 .	37.92	0.09	21.51	24.27	1.55	4.99	9.40	0.03	0.01	99.81	Grt profile ds33	373
TA14	33 / 25 .	38.05	0.14	21.14	24.17	1.61	5.06	9.64	0.09	0.01	99.94	Grt profile ds33	389

Sample	Point	SiO2	TiO2	Al2O3	FeO	MnO	MgO	CaO	Na2O	K2O	Total	Comment	Distance (µm)
TA14	33 / 26 .	37.91	0.16	21.25	23.91	1.57	4.96	9.89	0.04	-0.01	99.70	Grt profile ds33	406
TA14	33 / 27 .	47.69	0.10	8.80	18.25	0.30	9.68	10.35	2.02	0.35	97.54	[mx]Grt profile ds33	422
TA14	33 / 28 .	45.46	0.33	7.04	24.53	0.53	6.07	11.09	1.55	0.30	96.89	[mx]Grt profile ds33	438
TA14	33 / 29 .	38.08	0.14	21.29	24.50	1.61	4.98	9.62	0.05	0.01	100.28	Grt profile ds33	454
TA14	33 / 30 .	37.82	0.17	21.42	24.09	1.58	4.98	9.76	0.03	0.00	99.87	Grt profile ds33	470
TA14	33 / 31 .	37.85	0.15	21.26	23.76	1.62	5.09	9.82	0.08	0.00	99.65	Grt profile ds33	487
TA14	33 / 32 .	37.96	0.11	21.06	24.12	1.52	5.14	9.57	0.04	0.00	99.55	Grt profile ds33	503
TA14	33 / 33 .	35.32	0.10	21.58	20.49	1.13	3.68	10.69	0.28	0.08	93.35	[fx]Grt profile ds33	519
TA14	33 / 34 .	37.79	0.08	21.65	24.25	1.59	5.31	8.74	0.00	0.00	99.45	Grt profile ds33	535
TA14	33 / 35 .	19.83	0.07	13.11	23.66	1.32	2.60	8.48	0.42	0.09	69.60	[fx]Grt profile ds33	552
TA14	33 / 36 .	37.67	0.08	21.74	24.55	1.84	4.89	9.06	0.05	0.01	99.94	Grt profile ds33	568
TA14	33 / 37 .	36.67	0.09	22.16	24.67	1.81	4.21	9.15	0.11	0.04	98.95	Grt profile ds33	584
TA14	33 / 38 .	36.74	0.11	21.60	26.04	2.13	4.39	7.43	0.06	0.01	98.57	Grt profile ds33	600
TA14	33 / 39 .	50.83	0.09	11.44	23.09	0.46	4.46	4.23	0.27	0.98	95.92	[fx]Grt profile ds33	616
TA14	33 / 40 .	49.65	0.45	9.33	9.86	0.18	12.13	19.69	1.48	0.01	102.82	*Grt profile ds33	633
TA14	33 / 41 .	48.49	0.48	4.92	10.14	0.16	10.56	19.44	1.18	0.03	95.42	cpx (Grt profile ds33)	649
TA14	33 / 42 .	49.37	0.44	5.44	10.17	0.19	10.68	20.30	1.44	0.06	98.15	cpx (Grt profile ds33)	665
TA14	33 / 43 .	49.45	0.51	5.24	10.65	0.23	10.82	20.51	1.32	0.06	98.82	cpx (Grt profile ds33)	681
TA14	33 / 44 .	49.40	0.45	4.97	10.45	0.20	10.52	20.82	1.24	0.00	98.04	cpx (Grt profile ds33)	698
TA14	33 / 45 .	49.32	0.44	4.76	10.37	0.24	10.59	20.44	1.28	0.02	97.48	cpx (Grt profile ds33)	714
TA14	33 / 46 .	49.09	0.46	5.12	11.01	0.22	10.45	19.84	1.35	0.05	97.63	cpx (Grt profile ds33)	730
TA14	33 / 47 .	49.65	0.39	4.59	10.79	0.28	10.89	20.16	1.32	0.01	98.16	cpx (Grt profile ds33)	746
TA14	33 / 48 .	49.78	0.41	4.39	10.68	0.23	10.85	20.27	1.35	0.01	98.02	cpx (Grt profile ds33)	762
TA14	33 / 49 .	52.19	0.32	5.27	8.86	0.16	10.77	18.59	1.84	0.03	98.12	[fx]cpx Grt profile ds33	779
TA14	33 / 50 .	58.10	0.03	20.09	1.18	0.01	0.27	1.80	7.30	0.09	88.87	[fx]cpx Grt profile ds33	795
TA14	34 / 1 .	42.15	2.10	12.55	15.80	0.23	10.27	10.80	2.32	0.53	96.77	amp profile ds34	0
TA14	34 / 2 .	42.36	1.98	12.16	15.64	0.20	10.22	10.84	2.28	0.52	96.23	amp profile ds34	28
TA14	34 / 3 .	19.64	1.85	6.08	16.22	0.19	4.21	10.08	0.90	0.49	59.68	[fx]amp profile ds34	56
TA14	34 / 4 .	42.16	2.06	12.56	15.91	0.20	10.43	10.69	2.41	0.54	97.02	amp profile ds34	84
TA14	34 / 5 .	42.00	2.11	12.86	16.12	0.23	10.25	10.58	2.48	0.52	97.16	amp profile ds34	112
TA14	34 / 6 .	39.20	2.13	11.93	16.14	0.23	9.01	10.36	2.16	0.58	91.79	[fx]amp profile ds34	140
TA14	34 / 7 .	42.13	2.10	12.56	16.03	0.21	10.22	10.62	2.39	0.56	96.85	amp profile ds34	168
TA14	34 / 8 .	42.25	2.11	12.66	16.00	0.23	10.35	10.61	2.34	0.51	97.10	amp profile ds34	196
TA14	34 / 9 .	42.51	2.02	12.28	16.30	0.24	10.03	10.60	2.25	0.57	96.85	amp profile ds34	223
TA14	34 / 10 .	42.40	2.06	12.36	15.75	0.22	10.32	10.69	2.26	0.52	96.65	amp profile ds34	251
TA14	34 / 11 .	42.11	1.99	12.74	15.76	0.23	10.33	10.86	2.37	0.58	97.03	amp profile ds34	279
TA14	34 / 12 .	38.18	0.40	23.08	10.07	0.05	2.42	20.80	0.35	0.47	95.85	[mx]profile ds34	307
TA14	34 / 13 .	42.56	1.82	12.50	15.75	0.20	10.44	10.89	2.30	0.59	97.08	amp profile ds34	335
TA14	34 / 14 .	42.46	1.50	10.89	17.40	0.15	9.85	10.24	1.88	0.53	94.94	amp profile ds34	363
TA14	34 / 15 .	41.92	1.66	11.89	16.46	0.19	9.39	10.91	1.89	0.73	95.06	amp profile ds34	391
TA14	34 / 16 .	42.62	1.91	12.54	15.59	0.20	10.38	10.84	2.27	0.52	96.91	amp profile ds34	419
TA14	34 / 17 .	42.46	1.98	12.41	15.63	0.18	10.27	10.80	2.23	0.58	96.56	amp profile ds34	447
TA14	34 / 18 .	41.99	1.77	12.38	15.71	0.22	10.10	10.97	2.07	0.49	95.75	[fx]amp profile ds34	475
TA14	34 / 19 .	42.48	1.95	12.73	15.54	0.19	10.26	11.02	2.28	0.55	97.06	amp profile ds34	503
TA14	34 / 20 .	43.03	1.85	12.20	15.41	0.23	10.51	10.97	2.21	0.50	96.91	amp profile ds34	531
TA14	34 / 21 .	43.00	1.71	12.35	14.67	0.17	11.44	11.16	2.14	0.51	97.22	amp profile ds34	559
TA14	34 / 22 .	42.57	1.65	12.41	15.32	0.21	10.52	11.09	2.16	0.50	96.46	amp profile ds34	587
TA14	34 / 23 .	42.55	1.60	12.81	15.14	0.17	10.70	11.19	2.19	0.50	96.92	amp profile ds34	614
TA14	34 / 24 .	42.04	0.18	13.78	22.12	0.11	5.26	9.12	3.10	0.73	96.49	[incl]amp profile ds34	642
TA14	34 / 25 .	41.44	1.75	12.49	16.68	0.19	10.59	9.84	2.06	0.54	95.61	[fx]amp profile ds34	670
TA14	34 / 26 .	42.17	1.98	12.31	15.89	0.19	10.33	10.88	2.24	0.53	96.55	amp profile ds34	698
TA14	34 / 27 .	42.06	2.03	12.47	15.93	0.21	10.31	10.88	2.25	0.56	96.76	amp profile ds34	726
TA14	34 / 28 .	42.12	1.99	12.34	16.07	0.20	10.29	10.99	2.33	0.55	96.94	amp profile ds34	754
TA14	34 / 29 .	41.63	1.99	12.69	16.17	0.18	10.07	11.12	2.34	0.57	96.81	amp profile ds34	782
TA14	34 / 30 .	41.27	1.97	13.06	16.07	0.15	10.10	11.22	2.33	0.66	96.87	amp profile ds34	810
TA14	34 / 31 .	42.16	1.89	12.37	15.91	0.18	10.33	10.91	2.22	0.51	96.49	amp profile ds34	838
TA14	34 / 32 .	42.05	1.94	12.27	16.05	0.21	10.27	10.92	2.29	0.53	96.58	amp profile ds34	866
TA14	34 / 33 .	46.52	1.83	15.25	15.42	0.17	11.55	10.72	2.62	0.50	104.60	*amp profile ds34	894
TA14	34 / 34 .	32.26	1.81	10.65	25.79	0.17	6.34	6.42	0.75	0.46	84.68	[fx]amp profile ds34	922
TA14	34 / 35 .	42.35	1.95	12.77	15.88	0.19	10.19	11.06	2.25	0.55	97.25	amp profile ds34	950
TA14	34 / 36 .	42.12	1.91	13.03	15.89	0.21	10.08	10.94	2.27	0.54	97.01	amp profile ds34	978
TA14	34 / 37 .	41.81	1.96	12.51	16.05	0.20	10.20	11.02	2.33	0.51	96.59	amp profile ds34	1005
TA14	34 / 38 .	41.35	2.13	12.80	16.13	0.19	10.10	11.01	2.39	0.51	96.67	amp profile ds34	1033
TA14	34 / 39 .	41.84	1.92	12.96	15.60	0.19	10.22	10.96	2.26	0.54	96.57	amp profile ds34	1061
TA14	34 / 40 .	42.11	2.07	13.07	15.74	0.20	10.20	11.09	2.40	0.53	97.44	amp profile ds34	1089
TA14	34 / 41 .	41.97	2.06	12.90	15.72	0.21	10.30	11.07	2.31	0.56	97.14	amp profile ds34	1117
TA14	34 / 42 .	39.64	1.93	14.30	15.93	0.20	10.73	10.47	2.40	0.55	96.21	[incl]amp profile ds34	1145
TA14	34 / 43 .	42.32	2.05	12.70	15.59	0.18	10.32	11.02	2.26	0.57	97.09	amp profile ds34	1173
TA14	34 / 44 .	42.46	1.89	12.15	16.16	0.16	10.29	10.86	2.24	0.54	96.82	amp profile ds34	1201
TA14	34 / 45 .	41.00	1.70	14.02	15.79	0.18	9.61	11.08	2.34	0.63	96.41	amp profile ds34	1229
TA14	34 / 46 .	40.19	1.22	14.05	19.35	0.19	7.86	9.04	1.45	0.47	93.84	[fx]amp profile ds34	1257
TA14	34 / 47 .	39.99	1.41	13.48	16.43	0.15	11.75	10.13	2.96	0.52	96.86	[incl]amp profile ds34	1285

Sample	Point	SiO2	TiO2	Al2O3	FeO	MnO	MgO	CaO	Na2O	K2O	Total	Comment	Distance (µm)
TA14	34 / 48 .	39.20	1.26	13.89	18.00	0.15	8.57	10.38	2.05	0.59	94.18	[fx]amp profile ds34	1313
TA14	34 / 49 .	1.01	50.19	-0.01	43.46	0.73	0.04	1.36	0.02	0.00	96.83	ilm	1341
TA14	34 / 50 .	0.11	50.32	0.87	43.32	0.81	0.04	0.46	0.31	0.03	96.36	ilm	1368
TA14		58.50	0.00	25.40	0.20	0.00	0.00	7.70	7.30	0.80		saus1	
TA14		58.00	0.00	25.50	0.40	0.00	0.00	7.80	7.10	0.40		saus2	
TA14		58.60	0.00	25.50	0.20	0.00	0.00	7.50	7.30	0.90		saus3	
TA14		57.70	0.00	25.20	0.60	0.00	0.00	9.20	7.10	0.20		saus4	
TA14		57.50	0.00	25.20	0.80	0.00	0.00	9.50	6.90	0.20		saus5	
TA14		58.50	0.00	25.00	0.40	0.00	0.00	8.40	7.30	0.30		saus6	
TA14		57.10	0.00	25.40	0.60	0.00	0.00	9.90	6.90	0.10		saus7	
TA14		57.80	0.00	25.00	0.80	0.00	0.00	8.90	7.10	0.30		saus8	
TA14		57.40	0.00	25.50	1.00	0.00	0.00	9.50	6.90	0.10		saus9	
TA14		57.30	0.00	25.30	0.70	0.00	0.00	9.50	6.90	0.10		saus10	
TA16	1 / 1 .	38.27	0.13	20.44	24.02	1.35	4.44	11.01	0.01	0.00	99.67	grt yellow1	0
TA16	1 / 2 .	38.40	0.09	20.42	23.64	1.36	4.46	11.24	0.00	0.00	99.62	grt yellow1	52
TA16	1 / 3 .	38.31	0.13	20.45	23.65	1.33	4.79	11.13	0.02	0.00	99.82	grt yellow1	104
TA16	1 / 4 .	38.74	0.08	20.57	23.48	1.33	4.98	10.64	0.01	-0.01	99.84	grt yellow1	156
TA16	1 / 5 .	38.72	0.09	20.53	23.59	1.28	5.12	10.52	0.01	-0.01	99.86	grt yellow1	208
TA16	1 / 6 .	38.36	0.10	20.35	24.74	1.35	5.01	9.64	0.00	0.00	99.56	grt yellow1	260
TA16	1 / 7 .	42.60	0.94	11.01	18.53	0.12	8.93	12.13	2.22	0.43	96.91	[fx]cpx yellow1	312
TA16	1 / 8 .	41.18	0.50	7.38	12.81	0.16	6.53	19.58	0.63	0.03	88.79	[fx]cpx yellow1	364
TA16	1 / 9 .	49.10	0.50	5.16	11.48	0.21	10.03	21.44	1.11	0.01	99.04	cpx yellow1	416
TA16	1 / 10 .	48.64	0.55	5.36	11.81	0.19	9.94	21.10	1.17	0.01	98.77	cpx yellow1	468
TA16	2 / 1 .	41.45	1.86	12.42	16.66	0.14	9.20	11.87	2.08	0.75	96.45	amp1	
TA16	3 / 1 .	41.10	2.22	12.46	16.85	0.13	9.18	11.98	2.03	0.81	96.75	amp2	
TA16	4 / 1 .	41.89	1.20	12.68	17.46	0.15	8.69	12.11	2.22	0.69	97.09	amp3	
TA16	5 / 1 .	46.73	0.81	7.84	13.39	0.16	9.44	18.22	1.63	0.22	98.43	[mx]amp4	
TA16	6 / 1 .	49.07	0.59	5.50	11.16	0.14	9.95	21.72	1.19	0.01	99.33	cpx(amp5)	
TA16	7 / 1 .	41.06	2.25	12.92	16.41	0.13	9.12	12.00	1.96	0.85	96.69	amp6	
TA16	8 / 1 .	41.64	1.83	12.58	16.20	0.13	9.40	12.08	2.19	0.84	96.90	amp7	
TA16	9 / 1 .	40.79	2.00	13.13	16.42	0.15	9.20	12.04	2.15	0.84	96.71	amp8	
TA16	10 / 1 .	38.43	0.07	27.16	6.60	0.06	-0.04	24.74	0.00	0.00	97.06	ep1	
TA16	11 / 1 .	41.48	2.04	12.45	16.16	0.14	9.42	12.17	1.91	0.80	96.56	amp9	
TA16	12 / 1 .	41.12	2.11	12.79	16.30	0.13	9.22	12.02	1.95	0.81	96.44	amp10	
TA16	13 / 1 .	41.60	1.73	12.48	16.02	0.16	9.65	12.02	2.20	0.69	96.55	amp11	
TA16	14 / 1 .	49.16	0.54	4.54	10.90	0.20	10.04	22.95	0.98	0.01	99.32	cpx1	
TA16	15 / 1 .	37.77	0.07	20.66	24.69	1.36	4.93	9.56	0.00	-0.01	99.05	grt yellow2	0
TA16	15 / 2 .	37.60	0.09	20.47	26.09	1.86	3.84	9.13	0.03	0.00	99.12	grt yellow2	33
TA16	15 / 3 .	49.70	0.25	2.88	11.09	0.13	10.97	22.83	0.88	0.05	98.78	cpx yellow2	66
TA16	15 / 4 .	49.19	0.53	4.83	10.77	0.19	9.89	22.73	1.05	-0.01	99.16	cpx yellow2	99
TA16	15 / 5 .	30.25	36.79	1.37	1.04	0.01	0.00	28.57	0.06	0.01	98.10	ttn (yellow2)	132
TA16	15 / 6 .	48.50	0.57	4.93	10.85	0.21	10.00	22.86	1.02	0.00	98.95	cpx yellow2	165
TA16	15 / 7 .	49.13	0.41	4.28	10.75	0.16	10.13	22.84	1.05	0.01	98.77	cpx yellow2	198
TA16	15 / 8 .	48.52	0.50	5.15	11.30	0.19	9.96	22.38	1.11	0.00	99.11	cpx yellow2	231
TA16	15 / 9 .	44.52	0.46	8.36	11.98	0.20	8.82	20.46	0.97	0.04	95.81	[fx]yellow2	264
TA16	15 / 10 .	48.58	0.49	5.10	11.19	0.16	9.89	22.29	1.10	0.03	98.83	cpx yellow2	297
TA16	16 / 1 .	56.73	0.19	12.82	5.75	0.07	4.77	9.25	6.19	0.14	95.91	[incl]amp12	
TA16	17 / 1 .	58.36	0.19	13.12	5.91	0.04	4.73	9.39	3.28	0.16	95.18	[fx]yellow3	0
TA16	17 / 2 .	49.20	0.57	4.87	10.60	0.19	10.01	22.45	1.11	0.01	99.00	cpx yellow3	59
TA16	17 / 3 .	48.78	0.57	5.50	10.92	0.19	9.99	22.01	1.11	0.02	99.09	cpx yellow3	117
TA16	17 / 4 .	48.57	0.60	5.32	10.68	0.19	10.03	22.23	1.19	0.00	98.81	cpx yellow3	176
TA16	17 / 5 .	49.22	0.56	5.18	10.70	0.20	10.05	22.51	1.18	0.01	99.62	cpx yellow3	234
TA16	17 / 6 .	32.31	0.44	4.42	11.78	0.22	4.03	12.03	0.51	0.01	65.75	[fx]yellow3	292
TA16	17 / 7 .	48.87	0.55	5.02	11.08	0.19	10.12	22.22	1.09	0.01	99.14	cpx yellow3	351
TA16	17 / 8 .	48.77	0.60	5.16	11.25	0.21	10.09	21.63	1.13	0.00	98.85	cpx yellow3	409
TA16	17 / 9 .	48.36	0.57	5.90	12.15	0.20	10.21	20.10	1.26	0.01	98.76	cpx yellow3	468
TA16	17 / 10 .	48.41	0.60	5.60	11.57	0.21	9.98	21.13	1.16	0.00	98.66	cpx yellow3	526
TA16	18 / 1 .	0.02	52.72	0.00	41.41	3.37	0.11	0.14	0.01	0.00	97.78	ilm (ox1)	
TA16	19 / 1 .	40.88	2.13	13.10	17.00	0.09	8.62	12.22	1.95	0.85	96.85	amp13	
TA16	20 / 1 .	40.80	1.61	13.10	16.53	0.12	9.14	12.12	2.29	0.77	96.49	amp14	
TA16	21 / 1 .	42.27	1.78	11.73	15.91	0.14	9.75	12.01	2.16	0.67	96.42	amp15	
TA16	22 / 1 .	41.05	1.88	12.50	16.93	0.15	9.12	12.11	1.94	0.77	96.45	amp green1	0
TA16	22 / 2 .	41.92	1.66	12.17	16.90	0.16	9.31	11.70	1.86	0.80	96.48	amp green2	23
TA16	22 / 3 .	41.37	1.69	12.66	16.69	0.14	9.07	12.12	1.93	0.72	96.40	amp green3	45
TA16	22 / 4 .	42.11	1.42	12.22	16.23	0.14	9.42	12.16	1.88	0.61	96.17	amp green4	68
TA16	22 / 5 .	41.46	1.66	13.05	16.43	0.13	8.89	11.95	2.15	0.65	96.36	amp green5	91
TA16	22 / 6 .	49.19	0.35	4.97	9.86	0.17	11.13	21.59	0.81	0.04	98.10	cpx green1	114
TA16	22 / 7 .	48.77	0.60	5.10	10.58	0.18	10.05	22.75	1.07	0.02	99.13	cpx green1	136
TA16	22 / 8 .	48.87	0.58	5.28	10.96	0.21	10.09	22.19	1.15	0.02	99.34	cpx green1	159
TA16	22 / 9 .	47.81	0.66	6.69	12.20	0.19	9.82	20.15	1.30	0.05	98.86	cpx green1	182
TA16	22 / 10 .	49.55	0.52	4.90	10.80	0.19	10.01	22.52	1.15	0.01	99.65	cpx green1	204
TA16	23 / 1 .	40.81	1.96	12.32	17.37	0.13	9.06	12.00	2.01	0.78	96.45	amp16	
TA16	24 / 1 .	40.73	2.05	12.82	16.69	0.16	8.94	12.08	2.03	0.83	96.32	amp17	

Sample	Point	SiO2	TiO2	Al2O3	FeO	MnO	MgO	CaO	Na2O	K2O	Total	Comment	Distance (µm)
TA16	25 / 1 .	0.03	46.57	0.02	48.21	0.40	0.04	0.06	0.00	0.00	95.33	ilm (ox2)	
TA16	26 / 1 .	30.51	37.73	1.34	0.84	0.02	-0.09	29.37	0.00	0.00	99.81	ttn (ox3)	
TA16	27 / 1 .	49.65	0.50	4.21	10.62	0.17	10.43	22.55	1.02	0.01	99.16	cpx2	
TA16	28 / 1 .	48.83	0.56	5.34	12.11	0.18	10.07	20.73	1.22	0.03	99.07	cpx3	
TA16	1 / 1 .	49.72	0.57	5.40	10.61	0.15	10.01	22.91	1.02	0.01	100.39	cpx ds1	0
TA16	1 / 2 .	50.71	0.34	4.14	10.35	0.16	10.74	22.93	0.87	0.03	100.27	cpx ds1	17
TA16	1 / 3 .	38.14	0.08	20.49	24.99	1.99	3.65	10.27	0.04	0.03	99.68	grt ds1	34
TA16	1 / 4 .	38.65	0.07	21.10	23.85	1.34	4.72	10.30	0.01	0.00	100.05	grt ds1	51
TA16	1 / 5 .	38.62	0.07	21.40	23.57	1.34	4.97	10.15	0.02	0.00	100.13	grt ds1	68
TA16	1 / 6 .	38.69	0.09	21.09	23.75	1.38	4.88	10.38	0.01	0.00	100.27	grt ds1	85
TA16	1 / 7 .	38.66	0.09	21.23	23.79	1.35	4.78	10.59	0.01	0.00	100.50	grt ds1	103
TA16	1 / 8 .	38.78	0.10	21.01	23.77	1.31	4.77	10.64	0.01	0.01	100.41	grt ds1	120
TA16	1 / 9 .	38.58	0.09	21.10	23.56	1.34	4.62	10.96	0.00	0.00	100.25	grt ds1	137
TA16	1 / 10 .	38.84	0.11	21.15	23.52	1.33	4.60	10.99	0.01	0.02	100.55	grt ds1	154
TA16	1 / 11 .	38.77	0.10	21.06	23.58	1.30	4.50	11.11	0.02	0.00	100.43	grt ds1	171
TA16	1 / 12 .	38.83	0.11	21.19	23.45	1.30	4.45	11.18	0.01	0.00	100.52	grt ds1	188
TA16	1 / 13 .	38.66	0.12	21.12	23.46	1.34	4.52	11.27	0.01	0.00	100.50	grt ds1	205
TA16	1 / 14 .	38.61	0.13	20.96	23.36	1.29	4.40	11.32	0.00	0.00	100.07	grt ds1	222
TA16	1 / 15 .	38.52	0.13	21.20	23.19	1.34	4.53	11.33	0.00	0.01	100.24	grt ds1	239
TA16	1 / 16 .	38.48	0.18	20.83	23.80	1.35	4.58	10.56	0.01	0.00	99.80	grt ds1	256
TA16	1 / 17 .	38.34	0.12	21.22	25.26	1.50	4.08	9.54	0.00	0.00	100.05	grt ds1	274
TA16	1 / 18 .	49.63	0.60	4.94	10.94	0.13	10.58	21.89	1.03	0.02	99.75	cpx ds1	291
TA16	1 / 19 .	49.09	0.64	5.52	11.07	0.18	10.26	21.70	1.08	0.02	99.56	cpx ds1	308
TA16	1 / 20 .	49.08	0.62	5.47	11.32	0.17	10.24	21.57	1.10	0.02	99.60	cpx ds1	325
TA16	2 / 1 .	49.61	0.54	5.07	11.07	0.20	9.78	22.41	1.08	0.01	99.76	cpx4	
TA16	3 / 1 .	38.83	0.08	21.24	23.32	1.31	4.75	11.11	0.01	0.00	100.66	grt ds3	0
TA16	3 / 2 .	39.01	0.09	21.19	23.58	1.27	4.75	11.12	0.00	0.01	101.02	grt ds3	23
TA16	3 / 3 .	38.97	0.09	21.31	23.57	1.30	4.82	10.84	0.01	0.01	100.93	grt ds3	47
TA16	3 / 4 .	38.70	0.30	20.75	23.47	1.24	4.59	11.51	0.03	0.01	100.60	grt ds3	70
TA16	3 / 5 .	39.21	0.26	21.03	23.01	1.25	4.38	12.02	0.02	0.00	101.19	grt ds3	93
TA16	3 / 6 .	39.43	0.26	20.98	22.81	1.24	4.37	12.11	0.04	-0.01	101.23	grt ds3	117
TA16	3 / 7 .	39.10	0.19	21.16	22.91	1.26	4.29	12.13	0.04	0.00	101.08	grt ds3	140
TA16	3 / 8 .	38.97	0.16	21.06	23.01	1.26	4.35	11.98	0.00	0.01	100.81	grt ds3	163
TA16	3 / 9 .	39.07	0.14	21.12	23.16	1.21	4.46	11.92	0.00	-0.01	101.08	grt ds3	187
TA16	3 / 10 .	39.06	0.21	21.02	23.25	1.23	4.50	11.76	0.02	0.00	101.05	grt ds3	210
TA16	3 / 11 .	39.16	0.21	21.11	23.32	1.25	4.50	11.72	0.01	0.00	101.28	grt ds3	233
TA16	3 / 12 .	38.97	0.18	21.04	23.28	1.18	4.56	11.60	0.03	0.00	100.83	grt ds3	257
TA16	3 / 13 .	39.18	0.21	21.08	23.45	1.23	4.59	11.64	0.03	-0.01	101.41	grt ds3	280
TA16	3 / 14 .	39.27	0.18	21.09	23.28	1.24	4.68	11.71	0.00	0.00	101.45	grt ds3	303
TA16	3 / 15 .	39.17	0.14	21.14	23.72	1.38	4.83	10.69	0.01	0.01	101.08	grt ds3	326
TA16	3 / 16 .	39.10	0.08	21.31	24.52	1.49	4.92	9.84	0.00	0.00	101.27	grt ds3	350
TA16	3 / 17 .	39.41	0.07	21.04	25.30	1.56	4.46	9.36	0.11	0.01	101.32	grt ds3	373
TA16	3 / 18 .	24.88	0.77	8.43	19.36	0.17	7.71	10.72	1.85	0.41	74.31	^{fx}ds3	396
TA16	3 / 19 .	49.17	0.57	5.82	12.65	0.17	10.58	20.27	1.26	0.13	100.61	cpx ds3	420
TA16	3 / 20 .	50.60	0.47	4.33	10.77	0.18	10.82	23.04	0.82	0.03	101.06	cpx ds3	443
TA16	4 / 1 .	50.16	0.50	5.30	11.64	0.20	10.13	21.38	1.12	0.01	100.44	cpx ds4	0
TA16	4 / 2 .	49.64	0.50	5.38	11.66	0.21	10.19	21.24	1.13	0.02	99.97	cpx ds4	15
TA16	4 / 3 .	50.29	0.48	4.94	11.16	0.23	10.16	22.07	1.11	0.00	100.44	cpx ds4	31
TA16	4 / 4 .	50.01	0.50	4.98	11.28	0.20	10.33	21.90	1.09	0.01	100.29	cpx ds4	46
TA16	4 / 5 .	49.96	0.52	5.30	11.70	0.21	10.14	21.48	1.12	0.01	100.44	cpx ds4	61
TA16	4 / 6 .	50.19	0.50	4.95	11.14	0.23	10.21	22.22	1.12	0.01	100.58	cpx ds4	77
TA16	4 / 7 .	49.91	0.51	5.08	11.02	0.21	9.98	22.19	1.08	-0.01	99.98	cpx ds4	92
TA16	4 / 8 .	50.06	0.52	5.03	11.01	0.20	10.13	22.19	1.12	0.01	100.26	cpx ds4	108
TA16	4 / 9 .	49.85	0.52	5.16	11.32	0.17	10.29	21.69	1.12	0.01	100.13	cpx ds4	123
TA16	4 / 10 .	49.90	0.56	5.27	10.89	0.17	10.04	22.34	1.09	0.01	100.28	cpx ds4	138
TA16	4 / 11 .	50.12	0.54	4.82	10.82	0.19	10.30	22.47	1.01	0.02	100.29	cpx ds4	154
TA16	4 / 12 .	50.34	0.56	4.63	10.46	0.18	10.52	22.80	0.98	0.02	100.50	cpx ds4	169
TA16	4 / 13 .	51.64	0.37	3.19	10.09	0.18	11.36	23.11	0.83	0.01	100.78	cpx ds4	184
TA16	4 / 14 .	40.54	1.76	14.03	17.30	0.16	8.55	11.47	2.00	0.85	96.65	amp ds4	200
TA16	4 / 15 .	42.16	2.00	12.85	17.01	0.14	8.92	11.81	1.89	0.79	97.57	amp ds4	215
TA16	4 / 16 .	41.96	2.09	12.87	17.09	0.15	8.76	11.74	1.85	0.85	97.36	amp ds4	230
TA16	4 / 17 .	41.60	2.07	12.73	17.24	0.15	8.88	11.82	1.92	0.90	97.31	amp ds4	246
TA16	4 / 18 .	41.39	2.09	12.90	17.48	0.14	8.81	11.88	1.98	0.92	97.60	amp ds4	261
TA16	4 / 19 .	41.46	2.12	12.90	17.47	0.16	8.70	11.84	1.89	0.88	97.43	amp ds4	277
TA16	4 / 20 .	41.38	2.14	12.95	17.47	0.16	8.71	11.77	1.97	0.91	97.45	amp ds4	292
TA16	5 / 1 .	49.24	0.67	5.65	10.67	0.16	9.97	22.50	1.06	0.00	99.93	cpx ds5	0
TA16	5 / 2 .	49.22	0.69	5.74	10.85	0.17	10.09	22.48	1.02	0.00	100.25	cpx ds5	15
TA16	5 / 3 .	49.30	0.66	5.81	10.99	0.15	10.17	21.89	1.01	0.00	99.99	cpx ds5	30
TA16	5 / 4 .	50.14	0.60	5.04	10.62	0.16	10.34	22.74	0.94	0.00	100.58	cpx ds5	45
TA16	5 / 5 .	38.11	0.10	20.77	25.60	1.82	3.89	9.83	0.01	0.01	100.14	grt ds5	59
TA16	5 / 6 .	38.89	0.09	21.21	24.32	1.42	4.67	10.23	0.00	-0.01	100.83	grt ds5	74
TA16	5 / 7 .	38.75	0.10	21.05	23.63	1.32	4.75	10.84	0.01	0.00	100.45	grt ds5	89
TA16	5 / 8 .	39.05	0.11	21.15	23.62	1.27	4.73	11.05	0.02	0.00	101.00	grt ds5	104
TA16	5 / 9 .	39.02	0.08	21.17	23.13	1.26	4.58	11.49	0.04	0.00	100.76	grt ds5	119
TA16	5 / 10 .	39.27	0.07	21.12	23.12	1.35	4.41	11.71	0.07	0.01	101.13	grt ds5	134

Sample	Point	SiO2	TiO2	Al2O3	FeO	MnO	MgO	CaO	Na2O	K2O	Total	Comment	Distance (µm)
TA16	5 / 11 .	39.25	0.07	21.12	23.54	1.36	4.52	11.26	0.02	0.00	101.13	grt ds5	148
TA16	5 / 12 .	38.93	0.08	21.57	24.19	1.36	4.30	10.73	0.02	-0.01	101.17	grt ds5	163
TA16	5 / 13 .	39.20	0.07	21.33	23.89	1.36	4.57	10.97	0.02	-0.01	101.40	grt ds5	178
TA16	5 / 14 .	38.95	0.08	20.95	23.31	1.27	4.52	11.25	0.02	0.02	100.36	grt ds5	193
TA16	5 / 15 .	39.10	0.08	21.26	23.97	1.38	4.60	10.99	0.00	-0.01	101.37	grt ds5	208
TA16	5 / 16 .	38.83	0.10	20.70	22.77	1.28	4.15	12.80	0.04	0.00	100.67	grt ds5	223
TA16	5 / 17 .	39.19	0.13	21.16	23.83	1.40	4.47	11.09	0.01	0.00	101.27	grt ds5	237
TA16	5 / 18 .	39.31	0.13	21.06	23.72	1.39	4.47	11.24	0.02	0.00	101.33	grt ds5	252
TA16	5 / 19 .	39.29	0.07	21.25	23.58	1.40	4.47	11.28	0.01	0.01	101.35	grt ds5	267
TA16	5 / 20 .	39.30	0.09	21.04	23.70	1.35	4.44	11.41	0.02	0.01	101.36	grt ds5	282
TA16	5 / 21 .	39.26	0.09	21.22	23.67	1.34	4.53	11.33	0.01	0.00	101.45	grt ds5	297
TA16	5 / 22 .	39.24	0.09	21.18	23.89	1.38	4.53	11.14	0.00	0.00	101.46	grt ds5	312
TA16	5 / 23 .	39.41	0.08	21.17	23.71	1.38	4.53	11.11	0.02	0.00	101.42	grt ds5	326
TA16	5 / 24 .	39.23	0.09	21.02	23.75	1.36	4.52	11.18	0.30	0.02	101.46	grt ds5	341
TA16	5 / 25 .	39.35	0.08	21.06	23.61	1.33	4.54	11.22	0.20	0.01	101.40	grt ds5	356
TA16	5 / 26 .	39.01	0.08	21.12	24.43	1.42	4.32	10.94	0.02	0.00	101.35	grt ds5	371
TA16	5 / 27 .	44.91	0.22	15.05	18.61	1.02	7.17	13.21	0.40	0.12	100.71	^{mix}ds5	386
TA16	5 / 28 .	40.64	18.13	2.90	5.18	0.10	5.98	26.12	0.45	0.00	99.51	^{mix}ds5	401
TA16	5 / 29 .	50.04	0.70	5.91	10.91	0.15	10.44	22.68	0.97	0.00	101.80	cpx ds5	416
TA16	5 / 30 .	49.64	0.71	6.10	11.29	0.15	10.24	22.47	1.01	0.01	101.63	cpx ds5	430
TA16	6 / 1 .	50.97	0.52	4.62	9.43	0.12	11.13	22.59	0.92	-0.01	100.30	cpx ds6	0
TA16	6 / 2 .	49.93	0.65	5.77	10.04	0.11	10.97	21.74	1.01	0.00	100.23	cpx ds6	11
TA16	6 / 3 .	50.08	0.69	5.72	9.89	0.12	10.98	22.07	1.05	0.00	100.60	cpx ds6	23
TA16	6 / 4 .	50.20	0.68	5.73	9.93	0.11	10.91	22.04	1.05	0.01	100.66	cpx ds6	34
TA16	6 / 5 .	50.59	0.54	4.95	10.01	0.13	11.09	22.54	0.95	0.01	100.81	cpx ds6	46
TA16	6 / 6 .	38.66	0.19	20.66	24.88	1.35	4.37	9.99	0.01	0.01	100.12	grt ds6	57
TA16	6 / 7 .	39.01	0.24	20.63	24.38	1.31	4.70	10.35	0.02	0.01	100.65	grt ds6	68
TA16	6 / 8 .	39.15	0.28	20.59	24.00	1.30	4.75	10.67	0.03	0.01	100.78	grt ds6	80
TA16	6 / 9 .	38.82	0.24	20.56	23.78	1.28	4.70	10.79	0.02	0.00	100.20	grt ds6	91
TA16	6 / 10 .	38.78	0.21	20.88	23.49	1.33	4.73	11.00	0.02	0.01	100.44	grt ds6	103
TA16	6 / 11 .	38.84	0.24	20.72	23.61	1.30	4.64	11.16	0.01	0.00	100.52	grt ds6	114
TA16	6 / 12 .	38.87	0.25	20.74	23.61	1.27	4.64	11.29	0.01	-0.02	100.68	grt ds6	126
TA16	6 / 13 .	39.17	0.27	20.74	23.48	1.23	4.55	11.40	0.02	0.00	100.86	grt ds6	137
TA16	6 / 14 .	38.99	0.21	20.72	23.40	1.26	4.59	11.20	0.03	0.00	100.40	grt ds6	148
TA16	6 / 15 .	38.77	0.12	20.91	22.78	1.24	4.53	11.69	0.02	0.02	100.08	grt ds6	160
TA16	6 / 16 .	39.01	0.09	21.20	23.46	1.30	4.65	11.20	0.02	-0.01	100.93	grt ds6	171
TA16	6 / 17 .	38.81	0.10	21.09	23.32	1.27	4.72	10.92	-0.01	0.01	100.22	grt ds6	183
TA16	6 / 18 .	38.70	0.08	21.02	23.25	1.27	4.69	10.82	0.01	0.01	99.84	grt ds6	194
TA16	6 / 19 .	38.73	0.09	21.74	23.41	1.32	4.66	10.56	0.01	0.01	100.51	grt ds6	205
TA16	6 / 20 .	34.07	0.09	21.61	26.12	0.92	5.85	7.13	0.03	0.04	95.85	^{fx}grt ds6	217
TA16	6 / 21 .	38.78	0.08	20.64	21.51	1.12	4.15	12.55	0.41	0.02	99.27	^{fx}grt ds6	228
TA16	6 / 22 .	38.84	0.08	20.85	23.45	1.29	4.64	11.41	0.04	0.00	100.61	^{fx}grt ds6	240
TA16	6 / 23 .	38.73	0.08	21.04	23.62	1.33	4.85	10.25	0.10	0.00	100.01	grt ds6	251
TA16	6 / 24 .	38.36	0.08	20.96	24.33	1.33	4.88	9.60	0.02	0.01	99.55	grt ds6	263
TA16	6 / 25 .	37.95	0.11	21.91	24.05	1.35	4.61	9.32	0.02	0.01	99.34	grt ds6	274
TA16	6 / 26 .	38.53	0.09	21.15	24.73	1.40	4.72	9.49	0.01	0.01	100.14	grt ds6	285
TA16	6 / 27 .	38.51	0.08	21.11	25.28	1.52	4.54	9.33	0.00	0.00	100.38	grt ds6	297
TA16	6 / 28 .	38.25	0.09	20.89	25.80	1.78	3.64	9.34	0.00	0.01	99.81	grt ds6	308
TA16	6 / 29 .	44.79	0.30	12.51	18.11	0.77	7.26	14.23	1.13	0.15	99.25	^{mix}grt ds6	320
TA16	6 / 30 .	50.70	0.31	3.35	10.29	0.17	10.61	23.02	0.86	0.01	99.31	cpx ds6	331
TA16	7 / 1 .	49.15	0.71	5.85	11.18	0.15	9.86	22.07	1.09	-0.01	100.06	cpx5	
TA16	8 / 1 .	42.41	2.02	12.97	16.74	0.14	9.08	12.01	1.87	0.78	98.02	amp18	
TA16	9 / 1 .	41.55	2.27	13.05	16.78	0.12	8.90	11.77	1.98	0.79	97.23	amp19	
TA16	10 / 1 .	49.65	0.58	5.67	11.21	0.15	10.03	21.66	1.15	0.02	100.12	cpx6	
TA16		53.10	0.00	28.00	0.40	0.00	0.00	12.50	5.60	0.30		saus1	
TA16		53.30	0.00	27.30	0.70	0.00	0.00	13.00	5.50	0.20		saus2	
TA16		56.20	0.00	26.10	0.40	0.00	0.00	9.80	6.70	0.40		saus3	
TA16		55.90	0.00	26.40	0.40	0.00	0.00	10.20	6.60	0.40		saus4	
TA16		56.60	0.00	26.10	0.30	0.00	0.00	9.90	6.80	0.30		saus5	
TA16		56.60	0.00	26.10	0.30	0.00	0.00	9.90	6.80	0.30		saus6	
TA16		56.30	0.00	25.70	0.30	0.00	0.00	10.30	6.90	0.00		saus7	
TA16		56.10	0.00	26.00	0.50	0.00	0.00	10.10	6.80	0.20		saus8	
TA16		57.30	0.00	25.40	0.50	0.00	0.00	9.60	7.10	0.10		saus9	
TA16		57.30	0.00	26.00	0.10	0.00	0.00	9.10	7.10	0.40		saus10	
TA17	3 / 1 .	29.99	37.92	1.19	0.98	0.06	-0.06	28.80	0.00	0.00	98.96	ttn (Ox1)	
TA17	4 / 1 .	37.39	0.02	23.88	11.02	0.22	-0.02	23.63	0.01	-0.01	96.17	Ep1	
TA17	5 / 1 .	37.19	0.10	22.72	11.84	0.22	-0.01	23.40	0.01	0.01	95.49	Ep2	
TA17	6 / 1 .	38.41	0.08	20.76	22.93	1.00	5.44	10.38	0.01	0.01	99.02	Grt1	
TA17	7 / 1 .	38.29	0.14	20.69	22.39	0.87	4.89	11.62	0.02	0.00	98.91	Grt2	
TA17	8 / 1 .	37.61	0.12	17.78	18.53	0.31	6.27	11.49	2.49	1.01	95.59	altered (Amp1)	
TA17	9 / 1 .	40.08	0.17	14.85	18.04	0.30	7.58	11.53	2.52	0.78	95.85	altered (Amp2)	
TA17	10 / 1 .	50.03	0.53	3.99	9.77	0.20	10.71	22.57	1.11	0.00	98.91	cpx (Amp3)	
TA17	11 / 1 .	49.32	0.58	5.14	10.15	0.19	10.34	21.44	1.17	0.01	98.33	cpx (Amp4)	
TA17	12 / 1 .	50.00	0.42	4.10	9.80	0.21	10.62	21.78	1.07	0.00	98.01	cpx (Amp5)	

Sample	Point	SiO2	TiO2	Al2O3	FeO	MnO	MgO	CaO	Na2O	K2O	Total	Comment	Distance (µm)
TA17	13 / 1 .	29.66	37.38	1.37	0.64	0.07	-0.07	28.50	0.01	0.01	97.63	ttn (Ox2)	
TA17	14 / 1 .	41.06	2.06	12.46	15.94	0.19	9.40	11.63	2.40	0.78	95.92	Amp6	
TA17	15 / 1 .	40.44	2.04	13.30	15.94	0.20	9.16	11.74	2.35	0.85	96.02	Amp7	
TA17	16 / 1 .	51.85	0.19	1.67	8.62	0.19	12.06	24.27	0.52	0.02	99.39	cpx (Amp8)	
TA17	17 / 1 .	49.47	0.55	4.90	10.48	0.19	10.55	21.70	1.14	0.01	99.02	cpx (Amp9)	
TA17	18 / 1 .	38.28	0.15	27.36	6.45	0.11	0.16	23.82	0.03	0.02	96.38	Ep3	
TA17	19 / 1 .	39.79	1.69	12.89	16.91	0.13	9.57	11.23	2.06	0.83	95.10	Amp10	
TA17	20 / 1 .	49.65	0.52	4.64	9.68	0.17	10.59	22.79	0.96	0.00	99.00	cpx (Amp11)	
TA17	21 / 1 .	38.36	0.08	28.21	5.57	0.04	-0.01	24.61	0.01	0.00	96.87	Ep4	
TA17	22 / 1 .	37.77	0.08	24.85	9.48	0.07	-0.03	24.15	0.01	-0.01	96.41	Ep5	
TA17	23 / 1 .	42.29	1.87	11.71	15.00	0.17	10.15	11.89	2.18	0.71	95.98	Amp12	
TA17	24 / 1 .	49.89	0.49	4.11	10.39	0.22	10.38	21.95	1.04	0.02	98.51	cpx (Amp13)	
TA17	25 / 1 .	41.34	2.16	12.43	15.56	0.16	9.49	11.60	2.34	0.81	95.89	Amp14	
TA17	26 / 1 .	41.68	1.85	12.48	15.67	0.15	9.57	11.70	2.32	0.79	96.20	Amp15	
TA17	27 / 1 .	49.13	0.63	5.13	10.36	0.20	10.29	21.96	1.09	0.01	98.80	cpx (Amp16)	
TA17	28 / 1 .	49.34	0.57	4.98	10.18	0.17	10.55	22.05	1.14	0.01	98.98	Cpx1	
TA17	29 / 1 .	49.77	0.60	5.07	10.07	0.17	10.62	21.89	1.13	0.01	99.35	Cpx2	
TA17	30 / 1 .	37.26	0.14	18.19	19.14	0.35	6.00	11.42	2.39	1.08	95.98	Ep6	
TA17	31 / 1 .	0.12	52.74	0.01	38.89	3.70	0.03	0.14	0.02	0.01	95.66	im (FeOx)	
TA17	32 / 1 .	38.32	0.09	20.84	23.34	1.02	5.51	9.76	0.01	0.00	98.88	Grt3	
TA17	33 / 1 .	38.30	0.09	20.79	22.53	1.05	5.45	10.79	0.00	0.00	98.99	Grt4	
TA17	34 / 1 .	38.30	0.26	20.55	21.78	0.96	4.69	12.47	0.03	0.00	99.05	Grt5	
TA17	35 / 1 .	38.21	0.30	20.57	22.15	1.02	4.71	12.36	0.01	0.00	99.33	Grt6	
TA17	36 / 1 .	38.28	0.17	20.44	23.81	1.06	5.13	10.16	0.03	0.00	99.09	Grt7	
TA17	37 / 1 .	38.15	0.18	20.51	23.75	1.08	5.19	10.18	0.01	-0.01	99.04	Grt8	
TA17	38 / 1 .	38.10	0.16	20.48	24.05	1.07	5.28	9.65	0.02	0.00	98.80	Grt9	
TA17	39 / 1 .	37.44	0.14	20.19	23.25	1.28	4.72	11.53	0.01	0.05	98.60	Grt10	
TA17	40 / 1 .	38.20	0.11	20.72	24.60	1.15	5.44	8.89	0.01	0.02	99.15	Grt11	
TA17	41 / 1 .	38.08	0.12	20.53	24.61	1.13	5.59	8.93	0.00	0.02	99.01	Grt12	
TA17	42 / 1 .	38.15	0.09	20.74	23.96	1.05	5.59	9.14	0.01	-0.01	98.73	Grt13	
TA17	43 / 1 .	38.33	0.13	20.65	23.93	1.13	5.44	9.84	0.02	-0.01	99.46	Grt14	
TA17	44 / 1 .	38.15	0.12	20.53	24.57	1.21	5.53	8.74	0.02	0.00	98.87	Grt15	
TA17	45 / 1 .	38.33	0.13	20.50	24.16	1.14	5.48	9.44	0.03	0.01	99.22	Grt16	
TA17	46 / 1 .	49.36	0.57	5.09	11.04	0.15	10.12	21.48	1.21	0.02	99.04	Cpx3	
TA17	47 / 1 .	49.46	0.59	5.06	10.70	0.15	10.55	21.54	1.07	-0.01	99.12	Cpx4	
TA17	48 / 1 .	49.93	0.61	4.87	9.99	0.14	10.81	21.62	1.11	0.00	99.08	Cpx5	
TA17	49 / 1 .	49.46	0.61	5.04	10.40	0.14	10.62	21.45	1.22	0.00	98.93	Cpx6	
TA17	50 / 1 .	49.20	0.68	5.27	10.45	0.14	10.52	21.70	1.03	0.01	99.00	Cpx7	
TA17	51 / 1 .	49.40	0.64	5.27	10.39	0.16	10.49	21.67	1.08	0.00	99.10	Cpx8	
TA17	52 / 1 .	37.75	0.04	23.45	11.10	0.13	-0.02	23.99	0.00	0.01	96.48	Ep7	
TA17	53 / 1 .	41.52	1.89	12.74	15.75	0.16	9.54	11.70	2.22	0.78	96.30	Amp17	
TA17	54 / 1 .	48.14	0.47	6.63	11.81	0.21	10.45	19.45	1.51	0.14	98.79	cpx (Amp18)	
TA17	55 / 1 .	48.61	0.50	4.55	10.19	0.17	10.42	21.40	1.22	0.00	97.08	Cpx9	
TA17	56 / 1 .	49.25	0.62	5.14	9.94	0.18	10.38	22.51	1.00	0.00	99.03	Cpx10	
TA17	57 / 1 .	49.68	0.60	5.11	9.79	0.19	10.59	21.87	1.20	0.00	99.02	Cpx11	
TA17	58 / 1 .	49.93	0.56	4.90	10.16	0.19	10.63	21.62	1.19	0.00	99.17	Cpx12	
TA17	59 / 1 .	49.20	0.55	5.09	10.72	0.16	10.60	21.23	1.32	0.00	98.86	Cpx13	
TA17	60 / 1 .	41.93	1.50	12.28	15.56	0.23	9.75	11.73	2.32	0.77	96.07	Amp19	
TA17	61 / 1 .	41.02	1.79	12.49	16.79	0.27	8.98	11.58	2.32	0.82	96.06	Amp20	
TA17	62 / 1 .	46.60	0.36	7.87	15.37	0.28	11.63	11.89	1.64	0.31	95.95	Amp21	
TA17	63 / 1 .	66.21	-0.01	20.71	0.11	0.01	0.00	1.89	10.28	0.10	99.31	pl1	
TA17	64 / 1 .	65.95	-0.01	20.58	0.10	0.00	-0.02	1.70	10.56	0.10	98.99	pl2	
TA17	65 / 1 .	66.75	0.00	20.21	0.19	0.01	0.01	1.31	10.70	0.10	99.28	pl3	
TA17	66 / 1 .	49.10	0.51	5.11	10.93	0.17	10.14	21.40	1.12	0.02	98.49	Cpx14	
TA17	67 / 1 .	49.13	0.55	5.21	11.23	0.20	10.23	21.53	1.04	0.00	99.12	Cpx15	
TA17	68 / 1 .	49.30	0.56	5.28	11.12	0.14	10.30	20.76	1.24	0.01	98.73	Cpx16	
TA17	69 / 1 .	49.34	0.52	4.95	10.96	0.20	10.41	20.97	1.25	0.00	98.61	Cpx17	
TA17	70 / 1 .	37.45	0.03	23.42	11.40	0.35	0.01	23.13	0.00	0.00	95.80	Ep7	
TA17	71 / 1 .	66.36	0.00	20.50	0.05	0.00	0.00	1.65	10.57	0.08	99.22	Pl4	
TA17	72 / 1 .	48.89	0.55	5.43	10.98	0.23	10.13	20.85	1.42	0.00	98.47	Cpx18	
TA17	73 / 1 .	37.55	0.03	24.65	9.69	0.13	-0.02	24.03	0.00	-0.01	96.07	Ep8	
TA17	74 / 1 .	37.77	0.27	20.37	22.03	1.47	3.97	13.04	0.02	0.01	98.94	Grt 17	
TA17	75 / 1 .	37.89	0.19	20.31	22.28	1.52	3.79	12.81	0.01	0.00	98.81	Grt 18	
TA17	76 / 1 .	38.12	0.12	22.95	11.12	0.20	0.85	22.37	0.27	0.08	96.08	sym1	
TA17	77 / 1 .	36.89	0.14	21.79	13.09	0.22	0.02	23.37	0.00	0.00	95.52	sym2	
TA17	78 / 1 .	42.42	0.34	11.80	15.82	0.27	10.39	11.35	2.47	0.58	95.45	sym3	
TA17	79 / 1 .	37.14	0.15	22.00	12.96	0.22	-0.01	23.48	0.00	0.00	95.94	sym4	
TA17	80 / 1 .	37.72	0.09	23.36	10.83	0.17	0.53	23.34	0.09	0.03	96.16	sym5	
TA17	81 / 1 .	37.34	0.08	23.48	10.98	0.20	0.08	23.61	0.04	0.01	95.82	sym81	
TA17	81 / 2 .	37.47	0.09	23.62	11.16	0.18	-0.01	23.65	0.00	0.00	96.17	sym81	
TA17	81 / 3 .	37.82	0.12	22.02	12.02	0.24	0.93	22.43	0.22	0.05	95.85	sym81	
TA17	81 / 4 .	37.46	0.11	22.88	11.87	0.22	0.00	23.59	0.01	0.02	96.15	sym81	
TA17	81 / 5 .	37.56	0.26	19.77	20.65	1.26	3.98	14.28	0.08	0.33	98.18	sym81	
TA17	81 / 6 .	37.86	0.28	20.46	21.99	1.39	3.92	12.78	0.01	-0.01	98.69	sym81	
TA17	81 / 7 .	30.26	38.60	0.99	1.12	0.06	-0.08	28.75	-0.01	0.00	99.79	ttn (sym81)	

Sample	Point	SiO2	TiO2	Al2O3	FeO	MnO	MgO	CaO	Na2O	K2O	Total	Comment	Distance (µm)
TA17	81 / 8 .	37.89	0.27	20.29	22.19	1.51	3.83	12.99	0.03	0.00	99.00	sym81	
TA17	81 / 9 .	37.97	0.22	20.34	21.96	1.57	3.77	13.09	0.03	0.01	98.97	sym81	
TA17	81 / 10 .	37.98	0.20	20.41	21.98	1.58	3.75	12.91	0.02	0.00	98.83	sym81	
TA17	82 / 1 .	40.88	1.79	13.20	15.86	0.15	9.30	11.67	2.26	0.87	95.99	amp22	
TA17	83 / 1 .	45.86	0.36	8.41	15.30	0.25	11.71	11.54	1.77	0.40	95.61	amp23	
TA17	84 / 1 .	37.96	0.10	20.78	24.44	1.31	5.32	8.99	0.00	-0.01	98.91	grtds84	
TA17	84 / 2 .	38.09	0.24	20.48	22.36	1.26	4.74	11.64	0.02	0.01	98.84	grtds84	
TA17	84 / 3 .	38.12	0.25	20.48	21.77	1.32	4.48	12.72	0.01	0.00	99.15	grtds84	
TA17	84 / 4 .	38.15	0.21	20.31	21.64	1.40	4.40	12.79	0.03	-0.01	98.92	grtds84	
TA17	84 / 5 .	38.14	0.24	20.47	21.60	1.44	4.45	12.73	0.03	0.00	99.10	grtds84	
TA17	84 / 6 .	37.23	0.23	20.00	20.70	1.31	4.33	13.98	0.05	0.02	97.86	[fx]grtds84	
TA17	84 / 7 .	37.74	0.15	20.19	21.87	1.48	4.49	12.00	0.00	0.02	97.94	grtds84	
TA17	84 / 8 .	30.19	38.08	1.27	0.91	0.07	-0.07	28.75	0.00	-0.01	9§9.2711	ttn (grtds84)	
TA17	84 / 9 .	38.18	0.26	20.44	22.26	1.50	4.49	11.94	0.01	0.00	99.08	grtds84	
TA17	84 / 10 .	38.05	0.24	20.48	21.71	1.44	4.36	12.67	0.03	0.00	98.96	grtds84	
TA17	84 / 11 .	38.20	0.24	20.52	21.64	1.51	4.31	12.93	0.02	0.01	99.37	grtds84	
TA17	84 / 12 .	38.03	0.26	20.43	21.71	1.49	4.31	12.85	0.03	-0.01	99.10	grtds84	
TA17	84 / 13 .	38.15	0.25	20.41	21.63	1.48	4.31	12.91	0.03	0.01	99.17	grtds84	
TA17	84 / 14 .	38.08	0.24	20.45	21.77	1.50	4.35	12.89	0.03	-0.01	99.30	grtds84	
TA17	84 / 15 .	30.06	0.16	16.74	20.25	1.00	5.04	15.14	0.04	0.02	88.44	[incl]grtds84	
TA17	84 / 16 .	38.10	0.24	20.39	21.60	1.47	4.34	12.77	0.03	-0.02	98.93	grtds84	
TA17	84 / 17 .	38.02	0.23	20.40	21.60	1.49	4.40	12.88	0.04	0.01	99.07	grtds84	
TA17	84 / 18 .	38.30	0.25	20.46	21.69	1.62	4.18	13.03	0.02	-0.01	99.55	grtds84	
TA17	84 / 19 .	38.26	0.25	20.47	21.58	1.41	4.35	12.78	0.03	-0.02	99.13	grtds84	
TA17	84 / 20 .	37.55	0.18	20.23	23.10	1.26	4.81	11.21	0.01	0.00	98.37	grtds84	
TA17	85 / 1 .	37.45	0.53	23.36	10.83	0.12	0.02	23.58	0.01	0.00	95.90	ep9	
TA17	86 / 1 .	38.26	0.09	20.59	22.97	1.06	4.68	11.55	0.01	-0.01	99.22	grt19	
TA17	87 / 1 .	38.37	0.07	20.76	22.67	1.03	4.57	11.83	0.03	0.00	99.33	grt19	
TA17	88 / 1 .	38.18	0.08	20.64	22.19	1.03	4.43	12.49	0.01	-0.01	99.06	grt19	
TA17	89 / 1 .	38.32	0.10	20.65	22.08	1.02	4.48	12.59	0.01	-0.01	99.25	grt19	
TA17	90 / 1 .	38.25	0.12	20.65	22.44	1.02	4.69	11.98	0.01	0.01	99.17	grt19	
TA17	91 / 1 .	38.29	0.13	20.72	22.96	1.03	4.84	11.35	-0.01	-0.01	99.32	grt19	
TA17	92 / 1 .	38.18	0.15	20.70	23.37	1.01	4.97	10.86	0.02	-0.01	99.25	grt19	
TA17	93 / 1 .	38.38	0.32	20.62	23.52	1.03	4.98	10.59	0.01	0.00	99.45	grt19	
TA17	94 / 1 .	38.31	0.11	20.89	22.97	0.97	5.15	10.78	0.00	0.00	99.19	grt19	
TA17	95 / 1 .	38.18	0.17	20.41	23.45	0.97	5.32	10.45	0.02	-0.02	98.98	grt19	
TA17	96 / 1 .	41.45	2.53	12.44	15.34	0.15	9.78	11.57	2.22	0.89	96.37	amp24	
TA17	97 / 1 .	40.98	1.77	13.00	15.48	0.19	9.64	11.73	2.38	0.91	96.09	amp25	
TA17	98 / 1 .	50.54	0.16	3.22	9.86	0.19	11.05	23.39	0.98	-0.01	99.40	cpx (amp26)	
TA17	99 / 1 .	40.88	4.36	12.02	15.23	0.14	9.46	11.38	2.30	0.83	96.60	inclusion (amp27)	
TA17	100 / 1 .	41.36	2.15	12.66	15.54	0.14	9.44	11.67	2.42	0.90	96.29	amp28	
TA17	101 / 1 .	48.89	0.54	5.36	10.91	0.18	10.34	21.08	1.37	0.02	98.68	cpx19	
TA17	102 / 1 .	49.73	0.54	4.77	10.28	0.17	10.59	21.77	1.31	0.01	99.17	cpx20	
TA17		56.00	0.00	26.30	0.20	0.00	0.00	10.60	6.60	0.20		saus1	
TA17		57.00	0.00	25.20	0.40	0.00	0.00	9.70	7.20	0.00		saus2	
TA17		58.50	0.00	24.60	0.50	0.00	0.00	8.50	7.70	0.20		saus3	
TA17		56.60	0.00	25.80	0.40	0.00	0.00	10.20	7.10	0.00		saus4	
TA17		56.10	0.00	26.10	0.30	0.00	0.00	9.80	6.70	0.40		saus5	
TA17		57.60	0.00	25.30	0.40	0.00	0.00	9.50	7.30	0.00		saus6	
TA17		58.20	0.00	25.10	0.30	0.00	0.00	8.60	7.50	0.30		saus7	
TA17		56.50	0.00	25.70	0.50	0.00	0.00	10.10	6.90	0.30		saus8	
TA17		57.10	0.00	26.00	0.40	0.00	0.00	8.70	7.20	0.60		saus9	
TA46	64 / 1 .	4.27	0.00	0.25	77.10	0.16	0.41	0.56	0.06	0.04	82.89	[fx]oxide	
TA46	65 / 1 .	4.22	0.00	0.24	78.23	0.20	0.33	0.56	0.10	0.03	83.95	[fx]oxide	
TA46	66 / 1 .	65.14	0.00	22.03	0.04	0.03	0.00	1.95	11.28	0.11	100.58	pl	
TA46	67 / 1 .	65.77	0.00	20.33	0.04	0.00	0.00	0.81	11.15	0.08	98.25	pl	
TA46	68 / 1 .	64.52	0.00	21.43	0.05	0.00	0.00	1.98	10.29	0.21	98.48	pl	
TA46	69 / 1 .	36.41	0.17	25.43	10.35	0.10	0.00	23.60	0.00	0.00	96.10	ep	
TA46	76 / 1 .	46.39	0.49	9.60	13.94	0.26	12.75	11.44	1.16	1.04	97.13	amp	
TA46	77 / 1 .	38.02	0.25	25.24	10.33	0.17	0.06	22.44	0.01	0.01	96.59	ep	
TA46	78 / 1 .	37.90	0.32	25.24	10.14	0.17	0.05	22.34	0.01	0.00	96.20	ep (amp)	
TA46	79 / 1 .	47.34	0.45	9.04	13.68	0.26	12.99	11.40	1.07	0.90	97.15	amp	
TA46	80 / 1 .	53.87	0.05	2.79	10.42	0.27	17.04	12.10	0.46	0.15	97.17	amp	
TA46	81 / 1 .	67.31	0.00	20.97	0.04	0.00	0.00	0.82	10.53	0.09	99.77	albite (amp)	
TA46	82 / 1 .	53.42	0.03	2.89	10.95	0.28	16.29	11.86	0.46	0.17	96.45	amp core	
TA46	83 / 1 .	53.59	0.10	3.19	11.51	0.23	16.30	12.00	0.50	0.19	97.72	amp rim	
TA46	84 / 1 .	37.78	0.29	26.19	9.74	0.12	0.12	22.75	0.02	0.00	97.10	ep	
TA46	85 / 1 .	38.03	0.17	24.63	11.42	0.16	0.00	22.61	0.01	0.00	97.03	ep	
TA46	86 / 1 .	38.09	0.30	25.95	9.95	0.11	0.10	22.47	0.01	0.00	96.97	ep core	
TA46	87 / 1 .	38.05	0.21	25.63	10.10	0.11	0.00	22.59	0.00	0.01	96.84	ep rim	
TA46	88 / 1 .	69.44	0.00	23.42	0.10	0.04	0.00	0.98	12.16	0.12	106.27	*pl	
TA46	89 / 1 .	53.89	0.12	4.30	9.72	0.31	16.94	11.55	0.48	0.65	98.03	amp core	
TA46	90 / 1 .	54.53	0.03	1.13	12.47	0.28	15.70	12.41	0.11	0.10	96.90	amp rim	
TA46	91 / 1 .	37.45	0.04	25.29	10.70	0.09	0.00	23.18	0.00	0.00	96.82	ep (amp core)	

Sample	Point	SiO2	TiO2	Al2O3	FeO	MnO	MgO	CaO	Na2O	K2O	Total	Comment	Distance (µm)
TA46	92 / 1 .	37.96	0.13	25.95	9.76	0.16	0.05	22.91	0.00	0.01	96.95	ep	
TA46	93 / 1 .	49.66	0.06	30.48	2.49	0.03	2.81	0.07	0.13	11.84	97.57	ms	
TA46	94 / 1 .	51.18	0.03	30.70	2.15	0.03	3.01	0.16	0.23	11.80	99.28	mxPl	0
TA46	94 / 2 .	67.02	0.00	21.54	0.05	0.00	0.00	1.12	9.92	0.25	99.91	Pl	58
TA46	94 / 3 .	65.91	0.00	22.71	0.01	0.01	0.00	1.86	10.12	0.70	101.32	Pl	116
TA46	94 / 4 .	65.86	0.00	21.52	0.01	0.01	0.00	1.70	10.20	0.09	99.39	Pl	174
TA46	94 / 5 .	65.38	0.00	22.41	0.02	0.02	0.00	2.32	10.30	0.09	100.55	Pl	232
TA46	94 / 6 .	65.53	0.00	20.92	0.02	0.02	0.00	1.42	9.26	0.09	97.29	Pl	290
TA46	94 / 7 .	66.83	0.01	21.23	0.00	0.00	0.02	1.25	10.88	0.09	100.34	Pl	349
TA46	94 / 8 .	66.47	0.00	21.26	0.08	0.03	0.00	1.36	9.97	0.09	99.26	Pl	407
TA46	94 / 9 .	66.90	0.01	20.62	0.04	0.00	0.00	0.90	10.70	0.14	99.33	Pl	465
TA46	94 / 10 .	45.51	0.66	11.03	12.93	0.25	13.14	11.69	1.39	1.21	97.93	amp (Pl)	523
TA46	95 / 1 .	50.34	0.00	29.36	2.64	0.03	3.00	0.01	0.18	12.35	97.91	ms	
TA46	96 / 1 .	53.06	0.05	3.86	10.51	0.22	16.78	12.26	0.55	0.24	97.57	amp	
TA46	97 / 1 .	46.32	0.72	10.00	12.98	0.25	13.01	11.69	1.30	1.11	97.48	amp	
TA46	98 / 1 .	36.22	0.10	24.43	11.55	0.21	0.00	23.22	0.00	0.00	95.79	ep (amp)	
TA46	99 / 1 .	37.27	0.04	25.40	11.16	0.22	0.01	23.10	0.00	0.00	97.21	ep	
TA46	100 / 1 .	52.79	0.08	3.18	9.63	0.25	17.14	12.50	0.43	0.21	96.24	amp	
TA46	101 / 1 .	67.08	0.00	21.77	0.11	0.00	0.02	1.47	10.85	0.09	101.40	pl	
TA46	102 / 1 .	37.28	0.18	25.94	9.92	0.11	0.07	23.43	0.00	0.00	96.97	ep	
TA46	103 / 1 .	50.84	0.07	3.68	11.35	0.32	15.66	12.09	0.44	0.22	94.76	low total (amp core)	
TA46	104 / 1 .	52.67	0.06	2.61	10.77	0.31	16.65	12.60	0.43	0.12	96.23	amp rim	
TA46	105 / 1 .	37.30	0.26	25.75	10.07	0.15	0.10	23.06	0.01	0.00	96.80	ep	
TA46	106 / 1 .	37.08	0.19	26.24	9.79	0.14	0.05	23.18	0.00	0.00	96.74	ep	
TA46	107 / 1 .	67.09	0.01	21.38	0.04	0.01	0.00	1.48	10.71	0.13	100.85	pl	
TA46	108 / 1 .	37.27	0.16	24.60	11.32	0.11	0.00	23.07	0.00	0.00	96.54	ep	
TA46	109 / 1 .	51.61	0.06	4.04	11.34	0.23	15.99	12.25	0.65	0.24	96.75	amp	0
TA46	109 / 2 .	51.63	0.07	3.62	11.47	0.28	15.91	12.29	0.56	0.26	96.32	amp	21
TA46	109 / 3 .	53.58	0.05	2.58	11.44	0.29	16.03	12.25	0.42	0.20	97.07	amp	41
TA46	109 / 4 .	51.56	0.05	4.06	12.27	0.32	15.77	12.17	0.62	0.28	97.30	amp	62
TA46	109 / 5 .	51.81	0.00	3.42	11.50	0.25	16.06	12.32	0.52	0.20	96.11	amp	83
TA46	109 / 6 .	37.90	0.18	24.91	9.90	0.14	0.88	22.25	0.07	0.04	96.45	fxep	104
TA46	109 / 7 .	38.25	0.17	26.37	10.34	0.15	0.07	23.03	0.00	0.00	98.44	ep	124
TA46	109 / 8 .	37.15	0.23	25.80	10.23	0.17	0.06	23.21	0.01	0.00	96.96	ep	145
TA46	109 / 9 .	35.60	0.23	26.41	9.07	0.13	0.09	22.68	0.02	0.00	94.32	fxep	166
TA46	109 / 10 .	37.37	0.24	26.55	9.32	0.14	0.04	23.36	0.00	0.00	97.10	ep	187
TA46	110 / 1 .	37.56	0.18	25.95	9.42	0.09	0.06	23.14	0.00	0.01	96.50	ep	
TA46	113 / 1 .	30.16	38.64	1.31	0.56	0.02	0.00	27.35	0.04	0.01	98.14	ttn	
TA46	114 / 1 .	37.48	0.28	25.02	11.06	0.36	0.00	22.30	0.00	0.00	96.55	ep core	
TA46	115 / 1 .	37.21	0.33	24.91	11.12	0.35	0.02	22.32	0.00	0.01	96.28	ep rim	
TA46	116 / 1 .	30.12	38.61	1.23	0.59	0.03	0.00	27.33	0.00	0.01	97.91	ttn	
TA46	117 / 1 .	53.65	0.00	3.14	10.69	0.26	16.93	12.10	0.47	0.16	97.50	amp	
TA46	118 / 1 .	44.24	0.83	11.75	13.99	0.23	12.04	11.20	1.45	1.37	97.22	amp	
TA46	119 / 1 .	52.88	0.08	3.83	11.01	0.23	16.15	12.13	0.60	0.23	97.17	amp	
TA46	120 / 1 .	52.88	0.11	4.02	12.10	0.22	15.95	11.84	0.57	0.26	98.03	amp	
TA46	121 / 1 .	30.06	38.58	1.24	0.55	0.07	0.00	27.01	0.01	0.01	97.61	ttn	
TA50	2 / 1 .	48.57	0.63	6.00	10.97	0.11	9.64	22.26	1.00	0.01	99.21	cpx (ep1)	
TA50	3 / 1 .	40.55	1.22	13.66	17.65	0.14	8.27	11.73	1.66	1.54	96.42	amp1	
TA50	4 / 1 .	39.84	1.48	14.25	18.14	0.11	7.57	11.63	1.60	1.60	96.20	amp2	
TA50	5 / 1 .	38.40	0.07	26.66	7.39	0.28	0.01	24.17	0.01	0.01	97.00	ep2	
TA50	6 / 1 .	49.40	0.44	4.67	10.87	0.16	10.04	22.64	0.84	0.02	99.06	cpx1	
TA50	7 / 1 .	48.85	0.59	5.85	11.23	0.17	9.76	21.86	1.01	0.00	99.34	cpx2	
TA50	8 / 1 .	40.66	1.32	14.40	16.81	0.17	8.40	11.77	1.83	1.22	96.58	amp3	
TA50	9 / 1 .	39.09	0.14	20.93	23.56	0.87	4.82	11.08	0.01	0.01	100.51	grt grtprofileblue2	0
TA50	9 / 2 .	38.64	0.14	20.71	23.46	0.83	4.82	11.03	0.01	0.00	99.64	grt grtprofileblue2	22
TA50	9 / 3 .	38.24	0.16	20.53	23.55	0.84	4.87	10.89	0.00	0.00	99.09	grt grtprofileblue2	44
TA50	9 / 4 .	38.16	0.14	20.62	23.28	0.89	4.74	11.15	0.04	0.02	99.03	grt grtprofileblue2	66
TA50	9 / 5 .	44.94	0.31	9.04	16.19	0.24	8.80	16.27	1.69	0.37	97.85	fxgrtprofileblue2	88
TA50	9 / 6 .	48.72	0.59	5.92	11.13	0.15	9.97	22.02	1.05	0.02	99.57	cpx grtprofileblue2	109
TA50	9 / 7 .	48.60	0.58	6.07	11.09	0.12	9.93	21.75	1.08	0.04	99.26	cpx grtprofileblue2	131
TA50	9 / 8 .	47.38	0.57	7.82	12.04	0.10	7.83	20.06	0.79	0.04	96.63	fxcpx grtprofileblue2	153
TA50	9 / 9 .	48.42	0.61	5.73	11.01	0.16	9.78	22.20	0.97	0.00	98.88	cpx grtprofileblue2	175
TA50	9 / 10 .	48.44	0.60	5.84	11.06	0.12	9.76	22.03	0.95	0.02	98.81	cpx grtprofileblue2	197
TA50	10 / 1 .	38.56	0.21	20.39	23.65	0.84	4.83	11.11	0.01	-0.02	99.60	grtprofileblue3	0
TA50	10 / 2 .	38.53	0.19	20.38	23.70	0.89	4.90	11.16	0.00	0.02	99.77	grtprofileblue3	26
TA50	10 / 3 .	38.41	0.20	20.39	23.73	0.85	4.86	10.91	-0.01	-0.01	99.35	grtprofileblue3	51
TA50	10 / 4 .	37.77	0.18	20.10	23.63	0.90	4.80	10.91	0.02	0.01	98.31	grtprofileblue3	77
TA50	10 / 5 .	38.79	0.15	20.64	23.51	0.87	4.78	10.95	0.00	0.02	99.72	grtprofileblue3	102
TA50	10 / 6 .	42.40	0.43	12.11	17.53	0.15	8.58	13.72	1.79	0.71	97.42	fxgrtprofileblue3	128
TA50	10 / 7 .	49.21	0.56	5.63	10.43	0.14	9.78	22.52	1.01	0.01	99.29	cpx grtprofileblue3	154
TA50	10 / 8 .	49.51	0.54	5.58	10.47	0.16	9.68	22.57	0.93	0.00	99.44	cpx grtprofileblue3	179
TA50	10 / 9 .	43.88	0.58	5.38	10.43	0.14	8.45	21.73	0.83	0.01	91.42	fxcpx grtprofileblue3	205
TA50	10 / 10 .	49.06	0.58	5.88	10.85	0.15	9.81	21.99	1.08	0.03	99.44	cpx grtprofileblue3	231
TA50	11 / 1 .	48.41	0.63	6.10	10.89	0.15	9.65	21.97	1.06	0.00	98.85	cpx grtprofileblue4	0

Sample	Point	SiO2	TiO2	Al2O3	FeO	MnO	MgO	CaO	Na2O	K2O	Total	Comment	Distance (µm)
TA50	11 / 2 .	49.96	0.44	4.21	10.56	0.15	10.20	23.02	0.81	0.01	99.36	cpx grtprofileblue4	33
TA50	11 / 3 .	48.89	0.56	6.10	10.74	0.15	9.67	22.18	1.00	0.01	99.29	cpx grtprofileblue4	66
TA50	11 / 4 .	3.35	0.27	1.42	22.51	1.14	2.97	10.57	0.04	0.04	42.32	[fx]grtprofileblue4	99
TA50	11 / 5 .	38.35	0.33	20.36	23.38	1.04	4.52	11.52	0.03	0.00	99.53	grtprofileblue4	132
TA50	11 / 6 .	38.26	0.31	20.33	23.37	1.10	4.61	11.48	0.02	0.00	99.47	grtprofileblue4	165
TA50	11 / 7 .	38.38	0.31	20.22	23.37	1.04	4.58	11.44	0.03	-0.01	99.37	grtprofileblue4	198
TA50	11 / 8 .	32.36	0.34	18.38	24.06	1.05	3.38	11.07	0.10	0.05	90.79	[fx]grtprofileblue4	231
TA50	11 / 9 .	46.17	0.49	6.94	12.67	0.10	10.52	18.55	1.19	0.28	96.91	[fx]grtprofileblue4	264
TA50	11 / 10 .	48.98	0.56	5.66	10.50	0.12	10.04	22.56	1.00	0.00	99.42	cpx grtprofileblue4	297
TA50	12 / 1 .	37.59	0.31	24.19	10.00	0.17	0.12	23.68	-0.01	0.00	96.06	ep3	
TA50	13 / 1 .	38.28	0.28	20.47	23.41	1.03	4.63	11.40	0.01	-0.01	99.51	grtprofileblue5	0
TA50	13 / 2 .	38.36	0.27	20.26	23.33	0.99	4.61	11.45	0.02	0.01	99.31	grtprofileblue5	15
TA50	13 / 3 .	38.12	0.29	20.64	23.34	0.98	4.45	11.38	0.03	-0.01	99.24	grtprofileblue5	31
TA50	13 / 4 .	38.11	0.29	20.24	23.45	0.97	4.59	11.44	0.02	0.00	99.10	grtprofileblue5	46
TA50	13 / 5 .	38.15	0.29	20.41	23.56	1.04	4.20	11.40	0.03	0.01	99.08	grtprofileblue5	62
TA50	13 / 6 .	41.36	0.48	12.98	18.71	0.29	7.89	11.99	1.98	0.59	96.27	[fx]grtprofileblue5	77
TA50	13 / 7 .	48.78	0.50	5.39	11.27	0.22	9.89	22.28	0.96	0.04	99.33	cpx grtprofileblue5	92
TA50	13 / 8 .	48.93	0.61	5.81	10.50	0.17	9.61	22.97	0.96	0.00	99.58	cpx grtprofileblue5	108
TA50	13 / 9 .	48.95	0.60	5.79	10.33	0.18	9.76	22.78	1.01	-0.01	99.40	cpx grtprofileblue5	123
TA50	13 / 10 .	48.95	0.61	5.73	10.56	0.15	9.71	22.76	0.97	0.00	99.44	cpx grtprofileblue5	139
TA50	14 / 1 .	49.03	0.53	5.59	11.10	0.16	9.85	22.33	1.01	0.02	99.61	cpx (ep4)	
TA50	15 / 1 .	42.86	1.09	12.60	14.67	0.15	10.21	11.74	1.68	1.32	96.31	amp4	
TA50	16 / 1 .	50.52	0.48	7.19	8.30	0.19	16.07	12.57	1.32	0.27	96.91	amp5	
TA50	17 / 1 .	38.09	0.16	25.57	8.79	0.05	0.00	24.09	0.00	0.00	96.75	ep5	
TA50	18 / 1 .	48.45	0.57	5.98	10.71	0.18	9.88	22.11	1.16	0.02	99.05	cpx3	
TA50	19 / 1 .	48.72	0.57	5.94	10.58	0.15	10.03	22.43	0.98	0.00	99.40	cpx4	
TA50	20 / 1 .	49.63	0.52	5.33	9.53	0.14	10.68	23.07	0.93	-0.01	99.81	cpx5	
TA50	21 / 1 .	38.43	0.12	20.66	23.05	1.10	5.01	11.35	0.01	0.00	99.74	grtprofilered	0
TA50	21 / 2 .	38.62	0.13	20.56	23.27	1.07	5.00	11.34	0.02	-0.01	100.01	grtprofilered	34
TA50	21 / 3 .	38.57	0.17	20.69	23.29	1.08	5.09	11.32	0.01	0.02	100.24	grtprofilered	68
TA50	21 / 4 .	38.88	0.20	21.57	22.90	1.00	5.26	10.86	0.08	0.06	100.82	grtprofilered	102
TA50	21 / 5 .	38.91	0.14	20.67	22.92	1.09	4.87	11.29	0.01	0.01	99.90	grtprofilered	136
TA50	21 / 6 .	15.01	0.28	8.19	22.67	1.06	5.27	11.02	0.06	0.03	63.59	[fx]grtprofilered	170
TA50	21 / 7 .	31.61	31.83	5.39	5.25	0.19	0.54	25.26	0.06	0.03	100.16	ttn grtprofilered	203
TA50	21 / 8 .	38.63	0.22	20.45	22.92	1.04	4.88	11.37	0.00	0.00	99.50	grtprofilered	237
TA50	21 / 9 .	38.54	0.15	20.52	23.00	1.11	4.91	11.39	0.02	0.01	99.64	grtprofilered	271
TA50	21 / 10 .	31.71	0.17	18.09	22.76	1.01	4.98	10.67	0.13	0.07	89.60	[fx]grtprofilered	305
TA50	21 / 11 .	38.64	0.15	20.40	22.89	1.13	4.86	11.41	0.02	0.00	99.50	grtprofilered	339
TA50	21 / 12 .	38.72	0.16	20.63	23.09	1.08	4.87	11.35	0.01	0.00	99.91	grtprofilered	373
TA50	21 / 13 .	38.60	0.15	20.51	23.17	1.08	4.91	11.29	0.01	0.00	99.74	grtprofilered	407
TA50	21 / 14 .	38.57	0.15	20.60	22.95	1.13	4.74	11.42	0.00	0.00	99.56	grtprofilered	441
TA50	21 / 15 .	38.60	0.14	20.50	23.12	1.04	4.84	11.55	0.02	-0.01	99.81	grtprofilered	475
TA50	21 / 16 .	38.52	0.10	20.76	23.04	1.15	4.86	11.37	0.02	0.00	99.83	grtprofilered	509
TA50	21 / 17 .	38.44	0.13	20.57	23.05	1.13	4.64	11.40	0.02	-0.01	99.36	grtprofilered	542
TA50	21 / 18 .	44.32	0.69	15.06	14.12	0.14	10.43	11.63	1.59	0.75	98.71	mxgrtprofilered	576
TA50	21 / 19 .	50.24	0.51	5.12	8.40	0.11	11.45	23.22	0.83	0.02	99.89	cpx grtprofilered	610
TA50	21 / 20 .	48.76	0.59	5.87	9.75	0.10	10.42	22.26	0.92	0.03	98.70	cpx grtprofilered	644
TA50	21 / 21 .	38.59	0.22	20.35	22.72	1.25	4.41	12.11	0.01	-0.01	99.65	grtprofilered	678
TA50	21 / 22 .	38.74	0.20	20.53	22.34	1.44	4.40	12.29	0.00	0.00	99.94	grtprofilered	712
TA50	21 / 23 .	38.54	0.13	20.56	22.23	1.54	4.46	12.04	0.00	-0.01	99.49	grtprofilered	746
TA50	21 / 24 .	68.59	-0.01	20.31	0.39	0.01	0.00	0.45	11.08	0.13	100.96	pl (grtprofilered)	780
TA50	21 / 25 .	68.42	0.00	20.35	0.39	0.01	0.00	0.38	11.06	0.10	100.70	pl (grtprofilered)	814
TA50	21 / 26 .	68.54	0.01	19.99	0.64	0.05	0.01	0.51	10.97	0.11	100.83	pl (grtprofilered)	847
TA50	21 / 27 .	38.56	0.19	20.37	22.68	1.41	4.48	12.11	0.01	0.01	99.83	grtprofilered	881
TA50	21 / 28 .	46.58	0.12	20.24	16.27	0.96	3.17	8.80	2.81	0.01	98.96	mxgrtprofilered	915
TA50	21 / 29 .	38.58	0.14	20.43	22.61	1.23	4.41	11.98	0.01	0.00	99.40	grtprofilered	949
TA50	21 / 30 .	38.42	0.17	20.49	22.90	1.31	4.48	11.97	0.02	0.00	99.77	grtprofilered	983
TA50	21 / 31 .	38.54	0.14	20.53	22.76	1.17	4.59	12.14	0.01	0.00	99.87	grtprofilered	1017
TA50	21 / 32 .	38.68	0.11	20.61	22.54	1.19	4.52	12.29	0.02	0.01	99.96	grtprofilered	1051
TA50	21 / 33 .	38.45	0.17	20.56	22.61	1.25	4.45	12.25	0.02	0.00	99.77	grtprofilered	1085
TA50	21 / 34 .	38.67	0.17	20.53	22.50	1.36	4.46	12.20	0.01	0.00	99.89	grtprofilered	1119
TA50	21 / 35 .	38.66	0.13	20.42	22.42	1.34	4.49	12.09	0.01	0.01	99.56	grtprofilered	1153
TA50	21 / 36 .	38.62	0.16	20.55	22.89	1.28	4.58	11.92	-0.01	-0.01	99.99	grtprofilered	1186
TA50	21 / 37 .	37.55	0.09	20.02	22.82	1.17	5.56	10.71	0.01	0.04	97.96	[fx]grtprofilered	1220
TA50	21 / 38 .	38.80	0.12	20.59	22.28	1.36	4.41	12.19	0.01	0.00	99.77	grtprofilered	1254
TA50	21 / 39 .	38.81	0.13	20.48	22.25	1.36	4.40	12.53	0.02	0.00	99.97	grtprofilered	1288
TA50	21 / 40 .	38.65	0.10	20.67	22.36	1.37	4.46	12.16	0.02	-0.01	99.79	grtprofilered	1322
TA50	21 / 41 .	35.79	0.13	20.78	22.67	1.30	4.46	11.59	0.05	0.04	96.81	[fx]grtprofilered	1356
TA50	21 / 42 .	38.73	0.10	20.65	22.57	1.35	4.46	12.12	0.02	0.00	100.00	grtprofilered	1390
TA50	21 / 43 .	38.66	0.08	20.76	22.90	1.31	4.41	11.86	0.01	0.00	100.00	grtprofilered	1424
TA50	21 / 44 .	38.11	0.18	20.47	22.38	1.30	4.43	12.27	0.02	-0.01	99.16	grtprofilered	1458
TA50	21 / 45 .	38.78	0.15	20.61	22.36	1.46	4.46	12.16	0.01	-0.01	99.99	grtprofilered	1492
TA50	21 / 46 .	38.71	0.30	20.22	22.22	1.39	4.48	12.28	0.03	0.00	99.63	grtprofilered	1525

Sample	Point	SiO2	TiO2	Al2O3	FeO	MnO	MgO	CaO	Na2O	K2O	Total	Comment	Distance (µm)
TA50	21 / 47 .	39.07	0.26	20.49	22.32	1.39	4.41	12.40	0.02	0.00	100.35	grtprofilered	1559
TA50	21 / 48 .	38.12	0.30	20.59	22.29	1.26	4.36	12.40	0.03	0.02	99.37	grtprofilered	1593
TA50	21 / 49 .	38.57	0.25	20.36	23.13	1.23	4.12	12.20	0.01	-0.01	99.88	grtprofilered	1627
TA50	21 / 50 .	38.30	0.26	20.19	23.27	1.20	3.87	12.19	0.00	0.00	99.29	grtprofilered	1661
TA50	22 / 1 .	49.15	0.53	5.47	10.33	0.15	10.06	23.07	0.87	0.00	99.63	cpx (ep6)	
TA50	23 / 1 .	38.03	0.16	24.81	9.68	0.07	0.00	24.07	0.01	0.00	96.82	ep7	
TA50	24 / 1 .	42.21	0.94	12.86	14.57	0.21	10.18	12.13	1.80	1.27	96.17	amp6	
TA50	25 / 1 .	49.75	0.42	6.77	11.19	0.22	14.40	12.54	1.03	0.50	96.81	amp7	
TA50	26 / 1 .	41.26	1.41	13.37	16.33	0.16	9.08	12.04	1.68	1.39	96.72	amp8	
TA50	27 / 1 .	49.98	0.44	5.85	12.16	0.12	14.30	12.36	0.90	0.32	96.42	amp9	
TA50	28 / 1 .	41.38	1.21	13.48	15.88	0.16	9.35	11.98	1.61	1.40	96.46	amp10	
TA50	29 / 1 .	41.76	1.14	13.36	15.75	0.15	9.41	11.87	1.89	1.22	96.54	amp11	
TA50	30 / 1 .	38.31	0.03	26.30	8.18	0.10	-0.02	24.30	0.00	0.00	97.23	ep7	
TA50	31 / 1 .	37.89	0.06	25.17	9.18	0.09	-0.03	24.28	0.00	-0.01	96.67	ep8	
TA50	32 / 1 .	53.72	0.13	3.36	8.86	0.20	16.97	12.92	0.77	0.10	97.02	amp12	
TA50	33 / 1 .	49.56	0.47	5.26	10.08	0.22	10.06	22.60	1.01	0.00	99.26	cpx (amp13)	
TA50	34 / 1 .	49.48	0.47	5.23	10.24	0.27	10.02	22.86	0.97	0.01	99.54	cpx (amp14)	
TA50	35 / 1 .	49.95	0.51	6.13	11.16	0.22	14.72	12.66	1.20	0.30	96.84	amp15	
TA50	36 / 1 .	49.19	0.45	5.44	10.30	0.25	10.08	22.41	1.08	0.01	99.21	cpx (amp16)	
TA50	37 / 1 .	48.85	0.56	7.26	12.43	0.24	13.45	12.41	1.35	0.32	96.88	amp17	
TA50	38 / 1 .	38.54	0.14	20.63	23.67	0.76	4.31	11.86	0.00	0.00	99.91	grt1	
TA50	39 / 1 .	38.40	0.16	20.31	23.64	0.75	4.37	12.05	0.02	0.00	99.70	grt2	
TA50	40 / 1 .	38.36	0.16	20.40	23.78	0.76	4.24	12.13	0.01	0.01	99.86	grt3	
TA50	41 / 1 .	38.35	0.14	20.30	23.67	0.75	4.31	12.13	0.02	0.00	99.68	grt4	
TA50	42 / 1 .	38.17	0.19	20.24	23.61	0.67	4.20	12.08	0.01	0.00	99.18	grt5	
TA50	43 / 1 .	38.07	0.15	20.29	23.88	0.70	3.94	12.04	0.03	0.00	99.10	grt6	
TA50	44 / 1 .	38.35	0.16	19.99	23.28	0.75	3.21	13.80	0.01	0.00	99.56	grt7	
TA50	45 / 1 .	37.97	0.21	19.91	23.48	0.76	3.45	13.45	0.02	0.01	99.27	grt8	
TA50	46 / 1 .	38.22	0.24	19.94	23.32	0.79	3.43	13.63	0.01	0.01	99.58	grt9	
TA50	47 / 1 .	49.06	0.59	5.94	11.59	0.05	9.28	22.37	0.99	0.01	99.87	cpx6	
TA50	48 / 1 .	48.88	0.64	6.01	11.66	0.06	9.25	22.47	1.05	0.03	100.05	cpx7	
TA50	49 / 1 .	48.89	0.59	5.83	11.18	0.06	9.51	22.55	0.99	0.01	99.62	cpx8	
TA50	50 / 1 .	37.25	0.31	22.31	12.41	0.36	0.00	23.61	-0.01	0.01	96.27	ep9	
TA50	51 / 1 .	37.98	0.03	24.16	10.69	0.08	-0.01	24.14	0.00	0.00	97.08	ep10	
TA50	52 / 1 .	56.19	0.04	1.45	6.88	0.14	19.16	13.37	0.33	0.04	97.61	amp18	
TA50	53 / 1 .	55.04	0.04	2.45	6.49	0.13	19.05	13.18	0.49	0.12	96.98	amp19	
TA50	54 / 1 .	38.10	0.11	24.71	9.59	0.10	-0.04	24.28	0.00	0.01	96.89	ep11	
TA50	55 / 1 .	37.92	0.15	25.14	9.10	0.04	0.00	24.13	0.00	-0.01	96.48	ep12	
TA50	56 / 1 .	62.34	0.03	26.17	0.07	-0.01	0.01	0.69	8.31	3.06	100.66	pl1	
TA50	57 / 1 .	65.61	0.01	21.27	0.11	0.01	-0.01	2.65	10.09	0.05	99.81	pl2	
TA50	58 / 1 .	65.29	0.00	21.58	0.11	0.00	-0.01	2.80	9.96	0.05	99.79	pl3	
TA50	1 / 1 .	52.31	0.11	4.90	9.87	0.23	16.15	12.44	0.96	0.18	97.15	amp (cpx1)	
TA50	2 / 1 .	41.88	1.62	13.18	14.75	0.18	9.83	12.02	1.77	1.24	96.47	amp1	
TA50	3 / 1 .	37.18	0.04	24.80	4.64	0.07	2.41	23.52	0.07	0.01	92.74	^{fx}amp2	
TA50	4 / 1 .	38.57	0.10	20.69	23.55	1.23	4.62	11.13	-0.01	-0.01	99.88	grtyellow	0
TA50	4 / 2 .	38.64	0.15	20.39	23.20	1.51	4.51	11.14	0.02	-0.02	99.58	grtyellow	19
TA50	4 / 3 .	38.76	0.16	20.50	23.65	1.18	4.83	10.83	0.02	0.03	99.95	grtyellow	37
TA50	4 / 4 .	38.65	0.16	20.49	23.44	1.14	4.70	11.23	0.01	0.01	99.83	grtyellow	56
TA50	4 / 5 .	38.80	0.17	20.39	23.41	1.23	4.74	11.20	0.02	-0.01	99.96	grtyellow	75
TA50	4 / 6 .	38.55	0.19	20.42	23.63	1.13	4.77	11.05	0.01	0.00	99.75	grtyellow	93
TA50	4 / 7 .	38.67	0.15	20.45	23.43	1.22	4.72	11.18	-0.01	0.01	99.82	grtyellow	112
TA50	4 / 8 .	38.68	0.15	20.60	23.48	1.19	4.79	11.11	0.01	0.01	100.01	grtyellow	131
TA50	4 / 9 .	38.62	0.15	20.57	23.45	1.20	4.82	11.13	0.00	0.01	99.96	grtyellow	149
TA50	4 / 10 .	38.72	0.27	20.53	23.70	1.24	4.61	11.07	0.01	0.00	100.16	grtyellow	168
TA50	5 / 1 .	37.98	0.02	23.95	11.05	0.23	-0.04	23.80	0.02	0.00	97.07	ep1	
TA50	6 / 1 .	40.87	1.31	13.79	16.70	0.16	8.61	12.05	1.68	1.39	96.55	amp3	
TA50	7 / 1 .	40.82	1.33	13.59	16.68	0.16	8.53	11.89	1.61	1.34	95.96	amp4	
TA50	8 / 1 .	37.95	0.16	25.36	9.22	0.07	0.00	24.31	0.01	0.01	97.10	ep2	
TA50	9 / 1 .	38.01	0.16	24.27	10.49	0.58	0.01	23.74	0.01	0.00	97.28	ep3	
TA50	10 / 1 .	37.83	0.28	23.91	10.64	0.36	-0.02	24.02	0.00	0.01	97.05	ep4	
TA50	11 / 1 .	67.55	0.00	20.20	0.05	0.00	0.01	0.97	11.08	0.06	99.92	pl1	
TA50	12 / 1 .	41.77	1.67	13.06	15.81	0.21	9.22	11.97	1.71	1.18	96.59	amp5	
TA50	13 / 1 .	52.28	0.09	5.11	9.56	0.25	16.37	12.39	1.00	0.30	97.34	amp (cpx2)	
TA50	14 / 1 .	41.41	1.68	13.22	15.81	0.21	9.17	11.94	1.69	1.27	96.41	amp6	
TA50	15 / 1 .	41.94	1.56	12.73	16.22	0.21	9.16	12.00	1.74	1.30	96.84	amp7	
TA50	16 / 1 .	41.55	1.69	13.00	16.05	0.20	9.00	12.08	1.75	1.30	96.62	amp8	
TA50	17 / 1 .	51.52	0.12	5.44	11.17	0.21	15.15	12.31	1.35	0.20	97.47	amp9	
TA50	18 / 1 .	50.36	0.13	5.92	11.92	0.21	14.50	12.30	1.13	0.19	96.65	amp10	
TA50	19 / 1 .	37.81	0.08	24.66	9.48	0.11	-0.04	24.14	0.00	0.00	96.30	ep5	
TA50	20 / 1 .	65.86	0.00	21.46	0.16	-0.01	0.00	2.78	9.98	0.04	100.29	pl2	
TA50	21 / 1 .	42.45	1.70	12.97	14.48	0.21	10.17	12.10	1.69	1.10	96.87	amp11	
TA50	22 / 1 .	38.17	0.34	24.88	9.40	0.19	0.03	23.91	-0.01	0.00	96.91	ep6	
TA50	23 / 1 .	41.67	1.63	13.90	14.08	0.22	10.07	12.04	1.82	1.26	96.70	amp12	
TA50	24 / 1 .	46.93	0.43	9.39	12.53	0.23	12.88	12.10	1.46	0.62	96.57	amp13	
TA50	25 / 1 .	41.48	1.48	14.06	14.09	0.21	9.90	12.05	1.73	1.32	96.33	amp14	

Sample	Point	SiO2	TiO2	Al2O3	FeO	MnO	MgO	CaO	Na2O	K2O	Total	Comment	Distance (µm)
TA50	26 / 1 .	47.12	0.40	9.12	12.47	0.22	13.09	12.21	1.47	0.58	96.69	amp15	
TA50	27 / 1 .	38.15	0.15	25.57	8.86	0.16	0.01	24.25	0.02	0.00	97.17	ep7	
TA50	28 / 1 .	47.89	0.37	8.58	12.21	0.21	13.40	12.30	1.41	0.44	96.80	amp16	
TA50	29 / 1 .	41.61	1.46	13.98	14.24	0.21	10.08	12.02	1.79	1.28	96.67	amp17	
TA50	30 / 1 .	37.45	0.03	25.32	3.44	0.05	2.96	23.21	0.04	0.00	92.51	fxamp18	
TA50	31 / 1 .	41.57	1.56	13.54	14.39	0.22	9.87	11.95	1.77	1.27	96.13	amp19	
TA50	32 / 1 .	38.28	0.10	25.53	8.54	0.10	-0.01	24.46	0.01	0.01	97.03	ep8	
TA50	33 / 1 .	38.27	0.22	25.39	8.96	0.11	0.04	24.12	0.00	0.00	97.11	ep9	
TA50	34 / 1 .	41.68	1.59	13.41	14.80	0.21	9.53	12.06	1.68	1.29	96.24	amp20	
TA50		54.10	0.00	28.00	0.20	0.00	0.00	11.10	5.80	0.80		saus1	
TA50		54.60	0.00	27.90	0.30	0.00	0.00	10.30	5.80	1.00		saus2	
TA50		55.20	0.00	27.10	0.50	0.00	0.00	10.50	6.20	0.60		saus3	
TA50		55.90	0.00	27.40	0.00	0.00	0.00	9.40	6.40	0.90		saus4	
TA50		54.40	0.00	28.00	0.20	0.00	0.00	10.50	6.00	0.80		saus5	
TA50		54.20	0.00	27.90	0.10	0.00	0.00	11.40	6.00	0.40		saus6	
TA50		55.30	0.00	27.70	0.20	0.00	0.00	9.50	6.50	0.80		saus7	
TA50		54.70	0.00	28.10	0.30	0.00	0.00	9.80	6.10	1.10		saus8	
TA50		54.30	0.00	27.60	0.20	0.00	0.00	11.40	6.00	0.40		saus9	
TA50		55.80	0.00	27.10	0.20	0.00	0.00	9.70	6.60	0.70		saus10	
TA50		54.10	0.00	27.70	0.50	0.00	0.00	11.00	5.90	0.80		saus11	
TA51A	4 / 1 .	55.07	0.01	27.73	0.15	0.00	-0.01	10.85	5.41	0.22	99.42	pl2	
TA51A	5 / 1 .	55.29	0.00	27.63	0.09	-0.01	-0.03	10.45	5.56	0.19	99.21	pl3	
TA51A	6 / 1 .	56.97	0.01	26.82	0.17	0.02	-0.02	9.69	5.95	0.26	99.88	pl4	
TA51A	7 / 1 .	54.92	0.01	28.06	0.12	-0.01	-0.02	11.08	5.23	0.23	99.65	pl5	
TA51A	8 / 1 .	0.02	28.26	0.09	63.06	0.07	0.07	0.02	-0.02	-0.01	91.59	ilm	
TA51A	9 / 1 .	55.88	0.01	27.25	0.16	0.03	-0.01	10.22	5.73	0.22	99.50	pl6	
TA51A	10 / 1 .	56.39	0.00	26.90	0.14	-0.01	-0.02	9.83	6.02	0.24	99.52	pl7	
TA51A	11 / 1 .	48.57	0.60	6.58	9.10	0.32	10.57	22.12	1.11	0.00	98.97	cpx (amp1)	
TA51A	12 / 1 .	42.00	1.71	13.08	12.69	0.28	11.73	11.78	1.65	1.19	96.11	amp2	
TA51A	13 / 1 .	41.48	1.80	13.33	12.90	0.20	11.19	12.01	1.59	1.45	95.95	amp3	
TA51A	14 / 1 .	40.64	1.96	13.63	13.16	0.21	11.01	12.12	1.53	1.58	95.84	amp4	
TA51A	15 / 1 .	42.03	1.40	12.99	12.77	0.25	11.80	12.20	1.47	1.40	96.31	amp5	
TA51A	16 / 1 .	41.70	1.43	13.17	13.05	0.22	11.43	11.76	1.62	1.21	95.58	amp6	
TA51A	17 / 1 .	48.66	0.51	6.46	9.14	0.34	10.96	21.80	1.00	0.00	98.89	cpx1	
TA51A	18 / 1 .	48.86	0.51	6.38	8.73	0.29	11.13	22.17	1.10	0.01	99.18	cpx2	
TA51A	19 / 1 .	48.85	0.61	6.26	8.90	0.31	10.92	22.24	1.03	-0.01	99.12	cpx3	
TA51A	20 / 1 .	48.72	0.58	6.16	8.83	0.30	11.01	22.44	1.10	-0.01	99.15	cpx (amp7)	
TA51A	21 / 1 .	42.17	1.58	13.10	12.73	0.22	11.82	11.96	1.62	1.27	96.45	amp8	
TA51A	22 / 1 .	38.45	0.05	20.95	20.84	2.48	6.38	9.60	0.01	0.02	98.78	^{mx}grt1	
TA51A	23 / 1 .	38.09	0.13	20.79	22.41	2.09	4.99	10.63	0.01	0.02	99.15	grt2	
TA51A	24 / 1 .	38.16	0.06	20.77	22.36	2.05	5.00	10.86	0.01	-0.01	99.27	grt3	
TA51A	25 / 1 .	55.28	0.02	27.70	0.25	-0.01	-0.03	10.61	5.44	0.28	99.58	pl (grt3)	
TA51A	26 / 1 .	54.86	0.02	27.68	0.26	0.00	-0.02	10.60	5.45	0.24	99.11	pl8	
TA51A	27 / 1 .	56.15	0.00	27.05	0.16	-0.02	-0.01	9.79	5.92	0.28	99.36	pl9	
TA51A	28 / 1 .	50.61	0.40	4.86	7.46	0.26	12.11	23.34	0.90	0.02	99.95	cpx4	
TA51A	29 / 1 .	49.76	0.42	6.03	8.35	0.33	11.55	22.55	1.03	0.00	100.02	cpx5	
TA51A	30 / 1 .	48.92	0.54	6.51	8.44	0.31	10.97	22.07	1.08	0.00	98.84	cpx6	
TA51A	31 / 1 .	48.24	0.59	6.42	10.35	0.28	10.18	21.72	1.08	-0.01	98.85	cpx7	
TA51A	32 / 1 .	48.78	0.53	6.35	9.23	0.27	10.92	22.26	0.96	-0.01	99.31	cpx8	
TA51A	33 / 1 .	41.98	1.66	13.16	12.32	0.25	12.01	12.07	1.58	1.27	96.28	amp9	
TA51A	34 / 1 .	41.83	1.46	13.18	13.16	0.25	11.53	11.77	1.74	1.02	95.95	amp10	
TA51A	35 / 1 .	38.53	0.08	21.01	20.80	2.32	5.74	11.01	0.02	0.02	99.52	grtblue	
TA51A	35 / 2 .	38.39	0.23	20.69	21.67	1.95	5.35	10.95	0.02	0.01	99.26	grtblue	
TA51A	35 / 3 .	38.19	0.10	20.83	22.88	1.75	4.87	10.88	0.03	0.01	99.52	grtblue	
TA51A	35 / 4 .	38.21	0.18	20.69	23.21	1.75	4.57	10.95	0.04	-0.01	99.59	grtblue	
TA51A	35 / 5 .	38.17	0.27	20.54	23.55	1.75	4.54	10.87	0.05	-0.02	99.73	grtblue	
TA51A	35 / 6 .	38.22	0.24	20.48	23.48	1.80	4.56	10.88	0.03	0.00	99.70	grtblue	
TA51A	35 / 7 .	38.25	0.23	20.64	23.06	1.83	4.56	10.87	0.03	0.00	99.47	grtblue	
TA51A	35 / 8 .	38.28	0.17	20.83	22.78	1.92	4.71	10.84	0.02	0.00	99.55	grtblue	
TA51A	35 / 9 .	38.14	0.22	20.63	22.50	1.96	4.87	11.03	0.01	0.00	99.35	grtblue	
TA51A	35 / 10 .	38.22	0.25	20.60	22.49	1.95	4.86	11.16	0.03	0.00	99.56	grtblue	
TA51A	36 / 1 .	41.53	1.15	13.42	13.09	0.27	11.62	12.40	1.56	1.04	96.07	amp11	
TA51A	37 / 1 .	40.75	1.66	13.67	13.10	0.22	11.09	12.26	1.54	1.33	95.61	amp12	
TA51A	38 / 1 .	48.03	0.54	6.46	9.94	0.27	10.46	21.84	1.09	0.01	98.65	cpx9	
TA51A	39 / 1 .	48.64	0.56	6.35	9.39	0.29	10.62	22.05	1.08	0.00	98.97	cpx10	
TA51A	40 / 1 .	48.17	0.49	6.50	9.66	0.28	10.53	22.23	1.01	0.00	98.88	cpx11	
TA51A	41 / 1 .	48.93	0.42	5.49	8.34	0.27	11.67	22.70	0.95	0.01	98.79	cpx (transect41)	
TA51A	41 / 2 .	47.85	0.52	6.58	9.13	0.28	10.87	22.46	1.07	0.01	98.77	cpx (transect41)	
TA51A	41 / 3 .	48.51	0.54	6.95	9.00	0.25	10.77	22.54	1.02	0.00	99.58	cpx (transect41)	
TA51A	41 / 4 .	41.44	1.40	12.01	13.70	0.20	11.54	12.44	1.46	1.25	95.43	^{mx}amp (transect41)	
TA51A	41 / 5 .	40.91	1.49	12.94	13.76	0.18	11.21	12.03	1.46	1.42	95.39	^{mx}amp (transect41)	
TA51A	41 / 6 .	45.92	0.90	8.90	16.56	0.36	10.82	10.51	2.09	0.93	97.00	^{mx}amp (transect41)	
TA51A	41 / 7 .	44.46	1.02	9.23	14.61	0.22	11.82	11.11	1.64	1.12	95.24	^{mx}amp (transect41)	
TA51A	41 / 8 .	48.30	0.52	6.37	8.43	0.27	11.31	22.34	0.99	0.02	98.56	cpx (transect41)	

Sample	Point	SiO2	TiO2	Al2O3	FeO	MnO	MgO	CaO	Na2O	K2O	Total	Comment	Distance (µm)
TA51A	41 / 9 .	41.79	0.80	14.05	14.71	0.66	9.76	12.36	1.44	0.83	96.40	[mx]transect41	
TA51A	41 / 10 .	38.39	0.24	20.58	21.44	2.20	5.49	10.97	0.04	0.00	99.35	grt (transect41)	
TA51A	41 / 11 .	38.11	0.27	20.70	22.05	1.95	5.19	11.12	0.04	0.00	99.42	grt (transect41)	
TA51A	41 / 12 .	38.14	0.27	20.67	22.31	1.93	4.97	10.97	0.04	0.00	99.30	grt (transect41)	
TA51A	41 / 13 .	37.79	0.19	20.81	22.41	1.87	4.86	10.91	0.04	0.00	98.87	grt (transect41)	
TA51A	41 / 14 .	38.08	0.19	20.57	22.75	1.90	4.76	10.98	0.01	0.00	99.23	grt (transect41)	
TA51A	41 / 15 .	37.79	0.23	20.59	23.08	1.77	4.61	10.89	0.02	0.00	98.98	grt (transect41)	
TA51A	41 / 16 .	37.73	0.25	20.50	22.96	1.86	4.59	10.89	0.05	0.00	98.82	grt (transect41)	
TA51A	41 / 17 .	38.03	0.17	20.82	22.88	1.89	4.62	10.83	0.03	0.00	99.27	grt (transect41)	
TA51A	41 / 18 .	37.89	0.18	20.85	22.96	1.81	4.54	10.93	0.03	0.01	99.21	grt (transect41)	
TA51A	41 / 19 .	37.71	0.18	20.58	23.33	1.88	4.60	10.89	0.03	0.00	99.21	grt (transect41)	
TA51A	41 / 20 .	37.90	0.12	20.83	23.39	1.80	4.42	10.71	0.01	0.00	99.18	grt (transect41)	
TA51A	42 / 1 .	42.04	1.42	13.00	12.87	0.26	11.76	11.82	1.66	0.97	95.79	amp13	
TA51A	43 / 1 .	48.60	0.55	6.35	9.12	0.30	10.85	22.06	1.09	0.01	98.93	cpx12	
TA51A	44 / 1 .	0.05	17.92	0.11	71.78	0.05	0.06	0.05	0.00	-0.02	90.03	ilm(ox4)	
TA51A	45 / 1 .	48.51	0.45	6.00	7.96	0.34	11.36	22.67	1.03	0.00	98.32	cpx13	
TA51A	46 / 1 .	48.51	0.45	6.00	8.12	0.32	11.38	22.65	1.02	0.01	98.46	cpx (amp14)	
TA51A	47 / 1 .	56.94	0.00	26.48	0.16	0.01	-0.02	8.96	6.45	0.23	99.23	pl10	
TA51A	48 / 1 .	54.88	0.00	27.77	0.16	0.01	-0.03	10.81	5.44	0.22	99.28	pl11	
TA51A	49 / 1 .	55.87	0.00	26.93	0.13	-0.02	-0.03	9.87	5.95	0.20	98.96	pl12	
TA51A	50 / 1 .	57.36	0.00	25.99	0.10	0.01	-0.01	8.46	6.79	0.17	98.88	pl13	
TA51A	51 / 1 .	48.65	0.52	6.31	9.11	0.34	11.11	22.09	0.99	0.01	99.12	cpx14	
TA51A	52 / 1 .	41.48	2.05	12.27	12.20	0.19	12.11	12.07	1.15	1.01	94.52	[mx]amp transect52	
TA51A	52 / 2 .	43.14	1.08	11.96	12.08	0.23	12.64	12.37	1.43	1.15	96.07	[mx]amp transect52	
TA51A	52 / 3 .	48.83	0.56	6.44	8.25	0.32	11.17	22.56	1.07	-0.01	99.19	cpx transect52	
TA51A	52 / 4 .	48.94	0.59	6.43	8.74	0.34	10.83	22.14	1.16	0.00	99.16	cpx transect52	
TA51A	52 / 5 .	48.56	0.56	6.51	8.83	0.27	10.92	22.27	1.06	0.00	98.99	cpx transect52	
TA51A	52 / 6 .	48.83	0.55	6.40	8.58	0.30	10.94	22.16	1.12	-0.01	98.88	cpx transect52	
TA51A	52 / 7 .	48.72	0.59	6.51	8.72	0.31	10.81	22.12	1.07	0.00	98.85	cpx transect52	
TA51A	52 / 8 .	48.92	0.56	6.43	9.10	0.32	10.71	21.98	1.13	0.00	99.16	cpx transect52	
TA51A	52 / 9 .	49.18	0.41	7.22	10.13	0.40	9.72	19.21	1.74	0.14	98.15	[fx]cpx transect52	
TA51A	52 / 10 .	48.82	0.52	6.25	8.82	0.30	11.11	22.17	1.00	0.01	98.99	cpx transect52	
TA51A		48.85	0.54	6.52	8.90	0.32	10.78	21.83	1.17	0.02	98.92	cpx mean transect52	
TA51A		53.30	0.00	27.20	0.80	0.00	0.00	12.80	5.50	0.40		saus1	
TA51A		54.60	0.00	26.10	1.90	0.00	0.00	10.70	5.80	0.90		saus2	
TA51A		54.00	0.00	26.70	1.40	0.00	0.00	11.50	5.80	0.70		saus3	
TA51A		55.20	0.00	25.50	1.50	0.00	0.00	11.00	6.00	0.70		saus4	
TA51A		54.90	0.00	25.50	2.00	0.00	0.00	10.80	6.00	0.90		saus5	
TA51A		54.00	0.00	26.10	1.30	0.00	0.00	12.20	6.00	0.30		saus6	
TA51A		54.20	0.00	26.50	1.20	0.00	0.00	11.90	5.80	0.40		saus7	
TA51A		57.40	0.00	24.80	1.20	0.00	0.00	8.50	6.60	1.50		saus8	
TA53	18 / 1 .	54.09	0.01	28.71	0.63	0.03	0.63	1.05	3.85	6.83	95.83	[fx]pl7	
TA53	19 / 1 .	56.05	0.00	27.29	0.41	0.03	0.27	3.20	5.30	4.52	97.06	pl8	
TA53	20 / 1 .	43.70	0.90	12.64	12.69	0.26	11.69	11.93	1.69	0.37	95.86	amp1	
TA53	21 / 1 .	43.52	0.73	12.93	12.70	0.27	11.59	11.99	1.69	0.26	95.68	amp2	
TA53	22 / 1 .	43.18	0.90	13.30	12.39	0.23	11.38	11.80	1.58	0.94	95.70	amp3	
TA53	23 / 1 .	45.14	0.83	11.35	12.40	0.22	12.10	12.01	1.44	0.37	95.85	amp4	
TA53	24 / 1 .	43.50	0.92	12.95	12.75	0.25	11.67	12.14	1.58	0.43	96.19	amp5	
TA53	25 / 1 .	43.49	1.02	13.09	12.82	0.22	11.42	11.94	1.58	0.38	95.96	amp6	
TA53	26 / 1 .	43.72	1.07	13.06	12.54	0.24	11.40	11.93	1.58	0.64	96.19	amp7	
TA53	27 / 1 .	43.78	1.00	12.59	12.59	0.24	11.88	11.91	1.68	0.38	96.04	amp8	
TA53	28 / 1 .	38.01	0.09	26.92	7.38	0.13	0.00	24.39	0.00	-0.01	96.92	ep11	
TA53	29 / 1 .	37.96	0.15	26.76	7.57	0.16	0.05	24.13	-0.01	0.00	96.79	ep12	
TA53	30 / 1 .	100.09	0.01	0.01	0.16	-0.01	0.00	0.03	0.00	0.01	100.31	qz (pl9)	
TA53	31 / 1 .	99.74	0.01	0.02	0.21	0.02	0.00	0.06	0.01	0.00	100.07	qz (pl10)	
TA53	32 / 1 .	37.72	0.27	26.06	8.26	0.11	0.06	24.32	0.01	-0.01	96.81	ep13	
TA53	33 / 1 .	43.06	1.04	12.95	13.29	0.25	11.28	11.95	1.63	0.39	95.83	amp9	
TA53	34 / 1 .	37.93	0.26	26.26	7.95	0.13	0.09	23.99	0.00	0.00	96.61	ep14	
TA53	35 / 1 .	28.63	0.24	24.74	7.16	0.13	0.23	21.82	0.04	0.05	83.03	[fx]ep15	
TA53	36 / 1 .	43.68	5.82	10.41	10.29	0.21	9.67	14.00	1.03	0.93	96.04	[incl]amp10	
TA53	37 / 1 .	37.72	0.27	26.24	7.98	0.10	0.09	24.15	0.00	0.00	96.55	ep16	
TA53	38 / 1 .	43.32	1.08	12.94	12.89	0.25	11.43	12.00	1.67	0.38	95.97	amp11	
TA53	39 / 1 .	43.90	0.95	12.68	12.63	0.24	11.71	12.02	1.65	0.27	96.07	amp12	
TA53	40 / 1 .	38.07	0.28	26.19	7.89	0.14	0.07	24.04	-0.01	0.01	96.69	ep17	
TA53	41 / 1 .	43.15	0.93	12.65	13.13	0.26	11.94	11.41	1.51	0.27	95.24	amp13	
TA53	42 / 1 .	44.00	1.01	12.46	12.60	0.25	11.65	12.00	1.59	0.39	95.95	amp13	
TA53	43 / 1 .	43.91	1.01	12.51	12.63	0.25	11.67	11.94	1.56	0.40	95.89	amp14	
TA53	44 / 1 .	37.97	0.24	26.54	7.72	0.11	0.06	24.13	0.00	0.00	96.77	ep17	
TA53	45 / 1 .	56.12	0.00	27.28	0.05	0.01	-0.03	10.10	6.02	0.11	99.69	pl11	
TA53	46 / 1 .	56.87	0.00	26.87	0.04	0.01	-0.02	9.43	6.29	0.04	99.55	pl12	
TA53	47 / 1 .	57.69	0.00	26.12	0.07	0.00	-0.02	8.35	6.96	0.05	99.24	pl13	
TA53	48 / 1 .	57.71	0.00	26.35	0.18	0.02	0.10	5.02	6.64	2.06	98.07	pl14	
TA53	49 / 1 .	56.47	0.01	27.09	0.04	0.03	-0.03	9.70	5.99	0.06	99.38	pl15	
TA53		54.00	0.00	27.60	0.20	0.00	0.00	11.10	5.70	1.10		saus1	

Sample	Point	SiO2	TiO2	Al2O3	FeO	MnO	MgO	CaO	Na2O	K2O	Total	Comment	Distance (µm)
TA53		54.40	0.00	27.20	0.20	0.00	0.00	11.10	6.00	0.90		saus2	
TA53		54.20	0.00	26.90	0.20	0.00	0.00	12.20	6.10	0.20		saus3	
TA53		54.20	0.00	26.90	0.20	0.00	0.00	12.20	6.10	0.20		saus4	
TA53		52.50	0.00	27.30	0.40	0.00	0.00	13.10	5.50	0.40		saus5	
TA53		55.30	0.00	26.50	0.00	0.00	0.00	10.90	6.50	0.40		saus6	
TA53		52.30	0.00	27.90	0.40	0.00	0.00	13.10	5.40	0.70		saus7	
TA94	1 / 1 .	0.01	12.18	0.12	76.70	0.08	0.05	0.04	0.01	0.02	89.21	ilm (ox1)	
TA94	2 / 1 .	37.23	0.10	25.22	9.23	0.26	0.12	23.74	-0.01	-0.01	95.90	ep1	
TA94	3 / 1 .	37.16	0.26	21.61	13.48	0.29	-0.03	23.39	-0.01	0.01	96.19	[mx]ep2	
TA94	4 / 1 .	37.47	0.10	24.88	10.04	0.32	0.10	23.62	0.00	-0.01	96.53	ep3	
TA94	5 / 1 .	37.19	0.07	24.84	9.06	0.23	0.24	23.27	0.03	0.00	94.94	ep4	
TA94	6 / 1 .	27.38	0.02	18.71	20.88	0.26	17.93	0.06	0.02	0.00	85.26	clay	
TA94	7 / 1 .	41.36	0.66	14.57	12.29	0.37	11.73	11.66	1.84	1.00	95.48	amp1	
TA94	8 / 1 .	37.60	0.10	24.82	9.45	0.25	0.10	23.50	0.01	0.00	95.83	ep5	
TA94	9 / 1 .	37.54	0.11	25.25	9.28	0.28	0.12	23.62	0.00	0.00	96.20	ep6	
TA94	10 / 1 .	0.03	12.93	0.10	76.26	0.04	0.00	0.03	0.00	0.00	89.39	ilm	
TA94	11 / 1 .	27.08	0.03	19.16	19.67	0.24	18.98	0.07	0.01	0.03	85.26	clay	
TA94	12 / 1 .	42.11	0.56	14.14	12.02	0.41	12.16	11.61	1.91	0.74	95.65	amp2	
TA94	13 / 1 .	41.52	0.68	14.66	12.21	0.40	11.66	11.65	1.91	0.96	95.65	amp3	
TA94	14 / 1 .	37.31	0.10	25.13	9.34	0.28	0.11	23.77	0.01	0.00	96.05	ep7	
TA94	15 / 1 .	41.89	0.62	14.56	11.93	0.38	12.01	11.72	1.97	0.83	95.93	amp4	
TA94	16 / 1 .	42.17	0.40	14.34	13.18	0.40	11.41	11.72	1.98	0.51	96.10	amp5	
TA94	17 / 1 .	41.67	0.62	14.64	12.18	0.37	11.79	11.63	1.95	0.84	95.69	amp6	
TA94	18 / 1 .	37.60	0.11	25.36	9.22	0.23	0.12	23.78	0.00	0.03	96.43	ep9	
TA94	19 / 1 .	42.45	0.58	14.07	11.82	0.36	12.03	11.48	1.95	0.63	95.37	amp7	
TA94	20 / 1 .	41.63	0.67	14.92	12.17	0.36	11.61	11.79	1.81	1.08	96.04	amp8	
TA94	21 / 1 .	37.87	0.10	25.30	9.30	0.36	0.22	23.57	-0.01	0.01	96.73	ep10	
TA94	22 / 1 .	42.97	0.60	13.71	11.82	0.36	12.31	11.66	1.86	0.68	95.97	amp9	
TA94	23 / 1 .	58.42	0.00	25.86	0.03	0.02	-0.03	8.21	7.01	0.08	99.62	pl1	
TA94	24 / 1 .	58.64	0.01	25.86	0.03	0.00	-0.03	8.12	7.03	0.07	99.76	pl2	
TA94	25 / 1 .	38.04	0.10	24.81	9.58	0.32	0.05	23.86	0.00	-0.01	96.76	ep11	
TA94	26 / 1 .	37.82	0.10	24.72	9.58	0.32	0.05	23.74	0.02	-0.01	96.34	ep12	
TA94	27 / 1 .	41.96	0.67	14.73	11.85	0.37	11.83	11.60	1.85	1.00	95.87	amp10	
TA94	28 / 1 .	43.27	0.58	13.88	11.75	0.35	12.48	11.67	2.00	0.57	96.54	amp11	
TA94	29 / 1 .	43.00	0.55	13.87	11.71	0.35	12.46	11.59	1.92	0.61	96.06	amp12	
TA94	30 / 1 .	42.71	0.56	14.18	11.98	0.35	12.06	11.61	1.95	0.65	96.05	amp13	
TA94	31 / 1 .	43.36	0.50	13.54	11.50	0.38	12.66	11.56	1.86	0.57	95.93	amp14	
TA94	32 / 1 .	37.77	0.08	24.91	9.63	0.25	0.09	23.62	0.02	0.00	96.36	ep13	
TA94	33 / 1 .	37.48	0.11	25.10	9.40	0.25	0.15	23.90	0.00	0.01	96.40	ep14	
TA94	34 / 1 .	0.05	13.61	0.19	74.16	0.24	-0.01	0.09	-0.02	0.00	88.34	ilm	
TA94	35 / 1 .	37.06	0.33	21.48	13.48	0.35	-0.02	23.34	0.00	0.01	96.04	[mx]ep15	
TA94	36 / 1 .	37.60	0.08	24.82	9.77	0.27	0.09	23.71	0.00	0.01	96.35	ep16	
TA94	37 / 1 .	41.82	0.61	14.57	12.19	0.37	11.97	11.72	1.90	0.83	95.99	amp15	
TA94	38 / 1 .	42.78	0.54	14.29	11.51	0.39	12.13	11.74	1.97	0.65	96.01	amp16	
TA94	39 / 1 .	60.03	0.00	24.77	0.10	0.02	-0.02	6.87	7.70	0.10	99.58	pl3	
TA94	40 / 1 .	59.16	0.00	25.14	0.09	0.03	-0.01	7.26	7.43	0.11	99.21	pl4	
TA94	41 / 1 .	59.59	0.00	24.88	0.07	0.00	-0.02	7.19	7.50	0.09	99.32	pl5	
TA94	42 / 1 .	42.24	0.58	14.15	12.08	0.36	12.08	11.82	1.94	0.71	95.95	amp16	
TA94	43 / 1 .	41.84	0.63	14.56	11.87	0.39	11.92	11.65	1.93	0.77	95.56	amp17	
TA94	44 / 1 .	59.78	-0.01	24.97	0.08	-0.01	-0.01	7.11	7.60	0.05	99.59	pl6	
TA94	45 / 1 .	1.96	0.00	0.73	0.11	0.00	-0.03	8.06	8.18	0.05	19.09	[fx]pl7	
TA94	46 / 1 .	57.69	0.00	26.08	0.09	0.02	-0.01	8.45	6.86	0.06	99.24	pl8	
TA94	47 / 1 .	58.07	0.01	25.92	0.10	-0.01	-0.02	8.30	6.87	0.06	99.32	pl9	
TA94	48 / 1 .	42.31	0.59	14.34	11.93	0.36	12.12	11.74	1.94	0.81	96.13	amp18	
TA94	49 / 1 .	41.73	0.62	14.28	12.05	0.38	12.17	11.61	1.90	0.78	95.52	amp19	
TA94	50 / 1 .	42.24	0.61	14.13	12.12	0.38	12.08	11.78	1.90	0.77	96.01	amp20	
TA94	51 / 1 .	59.51	0.00	25.31	0.03	-0.01	-0.04	7.36	7.39	0.05	99.65	pl10	
TA94	52 / 1 .	59.94	0.00	24.80	0.00	0.01	-0.02	6.98	7.76	0.04	99.53	pl11	
TA94	53 / 1 .	37.88	0.11	25.12	9.51	0.28	0.12	23.93	0.00	-0.01	96.95	ep17	
TA94	54 / 1 .	37.94	0.12	25.57	9.19	0.26	0.09	23.76	0.00	0.01	96.93	ep18	
TA95	1 / 1 .	36.64	0.05	21.76	24.12	1.80	3.80	10.86	0.21	0.00	99.26	Grt	0
TA95	1 / 2 .	36.99	0.10	21.75	22.76	1.32	5.25	11.02	0.01	0.00	99.26	Grt	38
TA95	1 / 3 .	36.93	0.12	22.00	22.41	1.47	5.17	11.29	-0.02	0.00	99.40	Grt	77
TA95	1 / 4 .	37.17	0.12	22.30	22.04	1.51	5.06	12.23	0.04	-0.01	100.50	Grt	115
TA95	1 / 5 .	36.80	0.16	21.72	21.74	1.59	4.72	12.45	0.02	0.00	99.24	Grt	153
TA95	1 / 6 .	37.02	0.27	21.78	21.51	1.62	4.78	12.75	0.04	-0.01	99.81	Grt	191
TA95	1 / 7 .	39.59	0.18	23.29	21.53	1.77	5.16	12.47	0.00	0.00	103.99	Grt	230
TA95	1 / 8 .	29.25	0.21	16.53	21.54	1.85	3.33	12.25	0.05	0.00	85.04	[fx]Grt	268
TA95	1 / 9 .	36.99	0.14	21.70	21.68	2.02	4.51	12.53	0.01	-0.01	99.62	Grt	306
TA95	1 / 10 .	36.80	0.21	21.70	21.60	2.07	4.52	12.60	0.03	0.00	99.56	Grt	344
TA95	1 / 11 .	36.90	0.20	21.80	21.91	1.92	4.56	12.23	0.01	-0.01	99.61	Grt	383
TA95	1 / 12 .	36.92	0.10	21.94	22.24	1.79	4.69	11.82	0.00	-0.01	99.50	Grt	421
TA95	1 / 13 .	36.97	0.09	21.85	22.81	1.65	4.86	11.15	0.01	0.00	99.43	Grt	459
TA95	1 / 14 .	36.78	0.09	22.29	22.69	1.55	4.99	11.20	0.00	-0.01	99.58	Grt	497

Sample	Point	SiO2	TiO2	Al2O3	FeO	MnO	MgO	CaO	Na2O	K2O	Total	Comment	Distance (µm)
TA95	1 / 15 .	37.11	0.06	21.90	22.42	1.61	4.99	11.73	0.01	-0.02	99.88	Grt	536
TA95	1 / 16 .	36.99	0.15	21.82	22.68	1.79	4.81	11.38	0.00	-0.01	99.64	Grt	574
TA95	1 / 17 .	36.98	0.14	21.97	22.84	1.90	4.86	11.35	-0.01	0.00	100.07	Grt	612
TA95	1 / 18 .	36.81	0.11	22.00	22.27	2.04	4.72	11.19	0.02	0.00	99.16	Grt	650
TA95	1 / 19 .	37.05	0.09	22.54	22.34	2.49	4.86	10.97	-0.03	-0.01	100.34	Grt	689
TA95	1 / 20 .	36.97	0.11	21.90	22.72	2.68	4.46	10.74	0.01	0.00	99.61	Grt	727
TA95	1 / 21 .	36.83	0.19	22.12	22.74	2.76	4.48	10.81	0.03	-0.01	100.00	Grt	765
TA95	1 / 22 .	36.96	0.19	21.99	22.73	2.94	4.32	10.89	0.01	0.00	100.02	Grt	803
TA95	1 / 23 .	37.03	0.17	21.87	23.30	2.90	4.29	10.59	0.03	0.00	100.20	Grt	842
TA95	1 / 24 .	36.85	0.08	21.84	23.54	2.95	4.34	9.99	-0.02	-0.01	99.64	Grt	880
TA95	1 / 25 .	37.01	0.06	22.17	23.72	3.09	4.35	9.87	0.01	-0.01	100.27	Grt	918
TA95	1 / 26 .	36.78	0.07	22.30	23.70	3.07	4.25	9.86	0.03	0.00	100.07	Grt	956
TA95	1 / 27 .	35.48	0.04	24.05	3.06	0.08	1.75	24.09	0.05	0.00	88.60	fxGrt	995
TA95	1 / 28 .	36.63	0.14	22.28	24.11	3.13	4.09	9.45	0.01	0.00	99.88	Grt	1033
TA95	1 / 29 .	36.76	0.15	22.12	24.38	2.99	4.29	9.40	0.00	0.00	100.15	Grt	1071
TA95	1 / 30 .	36.86	0.03	22.14	24.16	2.90	4.10	9.53	0.03	-0.02	99.76	Grt	1109
TA95	1 / 31 .	36.95	0.10	22.01	24.72	3.15	4.25	9.27	0.02	0.00	100.49	Grt	1148
TA95	1 / 32 .	36.86	0.16	21.89	24.12	3.07	4.02	9.67	0.00	0.01	99.82	Grt	1186
TA95	1 / 33 .	37.13	0.04	22.40	24.32	3.16	4.20	9.41	0.04	0.00	100.73	Grt	1224
TA95	1 / 34 .	37.56	0.10	23.37	23.88	2.73	4.31	9.49	0.06	0.00	101.57	Grt	1262
TA95	1 / 35 .	37.02	0.13	22.15	24.17	3.10	4.21	9.70	0.00	0.01	100.50	Grt	1301
TA95	1 / 36 .	37.19	0.14	22.04	23.86	2.92	4.25	9.80	0.01	-0.01	100.21	Grt	1339
TA95	1 / 37 .	37.29	0.10	22.03	23.74	3.00	4.10	9.89	0.01	0.00	100.18	Grt	1377
TA95	1 / 38 .	19.42	0.15	12.50	23.49	2.79	1.86	9.63	0.04	0.15	70.07	fxGrt	1415
TA95	1 / 39 .	37.09	0.14	22.06	23.19	2.94	4.43	10.25	0.01	0.00	100.14	Grt	1454
TA95	1 / 40 .	37.00	0.10	21.87	23.38	3.05	4.27	10.36	0.00	0.01	100.06	Grt	1492
TA95	1 / 41 .	36.11	0.24	21.23	22.01	2.61	4.21	11.57	0.04	0.01	98.06	Grt	1530
TA95	1 / 42 .	35.52	0.19	21.06	18.84	2.42	4.32	9.56	0.02	0.00	91.94	fxGrt	1568
TA95	1 / 43 .	36.43	0.14	21.69	20.77	2.53	4.43	10.03	0.02	0.01	96.05	fxGrt	1607
TA95	1 / 44 .	37.15	0.29	22.23	22.29	2.73	4.43	10.90	0.05	0.01	100.13	Grt	1645
TA95	1 / 45 .	36.96	0.25	21.85	22.67	2.60	4.35	11.22	0.03	-0.01	99.94	Grt	1683
TA95	1 / 46 .	37.07	0.26	21.74	22.26	2.59	4.57	11.31	0.03	-0.02	99.87	Grt	1721
TA95	1 / 47 .	37.18	0.20	21.71	22.14	2.45	4.39	11.55	0.04	0.00	99.71	Grt	1760
TA95	1 / 48 .	37.20	0.12	21.96	22.10	2.35	4.53	11.89	0.00	0.00	100.18	Grt	1798
TA95	1 / 49 .	37.29	0.07	21.96	21.91	2.32	4.46	12.08	0.02	-0.01	100.11	Grt	1836
TA95	1 / 50 .	37.36	0.14	21.89	21.87	2.23	4.39	12.31	0.01	-0.01	100.24	Grt	1874
TA95	1 / 51 .	37.03	0.20	21.81	21.54	2.20	4.41	12.43	0.01	0.00	99.64	Grt	1913
TA95	1 / 52 .	37.07	0.21	21.90	21.78	2.12	4.55	12.47	-0.01	0.00	100.13	Grt	1951
TA95	1 / 53 .	37.09	0.20	21.96	21.86	1.96	4.53	12.49	0.01	-0.01	100.15	Grt	1989
TA95	1 / 54 .	37.14	0.26	21.61	21.52	1.90	4.46	12.51	0.02	0.00	99.44	Grt	2027
TA95	1 / 55 .	36.98	0.15	22.00	21.75	1.70	4.61	12.50	-0.01	-0.01	99.73	Grt	2066
TA95	1 / 56 .	37.33	0.10	21.80	21.44	1.67	4.61	12.56	0.02	0.00	99.54	Grt	2104
TA95	1 / 57 .	37.43	0.14	21.89	21.79	1.45	4.91	12.26	0.03	0.00	99.95	Grt	2142
TA95	1 / 58 .	36.60	0.21	20.88	20.34	1.22	4.43	13.91	0.03	0.03	97.66	fxGrt	2180
TA95	1 / 59 .	37.07	0.14	22.14	22.65	1.27	5.24	11.41	-0.01	0.00	99.99	Grt	2219
TA95	1 / 60 .	38.60	0.07	23.01	20.34	1.55	3.02	11.78	0.50	0.01	98.92	Grt	2257
TA95	2 / 1 .	64.11	-0.01	19.91	0.55	0.01	0.03	1.02	11.13	0.09	96.86	Pl	
TA95	3 / 1 .	41.12	1.25	13.25	15.98	0.14	10.45	11.86	1.55	0.96	96.56	amp	
TA95	4 / 1 .	40.66	1.52	13.80	15.57	0.14	10.11	11.77	1.65	1.05	96.29	amp	
TA95	5 / 1 .	0.09	98.58	-0.09	0.48	0.02	0.00	0.80	0.01	0.01	100.10	rt	
TA95	6 / 1 .	27.82	37.89	1.43	0.61	0.03	-0.02	28.56	-0.01	0.00	96.39	ttn	
TA95	7 / 1 .	43.93	0.03	35.46	1.50	0.01	0.42	0.06	0.60	11.18	93.18	fxpl	
TA95	8 / 1 .	39.74	1.20	14.14	16.00	0.17	9.82	11.80	1.80	0.99	95.71	amp	
TA95	9 / 1 .	40.12	1.75	14.28	15.14	0.13	10.24	11.60	1.84	1.02	96.15	amp	
TA95	10 / 1 .	40.61	1.69	14.50	15.10	0.11	10.24	11.72	1.74	1.07	96.85	amp	
TA95	11 / 1 .	28.94	38.18	1.30	0.65	-0.01	-0.04	28.05	0.04	0.02	97.18	ttn	
TA95	12 / 1 .	66.29	0.00	19.80	0.24	0.02	0.05	0.30	11.41	0.05	98.17	pl	
TA95	13 / 1 .	66.06	0.02	19.86	0.15	0.01	0.01	0.15	11.80	0.05	98.14	pl	
TA95	14 / 1 .	47.89	0.42	4.52	9.48	0.14	11.44	23.01	0.76	0.00	97.66	cpx	0
TA95	14 / 2 .	44.33	0.53	4.96	9.88	0.15	10.18	22.28	0.74	0.00	93.05	fxcpx	18
TA95	14 / 3 .	46.60	0.54	5.37	9.83	0.16	11.08	22.19	0.87	0.00	96.67	cpx	36
TA95	14 / 4 .	46.35	0.54	6.23	11.22	0.15	11.14	20.08	0.98	0.02	96.72	cpx	54
TA95	14 / 5 .	46.64	0.66	5.52	9.60	0.13	10.49	22.37	0.84	0.01	96.29	cpx	72
TA95	14 / 6 .	47.01	0.53	6.64	10.44	0.15	10.36	20.32	0.80	0.13	96.43	cpx	90
TA95	14 / 7 .	46.70	0.54	5.53	9.96	0.16	10.83	22.04	0.85	0.01	96.65	cpx	108
TA95	14 / 8 .	46.55	0.57	5.65	9.88	0.16	10.90	22.06	0.89	0.00	96.66	cpx	126
TA95	14 / 9 .	46.70	0.51	5.66	9.90	0.17	11.00	22.07	0.96	0.01	97.02	cpx	144
TA95	14 / 10 .	46.48	0.50	5.54	9.72	0.16	11.01	22.22	0.85	0.04	96.53	cpx	162
TA95	15 / 1 .	39.13	1.45	13.84	15.64	0.16	9.49	11.77	1.62	1.04	94.18	fxamp	
TA95	16 / 1 .	28.08	37.32	2.07	0.55	0.07	-0.04	28.51	0.01	0.02	96.68	ttn	
TA95	17 / 1 .	37.43	0.05	22.05	24.31	1.48	4.62	10.72	0.02	0.00	100.75	grt	0
TA95	18 / 1 .	37.58	0.09	22.07	23.36	1.18	5.09	11.12	0.02	0.01	100.51	grt	24
TA95	19 / 1 .	37.57	0.12	21.95	22.46	1.17	4.78	12.11	0.02	0.00	100.19	grt	67
TA95	20 / 1 .	36.58	0.08	22.08	21.56	1.38	4.71	12.73	-0.01	0.00	99.13	grt	117

Sample	Point	SiO2	TiO2	Al2O3	FeO	MnO	MgO	CaO	Na2O	K2O	Total	Comment	Distance (µm)
TA95	21 / 1 .	36.32	0.28	21.66	21.46	1.74	4.44	12.89	0.02	-0.03	98.85	grt	255
TA95	22 / 1 .	36.47	0.17	21.86	21.63	1.76	4.40	12.92	0.03	0.00	99.28	grt	382
TA95	23 / 1 .	35.77	0.12	21.86	21.52	1.96	4.41	12.70	0.00	0.00	98.37	grt	507
TA95	24 / 1 .	35.59	0.17	21.73	21.48	1.97	4.53	12.93	0.02	0.00	98.43	grt	628
TA95	25 / 1 .	35.84	0.24	21.58	21.56	2.01	4.41	12.76	0.03	0.00	98.47	grt	743
TA95	26 / 1 .	35.81	0.15	21.93	21.52	1.90	4.53	12.83	0.03	0.00	98.72	grt	818
TA95	27 / 1 .	35.76	0.24	21.55	21.74	1.59	4.79	12.75	0.01	0.00	98.47	grt	926
TA95	28 / 1 .	36.47	0.22	21.63	22.20	1.52	4.57	12.35	0.01	-0.01	99.00	grt	944
TA95	29 / 1 .	37.07	0.07	21.95	22.84	1.30	4.95	11.37	0.02	0.00	99.58	grt	966
TA95	30 / 1 .	36.52	0.12	21.95	24.19	1.73	4.21	10.95	-0.01	0.00	99.68	grt	993
TA95	31 / 1 .	28.51	37.92	1.40	0.68	0.04	-0.06	28.54	0.02	0.00	97.18	ttn	
TA95	32 / 1 .	0.06	97.50	-0.13	0.92	0.01	0.06	0.87	0.03	0.00	99.51	ru	
TA95	33 / 1 .	28.52	37.54	1.43	0.81	0.09	-0.06	28.15	0.01	0.00	96.55	ttn	
TA95	34 / 1 .	39.08	0.97	17.55	13.20	0.11	8.76	14.20	1.56	1.14	96.60	^{mx}amp	
TA95	35 / 1 .	40.82	1.62	13.82	15.45	0.10	9.98	11.70	1.76	1.01	96.33	amp	
TA95	36 / 1 .	40.72	1.56	14.22	15.59	0.13	10.06	11.67	1.75	1.04	96.75	amp	
TA95	37 / 1 .	29.18	37.86	1.57	0.53	0.04	-0.03	28.68	0.01	0.00	97.93	ttn	
TA95	38 / 1 .	47.50	0.46	4.76	9.35	0.17	11.45	22.63	0.79	0.03	97.13	cpx	
TA95	39 / 1 .	47.54	0.56	5.39	9.13	0.18	10.81	22.64	0.90	0.01	97.16	cpx	
TA95	40 / 1 .	40.42	0.29	20.30	9.00	0.08	6.48	18.46	0.75	0.29	96.08	^{fx}cpx	
TA95	41 / 1 .	38.46	0.70	15.54	18.16	0.15	9.18	10.57	1.49	1.21	95.46	fxamp	
TA95	42 / 1 .	41.30	1.72	14.57	14.77	0.12	10.01	11.97	1.61	1.04	97.11	amp	
TA95	43 / 1 .	37.46	0.01	21.90	24.00	1.37	4.56	10.63	0.04	-0.01	100.00	grt	0
TA95	43 / 2 .	37.68	0.11	21.99	23.75	1.17	5.07	10.74	0.01	-0.01	100.57	grt	31
TA95	43 / 3 .	37.57	0.09	21.80	23.17	1.07	5.15	10.91	0.01	0.00	99.84	grt	62
TA95	43 / 4 .	37.45	0.09	22.02	23.04	1.12	5.28	10.93	-0.02	0.00	99.93	grt	93
TA95	43 / 5 .	10.33	0.06	7.14	23.34	1.07	1.37	10.61	0.01	0.00	53.92	fxGrt	123
TA95	43 / 6 .	37.77	0.08	22.12	22.65	1.01	5.12	11.74	0.01	0.00	100.54	grt	154
TA95	43 / 7 .	37.57	0.09	21.97	22.19	1.06	4.79	12.35	0.01	0.01	100.04	grt	185
TA95	43 / 8 .	37.52	0.06	21.93	22.23	1.11	4.67	12.34	-0.01	0.01	99.85	grt	216
TA95	43 / 9 .	37.70	0.06	22.15	21.86	1.41	4.72	12.25	0.00	0.00	100.24	grt	247
TA95	43 / 10 .	37.55	0.17	21.67	21.77	1.41	4.57	12.55	0.03	-0.01	99.78	grt	278
TA95	43 / 11 .	37.62	0.11	21.73	22.08	1.38	4.65	12.24	0.00	0.01	99.85	grt	309
TA95	43 / 12 .	37.53	0.15	22.16	22.06	1.45	4.52	12.55	0.01	-0.01	100.44	grt	339
TA95	43 / 13 .	37.65	0.09	21.87	22.12	1.59	4.52	12.33	0.01	-0.01	100.18	grt	370
TA95	43 / 14 .	37.75	0.08	21.74	22.20	1.69	4.58	12.45	0.00	0.00	100.48	grt	401
TA95	43 / 15 .	37.65	0.08	21.91	22.09	1.77	4.51	12.31	0.00	0.01	100.32	grt	432
TA95	43 / 16 .	36.21	0.07	22.58	21.36	1.49	4.11	12.33	0.02	0.03	98.20	grt	463
TA95	43 / 17 .	37.71	0.04	21.93	22.03	1.30	4.48	12.70	0.04	0.01	100.24	grt	494
TA95	43 / 18 .	37.61	0.10	22.02	21.94	1.13	4.84	12.42	0.05	-0.01	100.12	grt	524
TA95	43 / 19 .	37.69	0.14	21.92	22.53	1.07	4.98	11.77	0.00	-0.01	100.17	grt	555
TA95	43 / 20 .	37.34	0.07	21.58	24.00	1.33	4.60	10.67	0.02	-0.01	99.64	grt	586
TA95	44 / 1 .	47.63	0.65	5.75	9.56	0.22	10.67	22.24	0.92	0.02	97.69	cpx	
TA95	45 / 1 .	46.44	0.59	5.99	10.85	0.18	10.61	21.44	0.87	0.08	97.11	cpx	
TA95	46 / 1 .	47.74	0.65	5.44	9.94	0.20	10.87	22.20	0.81	0.01	97.93	cpx	
TA95	47 / 1 .	45.42	0.52	6.20	10.24	0.20	10.74	20.94	0.66	0.13	95.11	cpx	0
TA95	47 / 2 .	48.19	0.41	4.70	9.76	0.18	11.18	22.29	0.68	0.05	97.48	cpx	24
TA95	47 / 3 .	48.59	0.34	4.49	9.93	0.16	11.64	21.76	0.76	0.06	97.75	cpx	48
TA95	47 / 4 .	48.38	0.46	4.44	9.93	0.17	11.23	22.14	0.74	0.03	97.52	cpx	72
TA95	47 / 5 .	47.42	0.54	5.64	10.30	0.19	10.78	21.58	0.89	0.09	97.41	cpx	96
TA95	47 / 6 .	46.36	0.52	5.82	11.63	0.16	9.41	18.94	0.67	0.24	93.77	^{fx}cpx	120
TA95	47 / 7 .	46.47	0.62	7.41	12.30	0.21	10.73	18.66	1.12	0.19	97.71	cpx	144
TA95	47 / 8 .	47.33	0.49	6.40	11.36	0.24	10.40	20.84	0.88	0.11	98.06	cpx	168
TA95	47 / 9 .	42.34	1.19	11.10	17.02	0.18	10.05	12.14	1.35	0.85	96.21	amp	192
TA95	47 / 10 .	39.43	0.52	17.98	12.35	0.17	6.14	16.02	0.67	0.57	93.91	^{fx}amp	216
TA95	47 / 11 .	41.18	0.88	12.87	17.75	0.19	9.46	11.90	1.57	0.96	96.76	amp	240
TA95	47 / 12 .	50.77	0.13	4.08	14.71	0.08	13.27	12.60	0.46	0.27	96.40	^{fx}amp	264
TA95	47 / 13 .	44.93	2.17	8.97	15.60	0.10	10.68	12.94	1.01	0.68	97.15	^{fx}amp	288
TA95	47 / 14 .	46.27	0.55	10.11	16.22	0.15	10.77	11.68	1.34	0.89	98.02	amp	312
TA95	47 / 15 .	42.24	2.39	8.31	18.42	0.17	12.49	9.77	0.22	0.21	94.27	^{fx}amp	336
TA95	47 / 16 .	48.62	0.40	7.80	16.30	0.23	11.84	10.99	0.83	0.51	97.59	^{fx}amp	360
TA95	47 / 17 .	41.15	0.93	14.68	15.99	0.12	9.68	11.92	1.65	1.06	97.22	amp	384
TA95	47 / 18 .	43.11	0.68	12.56	15.71	0.12	10.30	11.93	1.30	0.93	96.68	amp	408
TA95	47 / 19 .	43.84	0.70	11.88	15.16	0.16	10.84	11.79	1.37	0.90	96.67	amp	432
TA95	47 / 20 .	41.21	0.89	14.99	15.15	0.10	9.64	11.83	1.46	1.10	96.39	amp	456
TA95	48 / 1 .	37.60	0.09	21.81	24.17	1.72	4.02	10.73	0.00	0.02	100.20	grt	0
TA95	48 / 2 .	37.82	0.12	21.73	23.14	1.25	4.80	11.47	0.00	0.00	100.43	grt	20
TA95	48 / 3 .	37.61	0.15	21.40	20.16	1.02	4.08	15.25	0.01	-0.01	99.71	^{incl}grt	40
TA95	48 / 4 .	38.11	0.12	22.01	22.05	1.07	4.66	12.72	0.02	0.01	100.77	grt	60
TA95	48 / 5 .	38.07	0.14	21.83	22.20	1.04	4.85	12.50	0.00	0.00	100.66	grt	80
TA95	48 / 6 .	37.95	0.15	21.71	22.17	1.22	4.79	12.39	-0.01	-0.01	100.40	grt	100
TA95	48 / 7 .	14.57	0.09	10.34	22.44	1.09	1.35	11.30	0.06	0.01	61.26	^{fx}Grt	121
TA95	48 / 8 .	37.93	0.05	22.16	22.27	1.21	4.79	12.27	0.01	-0.01	100.72	grt	141

Sample	Point	SiO2	TiO2	Al2O3	FeO	MnO	MgO	CaO	Na2O	K2O	Total	Comment	Distance (µm)
TA95	48 / 9 .	37.68	0.21	26.96	8.64	0.09	-0.02	23.58	0.02	-0.01	97.21	^{incl}grt	161
TA95	48 / 10 .	38.12	0.17	27.45	9.92	0.33	0.62	21.54	-0.01	0.03	98.25	^{incl}grt	181
TA95	48 / 11 .	37.72	0.18	21.25	22.15	1.22	4.48	12.45	0.03	0.00	99.48	grt	201
TA95	48 / 12 .	38.29	0.10	21.76	21.68	1.04	4.64	13.05	0.02	0.01	100.65	grt	221
TA95	48 / 13 .	38.03	0.05	22.08	21.60	1.09	4.51	12.93	0.01	-0.01	100.35	grt	241
TA95	48 / 14 .	38.34	0.13	21.93	21.41	1.04	4.63	12.91	0.02	0.00	100.47	grt	261
TA95	48 / 15 .	37.52	0.07	21.55	22.97	1.38	4.08	11.78	0.03	0.02	99.40	grt	281
TA95	49 / 1 .	42.15	1.38	13.65	14.91	0.14	10.38	11.69	1.74	1.02	97.08	amp	
TA95	50 / 1 .	33.72	0.07	19.56	23.30	1.86	2.37	12.33	0.04	0.01	93.26	^{fx}Grt	0
TA95	50 / 2 .	37.95	0.14	21.82	24.04	1.15	4.57	11.06	0.02	0.00	100.76	grt	43
TA95	50 / 3 .	37.94	0.17	21.73	22.71	0.92	4.63	12.41	0.02	0.00	100.59	grt	86
TA95	50 / 4 .	37.63	0.18	22.99	19.63	0.79	3.56	14.59	0.02	0.00	99.49	grt	129
TA95	50 / 5 .	37.89	0.19	21.39	22.06	0.94	4.17	12.77	0.01	0.00	99.44	grt	172
TA95	50 / 6 .	37.88	0.21	21.63	21.94	1.05	4.19	12.79	0.03	-0.01	99.72	grt	215
TA95	50 / 7 .	38.27	0.17	22.00	21.94	1.18	4.36	12.66	0.03	0.00	100.61	grt	259
TA95	50 / 8 .	38.05	0.23	21.67	21.96	1.42	4.35	12.67	0.00	0.00	100.41	grt	302
TA95	50 / 9 .	37.83	0.06	21.91	21.70	1.75	4.52	12.67	0.02	0.00	100.49	grt	345
TA95	50 / 10 .	37.91	0.11	22.11	21.77	2.03	4.21	12.15	0.06	0.00	100.35	grt	388
TA95	50 / 11 .	38.03	0.07	22.03	22.24	2.25	4.52	11.74	0.01	0.00	100.88	grt	431
TA95	50 / 12 .	37.89	0.17	21.89	22.49	2.47	4.59	11.20	0.06	-0.01	100.79	grt	474
TA95	50 / 13 .	39.68	0.19	22.58	22.01	2.40	4.50	10.53	0.50	0.00	102.39	grt	517
TA95	50 / 14 .	37.90	0.10	22.03	23.20	2.46	4.50	10.26	0.00	-0.02	100.49	grt	560
TA95	50 / 15 .	37.88	0.15	21.75	23.58	2.44	4.59	10.30	0.03	0.00	100.80	grt	603
TA95	50 / 16 .	37.90	0.15	22.01	23.96	2.41	4.43	10.11	-0.01	0.00	100.99	grt	646
TA95	50 / 17 .	29.66	0.21	20.01	22.77	2.35	3.12	9.74	0.07	0.01	87.93	^{fx}Grt	689
TA95	50 / 18 .	37.72	0.16	22.18	23.97	2.46	4.36	10.02	0.05	-0.01	100.92	grt	733
TA95	50 / 19 .	37.51	0.09	21.94	23.66	2.51	4.23	10.33	0.01	0.02	100.30	grt	776
TA95	50 / 20 .	37.67	0.09	22.08	23.88	2.45	4.36	10.00	0.04	0.01	100.61	grt	819
TA95	50 / 21 .	37.73	0.03	22.06	23.52	2.43	4.38	10.46	0.04	-0.01	100.69	grt	862
TA95	50 / 22 .	37.80	0.09	22.02	23.35	2.45	4.30	10.38	0.00	0.00	100.41	grt	905
TA95	50 / 23 .	37.52	0.09	22.16	23.29	2.42	4.50	10.54	0.02	0.00	100.57	grt	948
TA95	50 / 24 .	37.77	0.11	22.19	23.54	2.34	4.29	10.23	0.00	0.00	100.48	grt	991
TA95	50 / 25 .	37.29	0.08	21.94	23.42	2.37	4.34	10.52	0.05	0.01	100.03	grt	1034
TA95	50 / 26 .	37.34	0.13	22.00	23.65	2.46	4.49	10.28	0.05	0.00	100.43	grt	1077
TA95	50 / 27 .	38.39	0.15	22.67	23.54	2.43	4.51	10.37	0.01	-0.01	102.09	grt	1120
TA95	50 / 28 .	34.55	0.10	20.61	19.86	2.06	3.27	9.76	0.98	0.01	91.20	^{fx}Grt	1163
TA95	50 / 29 .	38.32	0.13	22.54	22.99	2.49	4.70	10.31	0.06	0.00	101.57	grt	1207
TA95	50 / 30 .	37.17	0.18	21.94	22.91	2.55	4.59	10.40	0.01	0.02	99.75	grt	1250
TA95	50 / 31 .	37.13	0.12	23.45	22.30	2.38	4.45	10.48	0.04	0.02	100.41	grt	1293
TA95	50 / 32 .	37.62	0.09	22.39	22.31	2.37	4.48	11.58	-0.01	0.00	100.85	grt	1336
TA95	50 / 33 .	37.12	0.13	21.83	22.20	2.12	4.31	11.97	0.01	-0.01	99.70	grt	1379
TA95	50 / 34 .	35.29	0.09	20.76	18.16	1.68	3.18	11.89	0.68	0.04	91.80	^{fx}Grt	1422
TA95	50 / 35 .	12.02	0.02	7.99	18.06	0.83	1.15	14.73	0.04	0.05	54.91	^{fx}Grt	1465
TA95	50 / 36 .	37.28	0.29	21.61	21.64	1.44	4.20	12.71	0.14	0.02	99.36	grt	1508
TA95	50 / 37 .	37.30	0.42	21.76	22.17	1.31	4.35	12.79	0.06	0.00	100.15	grt	1551
TA95	50 / 38 .	37.31	0.36	21.57	22.25	1.30	4.23	12.64	0.10	0.01	99.80	grt	1594
TA95	50 / 39 .	37.60	0.13	22.03	22.25	1.10	4.41	12.71	0.01	-0.01	100.24	grt	1637
TA95	50 / 40 .	29.28	36.94	2.19	0.94	0.08	-0.05	27.44	0.03	0.01	96.90	^{incl}grt	1680
TA95	50 / 41 .	39.04	0.21	21.48	19.46	0.82	3.91	12.93	0.30	0.00	98.17	grt	1724
TA95	50 / 42 .	37.69	0.20	21.95	22.46	0.94	4.50	12.67	0.02	0.00	100.46	grt	1767
TA95	50 / 43 .	40.35	0.14	23.90	21.86	0.87	4.91	12.33	0.02	0.00	104.44	grt	1810
TA95	50 / 44 .	40.90	0.15	23.11	22.40	0.89	5.07	11.37	0.04	-0.01	104.02	grt	1853
TA95	50 / 45 .	38.96	0.29	23.22	22.20	0.85	4.52	10.65	0.02	0.00	100.72	grt	1896
TA95	50 / 46 .	37.39	0.26	21.86	23.49	1.06	4.65	11.45	0.02	-0.01	100.17	grt	1939
TA95	50 / 47 .	29.57	36.73	1.49	0.64	0.04	-0.03	27.91	0.07	0.02	96.52	ttn	1982
TA95	50 / 48 .	29.20	38.23	1.47	0.62	0.05	0.01	28.02	0.02	-0.01	97.66	ttn	2025
TA95	50 / 49 .	29.23	37.81	1.49	0.66	0.02	-0.08	27.92	-0.01	0.02	97.16	ttn	2068
TA95	50 / 50 .	29.28	37.70	1.36	0.59	0.06	-0.10	27.77	0.01	0.00	96.76	ttn	2111
TA95	51 / 1 .	41.14	1.65	13.95	15.57	0.13	10.01	11.60	1.71	1.11	96.90	amp	
TA95	52 / 1 .	39.52	0.32	20.51	10.45	0.10	5.63	16.57	0.70	0.27	94.08	inclusion	
TA95	53 / 1 .	48.75	0.49	5.86	10.48	0.16	10.76	20.88	0.92	0.02	98.36	cpx	
TA95	54 / 1 .	48.16	0.57	5.54	10.18	0.16	10.56	21.93	0.86	0.00	97.98	cpx	
TA95	55 / 1 .	29.33	37.48	1.75	0.52	0.05	-0.01	28.21	0.00	0.00	97.34	ttn	
TA95	56 / 1 .	49.85	0.36	3.80	9.41	0.10	11.68	22.74	0.70	0.00	98.70	cpx	
TA95	57 / 1 .	41.56	1.40	13.83	15.36	0.11	10.24	11.60	1.65	0.95	96.72	amp (cpx)	
TA95	58 / 1 .	67.32	0.03	20.00	0.18	0.02	0.01	0.21	11.44	0.02	99.23	incl	
TA95	59 / 1 .	37.24	0.30	27.41	7.62	0.04	0.17	22.82	0.03	0.01	95.64	incl	
TA95	60 / 1 .	27.09	0.03	19.29	25.33	0.50	15.00	0.08	0.02	0.04	87.42	fx	
TA95	61 / 1 .	37.58	0.07	29.94	5.46	0.07	0.16	23.57	0.02	0.01	96.90	incl	
TA95	62 / 1 .	37.86	0.20	21.21	22.06	0.81	4.41	12.26	0.02	0.01	98.88	incl	
TA95	63 / 1 .	48.31	0.46	5.84	10.14	0.16	10.59	21.49	1.00	0.00	98.06	cpx	
TA95	64 / 1 .	39.33	0.12	17.51	14.97	0.08	8.95	12.49	0.35	0.26	94.06	^{fx}cpx	
TA95	65 / 1 .	37.03	0.03	21.83	22.53	1.06	2.53	14.16	0.22	0.04	99.43	^{fx}cpx	

Sample	Point	SiO2	TiO2	Al2O3	FeO	MnO	MgO	CaO	Na2O	K2O	Total	Comment	Distance (µm)
TA95	66 / 1 .	38.21	0.18	21.79	6.17	0.05	4.45	20.90	0.14	0.06	92.00	fxamp	
TA95	67 / 1 .	28.77	37.62	1.56	0.50	0.04	-0.06	28.20	0.02	0.01	96.72	ttn	
TA95	68 / 1 .	48.60	0.61	5.28	9.03	0.15	11.19	22.48	0.80	0.01	98.18	cpx	
TA95	69 / 1 .	48.27	0.53	5.35	9.59	0.20	10.91	22.30	0.91	0.02	98.10	cpx	
TA95	70 / 1 .	48.85	0.47	5.27	9.23	0.21	11.01	22.31	1.01	-0.01	98.35	cpx	
TA95	71 / 1 .	48.38	0.46	5.21	9.22	0.18	10.89	22.22	0.89	0.02	97.46	cpx	
TA95	72 / 1 .	37.78	1.07	14.71	17.87	0.14	11.09	8.70	1.17	0.81	93.34	low total (amp)	
TA95	73 / 1 .	48.74	0.52	5.44	9.46	0.13	10.81	22.04	0.95	0.00	98.09	cpx	
TA95	74 / 1 .	41.47	1.74	14.28	15.63	0.14	9.90	11.77	1.76	1.09	97.78	amp	
TA95	75 / 1 .	48.17	0.05	35.30	0.17	-0.01	0.15	0.19	1.32	10.15	95.49	pl	
TA95	76 / 1 .	63.84	0.02	22.64	0.05	-0.01	0.00	1.13	9.96	1.10	98.77	pl	
TA95	77 / 1 .	48.10	0.01	36.87	0.18	0.01	0.27	0.14	0.79	11.05	97.42	pl	
TA95	80 / 1 .	42.54	0.02	33.29	0.17	-0.02	-0.02	22.58	1.19	0.01	99.80	pl	0
TA95	80 / 2 .	48.10	0.01	29.92	0.43	0.01	-0.03	17.08	3.47	0.01	99.01	pl	135
TA95	80 / 3 .	47.72	0.01	29.89	0.56	-0.01	-0.02	17.51	4.00	0.01	99.71	pl	270
TA95	80 / 4 .	65.15	-0.01	21.47	0.13	0.00	-0.02	2.44	10.59	0.06	99.85	pl	404
TA95	80 / 5 .	50.56	0.02	29.06	0.41	0.02	-0.01	15.41	5.03	0.10	100.60	pl	539
TA95	81 / 1 .	50.25	0.00	29.18	0.25	0.01	0.00	15.37	5.09	0.01	100.16	pl	
TA95	82 / 1 .	45.68	0.02	31.11	0.20	0.02	-0.03	18.87	3.34	0.03	99.27	pl	
TA95	83 / 1 .	47.07	-0.04	29.93	0.61	0.00	-0.02	17.90	3.66	0.01	99.19	pl	
TA95	84 / 1 .	59.23	0.02	24.18	0.74	0.02	0.01	7.00	8.07	0.32	99.62	pl	
TA95	85 / 1 .	59.87	0.00	22.93	1.44	0.02	0.01	6.90	9.27	0.04	100.48	pl	
TA95	86 / 1 .	59.18	-0.02	24.37	0.36	0.02	-0.01	7.48	8.19	0.04	99.64	pl	
TA95	87 / 1 .	57.27	0.03	25.67	0.16	0.00	-0.01	9.27	7.65	0.06	100.11	pl	
TA95	88 / 1 .	60.27	-0.03	24.90	0.34	0.02	-0.02	7.60	8.63	0.08	101.84	pl	
TA95	89 / 1 .	51.82	0.09	27.98	0.86	0.01	0.05	13.60	4.90	0.41	99.71	pl	
TA95	90 / 1 .	55.94	0.00	27.43	1.04	0.04	0.04	6.85	6.60	2.63	100.58	pl	
TA95	91 / 1 .	55.73	0.02	26.82	0.23	0.02	0.03	10.70	6.63	0.06	100.26	pl	
TA95	92 / 1 .	51.99	0.05	28.51	0.39	0.01	0.02	14.65	5.40	0.02	101.04	pl	
TA95	93 / 1 .	54.53	0.00	25.97	0.59	0.01	0.03	11.65	6.69	0.02	99.48	pl	
TA95	94 / 1 .	54.22	0.04	25.47	2.12	0.02	0.69	10.58	7.09	0.03	100.26	pl	
TA95	95 / 1 .	61.65	0.00	24.87	0.25	0.01	0.04	2.12	9.07	2.05	100.08	pl	
TA95	96 / 1 .	50.40	0.06	28.47	0.75	0.04	-0.01	15.14	4.78	0.03	99.68	pl	
TA95	97 / 1 .	54.26	0.02	28.11	0.05	0.00	-0.01	10.59	5.36	0.55	98.95	pl	
TA95	98 / 1 .	48.15	0.00	29.64	0.50	0.03	-0.03	16.93	3.49	0.03	98.84	pl	
TA95		52.80	0.00	27.40	0.70	0.00	0.00	13.20	5.30	0.40		saus1	
TA95		54.80	0.00	27.00	0.50	0.00	0.00	11.10	5.90	0.70		saus2	
TA95		53.50	0.00	27.80	0.60	0.00	0.00	11.90	5.30	0.90		saus3	
TA95		54.70	0.00	27.20	0.30	0.00	0.00	11.30	5.90	0.60		saus4	
TA95		54.00	0.00	27.30	0.40	0.00	0.00	12.30	5.70	0.30		saus5	
TA95		51.80	0.00	27.80	0.90	0.00	0.00	14.30	5.00	0.10		saus6	
TA95		53.70	0.00	27.00	0.70	0.00	0.00	12.20	5.70	0.40		saus7	
TA95		51.20	0.00	28.20	0.80	0.00	0.00	14.90	4.60	0.20		saus8	
TA95		52.80	0.00	27.50	0.70	0.00	0.00	13.40	5.40	0.30		saus9	
TA95		50.30	0.00	28.30	1.00	0.00	0.00	15.80	4.40	0.10		saus10	
TA103	1 / 1 .	64.29	0.00	23.43	0.05	0.00	-0.01	4.56	9.28	0.07	101.69	pl1	
TA103	2 / 1 .	44.11	0.68	12.07	13.73	0.31	12.00	11.53	1.99	0.88	97.31	amp1	
TA103	3 / 1 .	38.43	0.11	24.22	10.78	0.28	0.02	23.84	0.02	0.00	97.70	ep1	
TA103	4 / 1 .	65.10	0.00	22.99	0.09	0.01	-0.01	3.93	9.54	0.06	101.72	pl2	
TA103	5 / 1 .	63.43	0.01	23.57	0.12	0.00	-0.01	4.79	8.93	0.08	100.93	pl3	
TA103	6 / 1 .	2.07	13.98	0.17	70.36	0.09	0.04	1.73	0.01	0.00	88.45	ilm (ox1)	
TA103	7 / 1 .	32.78	35.58	2.64	0.79	0.09	-0.08	26.76	0.99	0.00	99.63	Ttn (ox2)	
TA103	8 / 1 .	63.93	0.00	23.50	0.09	0.01	-0.02	4.65	9.01	0.07	101.26	pl4	
TA103	9 / 1 .	43.98	0.66	11.68	13.33	0.30	12.05	11.60	1.93	0.75	96.28	amp2	
TA103	10 / 1 .	37.91	0.12	24.15	10.90	0.25	0.03	23.95	-0.01	0.00	97.30	ep2	
TA103	11 / 1 .	64.61	0.01	23.27	0.14	0.00	-0.01	4.00	9.42	0.06	101.52	pl5	
TA103	12 / 1 .	44.36	0.66	11.63	13.29	0.32	12.11	11.72	1.96	0.74	96.79	amp3	
TA103	13 / 1 .	38.30	0.09	24.88	10.31	0.23	0.00	23.90	0.00	-0.01	97.72	ep3	
TA103	14 / 1 .	64.67	0.00	22.61	0.15	0.00	0.00	3.71	9.69	0.06	100.89	pl6	
TA103	15 / 1 .	63.99	0.00	23.15	0.10	-0.01	-0.01	4.25	9.19	0.10	100.78	pl7	
TA103	16 / 1 .	37.82	0.20	22.78	12.21	0.14	-0.01	23.89	0.01	0.01	97.07	ep4	
TA103	17 / 1 .	43.83	0.66	11.95	13.65	0.31	12.10	11.67	1.93	0.77	96.87	amp4	
TA103	18 / 1 .	37.64	0.14	23.10	12.09	0.32	-0.02	23.70	0.01	0.00	96.99	ep5	
TA103	19 / 1 .	37.99	0.09	24.05	11.17	0.20	-0.02	23.89	0.00	0.01	97.41	ep6	
TA103	20 / 1 .	44.59	0.64	11.45	13.55	0.35	12.42	11.74	1.87	0.71	97.31	amp5	
TA103	21 / 1 .	36.79	2.26	15.20	13.54	0.15	14.05	0.46	0.14	6.82	89.40	fxbt1	
TA103	22 / 1 .	37.61	2.23	15.72	14.21	0.17	14.57	0.26	0.14	8.32	93.23	bt2	
TA103	23 / 1 .	65.23	0.01	18.42	0.41	0.01	0.29	0.04	0.08	16.99	101.46	mxbt3	
TA103	24 / 1 .	33.12	1.00	15.83	17.24	0.24	17.68	0.17	0.07	3.72	89.06	fxbt4	
TA103	25 / 1 .	33.29	0.01	16.51	16.74	0.20	18.54	0.16	1.19	0.02	86.67	fxbt5	
TA103	26 / 1 .	68.11	0.00	20.71	0.39	-0.02	0.01	1.14	9.96	1.71	102.03	mxbt6	
TA103	27 / 1 .	63.78	0.01	23.44	0.12	0.00	-0.02	4.65	9.04	0.08	101.12	pl8	
TA103	28 / 1 .	64.06	-0.01	23.55	0.18	0.03	-0.02	4.69	9.05	0.08	101.64	pl9	
TA103	29 / 1 .	38.28	0.10	24.51	10.62	0.23	0.01	23.92	0.00	-0.02	97.67	ep7	

Sample	Point	SiO2	TiO2	Al2O3	FeO	MnO	MgO	CaO	Na2O	K2O	Total	Comment	Distance (µm)
TA103	30 / 1 .	45.03	0.56	11.55	13.33	0.32	12.48	11.57	2.01	0.61	97.45	amp6	
TA103	31 / 1 .	44.15	0.68	11.95	13.82	0.31	11.93	11.47	2.09	0.85	97.23	amp7	
TA103	32 / 1 .	44.07	0.68	12.00	13.83	0.32	11.98	11.55	2.06	0.77	97.27	amp8	
TA103	33 / 1 .	64.93	0.00	22.77	0.13	0.01	-0.01	3.71	9.48	0.06	101.09	pl10	
TA103	34 / 1 .	44.14	0.67	11.80	13.72	0.33	12.10	11.62	1.92	0.82	97.13	amp9	
TA103	35 / 1 .	64.01	0.00	23.06	0.15	0.00	-0.01	4.18	9.41	0.08	100.89	pl11	
TA103	36 / 1 .	37.78	0.12	24.39	10.89	0.23	0.00	23.97	0.00	0.01	97.38	ep8	
TA103	37 / 1 .	64.17	0.00	22.94	0.11	0.01	-0.03	4.23	9.11	0.08	100.65	pl12	
TA103	38 / 1 .	44.52	0.63	11.65	13.31	0.34	12.36	11.37	1.96	0.78	96.92	amp10	
TA103	39 / 1 .	44.40	0.67	11.84	13.72	0.33	12.19	11.63	1.96	0.81	97.56	amp11	
TA103	40 / 1 .	64.50	0.01	23.05	0.19	0.00	-0.02	4.19	9.32	0.07	101.34	pl13	
TA103	41 / 1 .	38.00	2.35	15.83	13.49	0.19	14.88	0.20	0.09	8.65	93.68	bt7	
TA103	42 / 1 .	38.05	0.10	23.83	11.32	0.36	-0.01	23.67	0.01	-0.01	97.34	ep9	
TA103	43 / 1 .	44.11	0.63	12.61	13.70	0.38	11.95	11.52	2.09	0.71	97.69	amp12	
TA103	44 / 1 .	48.20	0.51	14.10	11.08	0.23	9.67	9.74	3.42	0.66	97.61	^{mx}amp13	
TA103	45 / 1 .	65.15	0.00	22.62	0.17	0.04	-0.02	3.61	9.74	0.07	101.41	pl14	
TA103	46 / 1 .	37.59	2.16	15.77	13.69	0.18	15.06	0.57	0.13	7.85	92.99	bt8	
TA103	47 / 1 .	61.51	3.57	16.37	0.55	0.02	0.45	4.12	0.04	15.03	101.67	^{mx}bt9	
TA103	48 / 1 .	38.24	0.13	24.22	10.87	0.19	0.01	23.95	0.00	0.02	97.64	ep10	
TA103	49 / 1 .	38.63	0.10	25.23	9.98	0.40	-0.02	23.93	-0.01	-0.01	98.26	ep11	
TA103	50 / 1 .	38.17	0.13	24.39	10.98	0.18	0.04	23.94	-0.02	0.00	97.83	ep12	
TA103	51 / 1 .	44.10	0.66	11.88	13.79	0.37	12.05	11.69	1.97	0.78	97.29	amp14	
TA103	52 / 1 .	28.41	1.56	11.93	10.00	0.12	12.26	13.16	0.10	5.08	82.61	^{fx}bt10	
TA103	53 / 1 .	44.26	0.64	11.80	13.65	0.32	12.14	11.72	2.01	0.71	97.26	amp15	
TA103	54 / 1 .	65.40	0.01	22.64	0.26	-0.01	-0.01	3.38	9.65	0.07	101.42	pl15 (amp15.2)	